UNIVERSIDADE DE LISBOA
INSTITUTO SUPERIOR TÉCNICO

Development of a Radiation Detection System coupled to an Unmanned Aerial Vehicle for Security and Defence applications

Luís Miguel Cabeça Marques

Supervisor: Doctor José Pedro Miragaia Trancoso Vaz
Co-Supervisor: Doctor Alberto Manuel Martinho Vale

Thesis approved in public session to obtain the PhD Degree in Technological Physics Engineering

Jury final classification: Pass with Distinction and Honour

2025

UNIVERSIDADE DE LISBOA
INSTITUTO SUPERIOR TÉCNICO

Development of a Radiation Detection System coupled to an Unmanned Aerial Vehicle for Security and Defence applications

Luís Miguel Cabeça Marques

Supervisor: Doctor José Pedro Miragaia Trancoso Vaz
Co-Supervisor: Doctor Alberto Manuel Martinho Vale

Thesis approved in public session to obtain the PhD Degree in Technological Physics Engineering

Jury final classification: Pass with Distinction and Honour

Jury

Chairperson: Doctor Luís Paulo da Mota Capitão Lemos Alves, Instituto Superior Técnico, Universidade de Lisboa;

Members of the Committee:

Doctor Susana Isabel Barreto de Miranda Sargento, Universidade de Aveiro;
Doctor Luís José Proença de Figueiredo Neves, Faculdade de Ciências e Tecnologia, Universidade de Coimbra;
Doctor José Pedro Miragaia Trancoso Vaz, Instituto Superior Técnico, Universidade de Lisboa;
Doctor Alexandra Bento Moutinho, Instituto Superior Técnico, Universidade de Lisboa;
Colonel André Duarte Martins Caldeira Simões, Força Aérea Portuguesa.

2025

To my beloved wife, Regina, and our wonderful sons, Tomás and Simão. Your love, patience, and unwavering support have been my greatest source of strength and inspiration. I dedicate this achievement to you.

Acknowledgments

First and foremost, I would like to express my deepest gratitude to my supervisors, professor Pedro Vaz and professor Alberto Vale. Without their guidance and advice this work would not have been possible.

I am also immensely grateful to the Portuguese Air Force Academy for their logistical support and financial assistance, which were crucial for the completion of this research. My sincere thanks go to Major José Gouveia from the Laboratório de Solos e Pavimentos, located at Depósito-Geral de Material da Força Aérea, and to Captain Ricardo Poças from the Esquadrilha de Defesa NRBQ, located at Centro de Treino e Sobrevivência da Força Aérea, for their logistical support, enabling the practical aspects of my research to be conducted smoothly.

I extend my sincere thanks to the Centro de Investigação da Academia da Força Aérea for their invaluable support and understanding throughout my work. I am especially grateful to Lieutenant Colonel Luís Félix, Major Gonçalo Cruz, Captain Diogo Silva, Lieutenant Vasco Coelho and João Caetano for their exceptional assistance.

My deeply gratitude goes to my wife Regina and two sons Tomás and Simão for their endless patience and understanding throughout this demanding journey. Their love and support have been my anchor during the most challenging times.

I would like to extend my sincere appreciation to the researchers who supported me, Eng. Carlos Cruz and Prof. Luís Alves, for their technical advice and encouragement. I am also grateful to my friend and advisor, Luís Portugal, for his unwavering support and insightful counsel.

To my grandmother Iria and grandfather Armando, who live forever in my heart and were responsible for laying the foundations of my education, I owe my deepest appreciation. Their values and teachings have always been a guiding light in my life.

I am also grateful to my mother, Otília, and her husband, João Tomás, for their unconditional love, affection, and support.

To all my friends, your encouragement and companionship have been a source of strength and motivation.

This journey has been made possible by the collective support, guidance, and love of all these remarkable individuals. Thank you all for your contributions to this significant milestone in my life.

"Success is not the key to happiness.
Happiness is the key to success. If you love
what you are doing, you will be successful."

(Albert Schweitzer)

Abstract

Strengthening the detection and control of Special Nuclear Material (SNM) and other radioactive substances used across sectors such as, among others, Medicine, Industry, Environment, Energy, Agriculture, Space, and Research, is crucial for global security and the safe, sustainable use of radiation sources. SNM, including plutonium and highly enriched uranium, poses significant risks if misused, potentially leading to improvised nuclear devices. The illicit trafficking of radioactive materials also raises concerns about their malicious use in radiological dispersal devices (e.g., "dirty bombs") and radiological exposure devices, with highly disruptive consequences.

Effective control of radiation sources, from cradle to grave, requires stringent oversight during transportation, particularly at borders, airports, and seaports. While advanced detection systems like Radiation Portal Monitors are essential, their high cost and limited deployment create constraints in preventing the illicit trafficking of these hazardous materials.

This thesis details the development and optimization of an innovative radiation detection system tailored for security and defence applications in challenging environments with large source-detector distances and concealed sources. Utilizing EJ-200 and EJ-426HD scintillators with silicon photomultipliers, the system simultaneously detects gamma/beta and neutron radiation, respectively. Designed for unmanned aerial vehicles (UAVs), it offers a compact, lightweight, and cost-effective design, validated through Monte Carlo simulations, laboratory experiments, and field tests. When performing a radiological inspection of a maritime shipping container cargo the radiation detection system successfully detected and localized a 4 MBq ^{137}Cs radioactive source and a 1.45 GBq $^{241}Am-Be$ neutron source. Using a novel in-house search algorithm with informative path planning and profit functions, the system achieved superior gamma-ray source localization accuracy, and a better calculation of source activity compared to predefined paths, while also reducing inspection time through an optimized exit condition. The system's modular design and UAV integration offer an easily replicable, affordable alternative or complement to existing radiation detection technologies.

Keywords: UAV, Radiological inspection, Informative Path Planning, Scintillation detector, Radiological and Nuclear threats.

Resumo

A deteção e controlo de materiais nucleares especiais (SNM) e substâncias radioativas em setores como a medicina, indústria, ambiente, espaço e a investigação são cruciais para a segurança global e a utilização segura das fontes de radiação. SNM, como o plutónio e o urânio altamente enriquecido, representam riscos significativos, pois podem ser utilizados em dispositivos nucleares improvisados. Além disso, o tráfico ilícito de materiais radioativos levanta preocupações relativamente ao seu potencial uso em dispositivos de dispersão radiológica (e.g., "bombas sujas") e dispositivos de exposição radiológica, com consequências graves e disruptivas.

O controlo eficaz das fontes de radiação exige uma supervisão rigorosa durante o transporte, especialmente em postos fronteiriços, aeroportos e portos marítimos. Para tal são normalmente utilizados portais de monitorização de radiação, contudo o seu elevado custo e utilização limitada dificultam a prevenção do tráfico ilícito.

A tese descreve o desenvolvimento de um sistema inovador de deteção de radiações, concebido para aplicações de Segurança e Defesa em ambientes caracterizados por grandes distâncias entre a fonte e o detetor e pela presença de fontes ocultas. O sistema utiliza cintiladores EJ-200 e EJ-426HD, com fotomultiplicadores de silício, para detetar simultaneamente radiação gama/beta e neutrões respetivamente. Projetado para veículos aéreos não tripulados (VANTs), oferece um desenho compacto e leve. Validado por simulações de Monte Carlo, testes laboratoriais e de campo, foi capaz de detetar e localizar fontes radioativas de ^{137}Cs (4 MBq) e de $^{241}Am - Be$ (1.45 GBq). A utilização de um novo algoritmo, com planeamento de caminhos informativo e funções custo, aumentou a exatidão na localização e quantificação da fonte, reduzindo igualmente o tempo de inspeção com a utilização de uma condição de saída. O desenho modular, o custo efetivo, a integração num VANT e a facilidade de replicação tornam este sistema uma alternativa ou complemento às tecnologias de deteção de radiação existentes.

Palavras-chave: VANT, Inspeção radiológica, Planeamento de caminhos informativo, Detetor de cintilação, Ameaças Radiológicas e Nucleares.

Contents

List of Figures

List of Tables

Acronyms

ADC Analog-to-Digital Converter *(pp. xvii, 26, 27, 84, 213)*
ADS Accelerator Driven System *(p. 35)*
AI Artificial Intelligence *(pp. 54, 173)*
ANSI American National Standards Institute *(pp. 35, 39, 41)*
APD Avalanche Photodiode *(pp. 26, 28, 46)*
ASP Advanced Spectroscopic Portal *(p. 3)*

BGO Bismuth Germanate *(pp. 7, 43, 49, 50)*

CBRN Chemical, Biological, Nuclear, and Radiological *(p. 173)*
CBRNE Chemical, Biological, Radiological, Nuclear, and high-yield Explosives *(p. 54)*
CLLB Cerium-doped cesium lithium lanthanum bromide *(p. 45)*
CLLC Cerium-doped cesium lithium lanthanum chloride *(p. 45)*
CLYC Cerium-doped cesium lithium yttrium chloride *(pp. 45, 50–52)*
CMOS Complementary Metal–Oxide–Semiconductor *(p. 49)*
CNC Computer Numerical Control *(pp. 73, 74, 90)*
COTS Commercially available off-the-shelf *(pp. 3, 43, 48)*
cps Counts per second *(p. 97)*
CSV Comma-Separated Values *(pp. 64, 144)*
CZT Cadmium Zinc Telluride *(pp. 6, 7, 25, 43, 46, 48–51, 164)*

DGNSS Differential GNSS *(pp. 62, 90)*
DHS Department of Homeland Security *(pp. 2, 51)*

EW Energy Windowing *(pp. 38, 39, 90, 168)*

FDNPP Fukushima Daiichi Nuclear Power Plant *(pp. 46–48)*
FOV Field of View *(p. 63)*
FPR False Positive Rate *(p. 40)*
FRIENDS Fleet of drones for radiological inspection, communication, and rescue *(pp. 6, 50)*

GAGG(Ce)	Cerium-doped gadolinium aluminium gallium garnet *(p. 47)*
GM	Geiger-Muller *(pp. 6, 25, 42, 46, 47, 49, 76)*
GNSS	Global Navigation Satellite System *(pp. 6, 53, 54, 61, 62, 64, 89, 90, 99, 102, 110, 140, 143, 144, 147, 162, 165, 166, 172, 173)*
GPIO	General-Purpose Input/Output *(pp. 165, 214, 215)*
HDOP	Horizontal Dilution of Precision *(pp. 61, 62)*
HDPE	High-Density Polyethylene *(pp. xviii, 30, 51, 72, 73, 75, 77–81, 90, 167)*
HEU	Highly Enriched Uranium *(pp. 1, 7, 32–34, 164)*
HMWPE	High Molecular Weight Polyethylene *(pp. 30, 72–75, 90)*
HPGe	High-Purity Germanium *(pp. 25, 46, 47)*
IAEA	International Atomic Energy Agency *(pp. 1, 33, 39, 52)*
IEC	International Electrotechnical Commission *(p. 35)*
IMU	Inertial Measurement Unit *(pp. 61, 62, 90, 172)*
IND	Improvised Nuclear Device *(pp. 1, 32, 163)*
IPP	Informative Path Planning *(pp. 57, 58, 144, 152)*
IRSS	Intelligent Radiation Sensor Systems *(pp. 39, 40)*
ISR	Intelligence, Surveillance, and Reconnaissance *(p. 5)*
ITDB	Incident and Trafficking Database *(pp. 1, 2, 33, 34)*
LiDAR	Light Detection and Ranging *(pp. xvii, 6, 48, 62, 63, 89, 94, 138, 143, 147, 153)*
LSF	Least Squares Fitting *(pp. 39, 90)*
MARIA	Mobile Application for Radiation Intensity Assessment *(p. 47)*
MC	Monte Carlo *(pp. xvii, 4, 9, 11, 15, 24, 40, 57, 67, 71, 73, 76, 77, 80, 81, 83, 85, 89, 90, 135, 167, 168, 171)*
MCA	Multichannel Analyzer *(pp. xxiv, 27, 59, 61, 64, 76, 89, 165, 213–215)*
MCNP	Monte Carlo N-Particle *(pp. xxiii, 11, 71, 72, 82, 83, 171)*
MCS	Multi-Channel Scaling *(p. 215)*
MDA	Minimum Detectable Activity *(pp. 104, 114, 172)*
MLE	Maximum Likelihood Estimation *(pp. 9, 39, 40, 42, 57, 58, 60, 64, 67–69, 94, 99, 102, 108, 110, 113, 114, 118, 121, 126, 134, 138, 143–145, 147–150, 153, 154, 156, 164–166)*
MODES SNM	Modular Detection System for Special Nuclear Material *(pp. 50, 51)*
MORC	Material Out of Regulatory Control *(p. 33)*
MRDS	Mobile Radiation Detection System *(pp. 3–5, 9, 10, 13–15, 35–38, 41, 50, 51, 53, 55–57, 61, 62, 89, 114, 116–119, 134, 161)*
MSD	Mean Squared Deviation *(p. 119)*

MURS Mobile Urban Radiation Search *(pp. 50, 51)*

NORM Naturally Occurring Radioactive Materials *(pp. 1, 2, 6, 7, 31, 33, 35–38, 49, 50, 90, 164, 168)*

NPP Nuclear Power Plant *(pp. 5, 7, 36, 46, 47, 163)*

PET-G Polyethylene Terephthalate Glycol *(p. 72)*

PF Particle Filter *(pp. 40, 42)*

PHA Pulse-Height Analysis *(pp. 27, 215)*

PIN P-type, Intrinsic, and N-type *(pp. 46, 49)*

PLA Polylactic Acid *(pp. 72, 87)*

PMT Photomultiplier Tube *(pp. 6, 8, 12, 26, 28, 29, 45–47, 165, 171)*

PRD Personal Radiation Detectors *(pp. 34, 35, 51)*

PSD Pulse Shape Discrimination *(pp. 26, 30, 44, 45, 52)*

PVT Polyvinyltoluene *(pp. 2, 38, 39, 45, 163)*

Rad Map Radiological multi-sensor analysis platform *(pp. 50, 51)*

RDD Radiological Dispersal Device *(pp. 1, 32, 59, 163)*

RED Radiological Exposure Device *(pp. 1, 32, 163)*

REWARD Real-time Wide Area Radiation surveillance system *(pp. 50, 51)*

RID Radionuclide Identification Device *(p. 34)*

RN Radiological and Nuclear *(pp. 6, 31, 35, 46, 47, 50, 53, 163, 173)*

RPM Radiation Portal Monitors *(pp. 2, 3, 7, 13, 34–36, 38, 39, 44, 45, 55, 56, 118, 162–164, 166, 170, 172)*

RTK Real-Time Kinematic *(pp. 62, 90, 173)*

SAM Spectral Angle Mapping *(pp. 39, 90)*

SAR Search and rescue *(pp. 47, 48)*

SCoTSS Safety and Security Compton Telescope *(p. 47)*

SD Standard Deviation *(pp. 94, 98, 99, 102, 103)*

SDK Simulation Development Kit *(p. 64)*

SF Spontaneous Fission *(pp. 18, 23, 24, 30, 33)*

SiPM Silicon Photomultiplier *(pp. xvii, xxiv, 6, 8, 10–12, 26, 29, 37, 45–49, 53, 56, 59–61, 64, 76, 89, 90, 164, 165, 167, 168, 171, 213–215)*

SLAM Simultaneous Localization and Mapping *(p. 43)*

SLIMPORT Sistema mobile per analisi non distruttive e radiometriche *(pp. 50, 51)*

SNM Special Nuclear Material *(pp. 1, 2, 4, 6, 7, 21, 24, 31–33, 38, 50, 51, 55, 56, 90, 163, 164)*

SNR Signal-to-Noise Ratio *(pp. xviii, 87, 168)*

SNS Spallation Neutron Source *(p. 35)*

SORDS-3D 3D Stand-Off Radiation Detection System *(p. 47)*

SORIS Stand-Off Radiation Imaging System *(p. 47)*

STUD Step + Up and Down *(pp. xxii, 117, 121, 125–127, 131, 132, 135, 137, 138, 153–161, 169, 170)*

SUAS Small Unmanned Aerial System *(p. 24)*

TENORM Technologically Enhanced NORM *(p. 36)*

TPR True Positive Rate *(p. 40)*

TTL Transistor-Transistor-Logic *(pp. 60, 165, 214)*

UARM Unmanned Airplane for Radiation Monitoring system *(p. 48)*

UAV Unmanned Aerial Vehicle *(pp. 3, 5, 6, 9, 10, 18, 35, 47–51, 54, 57, 58, 63, 162, 163, 167, 170, 172, 173)*

UD Up and Down *(pp. xx–xxii, 116, 117, 121–123, 125–127, 132, 134, 135, 137, 138, 144–151, 153–161, 166, 169, 170)*

UGV Unmanned Ground Vehicle *(pp. 5, 47, 51, 54)*

VCI Volumetric Compton Imaging *(p. 47)*

VTOL Vertical Take-Off and Landing *(pp. 5, 48, 50, 54, 57)*

WGPu Weapons-Grade plutonium *(pp. 24, 39)*

Chemical Symbols

^{241}Am	americium-241 *(pp. xviii, xxiii, 32, 34, 39, 61, 83, 85, 90, 168)*
$^{241}Am - Be$	americium-241–beryllium *(pp. ix, xi, xvii, xviii, 7, 23, 24, 30, 33, 50, 71–73, 76–82, 93, 97, 98, 107, 108, 110, 152, 164–167, 169, 172)*
^{10}B	boron-10 *(pp. xvii, 28, 29, 44)*
BF_3	boron trifluoride *(pp. 7, 8, 29)*
$CdTe$	cadmium telluride *(pp. 49, 50)*
^{252}Cf	californium-252 *(pp. 7, 18, 23, 24, 32, 33, 50, 164, 165, 173)*
^{250}Cm	curium-250 *(p. 18)*
^{60}Co	cobalt-60 *(pp. 17, 32, 39)*
^{134}Cs	cesium-134 *(p. 32)*
^{137}Cs	cesium-137 *(pp. ix, xi, xviii–xxiv, 9, 17, 32, 34, 39–42, 59, 64, 67, 76, 83, 85–87, 90, 93, 94, 97–99, 101, 103–110, 114, 121, 122, 124–131, 134, 137–144, 151, 154–161, 166–170, 172)*
$CsI(Tl)$	thallium-doped cesium iodide *(pp. xviii, xxiii, 6, 7, 42, 43, 46–49, 52, 59–61, 82–87, 164, 165, 168)*
^{3}He	helium-3 *(pp. xvii, 2, 7, 8, 11, 28, 29, 38, 45, 53, 58, 61, 76, 164, 171)*
^{4}He	helium-4 *(pp. 17, 30)*
^{131}I	iodine-131 *(p. 32)*
^{192}Ir	iridium-192 *(p. 32)*
^{138}La	lanthanum-138 *(p. 45)*
$LaBr_3(Ce)$	cerium-doped lanthanum bromide *(pp. 38, 46, 47, 50)*
$TlBr$	thallium bromide *(p. 45)*
$ZnS : {}^{6}LiF$	lithium-6-fluoride and zinc sulfide phosphor *(pp. 8, 29)*
^{6}Li	lithium-6 *(pp. xvii, 11, 28, 29, 50, 60, 61, 165, 167, 171)*
$ZnS : Ag$	silver activated zinc sulfide *(p. 60)*
^{6}LiF	lithium-6-fluoride *(p. 60)*

^{54}Mn	manganese-54 *(p. 42)*
$NaI(Tl)$	thallium-doped sodium iodide *(pp. xvii, 3, 7, 38–40, 43, 46, 47, 49, 52, 54, 61, 161, 170)*
^{63}Ni	nickel-63 *(p. 54)*
^{210}Po	polonium-210 *(p. 32)*
^{239}Pu	plutonium-239 *(p. 18)*
^{240}Pu	plutonium-240 *(pp. 18, 24)*
^{238}Pu	plutonium-238 *(p. 32)*
$^{239}Pu-Be$	plutonium-239–beryllium *(pp. 7, 33, 34, 50)*
^{226}Ra	radium-226 *(pp. 17, 32, 39)*
^{106}Ru	ruthenium-106 *(p. 32)*
^{90}Sr	strontium-90 *(pp. 19, 32, 59, 83, 84, 165)*
^{232}Th	thorium-232 *(p. 18)*
^{99m}Tc	technetium-99m *(pp. 39, 90)*
^{3}H	tritium *(p. 36)*
^{235}U	uranium-235 *(p. 18)*
^{238}U	uranium-238 *(pp. 17, 18, 39)*
^{90}Y	yttrium-90 *(pp. 19, 84)*

1

Introduction

1.1 Motivation

Radioactive materials and sources used in medicine, industry, research, and other sectors of activity are characterized by their level of activity and type of ionizing radiation emitted (mainly gamma-rays, electrons and positrons, alpha particles and neutrons). If mishandled, may pose problems to human health due to their detrimental biological effects on human tissue. The extent of the tissue damage depends on various factors, including the duration of exposure, the distance to the radiation source, and the use of protective materials (shielding). The malicious use of radioactive materials and sources, used to produce devices such as Radiological Dispersal Devices (RDDs) and Radiological Exposure Devices (REDs), have the potential to become weapons of massive disruption with huge socioeconomic impact [1].

Special Nuclear Material (SNM), which include radionuclides such as *inter alia*, plutonium and Highly Enriched Uranium (HEU), can be located in a wide range of settings, in civilian and military installations and facilities. These materials are commonly encountered within the nuclear fuel cycle, which includes electricity-producing nuclear fission reactors, fuel manufacturing, reprocessing, and storage facilities. Additionally, SNM can also be found within nuclear-propulsion vessels like submarines, aircraft carriers and ice-breakers. The malevolent use of SNM can lead to the development of an Improvised Nuclear Device (IND) and cause mass casualties.

In Security and Defence scenarios, detecting SNM and other radioactive materials is particularly challenging due to the significant distance between the source and detector, the relatively low energy and intensity of certain gamma-ray sources, the weak emission of some neutron sources (e.g., SNM), and the potential shielding and masking by Naturally Occurring Radioactive Materials (NORM).

Since the Incident and Trafficking Database (ITDB) was established in 1993 by the International Atomic Energy Agency (IAEA), up to the end of 2022, 4075 incidents related to nuclear and other radioactive material out of regulatory control (including trafficking incidents) were registered, of which 14% were related to incidents involving nuclear material, 59% involved other radioactive material and around 27% involved contaminated material. Just in 2022, 146 incidents were reported, an increase of 22% compared to 2021, highlighting that unauthorized activities and events involving nuclear and other radioactive materials, including incidents of trafficking and malicious use are still a major concern for world´s Security. Furthermore, approximately 52% of all reported stolen sources in the ITDB have occurred during authorized material transportation. Over the last decade, the percentage has increased to nearly 62%, emphasizing the necessity for enhanced transport security measures [2].

The most effective deterrence of and prevention against the malicious use of SNM and other radioactive materials and sources involves controlling the transportation of such materials and sources at international land borders (border checkpoints), airports, and seaports [3]. Large and expensive Radiation Portal Monitors (RPM) are normally placed at key points to detect gamma-ray radiation and in some cases neutrons [1], [4]. RPM are generally composed of Polyvinyltoluene (PVT)-based scintillators (for gamma-ray detection) and ^{3}He proportional tubes for neutron detection – the scarcity of this gas imposes the deployment of an alternative technology [5]. Besides the substantial purchasing costs, RPM have also high installation[1] and maintenance costs (e.g. mainly due to the PVT life-cycling) [4], [6]. Since RPM are monitoring systems installed in fixed locations, cargo, vehicles, or persons must pass through the detection system plates at a limited speed in order to achieve the required detection efficiency.

Considering that approximately 80% of the world trade is performed by sea, it's crucial to control the goods arriving at seaports mainly in 20 ft and 40 ft[2] long maritime containers [7]. According to Department of Homeland Security (DHS) reports, RPM can inspect nearly 90% of the cargo deemed critical by the DHS, which is only 6% of all incoming cargo, leaving the great majority of containers and imports unchecked. When RPM triggers an alarm, the container undergoes a more extensive and thorough manual inspection, which typically takes 20 minutes [8]. Current portal monitors feature a reasonable rate of false alarms caused by concentrated amounts of NORM (e.g. bananas, fertilizers, granite tile, and ceramics) or other radioactive sources or materials in the cargo. Evaluations of various border scenarios have shown that nearly 80% of false alarms were triggered by such legitimate radioactive materials [9]. The false alarms not only slow down the normal flow of cargo but also reduce the sense of urgency among those who respond to them. For instance, between May 2001 and March 2005, 10,000 false alarms were reported [10]. Furthermore, the expense of temporarily shutting down a freight terminal such as the port of New York can reach $500,000 per hour [11]. To reduce the false alarm rates at large seaports (and international borders) and maintain the normal flow of commerce, enhanced RPM with gamma-ray spectroscopy capability,

[1]Based on 2005 values, the purchase price of an RPM ranges from $49,000 to $60,000, with average installation costs around $200,000.

[2]One foot (ft) is equal to 12 inches, which is equivalent to 30.48 centimeters.

a.k.a. Advanced Spectroscopic Portal (ASP), can be used. Since ASP is based on $NaI(Tl)$ inorganic scintillators or germanium semiconductors, their price can be approximately six to nine times higher than the standard RPM [4], [6]. Another challenge is the screening of transshipment containers since they are offloaded from one ship and after a few days loaded into another ship without passing through the RPM (normally placed at the seaport exit/entrance points). While portable RPM can be a viable alternative to fixed RPM and be deployed in monitoring vehicles and individuals during major events, their widespread adoption in Security and Safety scenarios is hindered by the lack of mobility and their high-cost [12].

While mobile RPM solutions are discussed in the literature, achieving the necessary sensitivity often entails equipping cars or vans with large and costly gamma and neutron detection systems. These mobile platforms are primarily designed for ground-level inspections [13]–[15].

An alternative to RPM is the use of a detector network for identifying and tracking moving radioactive sources. Instead of relying on a single detector, advantages such as improved detection coverage and increased confidence in results can be achieved [16]. Given the extensive coverage area and the need for multiple detectors placed at considerable distances from potential radiation sources, large-volume detection systems are typically required [17].

A combination of fixed and mobile radiation detection systems is proposed in [18] to achieve comprehensive coverage of seaport areas. Since the Mobile Radiation Detection System (MRDS) can be easily deployed, its effectiveness in deterring malicious and terrorist activities could be enhanced [19]. In scenarios involving the inspection of shipping containers at seaports or other critical infrastructures like nuclear facilities, where extensive areas and confined spaces are common, compact MRDS offer significant benefits.

In recent years, significant advancements in technology, engineering, and information systems have facilitated the widespread availability of affordable Commercially available off-the-shelf (COTS) Unmanned Aerial Vehicles (UAVs) such as multirotors (also known as drones). The exceptional maneuverability and ease of operation of multirotors make them ideal for performing inspections at various heights, such as the 13-meter height reached by five stacked maritime shipping containers. However, the tight payload of common multirotors (a few kilograms) implies the use of compact and lightweight detection systems, as highlighted in [20], [21]. The use of cost-effective detection systems can facilitate its reproduction and integration into various mobile platforms. Moreover, deploying autonomous unmanned vehicles, such as a fleet, can significantly reduce inspection and survey times, whether for source detection or mapping contaminated areas.

Therefore, the motivations for this study encompass the following issues, which are thoroughly covered in this thesis:

- The development of the prototype of an innovative MRDS for the detection and localization of gamma/beta and neutron sources in Security and Defence scenarios,

with a specific emphasis on preventing the illicit trafficking of SNMs and other radioactive materials and sources. By integrating the proposed radiation detection system into a multirotor platform, a significant reduction in both the source-detector distance and the size of the detectors was obtained, leading to cost savings while ensuring a consistently high level of detection efficiency;
- Use of state-of the-art Monte Carlo (MC) modelling and simulation tools in support of measurements performed using the aforementioned novel mobile radiation detection system in order to:
  - Perform and optimize the design of radiation detection components (geometry, material composition, physical properties, etc.)[3];
  - Assess the best strategies for an effective detection, localization, identification and quantification of radioactive sources and materials in Security and Defence scenarios.
- Validate the effectiveness of the developed MRDS to detect and localize hidden radioactive sources within shipping containers (proof-of-concept);
- Analyze the impact of using informative path planning over predefined paths to enhance the localization accuracy of gamma-ray sources;
- Assess the most effective methodology for detecting, localizing, identifying, and quantifying radioactive sources and materials, taking into account the algorithms for data acquisition and processing, the estimation of gamma-ray source localization, and the path followed by the MRDS.

1.2 Mobile radiation detection and localization systems

1.2.1 Detection of gamma sources

The right choice of the radiation detection system and the platform that will transport it is very important and depends on the scenario in which the measurements will take place and on the type of source to be detected. The radiation detection system can be carried by a human or by a mobile platform which can be ground-based, aerial-based, or hybrid. Considering the platform operation it can be teleoperated, semi-autonomous, or autonomous. In semi-autonomous and autonomous operations, the path followed by the MRDS should be optimized to achieve the main goal: (i) rapidly detect the radioactive material or source(s), and (ii) accurately localize hot spots[4] or radioactive source(s). This requires determining the uncertainty associated with the platform's position, which depends on the sensor(s) used, and the algorithms to decide the path followed by the MRDS and to estimate the source position. Ultimately, all radiation data and the MRDS

[3]The term "optimize" is used in a broad sense, referring to improving these components to enhance their efficiency, functionality, or effectiveness, rather than in the mathematical sense of finding a minimum or maximum in a cost function.

[4]In radiation mapping, a hot spot refers to a region where the level of radiation or contamination is significantly higher than in the surrounding areas.

coordinates need to be synchronized and processed. Although an algorithm could be designed to allow the MRDS to traverse the entire scenario (randomly or with a certain pattern), the mobile platform would likely lack sufficient energy or time for this. Therefore, reducing the time required to locate a radioactive source is crucial, given the significant effects of radiation on people. This underscores the importance of developing effective mitigation plans, such as defining evacuation routes and no-go zones.

When using ground-based platforms, the higher spatial resolution achieved for monitoring and mapping contaminated areas is advantageous. However, these platforms are constrained to existing road access and obstacles, which often result in significant distances between the source and detector, which require larger detection systems to ensure the required sensitivity [21].

Manned aircraft (fixed-wing and helicopters) are typically used for mapping extensive areas. However, operational limitations, such as a minimum altitude of approximately 150 m and radiation exposure risks to humans, prevent measurements close to the ground. This necessitates the use of large detection systems to achieve the required radiation sensitivity. In contrast, the use of UAV offer several advantages: (i) no crew onboard is necessary; (ii) autonomous or semi-autonomous operation is possible; and (iii) operation at lower altitudes (limited by obstacles on the terrain) and reduced speeds is feasible, improving the spatial resolution of measurements. An example is the use of fixed-wing UAVs, which can operate at speeds of 25-35 m/s, to obtain the radiation map of an extensive contaminated area. Moreover, the use of unmanned helicopters also enables the rapid mapping of extensive areas with a payload of around a few tens of kilograms. However, their cost, operational complexity, and maintenance challenges limit their widespread application. Notable are multirotors, small rotary-wing UAVs with Vertical Take-Off and Landing (VTOL) and hover capability like helicopters, can operate at a few meters from the ground and at very low speed (lower than 1 m/s if necessary), and are also more cost-effective and easier to operate. The high maneuverability of multirotors significantly reduces the distance between the source and the detector, allowing for the use of more compact and affordable detectors. However, their payload capacity is significantly less than that of helicopters or some larger fixed-wing UAVs. Therefore, new solutions for lighter, compact, and cost-effective detection systems are necessary to facilitate their integration in small mobile platforms and replication [21].

Recent breakthroughs in robotics and material processing have paved the way for the creation of increasingly compact unmanned systems, including robots and vehicles. The widespread use of unmanned systems to carry different types of sensors in Intelligence, Surveillance, and Reconnaissance (ISR) missions enables the collection of vital information for decision-makers and intervention teams. The unmanned systems also play a central role in executing tasks that are repetitive or take place in confined, hazardous environments where human presence is unfeasible or risky [22]. For instance, Unmanned Ground Vehicles (UGVs) were employed following the Chernobyl (1986) and Fukushima (2011) Nuclear Power Plant (NPP) accidents and in the decommissioning of old NPP to collect information about radiation doses in high-exposure risk areas for humans. Their payload capability allowed them to transport multiple sensors and to manipulate the environment (e.g. take samples for subsequent laboratory analysis) [23]. However, reports related to limitations between the operator and vehicles, electronics' sensitivity to radiation (semiconductors), and obstacle transposition (due to explosion debris or stairs) were reported. The first use of an UAV in a nuclear accident site was in Fukushima to obtain the initial images of the affected reactor buildings [24]. Subsequently, with the utilization of an unmanned helicopter, a high-resolution dose mapping around the nuclear facility was quickly obtained, surpassing the spatial resolution achieved by manned aircraft (operating at a safe altitude) [25].

The project Fleet of drones for radiological inspection, communication, and rescue (FRIENDS) proposes the use of a fleet of UAVs for the inspection and monitoring of scenarios involving radiological and nuclear threats or those caused by negligence (e.g., decommissioned mines, medical waste). Key outcomes of this project include [26]:

- Cooperative navigation between UAVs and flexibility (fleet of UAVs);
- Creation of an initial scenario map using tools such as Light Detection and Ranging (LiDAR) and Global Navigation Satellite System (GNSS) for a 3D georeferenced map;
- Automatic navigation to obtain a radiation heat map (exploration phase) using a radiation detector such as a Geiger-Muller (GM) counter, and land on identified hot spots for the source characterization (exploitation phase) using a Cadmium Zinc Telluride (CZT) gamma-ray spectrometer;
- Addressing communication problems in these scenarios.

In scenarios involving Radiological and Nuclear (RN) accidents and emergencies, radiation doses typically range from low levels, similar to natural background radioactivity, to much higher levels. In contrast, Security and Defence scenarios often focus on detecting low doses with a very low false alarm rate, necessitating specific requirements for the detectors. Challenges in Security and Defence scenarios may include long distances between the source and detectors (several meters), low-energy gamma sources or low-intensity neutron radiation (e.g., SNM), or for instance the presence of a shielded, concealed or masked source (with a significant concentration of NORM) within a shipping container [21].

In both Security and Safety scenarios, inorganic scintillators or semiconductors are commonly used due to their gamma spectroscopy and spectrometry capabilities and high intrinsic efficiency for radiation detection. However, the high cost of these detectors, the size and shape limitations of the crystals, as well as the significant weight of inorganic scintillators when coupled with photomultiplier tubes, restrict their use in small platforms. The use of Silicon Photomultiplier (SiPM) sensors instead of traditional Photomultiplier Tubes (PMTs) has enabled the use of lighter and more compact inorganic scintillators, facilitating their integration into small platforms, such as the use of two 32.8 cm^3 $CsI(Tl)$ scintillators (each SIGMA-50 weighs 300 g) in a fixed-wing UAV for the mapping of large contaminated areas (NPP post-disaster) [27] or a single $CsI(Tl)$ scintillator integrated in a multirotor to assess the effectiveness of the remediation efforts [28].

The better energy resolution of semiconductor CZT makes it a good alternative to inorganic scintillators with SiPM sensors for application in mobile platforms. However, to reach such energy resolutions CZT is normally limited to crystal volumes of around 1 cm^3. Although recently CZT crystal volumes can go up to 24 cm^3 [29], the high cost still limits their widespread use. In scenarios where the distance between the source and the detector is several meters or when the source has low-energy gamma rays or is shielded, it is necessary to find higher sensitivity sensors and consequently higher volumes to increase the geometric efficiency of the detection system. For example, for the monitoring of uranium anomalies (low dose scenario) near the village of Třebsko, Czech Republic, two 103 cm^3 Bismuth Germanate (BGO) scintillators were used. Despite the significant increase in sensitivity obtained, the payload weight (4 kg) limited the platform flight time and the poor energy resolution of BGO scintillators limited its spectroscopy ability (when compared to $NaI(Tl)$ and $CsI(Tl)$ scintillators) [30].

The next Section will describe the importance of using neutron detection systems as a complement to gamma detectors in Security and Defence scenarios.

1.2.2 Detection of neutron sources

Neutron detection offers, difficulty in shielding, and limited commercial sources, making neutron alarms a clear alert for the detection of nuclear material.

Commercial neutron sources include alpha emitters mixed with lighter nuclides such as $^{241}Am-Be$ and $^{239}Pu-Be$, spontaneous fission sources such as ^{252}Cf, plutonium isotopes, and HEU. Some applications for these sources include soil (e.g. composition and humidity) and concrete measurements, well logging, and the nuclear power industry. The detection of SNM such as plutonium and HEU is very challenging due to the low-energy gamma rays (easily shielded by a few centimeters of high-Z materials or masked using NORM) and the low-intensity neutrons emitted by these sources, in particular the HEU. Therefore, the use of neutron detection systems as a complement to gamma-ray detectors is crucial for the detection of radiological and nuclear threats.

Typically, neutron detection systems used in RPM rely on ^3He proportional counters, but a global shortage has prompted the exploration of alternative technologies and detection systems. A recent study evaluated four alternative technologies for possible use on RPM, namely BF_3 proportional counters, boron-lined proportional counters, lithium-loaded glass fibers, and coated wavelength-shifting plastic fibers, considering the following Security-related requirements [5]:

- High neutron detection efficiency;
- Detect both fast and slow neutron components, accounting for potential attenuation due to shielding or cargo composition (normally due to light Z-materials – neutron moderation); and

- Minimal sensitivity to gamma rays (to reduce false alarms, particularly in the presence of an intense gamma-ray source).

The BF_3 proportional counters met the Security criteria, despite their drawbacks like larger volume, higher voltage, and the use of a hazardous gas [5].

Both ^3He and BF_3 proportional tubes are sensitive to thermal neutrons, of typical kinetic energies 25 meV. However, to detect fast neutrons (kinetic energy above typically 100 keV) it is necessary to use a neutron moderator (hydrogen-rich material). Generally, the moderator shape is either spherical or cylindrical, with a fixed thickness (to have the required moderation), which increases significantly the weight and volume of the detection system [31]. Therefore, research is needed to have more compact, lightweight, and modular moderators for Security and Defence scenarios, for instance allowing the addition or removal of moderator layers according to the energy spectrum of the neutron source.

Recent studies showed that compact SiPM-based $ZnS : {}^6LiF$ plastic scintillator present good thermal neutron detection efficiency with low sensitivity to gamma radiation. Despite this detection system can be a good alternative to ^3He-based technology, further research is needed in terms of light collection improvement and SiPM dark counts suppression (which affects the neutron signals) [32]–[34].

Despite the low light yield of plastic scintillators, which limits their spectroscopy ability, advantages such as low cost, robustness, fast response, and sensitivity to charged particles, gamma-rays, and neutrons, make them the most widely used particle detection system in the fields of Nuclear and Particle Physics. Normally, large volumes and a variety of shapes of plastic scintillators are available with PMT. However, the vibration sensitivity of PMT, possible magnetic interference, and their reasonable size and weight still limit their application in field applications in particular their integration in small mobile platforms [21]. Recently, according to the literature, fixed detection systems based on plastic scintillators with SiPM sensors have been tested for applications such as the study of cosmic radiation [35], fast-timing measurements [36], or when a large area detection system is necessary [37].

While the integration of plastic scintillators with SiPM sensors present a highly promising solution in mobile platforms, especially for small unmanned vehicles, extensive research and rigorous testing are imperative to validate their viability for field measurements in crucial areas such as:

- Sensors integration in mobile platforms;
- Detector geometry optimization to obtain the best detection efficiency (depends on the radiation type and energy);
- Energy resolution;
- SiPM temperature dependence (dark counts), that affects the lower energy threshold of the detector.

Improving the accuracy of localizing concealed radiation sources typically involves a path optimization problem, where both the detection system's path and the employed source search algorithm must be considered. Once the optimal path for the MRDS is chosen, uncertainties remain regarding: (i) its position at each instance; (ii) measurements; (iii) the decision to raise the alarm; and (iv) the estimation of the localization and activity of potential sources. Utilizing predefined paths, such as parallel sweeping search patterns [38], [39] or Archimedean spiral search patterns [40], within specific areas of interest allows for the creation of radiation maps, optimizing battery consumption or fuel expenditure and saving time. However, real-time measurements enable dynamic adjustments to the initial path, enhancing source localization accuracy by focusing on areas where the source is most likely to be found. Therefore, informative path planning optimizes data collection during searches, significantly reducing survey time [41], [42].

Various algorithms have been used for detecting and localizing radioactive sources. For instance, in [17], a Maximum Likelihood Estimation (MLE) algorithm and a fixed detector network were used to localize a 189 kBq ^{137}Cs source within a $5\,m \times 5\,m \times 5\,m$ space domain with an accuracy better than 60 cm (2-3 minutes). Other methods include source-attractor radiation detection, triangulation-based radiation source detection, and the ratio of square distance-based radiation source detection [43]. Additionally, techniques like particle filter [44] and deep learning [5] have been explored to enhance source localization accuracy further.

In summary, mobile radiation detection and localization systems, whether ground-based or aerial-based, offer significant advantages for the timely and accurate identification of radioactive sources. The integration of optimized paths and advanced algorithms into MRDS platforms enhances their efficiency across diverse scenarios. By addressing uncertainties related to location, measurements, and decision-making, these systems contribute substantially to effective radiation detection and mitigation strategies. Continued advancements in technology and methodology are essential to further improve the accuracy and reliability of the MRDS, ensuring better protection and response in both Security and Safety contexts.

1.3 Objectives

The objectives of this thesis are:

- To analyze and review of the state-of-the-art in scientific, technological, and engineering aspects related to the use of UAV-equipped radiation detection systems associated with the monitoring, identification and quantification of radionuclides, for emerging applications in the fields of Security and Defence;
- To develop and test, combining experimental results obtained in field tests with results from MC modelling and simulation methods, an innovative MRDS for the

simultaneous detection and localization of gamma-ray and neutron sources in Security and Defence scenarios. By incorporating plastic scintillators with SiPM sensors technology into a UAV, this detection system emerges as a one-of-a-kind solution for inspecting cargo and safeguarding critical infrastructures. Its distinct advantages, including affordability, compactness, lightweight design, seamless integration into various mobile platforms, and exceptional geometric efficiency, set it apart as an invaluable asset for Security and inspection purposes;
- To develop and implement an informative path planning for the gamma-ray source localization, which leverages real-time measurements and data processing, instead of predefined paths. This approach facilitates the attainment of highly accurate and dynamically adaptable results in both source detection, localization, and quantification;
- To identify and assess existing limitations, shortcomings and "show stoppers" of the developed solutions;
- To develop scientific publications and participate in scientific dissemination events in order to share the knowledge acquired and the work carried out with scientific society and beyond.

1.4 Main contributions

The main contributions of this thesis can be summarized as follows:

1. State-of-the-art of radiation detection systems in Security and Defence scenarios;
2. Development and optimization of an innovative portable gamma-ray/beta and neutron detection system based on plastic scintillators with SiPM sensors. Design and prototyping of a compact and modular neutron moderator (allows both thermal and fast neutron detection). A source search methodology based on a two-stage process for a MRDS was also proposed consisting on the: (i) Fast source detection and localization using low cost and high geometric efficiency MRDS (e.g. fleet of MRDS); and (ii) Deployment of specialized MRDS, with excellent energy resolution, to the previously identified hot spots for source identification and quantification;
3. Integration of the innovative portable gamma-ray/beta and neutron detection system, other sensors, and associated electronics in a multirotor for Security and Defence applications. This required the implementation of data fusion, data synchronization, and remote real-time access to sensors' data. A proof-of-concept on the use of the developed MRDS to detect and localize gamma-ray and neutron sources within a shipping container was also achieved;
4. Informative path planning using the real-time measurements of the MRDS for the improvement of the source localization accuracy during the inspection of a shipping container (can be generalized to other critical infrastructures).

The following is a more detailed description of these contributions and their resulting scientific outputs: (i) Scientific publications, including journal articles, book chapters, and conference papers; (ii) Participation in conferences, congresses, and technical meetings; (iii) Articles and interviews aimed at scientific dissemination (outreach activities); and (iv) Awards received.

The state-of-the-art radiation detection systems used in various Security and Safety scenarios are described on Chapter 3, which was published in:

- L. Marques, A. Vale, and P.Vaz, "State-of-the-art mobile radiation detection systems for different scenarios", *Sensors*, vol. 21, no. 4, 2021. DOI:10.3390/s21041051.

Other oral presentations performed in seminars included:

- L. Marques, "Overview of recent developments in mobile radiation detection systems for different scenarios - challenges and opportunities," presented at *Instituto Superior Técnico*, Lisboa, Portugal, Mar. 24, 2021.
- L. Marques, "Veículos aéreos não tripulados: vantagens e desafios," presented at *Centro de Ciências e Tecnologias Nucleares*, Bobadela, Portugal, May 9, 2019.
- L. Marques, "Sistema de deteção de radiação acoplado a um veículo aéreo não tripulado para aplicações de segurança e defesa," presented at *Encontro Anual da Investigação e Desenvolvimento em Ciências Militares*, Pedrouços, Portugal, Dec. 12, 2018.

An innovative portable radiation detection system based on plastic scintillators with SiPM sensors was developed, designed for the detection of gamma radiation, beta particles, and neutrons. To optimize the detection system, MC modelling and simulations were conducted using the state-of-the-art MC computer code Monte Carlo N-Particle (MCNP) 6. The MC simulation results were subsequently validated by measurements in laboratory and field tests. Unlike methods that rely solely on inorganic scintillators and semiconductors for gamma radiation detection and radionuclide identification, or dual-mode detectors for simultaneous gamma and neutron detection, the use of plastic scintillators in separate or combined gamma and neutron detection systems offers enhanced geometric detection efficiency. This improvement is made possible by the availability of larger volumes and adaptable shapes, such as pancake-like designs, which are essential for detecting sources at greater distances from the detector. Furthermore, for neutron detection, ^{3}He-based detectors are commonly used, however, the global shortage of this gas dictates the exploration of alternative solutions. Therefore, the development of a neutron detection system based on ^{6}Li and a compact, modular neutron moderator for the detection of thermal and fast neutrons is highlighted. This innovative neutron moderator allows us to easily change the number and position of the moderator plates to optimize the detection efficiency of certain neutron sources or to detect, shielded or not, gamma/neutron sources. Despite plastic scintillators having very limited gamma-ray spectral capability, features such as being robust, cost-effective, and lightweight, without hygroscopic properties, facilitates their use and reproduction. Moreover, the utilization of SiPM sensors, instead of traditional PMT, has significantly reduced the size and weight of the detection system. Consequently, it can be asserted that the combined use of plastic scintillators with SiPM sensors offer the best detection efficiency per unit weight, making their integration into small mobile platforms with payload constraints more feasible. Several advantages of this approach are associated with the potential to employ a fleet of autonomous unmanned vehicles for the inspection or monitoring of an area/infrastructure, with an emphasis on expediting the process. In a first phase the rapid detection and localization of radionuclides using plastic scintillators could be performed, followed by the identification and quantification of these radionuclides using detection systems with good gamma energy resolution, such as inorganic scintillators or semiconductors. A significant part of these contributions, described in Chapter 4 and 5, was published as the following papers:

- L. Marques, A. Vale, and P. Vaz, "A mobile radiation detection system for security and defence", in *EDA research, technology, and innovation papers award 2023*. Brussels, Belgium: Publications Office of the European Union, 2023, pp. 40–47, presented orally at the *European Defence Agency Open Days*, May 31 – June 1, 2023. `DOI: 10.2836/568224`.
- L. Marques, A. Vale, and P. Vaz, "Development of a portable neutron detection system for Security and Defense applications", in *Developments and Advances in Defense and Security*, Á. Rocha, C. H. Fajardo-Toro, and J. M. Riola, Eds., Singapore: Springer, 2023, pp. 283–293, presented orally at the *Multidisciplinary International Conference of Research Applied to Defense and Security (MICRADS) 2022*. ISBN: 978-981-19-7689-6. `DOI:10.1007/978-981-19-7689-6_24`.

The results related to the development of the radiation detection system were presented orally in:

- L. Marques, A. Vale, and P. Vaz, "Use of plastic scintillators with silicon photomultipliers in mobile radiation detectors for the detection and localization of nuclear and radiological threats," in *International Society of Military Sciences Conference* [Conference presentation abstract], Lisbon, Portugal, Oct. 11–13, 2022.
- L. Marques, A. Vale, and P. Vaz, "A novel mobile radiation detection system for Security and Defense applications," in *Proceedings of the 3rd World Conference on Advanced Materials for Defense (AuxDefense)*, Guimarães, Portugal, Jul. 6–8, 2022.
- L. Marques, "Radiation detection system coupled to a multirotor for the inspection of shipping container cargo," presented orally at *Industry Day with the NATO Industrial Advisory Group*, Quartel Serra do Pilar, Vila Nova de Gaia, Nov. 28, 2022.

The integration of the detection system into a multirotor included the use of affordable materials and a straightforward, replicable process. To achieve this, the design and

3D printing of lightweight, custom-fit mounts for the detectors, as well as a carbon fiber sandwich plate for attaching the detectors, sensors, and associated electronics to the multirotor, were necessary. Mounting structures are usually designed for a specific platform, which makes integration with other platforms difficult. In this case, a lightweight carbon fiber sandwich plate was created to house the entire detection system and associated electronics, allowing for easy installation and removal from the platform. This stage of the work also involved the development from scratch of the algorithms for the: data processing and analyses of the sensor's data; data synchronization (data fusion); and real-time remote access to the sensors and output data. Additionally, the developed detection system is a stand-alone solution (operates independently of the way of transportation) that facilitates its integration in any mobile platform or to be used simply as handheld equipment (the portable configuration allows the comparison and validation of the results obtained using a MRDS). A proof-of-concept test demonstrated the potential of the developed mobile radiation detection system to perform the inspection of shipping container cargo. The use of the developed MRDS allowed the simultaneous detection of gamma-ray and neutron sources, the accurate localization of a gamma-ray source, and the approximate position of a neutron source inside the container. The maritime containers are normally inspected using large and expensive RPM, however, the proposed approach offers a low-cost alternative or complement to RPM and a faster method to perform secondary inspections currently carried out manually. In this thesis, this contribution is part of Chapters 5 and 6 and it was previously published as:

- L. Marques, L. Félix, G. Cruz, *et al.*, "Neutron and gamma-ray detection system coupled to a multirotor for screening of shipping container cargo", *Sensors*, vol. 23, no. 1, 2023. DOI:10.3390/s23010329.

The development of the MRDS was also awarded with the following prizes:

- L. Marques, A. Vale, and P. Vaz, "Improved radioactive source localization using plastic scintillators with silicon photomultipliers and informative path planning," *European Radiation Research Society Young Investigator Award*, 2024.
- L. Marques, A. Vale, and P. Vaz, "Development of a Portable Neutron Detection System for Security and Defense Applications," *Prémio de Investigação em Ciências Militares 2023*, best scientific article in Military Technologies field.
- L. Marques, L. Félix, J. Caetano, G. Cruz, V. Coelho, A. Vale, and P. Vaz, "Sistema de deteção de radiação gama, partículas beta e neutrões acoplado a um multirotor para inspeção de contentores marítimos e deteção, localização e identificação de fontes e materiais radioativos," *Prémio de Inovação nas Forças Armadas 2022*. https://www.emgfa.pt/Paginas/Premio-de-Inovacao-nas-Forcas-Armadas-2022.aspx

The developed MRDS and the findings from its application in detecting and localizing gamma and neutron sources within a shipping container were presented at the following conferences and meetings:

- L. Marques, "A Novel Radiation Detection System installed on UAV for Security and Safety Applications & State-of-the-art mobile radiation detection systems," presented orally at *IX Congresso de Proteção Contra Radiações da CPLP*, Coimbra, Dec. 14, 2023.
- L. Marques, "Sistema de Deteção de Radiação acoplado a um Veículo Aéreo Não Tripulado para Aplicações de Segurança e Defesa," presented orally at *17º Congresso do Comité Português da URSI – Materiais Inteligentes para a Radiociência*, ANACOM, Lisbon, Feb. 7, 2023.
- L. Marques, "Radiation detection system coupled to a multirotor for the inspection of shipping container cargo," presented orally at *International Atomic Energy Agency (IAEA) Technical Meeting on the Use of Uncrewed Aerial Systems for Radiation Detection and Surveillance*, Brno, Czech Republic, Sep. 26–30, 2022.

Some relevant outreach publications include television and magazine interviews:

- SIC Notícias, "Conheça o drone da Força Aérea Portuguesa capaz de detetar a radioatividade," Dec. 4, 2022. [Interview]. Available: .
- Exame Informática, "O caça radiação," *Exame Informática*, no. 330, pp. 52–53, Dec. 1, 2022.
- Exame-Informática, "Força Aérea Portuguesa cria sistema de sensores, acoplados a um drone, para deteção de radioatividade," Nov. 24, 2022. [Interview]. Available: .
- Força Aérea Portuguesa, "Prémio de Inovação nas Forças Armadas," *Revista Mais Alto*, no. 461, Artigo de divulgação nº 98, pp. 40–47, Feb. 2023.

In the detection and localization of radioactive sources, it is essential to consider not only the detection system but also the path it follows. To address this an informative path planning was proposed and implemented, which differ from other approaches, as they either rely on predefined paths or these paths do not apply to infrastructure inspection. With this work, we propose that the detection system follows a path based on the source position estimations or in real-time measurements, rather than relying on predefined paths. By focusing on areas with richer information, the informative path planning allows for enhanced accuracy in radioactive source localization and ultimately in the reduction of the inspection time. The results, based on a developed simulator, were validated in field tests, demonstrating promising outcomes regarding the use of the proposed MRDS and the presented methodology. A significant part of these contributions, described in Chapters 7 and 8, was published as the following papers:

- L. Marques, R. Coito, S. Fernandes, T. Costa, A. Vale, and P. Vaz, "A mobile radiation detection system for security inspection and monitoring," *EPJ Web Conf.*, vol. 288, no. 06001, Nov. 2023, presented orally at *ANIMMA 2023 – Advancements in Nuclear Instrumentation Measurement Methods and their Applications*, sec. Nuclear Safeguards, Homeland Security and CBRN. `DOI:10.1051/epjconf/202328806001`.

- L. Marques, R. Coito, T. Costa, S. Fernandes, A. Vale and P. Vaz, "Radioactive source localization using a mobile radiation detection system featuring informed path-based decisions," *IEEE Transactions on Nuclear Science*, vol. 71, no. 5, pp. 1064-1071, 2024. `DOI:10.1109/TNS.2024.3354461`.
- L. Marques, R. Coito, T. Costa, S. Fernandes, A. Vale, and P. Vaz, "Path optimization of a mobile radiation detection system in security inspection," in *Developments and Advances in Defense and Security*, Á. Rocha, C. H. Fajardo-Toro, and J. M. Riola, Eds., Smart Innovation, Systems and Technologies series, Singapore: Springer, 2025, pp. 293-305, presented orally at the *Multidisciplinary International Conference of Research Applied to Defense and Security (MICRADS) 2024*. ISBN: 978-981-96-0235-3. `DOI:10.1007/978-981-96-0235-3_24`

Finally, it is important to emphasize the diversity of tasks involved in the development and testing of the MRDS, particularly in fields such as materials engineering, electronics, and programming.

1.5 Dissertation outline

This thesis is organized into nine Chapters. Chapter 1 introduces the reader to the goal and motivation of this thesis, describing the importance of the radiation detection system and search methods chosen to accurately detect and localize a gamma-ray and neutron source.

Chapter 2 provides a concise overview of radiation interaction with matter and the fundamental principles of gamma-ray and neutron detection systems, with a particular emphasis on the use of scintillators.

The characteristics of some important scenario types where the radiation detection systems can be used, and the state-of-the-art of the gamma and neutron detection systems are described in Chapter 3. Additionally, a detailed description about the actual radiation detection systems and algorithms used to detect and localize radioactive sources hidden inside maritime shipping containers will be presented. Challenges, hot topics and emerging issues on technologies related to the radiation detection systems and mobile platforms will also be referred.

The proposed radiation detection system is presented in Chapter 4, detailing the hardware and software architecture, as well as the gamma-ray source localization algorithm.

Chapter 5 details the development and optimization of a portable detection system for gamma rays, beta particles, and neutrons. The results from MC simulations, validated by laboratory and field tests are presented. The chapter covers the prototyping of the neutron moderator, the design of detector supports, and the assembly of these components into a robust portable radiation detection system. Furthermore, it discusses the integration of this detection system onto a multirotor platform.

Chapter 6 presents the experimental results for detecting and localizing gamma and neutron sources inside a maritime shipping container, utilizing two configurations of the radiation detection system: handheld equipment and a multirotor-integrated setup. The tests were carried out along predefined paths around the container.

The development of a simulator code written in *python* code and the results obtained for the simulations of the detection and localization of gamma-ray sources placed inside a shipping container are presented in Chapter 7. The simulations included different source activities, paths (predefined paths vs informative path planning), and uncertainties.

Chapter 8 presents the experimental results for detecting, localizing and quantifying a gamma source placed inside a simulated maritime shipping container (since no container was available, its boundaries were marked on the ground), utilizing both predefined paths and informative path planning.

Finally, Chapter 9 draws upon the results obtained throughout the dissertation, highlights the main results obtained and proposes improvements and additional research to be undertaken in the future.

2

Nuclear radiation detection, measurement, and monitoring

2.1 Radioactivity

Radionuclides are radioactive forms of elements that emit ionizing radiation, such as alpha particles, beta particles, gamma rays, or neutron radiation. Some radionuclides occur naturally in the environment, such as ^{226}Ra and ^{238}U, while others are man-made, either deliberately or as byproducts of nuclear reactions (e.g. ^{137}Cs and ^{60}Co) [45]. The activity of a radionuclide (radioactivity) refers to the rate at which it undergoes radioactive decay (decay per second) and is given by the SI unit becquerel (Bq). For historical reasons, the curie (Ci) unit is also commonly employed, where 1 Ci is equivalent to 3.7×10^{10} Bq. Laboratory activity levels that are most frequently used are the millicurie (mCi) and microcurie (μCi). For comparison purposes, a banana, due to the presence of the naturally occurring radioactive potassium-40, has an activity of approximately 15 Bq, which is equivalent to 0.00041 μCi [46]. The *activity* A of a radioisotope is determined by the number of radioactive atoms present, $N(t)$, at a given instant of time, t, and can be obtained by the *exponential law of radioactive decay* [47], given by:

$$A(t) \equiv \lambda N(t) = A_0 \, e^{-\lambda t} \, , \tag{2.1}$$

where A_0 is the initial activity at t=0 s and λ is the decay constant of the radioisotope. The half-time $t_{1/2}$, as expressed in (2.2), represents the time necessary for half of the radionuclides initially present in the sample to decay [47].

$$t_{1/2} = \frac{0.693}{\lambda} \tag{2.2}$$

The most common radioactive types of decay (sometimes referred to as "decay modes") include the emission of alpha (α) particles, beta (β) particles, and gamma (γ) radiation. Alpha decay involves the emission of an alpha particle, which is a ^4He nucleus. Beta decay can be either beta-minus (emission of an electron) or beta-plus (positron emission).

Gamma decay is the emission of high-energy photons. Electron Capture (EC), Internal Conversion (IC) and Spontaneous Fission (SF) are, *inter alia*, other possible decay modes for certain radionuclides [31].

SF occurs in very heavy elements, where the nucleus splits into two lighter nuclei, often accompanied by the emission of neutrons and other particles, such as neutrinos. Only some transuranic elements (atomic number greater than 92) undergo SF at a considerable rate. For example, ^{252}Cf, a commonly used neutron source, exhibits a half-life of 2.645 years, but the probability of alpha emission is significantly higher than that for SF (which accounts for only 3.1%). In the naturally occurring radioactive decay series for ^{235}U, ^{238}U, and ^{232}Th, SF does occasionally occur. However, in artificially produced elements such as ^{239}Pu, ^{240}Pu, ^{250}Cm and ^{252}Cf, SF is more likely to occur [48]. For instance, the rate of spontaneous fission in ^{239}Pu is approximately 300 times higher than that in ^{235}U. For many heavy nuclei (Z greater or equal to 90), fission takes place if an amount of energy, at least equal to a critical energy, is provided in some way, as by neutron or gamma absorption and is often referred to as "induced fission". An example of induced fission is the ^{235}U neutron capture in a nuclear reactor [47], [49].

Ionizing radiation can penetrate living tissues and potentially cause biological damage [45]. Additionally, electronic equipment and circuits, especially those based on semiconductors, can be harmed by ionizing radiation, which can result in changed operational parameters and higher noise levels. Therefore, these radiation effects must be considered in applications requiring high levels of reliability and radiation hardness, such as space technology, nuclear facilities, and medical equipment [50].

Alpha particles have a very short range in air (up to 4 cm) and can be easily stopped by a sheet of paper or the outer layer of skin. Despite a higher range in air can be achieved with common radioactive beta sources (maximum ranges in air from around 3 m up to 11 m), they can be stopped by a thin layer of material like aluminum or plastic [51].

This thesis is centered on clarifying these interactions within the context of an UAV-based radiation detection system, engineered for measurements at distances on the order of meters from the radioactive source or material. Due to their ability to travel several meters in air, gamma and neutron radiation are typically taken into consideration for detection systems integrated into mobile platforms.

2.2 Interaction of radiation with matter

This section briefly describes the main mechanisms by which ionizing radiation interacts with matter. Understanding these interactions is vital, as radiation detection relies on the energy deposited in the detector's material.

Ionizing radiation can be divided into three groups [52]:

- Charged particles: beta particles which include electrons (e^-) and positrons (e^+), protons (p), deuterons (d), alpha particles (α), and heavy ions (atom's atomic mass

number greater than four);
- Photons: gamma rays (γ) and x-rays;
- Neutrons (n).

In the following Sections it will be briefly described the interactions of these radiation groups with matter.

2.2.1 Charged particles

When a charged particle traverses a material, its primary interactions involve Coulomb forces with atomic electrons and with protons inside the nuclei, leading to continuous energy loss and eventual stoppage after a finite distance – range. The range is influenced by particle type, energy, and material properties. Other energy loss mechanisms include: (i) "bremsstrahlung", consisting of electromagnetic radiation emission in the energy range under consideration, mainly significant for electrons especially when high-Z materials are considered (e.g. lead). Bremsstrahlung photons can have any energy ranging from zero to the maximum kinetic energy of the incident electrons; (ii) nuclear interactions, normally relevant for heavy ions; and (iii) Cerenkov radiation, in which very small fraction of energy loss occurs. The collisions with atomic electrons (more numerous), may result in ionization or excitation (inelastic collisions). The charged particle's interaction with multiple atoms involves Coulomb forces on millions of electrons, leading to an average energy loss per unit distance also known as the stopping power. Unlike heavy charged particles, which experience smaller energy losses per collision and nearly straight-line trajectories, beta particles (electrons and positrons) may lose a substantial fraction of their kinetic energy in a single collision (with orbital electrons), therefore exhibiting erratic trajectories [52].

While charged particles typically exhibit a short range in air, it is notable that beta particles emitted by ^{90}Sr, a prevalent radionuclide, and its daughter ^{90}Y, can extend several meters in air. ^{90}Y specifically demonstrates a maximum beta range in air of approximately 10.6 meters. In addition, if beta sources are encapsulated with high-Z materials, bremsstrahlung radiation can be produced[1], which will be detected by gamma-ray detection systems. Although beta particles can be detected by mobile radiation detection systems operating near the ground, effective shielding against these particles can easily be achieved with a 0.52 cm thick aluminum foil and a 1.1 cm thick plastic sheet, as outlined in [53].

Due to their limited range, typically of the order of a few tens of micrometers in several materials and only a few centimeters in air, the alpha particles detection will not be considered in this thesis. Nevertheless, it is important to note that alpha particles pose a significant hazard when alpha-emitting isotopes are introduced into the human body through ingestion or inhalation.

[1]Therefore, a good shielding material for beta particles, which minimizes bremsstrahlung radiation, is a low Z material such as plastic.

2.2.2 Gamma radiation and X-rays

Gamma radiation and X-rays interact with matter primarily through three processes: photoelectric effect, Compton scattering, and electron-positron pair creation. Through these processes, the initial energy of the incident photons is transferred, either partially or entirely, to the electrons present in the detector material [31].

The photoelectric effect is a process in which a photon is absorbed by a tightly bound electron (from an inner atomic layer), causing the ejection of the electron and ionization of the atom. The cross-section for the photoelectric effect strongly depends on the atomic number (Z) of the atom, and can be expressed by:

$$\sigma_{\mathrm{eff}} \sim Z^{\mathrm{n}} \tag{2.3}$$

where the n value depends on the photon's energy and is approximately equal to 4. In the photoelectric effect, all the energy of the incident photon (minus the binding energy of the ejected electron) is deposited in the detector. The vacancy in the electronic shell left by the ejected electron is filled by another electron from an outer atomic layer. This process can be followed by the emission of an X-ray characteristic of the atom, or by the emission of a secondary electron (Auger electron).

Compton scattering occurs when an incident photon interacts with an electron, typically in the outer layers of an atom. During this interaction, the original energy of the photon is distributed between the recoiling electron and the scattered photon. The scattered photon may either interact further or escape the detector's sensitive volume, resulting in only a partial deposition of the incident photon's energy in the detector material. The recoiling electron will deposit its energy as described in Section 2.2.1. Gamma rays scattered through large angles (> 120°) due to the presence of material around the source and detector (e.g. shielding, photomultiplier tube housing) are called backscattering gamma rays. The detection of backscattering gamma rays can give rise to a backscatter peak (normally a wide peak with energy < 250 keV) in the gamma-ray spectrum [31].

When a photon has an energy equal to or greater than twice the rest energy of an electron, i.e. $2\mathrm{m_e c^2}$ (1.022 MeV), it can undergo electron-positron pair creation. This process occurs when a photon interacts with the electromagnetic field surrounding an atomic nucleus. The energy of the incident photon is transformed into the rest energy of the electron-positron pair ($2\mathrm{m_e c^2}$) as well as in kinetic energy of the positron and electron. Subsequently, the electron and positron interact with matter through successive Coulomb interactions, depositing their energies within the detector. In the case of the positron, after interacting with the material, it annihilates with an electron generating two photons with energies of 511 keV emitted in nearly opposite directions. This interaction becomes more prevalent for energies exceeding those described for other processes, with the pair creation cross-section increasing approximately with the square of the atomic number (Z) of the atomic nuclei [52].

The dominance regions of the three processes described above for various absorber materials (atomic number) and gamma-ray energies are shown in Figure 2.1.

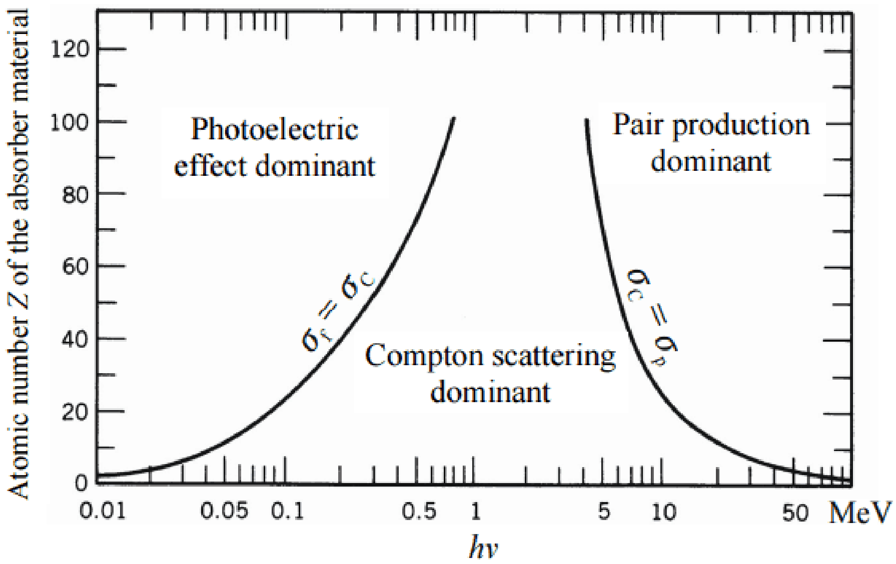

Figure 2.1: Relative importance of the three major processes of gamma-ray interaction [47].

In terms of electromagnetic radiation absorption, photoelectric absorption dominates at low photon energies – below 50 keV for aluminum (Z=13) and 500 keV for lead (Z=82). As the radiation energy increases, Compton scattering becomes more significant, prevailing in aluminum between 60 keV and 20 MeV and in lead between 500 keV and 5 MeV. At even higher energies (several MeV for most materials), pair production becomes the dominant process.

Depending on their initial energy, gamma rays can travel distances ranging from tens to hundreds of meters through air. Gamma rays are typically shielded using very dense materials (with high Z) such as lead [31].

In this thesis, only gamma rays with energies between 30 keV and 3 MeV will be considered for radiation detection purposes. This range encompasses the gamma rays emitted by radionuclides relevant to Security and Defence scenarios [2] [54].

2.2.3 Neutrons

Since neutrons are electrically neutral particles, they are not affected by the Coulomb force – the electric fields produced by nuclei and electrons. As a result, the neutron can interact directly with the nucleus through the nuclear force field after passing through the electronic cloud of the atom. Nuclear reactions can therefore result from neutrons with energies as low as meV.

[2]While higher energy gamma rays (> 3 MeV) can be emitted during active interrogation techniques – specifically as by-product gamma rays of nuclear reactions produced by incident neutrons in suspected materials, typically SNM – they will not be considered in this thesis.

The total neutron cross section, denoted by σ_t, is a measure of the likelihood of a neutron interacting with a target nucleus [3] [55] and is given by:

$$\sigma_\mathrm{t} = C/(N_\mathrm{a} I_0)\,, \tag{2.4}$$

where C is the number of neutron-nuclei interactions per cm^2 per second, N_a is the number of target atoms/cm^2 and I_0 is the intensity of the incident mono-directional neutron beam. The total cross section considers all types of nuclear reactions (e.g. scattering, capture, and fission), however a cross section for a given reaction can be obtained from data libraries such as ENDF/B-VII.1 [55].

The standard unit for measuring the cross section is the barn, which is equal to 10^{-28} m^2 or 10^{-24} cm^2. A larger neutron cross section indicates a higher probability of a neutron interacting with the nucleus. This concept is used in nuclear physics to express and quantify the likelihood of interaction between neutrons and atomic nuclei [56].

Since cross-sections in most materials are strongly dependent on neutron energy, an energy classification based in neutron energy regions is normally defined, as shown in Table 2.1. The designation of thermal neutrons stems from the fact that their kinetic energies exhibit a Maxwell-Boltzmann distribution. At ambient temperature (293 K), the peak of the thermal neutron fluence distribution occurs at an energy of 0.0253 eV.

Table 2.1: Approximate limits of neutron energy regimes classified by names [57].

Energy range	*Classification*		*Energy range for neutron scattering*
	Nuclear physics	*Neutron scattering*	
<1 keV	Slow	Ultra cold	<0.1 meV
		Very cold	0.1–0.5 meV
		Cold	0.5–5 meV
		Thermal	5–100 meV
		Epithermal or hot	0.1–1 eV
		Resonant	1–100 eV
1 keV–0.5 MeV	Intermediate		
0.5–10 MeV	Fast		
10–50 MeV	Very fast		
50 MeV–10 GeV	High energy or ultra fast		
>10 GeV	Relativistic		

Neutrons can interact with the atomic nucleus in the main following ways:

- **Elastic scattering.** In this process, the incoming neutron interacts with a target nucleus, which is generally in the ground state, transferring part of its initial kinetic energy to nucleus (often designated as "recoil nucleus") and is scattered at an angle θ relative to its initial direction. Kinetic energy conservation occurs in the interaction, symbolically represented by (n, n);
- **Inelastic scattering.** In this reaction, the nucleus becomes excited after the neutron interaction. It is an endothermic reaction and is represented by (n, n');

[3] σ_t corresponds to the microscopic cross-section, characterizing the effective "target area" for a single isotope and are a part of data libraries, such as ENDF/B-VII.1.

- **Radiative capture.** The neutron is absorbed by the nucleus, and one or more photons are emitted. The sum of the energies of the emitted photons is characteristic of each nuclide. Radiative capture is an exothermic reaction and is represented by (n, γ);
- **Particle emission.** These are reactions of the type (n, α), (n, p), (n, xn), etc. They can be endothermic or exothermic;
- **(Neutron-induced) Fission.** Neutrons cause the fragmentation of the nucleus into two lighter nuclides (called "fission fragments") and several (typically 2-3) neutrons are released. This reaction is represented by (n, f).

Neutrons can be produced in different nuclear technology facilities and in nuclear interactions of cosmic rays with the atmosphere, as shown in Table 2.2.

Table 2.2: Neutron production sources [58].

Neutron source	Description
Radionuclide sources	Via (α, n) and (γ, n) reactions, and by SF
Accelerated particle reactions	Mainly involving protons and deuterons, but also including photonuclear neutron production
Nuclear reactors	Induced fission (both prompt and delayed fission neutrons)
Fuel reprocessing plants	(α, n) reactions and SF occur in long irradiated nuclear fuel

Given that commercial neutron sources primarily rely on (α, n) reactions and SF nuclei, these mechanisms will be further detailed below. Considering the (α, n) reactions, heavy nuclei such as plutonium, uranium, and americium isotopes decay by alpha particle emission. When an alpha particle is absorbed by the low atomic number nuclei (e.g. Li, B, Be, O, F, C, and Si), a neutron is produced. Neutrons from (α, n) reactions are produced randomly (not time-correlated) and have a broad energy spectrum. The even-numbered isotopes of plutonium (^{238}Pu, ^{240}Pu, and ^{242}Pu) exhibit SF at rates of 1100, 471, and 800 SF neutrons per gram per second, respectively. Similar to (α, n) neutrons, SF neutrons possess a wide energy spectrum. These neutrons are time-correlated, with an average count per fission ranging between 2.16 and 2.26. In contrast, uranium isotopes and odd-numbered plutonium isotopes experience spontaneous fission at significantly lower rates (0.0003 to 0.006 SF neutrons per gram per second). Moreover, in spent fuel, significant neutron-emitting isotopes, such as curium (Cm) and californium (Cf), are present [59].

Some examples of neutron sources used in industry and research are the SF source ^{252}Cf and the $^{241}Am - Be$ source, which is a mixture of an alpha emitter and a light nucleus (in this case beryllium). These sources are often used in the oil and gas well logging sector as well as for measuring the density and moisture content of soil and concrete. A comparison of the energy spectra of several neutron sources is shown in Figure 2.2. Although some variations are observed between the spectra, all the neutron peaks fall within the fast neutron energy range.

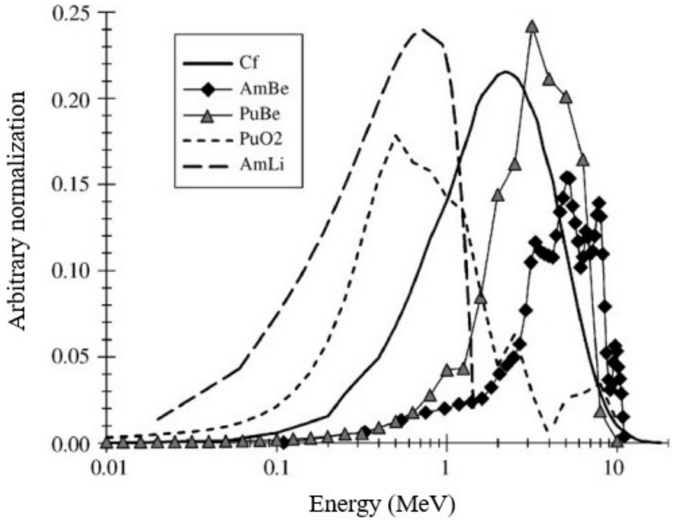

Figure 2.2: Energy spectra of several neutron sources [60].

Since the neutron spectra of ^{252}Cf and ^{240}Pu differs very slightly, in investigations involving spontaneous fission neutron emission, ^{252}Cf is a good surrogate for Weapons-Grade plutonium (WGPu) [61]. However, due to the limited availability of neutron sources, the MC simulations and experimental tests performed in Chapters 5 and 6 were conducted using $^{241}Am - Be$ sources.

Despite the fact that neutron induced fission normally happens in nuclear reactors, an external neutron source can also be used to produce induced fission of ^{239}Pu, ^{235}U, and ^{238}U for active neutron interrogation purposes. Although active neutron interrogation is an effective alternative to passive gamma and neutron detectors for detecting SNM, it poses a significant risk to humans due to the potential exposure to neutrons and by-products of fission reactions, such as induced fission neutrons and gamma rays. Similar to SF neutrons, induced fission neutrons exhibit a broad energy spectrum and are time-correlated [59].

2.3 Radiation measurement and monitoring technologies

This Section will briefly describe the different types of radiation detection systems, with special emphasis on scintillator detectors, which are the focus of this thesis. Due to their range in air, of several meters, normally gamma radiation and neutron detectors are used in portable or mobile radiation detection systems. However, since beta particles can travel in air up to 2 meters, they can also be detected by some ground-level detection systems or by low-altitude Small Unmanned Aerial System (SUAS).

In general, radiation detectors can be divided into the following main categories [31]:

- Gas-filled detectors;
- Scintillation detectors;
- Semiconductor detectors.

Gas-filled detectors consist of a volume of gas between two electrodes with an electric potential difference (voltage). When radiation ionizes the gas, the resulting ions are collected by the electrodes, generating an electrical signal. Examples of gas-filled detectors are: the GM detectors, ionization chambers, and proportional counters. Gas-filled detectors typically have low intrinsic efficiencies for detecting X-rays and gamma rays due to the low density and atomic number of the gases used. Because of their low cost, GM detectors (a.k.a. GM counters) are normally used to obtain the radiation dose rate. Whenever an energy-resolving capability is desired, a large number of charge carriers must be generated for each absorbed pulse to reduce the statistical limit on energy resolution. The best detectors to accomplish this are the semiconductor detectors, such as High-Purity Germanium (HPGe) or CZT. However, while for HPGe an excellent energy resolution is achieved with a cooling system (becoming too heavy and power consuming), CZT based detection systems work at room temperature but are only available in small crystals due to charge trapping and manufacturing issues (crystal growing). Both types of detectors are expensive. Although scintillator detectors present a poorer energy resolution, larger detector volumes are available at lower prizes which makes them a good alternative to semiconductors [31]. The following Section provides an in-depth explanation of the operational principles of scintillator detectors.

2.3.1 Scintillators

Scintillators play a crucial role in converting the energy of incident radiation into optical photons. When ionizing radiation hits the scintillator material, the absorbed energy is re-emited in the form of light (scintillation light), which is then converted into electrical signals by a photo-detector. The quantity of scintillation photons generated is directly proportional to the absorbed energy. A typical scintillator-based detection system comprises three essential components: a scintillator material, a photo-detector, and a read-out system. A light guide is normally necessary to link the scintillation material to the photo-detector. Scintillator materials vary widely, falling into the following categories [52]:

- Inorganic crystals;
- Organic (glasses, plastic and liquid);
- Gaseous (mixtures of noble gases).

The choice of scintillator material is contingent upon specific application requirements. Inorganic scintillators generally exhibit superior light yield and linearity, ensuring good energy resolution. However, their relatively slow response and the necessity for a crystalline structure contribute to their higher cost and challenges in achieving large volumes [31]. Plastic scintillators have similar detection performance to their liquid counterparts, with the advantage that they can be molded into various shapes without the need for a container. They are also resistant to oxygen, water and a range of chemicals, making them highly durable and adaptable to a variety of applications [52].

Considering the photo-detector, PMTs are known by their excellent signal to noise ratio. However, PMTs features several drawbacks when compared to other solid-state photo-detectors, such as: high operating voltage, high power consumption, large size, heavy, fragility of the glass bulb, and low quantum efficiency. In contrast, solid-state photo-detectors, such as photodiodes, besides the lower operating voltages and power consumption, presents a high quantum efficiency and insensitivity to magnetic fields. Geiger-mode Avalanche Photodiodes (APDs), also known as SiPM, have emerged as an alternative to traditional PMTs for detecting scintillation light, presenting a promising option in certain applications [62].

The final component of the photo-detector system is the signal processing unit, which includes pre-amplification, amplification, Pulse Shape Discrimination (PSD), and Analog-to-Digital Converter (ADC) stages. This, along with the data acquisition electronics (front-end electronics), is essential for accurate signal counting and amplitude quantification. Scintillation photons absorbed in the photocathode of PMT or APD release electrons. At this point energy absorbed in the scintillator has been converted into an electrical signal. Increased in magnitude by the electron multiplier, the signal at the PMT or APD output is a current pulse (analog signal). Integrated over time this pulse contains the signal charge, which is proportional to the absorbed energy. Depending on the gain provided by the electron multiplier (PMT or APD), a preamplifier may be necessary or not. A diagram of the signal acquisition and processing is shown in Figure 2.3 (top image) [63].

Pulse shaping is designed to account for two conflicting objectives (trade-off). The first is to limit the bandwidth to match the measurement time. Too large bandwidth will increase the noise without increasing the signal. Typically, the pulse shaper transforms a narrow sensor pulse into a broader pulse with a gradually rounded maximum at the peaking time so that it can be read by the ADC. The signal amplitude is measured at the peaking time. The second objective is to constrain the pulse width so that successive signal pulses can be measured without overlap (pileup), as shown in Figure 2.3 (bottom image). Reducing the pulse duration increases the allowable signal rate, but at the expense of electronic noise [63].

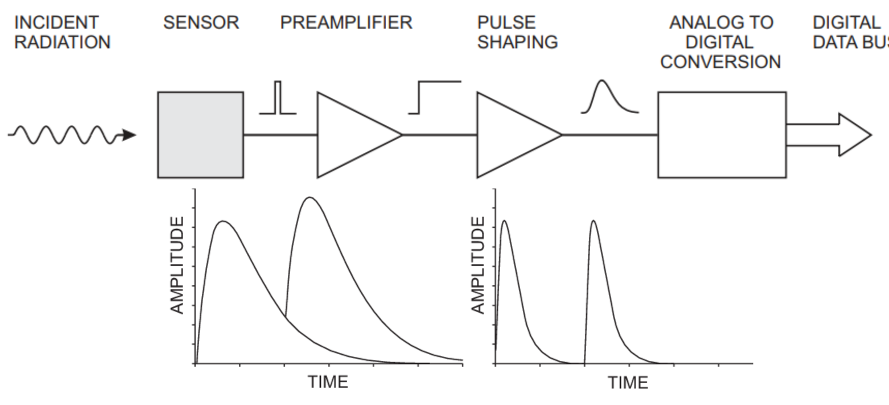

Figure 2.3: Basic detector functions (top image) and Amplitude pileup (bottom image) [63].

The shaper feeds an ADC, which converts the magnitude of the analog signal into a bit-pattern suitable for subsequent digital storage and processing. Conceptually, the simplest technique is to use a flash conversion, as shown in Figure 2.4. The signal is fed in parallel to a bank of threshold discriminators, also know as comparators. The individual threshold levels are set by a resistive divider. The comparator outputs are encoded such that the output of the highest-level comparator that fires yield the correct bit pattern. The threshold levels can be set to provide a linear conversion characteristic where each bit corresponds to the same analog increment, or non-linear characteristic, to provide increments proportional to the absolute level, which provides constant relative resolution over the range. The main advantage of this scheme is speed; conversion proceeds in one step and conversion times < 10 ns are readily achievable. The drawbacks are the number of components needed and power consumption, for example, an 8-bit converter requires 256 comparators [63].

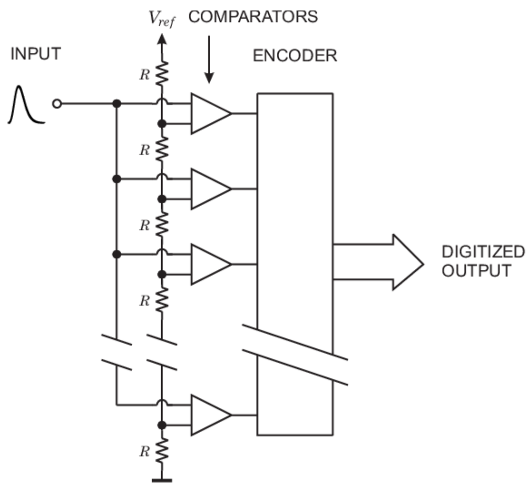

Figure 2.4: Block diagram of a flash ADC [63].

The ADC performs the fundamental Pulse-Height Analysis (PHA) and is located at the Multichannel Analyzer (MCA) input. The ADC input is an analog voltage pulse and its output is a binary number (address) that is proportional to the amplitude of the input pulse.

The number of channels into which the voltage range is divided is usually a power of 2 and is called the ADC conversion gain. Nowadays it is possible to find ADCs which divides 10 V into as many as 16384 channels (individual channel is only 0.6 mV wide). The required conversion gain varies with the detector type and with the energy range being examined. For example, to acquire a plutonium spectrum a high-resolution germanium detector uses 8192 channels. Therefore, enough channels are necessary to clearly discriminate the full-energy peaks (photo-peaks) in a spectrum. ADC speed is crucial for high-count-rate spectroscopy, as it determines how quickly pulses can be processed. During the ADC processing of one pulse, all other pulses are ignored, leading to a "deadtime". For example, a deadtime of 25% indicates that 25% of the information in the amplifier pulse stream is lost [64].

2.3.2 Neutron detection

Because neutrons have zero charge, they cannot directly produce ionization in a detector and therefore cannot be directly detected. Hence, neutron detectors rely on two main types of interactions of an incident neutron with a nucleus [65]:

- **Elastic[4] or inelastic[5] scattering.** The recoiling nucleus ionizes the surrounding material. Only effective with light nuclei (e.g. hydrogen and helium);
- **Nuclear absorption reactions.** Include neutron radiative capture and non-radiative capture, neutron induced fission, and other interactions that generate detectable reaction products, including gamma rays, protons, alpha particles, and fission fragments.

Considering their operating principle, neutron detectors can be divided on two main types [58]:

- Rely upon a measure of the ionization current (ionization detectors), e.g. ionization chambers, recombination ionization chambers, fission ionization detectors, proportional counters, and semiconductor detectors;
- Produce a light pulse to be measured with photosensors (e.g., PMTs or APDs). These detectors are known as scintillators.

Both methods can be used to produce pulses or a continuous current, which are proportional to the input neutron fluence as modified by the detector response.

2.3.2.1 Detection of thermal neutrons

Thermal neutron detection systems consist of three main components: (i) a material to convert neutrons into charged particles or gamma rays (by means of nuclear reactions, typically neutron capture reactions), (ii) a sensitive volume for converting the energy of these charged particles or gamma rays into an electric signal or light (scintillation light), and (iii) the data acquisition system. Common converter materials with large thermal neutron capture cross-sections include ^{3}He, ^{10}B, ^{6}Li and Gd[6], typically utilized in proportional counters or scintillators. While semiconductor detectors are expensive and mainly used for neutron imaging or spectrometry, most nuclear detectors used in Security scenarios prioritize sensitivity to thermal neutrons, often employing a moderator

[4] The most important mechanism for energy loss in the MeV range.

[5] The nucleus is left in an excited state which can lead to decay by gamma-ray emission. Inelastic scattering typically occurs if the neutron has energy in the range of 1 MeV or more (fast and relativistic neutrons).

[6] Gadolinium, a rare earth element, exhibits the highest natural affinity for interaction with thermal neutrons among all naturally occurring elements: Gd-157 (15.65%, 254000 b cross section) and Gd-155 (14.8%, 60900 b).

material to slow down fast neutrons and thus increasing the neutron capture cross section. A comparison of the neutron capture cross-sections of ^3He, ^{10}B and ^6Li[7] as a function of incident neutron energy is shown in Figure 2.5 [31].

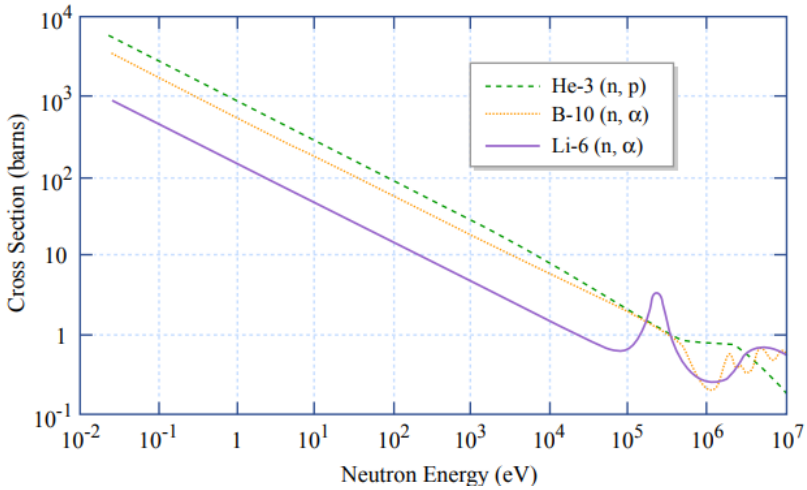

Figure 2.5: Neutron capture cross section of ^3He, ^{10}B and ^6Li [67].

The most common nuclear reaction is the thermal neutron capture by ^3He (reaction cross-section of 5330 barns for the neutron kinetic energy of 25 meV), as shown in (2.5).

$$n_{thermal} + {}^3He \longrightarrow p + {}^3H + 0.765\,MeV \tag{2.5}$$

where both the proton and the tritium are detected by gas-filled proportional counters using ^3He fill gas. Quench gas is also added to control the ionization process.

Another common method uses BF_3-filled detectors that utilize the thermal neutron capture by ^{10}B atoms (reaction cross-section of 3840 barns at 25 meV) resulting in two fission products: ^{4}He and ^{7}Li, as shown in (2.6).

$$n_{thermal} + {}^{10}B \longrightarrow \begin{cases} {}^4He + {}^7Li + 2.79\,MeV\,(6\%) \\ {}^4He + {}^7Li + 2.31\,MeV + \gamma(0.48\,MeV)\,(94\%) \end{cases} \tag{2.6}$$

The thermal neutron capture of ^6Li (940 barns for a neutron kinetic energy of 25 meV) is normally used in solid-state scintillators, such as Li-glass and ceramic $ZnS : {}^6LiF$ scintillators. In both types of scintillators the lithium content is enriched with the isotope ^6Li. The reaction products from the nuclear reactions, as indicated in (2.7), lose energy within the detector volume, and the resulting scintillation light is then collected by the photo-detector (PMT or SiPM) [68].

$$n_{thermal} + {}^6Li \longrightarrow \alpha + {}^3H + 4.78\,MeV \tag{2.7}$$

[7] While helium has a natural abundance of only 0.000137% of helium-3, boron has a natural abundance of 19.9% of boron-10, and lithium has a 7.59% abundance of lithium-6 [66].

2.3.2.2 Detection of fast neutrons

Detection of fast neutrons involves measuring the energy released by recoil particles resulting from elastic scattering. Materials with high hydrogen content, such as stilbene, organic liquid scintillators, plastic or liquid PSD-based scintillators, and gas scintillators like ^{4}He, serve as effective fast neutron detectors. Unlike thermal neutrons, detecting fast neutrons allows determination of the incident neutron direction, enabling source localization and neutron imaging, as well as identification of the neutron source type (e.g., $^{241}Am - Be$ source, SF source or shielded sources).

Fast neutrons can also be detected using a thermal neutron detection system surrounded by a neutron moderator. The process of moderation involves reducing neutron energy to the thermal energy range through scattering interactions within the chosen material serving as a moderator. Effective moderators typically consist of materials with a high content of protons, including hydrogenous compounds. Ideal moderation materials exhibit a substantial neutron scattering cross-section, minimal absorption cross-section, with a significant neutron kinetic energy loss per collision. Materials such as water and heavy water (D_2O) are effective moderators, requiring only approximately 20–30 collisions on average to thermalize fission neutrons with an initial energy of around 2 MeV [58]. Another material normally used as a moderator is polyethylene, which can be found as High-Density Polyethylene (HDPE) and High Molecular Weight Polyethylene (HMWPE).

3 State-of-the-art mobile radiation detection systems for different scenarios

This Chapter´s topics and findings are strongly related but go beyond those in [21].

3.1 Scenarios

The selection of a specific mobile radiation detection system depends on the unique characteristics of the given scenario. Although the main concern of this thesis is the use of radiation detection system in Security and Defence applications, in particular the illicit traffic of SNM and radioactive materials, it is important to describe other scenarios for comparison purposes. Four distinct types of scenarios will be briefly described in the following subsections, namely [21]:

- RN accidents and emergencies;
- Illicit trafficking of SNM and radioactive materials;
- Nuclear facilities, accelerators, targets, and irradiation facilities;
- Detection, monitoring, and identification of NORM.

Other possible scenarios, such as the radiation detection and monitoring for radiological protection purposes, will not be discussed in this thesis. This categorization provides a structured framework for understanding and addressing the diverse challenges associated with mobile radiation detection system across different contexts.

3.1.1 Radiological and nuclear accidents and emergencies

This scenario involves responding to intentional or unintentional releases of radioactive material, exemplified by events like radiological threats or major nuclear accidents such as Fukushima (2011). In the Fukushima nuclear power plant incident, the release of radioactive isotopes, primarily ^{137}Cs, ^{134}Cs, and ^{131}I, resulted in the enduring presence of these radionuclides in the soil. To reduce the radionuclide concentrations in the soils it was necessary to identify the radiation hot spots and to assess the effectiveness of the decontamination efforts [69], [70]. Ground-based monitoring systems faced challenges in covering large areas due to financial constraints and safety considerations; hence, airborne detection systems at safe altitudes offer an alternative with real-time monitoring methods [71]. In a post-accident scenario, detecting, localizing, quantifying, and identifying released radioactive materials or mapping radionuclide distribution becomes crucial, especially for understanding the effectiveness of remediation processes or the mobility of radionuclides in soils. For example, post-accident decommissioning of nuclear facilities presents unique challenges, such as compromised radiological and physical characterization due to limited access and the need for special remote tooling in regions with high radiation fields [72]. An additional example is the unprecedented release of ^{106}Ru in September 2017, detected across Europe [73].

3.1.2 Illicit trafficking of special nuclear material and radioactive materials

This scenario focuses on preventing the illicit traffic of SNMs, such as plutonium or HEU, for use in INDs, and other radioactive materials or sources (cesium, cobalt, etc.) for use in a RDD or a RED [3].

An IND is a weapon of mass destruction and its detonation can cause mass casualties. Nuclear materials, primarily plutonium and HEU, can be sourced from countries with nuclear weapons, nuclear programs, or internal enrichment and reprocessing facilities [74]. In contrast, the event of the use of a RDD, for example with the use of conventional explosives to disperse radioactive materials (a.k.a. dirty bomb), a low number of casualties is expected. However, significant safety, economic, and psychological impacts can be expected, posing severe threats to governments, financial centers, populations, and critical infrastructure [75].

Numerous radionuclides are important sources of radiation and radioactivity in a variety of fields, including industry, medicine, and research (as shown in Figures 3.1 and 3.2). Among the diverse radionuclides utilized globally, only a few are readily available in concentrated quantities suitable for deployment in RDDs. These include the ^{241}Am, ^{252}Cf, ^{137}Cs, ^{60}Co, ^{192}Ir, ^{238}Pu, ^{210}Po, ^{226}Ra, and ^{90}Sr. While ^{226}Ra exists in nature, as does a small amount of ^{210}Po, the other radionuclides are artificially created (anthropogenic origin) [76]. While gamma rays with energies ranging from hundreds of keV to just over 1 MeV are emitted by ^{137}Cs (0.662 MeV), ^{60}Co (1.173 and 1.332 MeV), and ^{192}Ir (0.206 and 0.485 MeV), low-energy gamma rays (below 0.2 MeV) are emitted by ^{241}Am, ^{238}Pu and ^{252}Cf. ^{90}Sr is a beta source, ^{241}Am, ^{252}Cf, ^{238}Pu, ^{210}Po, and ^{226}Ra are essentially alpha emitters and ^{252}Cf is a relevant neutron source.

Commercial neutron sources, including alpha emitters combined with light nucleus, such as $^{241}Am-Be$ and $^{239}Pu-Be$, as well as the spontaneous fission sources like ^{252}Cf, are used in applications such as soil measurements, well logging, and the nuclear power industry. Difficulties in detecting the low energy gamma rays of plutonium and HEU, and their possible shielding, masking (e.g. due to NORMs) or concealment, presents unique challenges which can only be solved by the use of neutron detection systems. Although plutonium emits significant SF neutrons, passive radiation detection systems may not be sufficient to detect concealed HEU due to low-energy gamma-rays up to 185 keV (easily shielded or masked) and very low emission rate of neutrons [60]. To achieve effective SNM detection, particularly HEU, active interrogation systems employ neutron or gamma-ray sources to prompt responses from concealed threat radionuclides in cargo. However, these techniques entail radiation exposure risks to humans. Tomographic imaging (X-rays or cosmic muons) can also be used in combination with passive detection systems for the recognition of high-density materials (e.g. SNMs or shielded nuclear sources) [77], [78].

Examples of Radionuclides in Common Use

Medicine		Industry/Commerce				Science
Diagnosis	*Treatment*	*Energy, Defense*	*Testing, Production*	*Food, Agriculture*	*Home*	*Research*
Tracer, flow *(Tc-99m, I-131)*	Gamma knife, blood/tissue sterilization *(Cs-137, Co-60)*	Commercial electricity *(U, Pu)*	Nondestructive test of structural integrity, radiographic imaging *(Co-60, Ir-192)*	Food product sterilization *(Co-60)*	Smoke detector *(Am-241)*	High-energy physics *(Cf-252, U-235)*
Tissue scan for clot, mass *(Ga-67)*	Needle, seed implants *(Cs-137, Ir-192, Ra-226)*	Remote power *(Sr-90)*	Density, moisture gauges *(Am-241, Cs-137)*	Pest (fruit fly) sterilization *(Cs-137, Co-60)*	Luminescent watch/clock dial *(H-3)*	Biokinetics *(Pu, Sr-90, others)*
X-ray *(Cs-137, Co-60)*	Pacemaker *(Pu-238)*	Defense/weapons *(Pu, H-3, U and depleted U)*	Material thickness, flow, conveyor, level gauges *(Am-241, Cs-137, Co-60, Kr-85)*	Seed, spice sterilization *(Cs-137, Co-60)*	Gas camping lantern *(Th-232)*	Biological tracer, protein/synthesis *(C-14, H-3, N-15 P-32, S-35)*

Am-americium, C-carbon, Cf-californium, Co-cobalt, Cs-cesium, Ga-gallium, H-3-tritium, I-iodine, Ir-iridium, K-potassium, Kr-krypton, N-nitrogen, P-phosphorous, Pu-plutonium, Ra-radium, S- sulfur, Sr-strontium, Tc- technetium, Th- thorium, U-uranium.

Figure 3.1: Examples of radionuclides and their usage in industry, medicine and research [76].

Despite most radioactive sources being well-regulated globally, incidents reveal lack or loss of regulatory control throughout their life cycle. Developed nations, with advanced regulatory systems, still encounter annual losses, leading to potentially hazardous orphan sources[1]. Ensuring the ongoing use of radioactive materials necessitates balancing safety and security in order to avoid accidents/incidents and minimize the risk of malevolent use. Since 1993 the IAEA ITDB records the incidents of illicit trafficking of nuclear and other radioactive Material Out of Regulatory Control (MORC), including sealed sources, unsealed samples, and contaminated materials. While not every occurrence indicates intentional theft, most involve unskilled or opportunistic thieves motivated by financial gain, such as accidental source theft that occurs during vehicle theft and the intent to resell valuable instruments or scrap metal for a substantial profit. However, a sizable

[1]A source which poses sufficient radiological hazard to warrant regulatory control, but which is not under regulatory control because it has never been so, or because it has been abandoned, lost, misplaced, stolen or otherwise transferred without proper authorization [79].

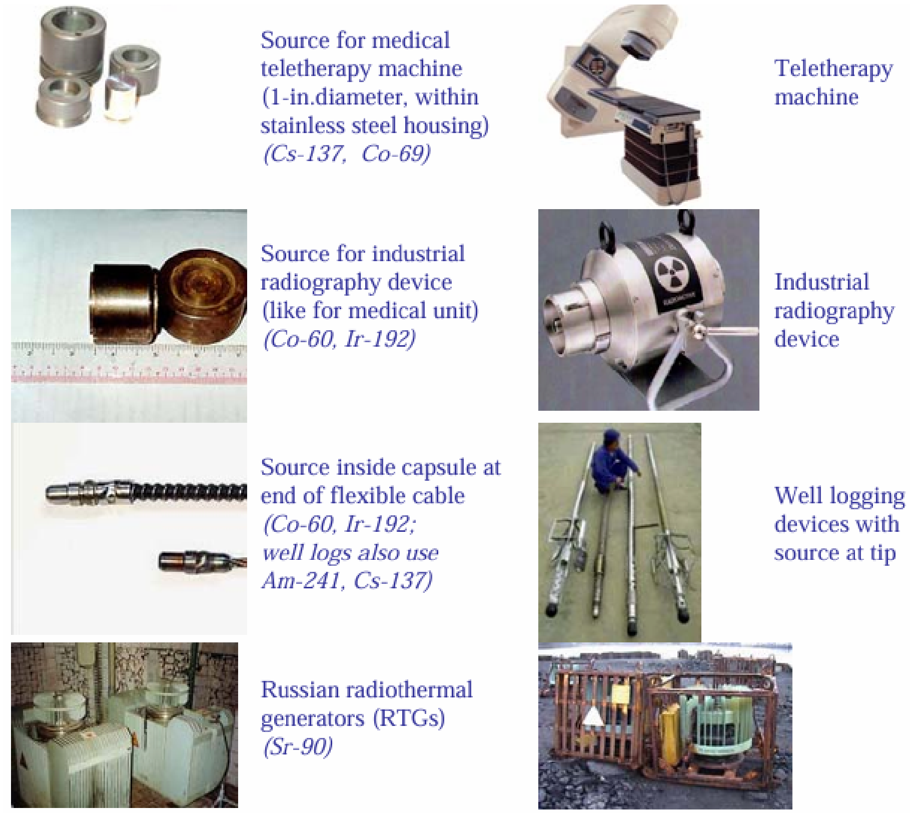

Figure 3.2: Examples of radioactive sources and their application in equipment used in the industry and medicine [76].

portion of cases involve people anticipating that purchasers would be interested in the stolen radioactive sources because of their potential for harm or threat. Industrial sources utilized for non-destructive testing and for mining and construction applications (mainly using ^{137}Cs and ^{241}Am sealed sources) accounted for the majority of reported theft, loss, or missing items [80]. A total of 4075 incidents were registered in ITDB between 1993 and 2022, from which 344 were related to trafficking or malicious use including HEU, plutonium, and $^{239}Pu - Be$ neutron sources [2]. For example, in 2022, a Troxler density and moisture gauge (with a gamma and neutron source inside) was stolen from a van near Madrid [81]. One year after, a 8 mm by 6 mm ^{137}Cs capsule with 19 GBq, part of a density gauge used in mining operations, was lost during its transportation by road in Western Australia, leading to a source search effort along 1,400 km. The source was spotted using a radiation detection system integrated in a vehicle and then accurately located using handheld equipment [82].

According to [3], four basic types of equipment are normally used for detecting illicit trafficking of nuclear and radioactive material: i) Fixed RPMs; ii) Personal Radiation Detectors (PRD); iii) Handheld gamma/neutron search detectors; and iv) Handheld Radionuclide Identification Devices (RIDs). The fixed RPMs, which can be divided in pedestrian monitors (for persons) and vehicle monitors (for vehicles and corresponding cargo), are only effective when the suspected objects pass through them ("choke point" where it is installed), requiring a very restrictive speed limit for vehicles (about 8 km/h). While a RPMs is used for primary inspections, a handheld equipment is normally used when an alarm confirmation is needed and for a detailed characterization of the source.

Considering other detection alternative methods, Coogan *et al.* [19] concluded that MRDS technology with at least one-tenth of the RPM efficiency can have the same or greater impact on the terrorist's success rate (by performing discrete operations) and can be deployed according to the needs (e.g. major events). The use of MRDSs to perform radioactive source search in urban areas is extensively described in literature (see Section 3.2). Cazalas [74] proposed a RN threat detection solution based on a network of radiation detectors at existing road traffic-monitoring system locations (e.g. stop light or red light cameras).

In the case a measured dose rate is above 0.1 mSv/h at 1 m from a surface or object, or neutron radiation or surface contamination is present, during an inadvertent movement or illicit trafficking of radioactive material, an emergency response should be activated for the prompt radiological assessment of the radiation risk [3], [83]. Therefore, neutron detection serves as a crucial complement to gamma-ray detection in countering RN threats. Unlike gamma rays, which can be easily shielded (few centimeters of high-Z material), shielding neutrons is a more complex task and neutron detection faces lower natural background, making it a prompt indicator for potential threats.

The challenge of detecting low-energy gamma-ray sources, which may be shielded or masked, and low-intensity neutron sources, especially at long distances, underscores the critical role of MRDSs in identifying, quantifying, and localizing radioactive sources in scenarios involving illicit trafficking. High-efficiency detection systems with a low rate of false alarms are essential to keep the normal flux of cargo/persons. In the same way to identify and discriminate threat sources from NORM or medical isotopes (legal transport) it is necessary to use high energy resolution detection systems (for source identification).

For Security scenarios (e.g. for Homeland Security purposes) various standards of the International Electrotechnical Commission (IEC) and the American National Standards Institute (ANSI) are available for RPMs, PRDs, handheld, backpack-type and vehicle-mounted (car or van) detection systems. These standards establish the required detection system performance, in terms of radiological, mechanical, electrical and magnetic properties, and the necessary test methods, promoting their interoperability and effectiveness [84]. Despite the widespread use of radiation detection systems integrated on UAVs for source search, radiation monitoring and mapping, no standard is available for these MRDSs [21].

3.1.3 Nuclear facilities, accelerators, targets, and irradiation facilities

This scenario encompasses a diverse range of nuclear facilities, including fission and fusion energy power plants, high-energy particle accelerators, and irradiation facilities dedicated to innovative nuclear technologies like Spallation Neutron Sources (SNSs) and Accelerator Driven Systems (ADSs). Safety in these environments, characterized by high dose rates, magnetic fields and temperatures, requires effective radiation monitoring during inspections, maintenance, and decommissioning.

The decommissioning of NPPs and accelerators spans up to years, involving decontamination, dismantling, and material removal. Advances in robotics are crucial for optimizing technology and to ensure worker safety during decommissioning, as discussed in relevant R&D activities [85]. Large particle accelerators used in research, pose radiological challenges during normal operation, beam losses, and decommissioning, producing byproducts like ^{3}H [86].

Decommissioning poses challenges due to residual radioactivity (of activation products in structural materials), with high doses rates and the need to comply to regulated dose limits. Fusion machines, while different, share decommissioning similarities [86]. In this context, MRDS play a vital role in identifying and localizing potential leaks and quantifying radiation during facility operations or decommissioning.

3.1.4 Detection, monitoring, and identification of naturally occurring radioactive material

Assessing and understanding the impact of natural radiation on the general public and environmental radiation safety is crucial, given that natural radiation significantly contributes to ionizing radiation exposure [87]. The radionuclides responsible for natural radiation can be categorized into terrestrial NORM and cosmogenic NORM. Terrestrial NORM, primarily from the Uranium and Thorium decay series, as well as ^{40}K, poses a more substantial contribution to radiation exposure, especially in regions with granitic soil leading to radon-related concerns. However, the focus extends to Technologically Enhanced NORM (TENORM) resulting from human activities such as mineral processing for industrial purposes. Industrial processes involving minerals like uranium ores, monazite, and phosphate rock can elevate radionuclide concentrations, presenting radiological risks through various exposure pathways such as food chain ingestion, inhalation of radon isotopes, and ingestion of airborne radioactive dust. Long-term monitoring of radiation levels and radionuclides´ identification on these sites is critical to prevent health impacts and ensure compliance with recommended dose limits [88].

The extended half-lives of NORM, spanning up to billions of years, mean that trace concentrations exist in almost all materials. This can lead to false alarms in RPMs at border crossings, triggering substantial nuisance alarms. In 2003, a significant portion of these nuisance alarms resulted from innocuous sources such as medical materials and cargo containing NORM, such as kitty litter, ceramic tiles or fertilizers. Other cargo materials with notable NORM concentrations include abrasives, refractory materials, mined products, Brazil nuts, and bananas. The impact of these false alarms on people and cargo traffic necessitates improvements in NORM detection, monitoring, and identification relative to other man-made sources [89].

MRDSs play a pivotal role in detecting, localizing, quantifying, and identifying NORM.

Due to the spatial and temporal variations in NORM distribution – arising from differences in soil mineral content and activities like ore extraction – it is crucial to map affected areas and continuously monitor radiation levels and NORM concentrations. These measures are vital for effectively managing the risks associated with natural radiation [21].

3.2 Mobile Radiation Detection System - Radiation detection, localization and identification

In the recent study by Marques *et al.* [21], notable progress in the realm of gamma-ray and neutron measurements through mobile radiation detection systems is comprehensively examined considering the scenarios described in Section 3.1. The review article encompasses an analysis of current gamma and neutron detectors, an exploration of the advantages and constraints associated with various combinations of mobile platforms, detection systems, and contextual sensors. Furthermore, the paper offers prospective insights into the fastly evolving landscape of this field. The review highlights several key features of the latest mobile radiation detection systems, namely:

- **Compact and lightweight design.** The development of more compact and lightweight radiation detection systems has enabled their application in handheld and small unmanned vehicles, particularly in air-based platforms;
- **Use of advanced technologies.** Advancements include the use of SiPM-based scintillators, new scintillating crystals with improved energy resolution, and compact dual-mode detectors for gamma and neutron measurements;
- **Data fusion and cooperative detection.** The incorporation of data fusion, mobile sensor networks, and cooperative detection methods has enhanced the capabilities of MRDS;
- **Gamma and neutron imaging.** Gamma cameras and dual-particle cameras (gamma and neutron) are increasingly being used for source location, demonstrating the integration of imaging capabilities into MRDS;
- **Source detection and localization algorithms.** The review discusses recent advancements in algorithms for the detection and search of radioactive sources, indicating a focus on improving detection accuracy and efficiency.

These features, detailed in this Section, showcase the cutting-edge capabilities of modern mobile radiation detection systems, enhancing their effectiveness and versatility across various applications.

The Section is organized into five subsections: (i) a brief review of the recent advancements in the radioactive source detection and localization algorithms, (ii) the new developments in scintillators for gamma and neutron detection and their advantage and drawbacks, (iii) the latest developments of mobile and portable radiation detection systems considering ground surveys, (iv) MRDS considering airborne surveys, and v) the combined use of gamma and neutron detection systems to increase the chances of detecting SNMs and to be able to detect neutron sources (Security and Defence scenarios).

3.2.1 Radioactive source detection and localization algorithms

3.2.1.1 Screening of shipping containers

Efficient screening systems at seaports are essential for detecting and identifying radioactive materials and SNMs, while maintaining the flow of cargo [90]. This typically involves a two-stage process: (i) primary inspection performed by a RPM using large plastic scintillators (PVT or polystyrene)[2] alongside neutron detectors like ^{3}He gas detectors, and (ii) secondary inspection for source identification and characterization. However, if a secondary inspection is inconclusive, a tertiary inspection is conducted, which involves unpacking the container's contents to confirm and locate the radioactive source. This process is highly time-consuming, often requiring a team of five people to manually inspect the container cargo (a 40-ft container can take up to three hours) [91]. During the primary screening stage, vehicles carrying maritime shipping containers pass through an RPM at speeds of approximately 8 m/s (as shown in Figure 3.3). The cost-effectiveness of plastic scintillators supports high throughput, but their low energy resolution often necessitates secondary screening using high-resolution detectors, such as $NaI(Tl)$ or $LaBr_3(Ce)$ scintillators [92], [93].

Figure 3.3: Radiation portal monitors used for screening shipping container cargo [94].

To determine which containers require secondary inspection, the "counts above threshold" alarm criterion is commonly used, comparing radiation detection events (counts) against background levels. To improve discrimination between NORMs, SNMs, and other radionuclides, the Energy Windowing (EW) method can be applied. EW uses prior knowledge of expected spectrum shapes to differentiate between NORM cargo, which resembles background radiation, and SNMs, which show higher counts in low-energy

[2] RPM with spectroscopic capabilities are available but are costly and not widely used.

channels. This method calculates ratios of counts in different spectral regions, making it less sensitive to background suppression effects[3] [95]–[97].

Alternatively, radionuclide identification can be achieved by comparing measured spectra with template spectra from a known library using methods like Least Squares Fitting (LSF), which emphasize spectral features and suppress noise [98]. Another approach, Spectral Angle Mapping (SAM), compares the cumulative count distributions of measured and reference spectra in Fourier space, focusing on shape similarity rather than absolute values. Using an organic scintillator (EJ-309) in a pedestrian RPM, SAM has successfully identified radioisotopes, including ^{137}Cs, ^{241}Am, and ^{99m}Tc [99].

Although LSF and SAM require extensive libraries, they have proven effective in enhancing radioisotope identification in plastic scintillator-based RPMs. A simpler method involves identifying isotopes by locating peaks in energy/channel-weighted spectra, particularly at the Compton edge, which has shown success in identifying sources like ^{238}U, ^{226}Ra, ^{137}Cs, and ^{60}Co in a PVT RPM [100], [101].

These methods significantly improve the ability of primary plastic scintillator-based RPMs to distinguish between different types of radioactive or nuclear material. By integrating energy-based algorithms, the primary screening phase can more accurately identify threat sources, such as WGPu and ^{137}Cs, meeting performance standards set by ANSI and IAEA [98]–[101].

3.2.1.2 Spatially distributed detector networks

Instead of relying on a single large RPM, a more effective approach involves deploying a network of fixed detectors distributed across a large area. This distributed network leverages collective measurements to inspect objects passing through the monitored zone, offering broader coverage and more reliable results. For shipping container screening, strategically placing detectors at key locations, such as entrances, exits, and bottlenecks, expands the sensitive region beyond that of traditional RPMs. For example, Figure 3.4 shows a schematic of the experimental setup from the Intelligent Radiation Sensor Systems (IRSS) C11 outdoor dataset, which used sixteen 5.08 × 5.08 cm cylindrical $NaI(Tl)$ scintillators distributed over an area of approximately $40\,m \times 40\,m$ to detect and localize a moving 6.5 MBq ^{137}Cs source [16]. These networks typically use smaller inorganic scintillators in each detector node, compensating for their size with dense spatial distribution, which enhances sensitivity and adaptability. The compact detectors also allow for discreet deployment and spectroscopic capabilities, improving the system's ability to differentiate between legitimate and false alarms [102], [103].

In a study by [17], a MLE algorithm was used with data from five stationary 5.08×5.08 cm cylindrical $NaI(Tl)$ detectors to estimate the location of a 189 kBq (5.1 µCi) ^{137}Cs source within a $5\,m \times 5\,m \times 5\,m$ volume. The algorithm's computational cost was reduced by iteratively refining the grid, retaining only the grids with the highest likelihoods based

[3] EW relies on count ratios rather than overall counts.

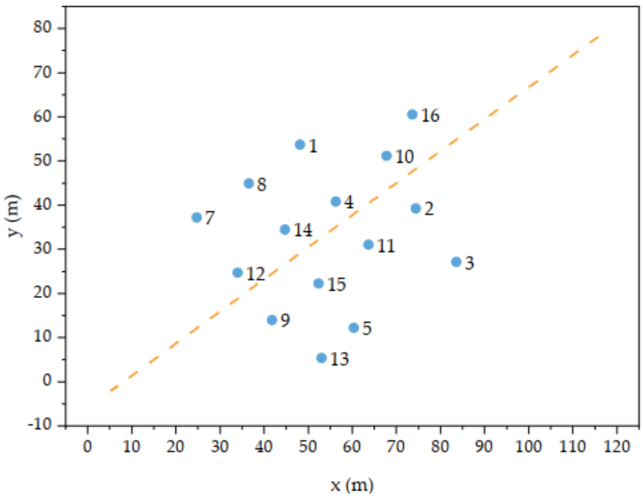

Figure 3.4: Experimental setup for the IRSS C11 outdoor dataset involving sixteen cylindrical $NaI(Tl)$ detectors placed at specific locations. The detectors are represented by the blue circles and the trajectory of a 6.5 MBq ^{137}Cs source is indicated by an orange dashed line [16].

on the inverse square relationship of source intensity to measured counts. The method successfully localized the ^{137}Cs source with an accuracy of approximately 0.53 m for a 3 minutes measurement time. The distances between the source and all detector positions ranged from 0.84 m to 1.77 m. Faster source localization is anticipated with higher activity sources; for instance, a measurement time of one second could accurately localize a source with an approximate activity of 22.5-34 MBq (0.61-0.92 mCi).

Similarly, a Particle Filter (PF) algorithm applied to experimental data from the IRSS tests using 22 stationary $NaI(Tl)$ scintillators, and a measurement time of 5 minutes, successfully localized a 281 kBq (7.6 µCi) ^{137}Cs source with an accuracy of 1.5 m in a $10 \times 10\, m^2$ area [44]. PF, a Bayesian method utilizing MC techniques, involves sampling particles representing potential source locations and activities, with particles weighted according to measurement likelihood. Iterative resampling refines the estimate, converging on the most likely source location [104], [105].

While requiring extended measurement times (few minutes), both MLE and PF algorithms demonstrated the capability to accurately localize point-like ^{137}Cs sources using a network of stationary detectors [17], [44]. This is particularly useful in scenarios that allow prolonged measurements on stationary containers, such as detector networks integrated into ships or comprehensive port-wide systems. However, the practical implementation of such networks is limited by costs associated with deploying a large, dense array of detectors, making it challenging for real-world applications [17], [18].

Other algorithms, such as triangulation radiation source detection and source region detection methods, prioritize the inference of source presence over accurate localization. These methods rely on clustering location estimates from various detector subsets and focus on metrics like detection True Positive Rate (TPR) and False Positive Rate (FPR) rather than localization error [18], [43].

Since accurately localizing a source within a shipping container requires an error margin smaller than the container's shortest dimension (the external standard container width is 2.43 m), achieving this would necessitate either high-efficiency detectors or an extensive network of detectors [18]. Although ANSI standards for spectroscopic portal monitors require the detection of a ~592 kBq (16 µCi) ^{137}Cs source, these distributed detector networks are expected to meet similar performance benchmarks if implemented in screening systems [106].

Given the vast scale of seaports, relying solely on numerous stationary detectors to achieve the required sensitivity is impractical. A more effective approach combines stationary and mobile detectors, enabling continuous radiation mapping throughout the port using advanced algorithms [16], [18].

Innovative applications include integrating detector networks into container ships for extended measurement times during voyages, enabling accurate source characterization and localization. Another approach involves embedding detectors into port lifting equipment, such as cranes used for unloading container ships. This method would enable close proximity to containers for longer periods (~60 s), although it may only screen one side of the container [107], [108].

3.2.1.3 Mobile Radiation Detection System - Detection and localization algorithms

To enhance the sensitivity of a detector network across a large area with a limited number of detectors, adopting mobile detectors may effectively contribute to create an adaptable and cost-effective network, particularly applicable to expansive regions like seaports [109]. This research area gained interest through initiatives like the "Detecting Radiological Threats in Urban Environments" challenge and Defense Advanced Research Projects Agency's (DARPA) SIGMA project, which employed over 1,000 portable radiation detectors in Washington, D.C. [110]–[112].

While the mobile radiation detector network literature is often focusing on urban environments with detector movement restricted to roads [44], [113], [114], similar constraints may apply to detectors mounted on port vehicles navigating shipping container stacks, arranged in a grid-like formation. While it is possible to deploy a mobile detector network on port vehicles, which are increasingly automated and feature real-time tracking as part of operational procedures, the predefined paths followed by these vehicles may limit the sensitivity of the mobile detector network at a seaport. This potential constraint warrants further investigation to assess its impact and optimize the network's performance [115]. The process of detection and localization of concealed radioactive sources is commonly thought of as a path optimization issue, which is contingent upon the selection of the detection system path [39], [116], [117] and the source search method [38]. A MRDS can follow predetermined paths to generate a radiation map or conduct a source search within a region of interest [39], [116]. Examples of such paths include parallel sweeping search patterns [38], [39] and Archimedean spiral search patterns [40], which are designed to minimize survey time, optimize battery or fuel consumption, and ultimately reduce operational costs. Nevertheless, employing informative path planning enables the system to dynamically adjust its predefined path based on real-time measurements. This adaptive approach enables the detection system to focus on regions with higher radiation counts, thereby maximizing information acquisition during the search. As a result, this strategy not only improves source localization accuracy but also significantly reduces survey time [41], [42]. An example, is the use of a profit function to make a trade-off between exploration and exploitation, i.e., maintain the initial defined path or change the path to scan a particular area (e.g. hot spot) [42]. In [17], a mobile robot moves closer to the radiation source and starts a perimeter path, by performing circles around the source, when an increase of gamma-ray counts occurs.

In [18], [21], a comprehensive review of the algorithms utilized in the detection and localization of radioactive sources is provided. For instance, in [113] a kernel density estimation and grid search are applied with a MLE algorithm to estimate the locations of four ~44 MBq ^{54}Mn sources in a simulated urban environment, demonstrating successful localization within 2 m in ~200 s with 50 randomly moving $CsI(Tl)$ detectors. Based on the simulated outcomes, a source localization error of ~2.43 m (lower dimension of a standard shipping container) could be attained for both 74 MBq and 18.5 MBq sources at distances of 10 m and 5 m respectively from the background measurement position. This indicates the relevance and applicability of the results to seaport scenarios.

PF algorithms, as discussed in [44], were utilized to process data from simulated mobile detector networks in urban environments. The study revealed that detectors, following predefined paths (roads) and clustered effectively around a simulated source, would allow to obtain a localization error on the order of meters. In another study [118], a PF method was explored, where one or more detectors autonomously navigated an area based on optimal estimated information gain from prior measurements. Monte Carlo simulations demonstrated superior performance in search time and localization error compared to random and uniform methods. Experimental measurements in a large outdoor area confirmed effective localization of two (~ 37 MBq) ^{137}Cs sources with an accuracy of around 3 m using a single mobile GM detector, with an average detection time of 93.4 s.

For seaport shipping container screening, the study suggested that road paths defined by port operations may limit the performance of mobile detector networks, due to difficult access to hot spots. However, introducing one or more detectors with an adaptable information-driven approach could significantly enhance the mobile detector network [18].

Additional algorithms, discussed in [109], [114], involved grid-splitting and graph theory methods for gamma-ray sources localization. The use of MLE, PF, and graph-theory methods provides essential source estimate locations for future screening systems. While source localization methods require substantial computational power, normally requiring a powerful central node to process data and align results from individual detectors, they contribute to a smart detector movement [118].

Techniques like Poisson Kriging were employed for radiation field spatial distribution and source location of anomalous radiation sources (e.g., nuclear bombs or weapons) using mobile sensor networks [119]. To achieve high accuracy, relatively strong sources (500 µCi or above) and small source-detector distances (less than 5 m) must be considered. Additionally, [120], [121] suggested using measurements from a mobile robot for autonomous hot spot detection. While Huo *et al.* [120] utilized a strategy based on a partially observable Markov decision process and Bayesian framework, Anderson *et al.* [121] employed a recursive Bayesian estimation. Future research is needed to address challenges like object attenuation, autonomous searching in obstacle-laden environments with multiple sources, and cooperative searches involving ground-based vehicles/robots and air-based vehicles.

Another approach involves integrating source position into a grid map using a mobile robot with autonomous positioning [122]. This method utilizes Simultaneous Localization and Mapping (SLAM) techniques along with a Markov chain Monte Carlo algorithm for source parameter estimation. While efficient, this approach must address challenges such as radiation scattering from walls, shielding effects from obstacles, and background fluctuations. This method may not be efficient for localizing distributed sources, and enhancement is suggested through the use of a gamma camera.

Learning-based methods, particularly machine learning algorithms, are gaining popularity. A review of machine learning applications in nuclear science, emphasizing risks and opportunities is presented in [123]. In [124] an artificial neural network is proposed to identify radioisotopes in natural gamma sources and determine the corresponding activity uncertainties. Another innovative application involves the use of artificial neural networks to reconstruct Compton edges in plastic scintillator spectra for pseudo gamma spectroscopy, even with limited counting statistics [125], and for radioactive hot spot localization and identification using deep learning [126].

3.2.2 Radiation detection and gamma spectrometry

Although semiconductor detectors offer superior energy resolution for gamma spectroscopy, they are not ideal for shipping container screening due to their high cost, the limited availability of large high-purity semiconductor crystals, and their vulnerability to radiation damage [127], [128]. For instance, COTS detectors made from CZT crystals can achieve energy resolutions better than 2.0% at 662 keV while operating at room temperature, but their high cost and small volumes (only a few cm^3) limit their practicality for large-scale applications [29], [129]. In contrast, the larger volumes and lower costs of scintillator detectors make them an excellent choice for Security and Defence applications.

Inorganic scintillators, characterized by high-Z crystals and high light output, are especially suitable for gamma-ray spectroscopy due to their excellent intrinsic detection efficiency, even for low-energy radiation. Examples include alkali halides such as $NaI(Tl)$ and $CsI(Tl)$, oxides as the BGO, and lanthanum halides as the $LaBr_3$[Ce+Sr], which offers improved energy resolution and photoelectron yield over standard $LaBr_3$ [130]. A summary of the characteristics of some inorganic scintillators is presented in Table 3.1.

Table 3.1: Resume of the inorganic scintillation crystal main characteristics.

Scintillator property	NaI(Tl)	CsI(Tl)	$LaBr_3$[Ce]	$LaBr_3$[Ce+Sr]	BGO	Ce:GAGG	Ref.
Density	3.67	4.51	5.08	5.08	7.13	6.63	[31], [130], [131]
Effective atomic number	49.7	54	45.2		74	50.5	[132], [133]
$\Delta E/E$ % at 662 keV	<7.5	6.5–8	2.6	2.2	16[1]	5.2	[130], [134]–[137]
Wavelength of max emission [nm][2]	415	550	380	385	480	520	[31], [130], [135]
Photoelectron yield [% NaI(Tl)]	100	45	165	>190	20	–	[130]
Light yield (photons/keV)	38	54	63	73	8–10	46	[130], [137]
Primary decay time (ns)	250	1000	16	25	300	90	[130], [137]
Hygroscopic	yes	slightly	yes	yes	no	no	[130], [135], [137]
Self activity	no	no	yes	yes	no	no	[130], [137]

Organic scintillators, made from scintillating materials suspended in solids (plastic scintillators) or liquid solvents, have certain limitations compared to inorganic scintillators, such as poorer energy resolution and low light yield. Due to their low-Z material composition, gamma-ray interactions are primarily through Compton scattering in the relevant energy range (between 30 keV and 3 MeV). Despite their limitations, organic scintillators offer significant advantages, including low cost, rapid response, and availability in various shapes and large volumes. For example, plastic scintillators can cover large areas (several m^2) and are cost-effective for applications like RPM, especially for gross gamma-ray counting above 100 keV [91]. While both gas flow proportional counters and plastic scintillators exhibit high efficiency for beta particles, plastic scintillators are significantly more efficient for gamma-rays ($\sim$ 500 times higher) and offer about 100 times higher gain than proportional counters [31], [138]. Additionally, the low-Z composition of organic scintillators allows for a high intrinsic detection efficiency to fast neutrons, particularly in elastic scattering interactions where neutrons transfer significant energy to the recoil nucleus [139]. Consequently, PSD techniques, which compare the measured current pulse over time, can be used for the discrimination between gamma rays and neutrons [140], [141]. Examples of gamma/neutron (dual-mode) detectors using PSD include the liquid scintillators EJ-301 (equivalent to NE-213) and EJ-309 (which can be loaded with natural boron for thermal neutron detection) [142]. In [140], a plastic scintillator was loaded with ^{10}B while maintaining the ability of neutrons and gamma rays discrimination. Table 3.2 outlines the advantages and drawbacks of plastic scintillators.

Table 3.2: Advantages and drawbacks of using plastic scintillators [31], [91], [138].

Advantages
- Gross counting gamma rays (above 100 keV) - High detection efficiency to charged particles and neutrons - Large size sheets (~m^2) available - Ruggedness and no regular maintenance - 500 times more efficient for detecting photons than a gas detector - Fast response - Low cost - Lightweight
Limitations
- Cannot be used for X-ray/gamma-ray spectroscopy - Light yield is a factor of 4 lower than that of NaI(Tl) scintillator - Lower intrinsic efficiency than inorganic scintillators

Although organic scintillators can detect fast neutrons, ^3He gas-based proportional counters remain the standard for neutron detection. ^3He-based detectors provide excellent gamma rejection properties and a high thermal neutron capture cross section (5330 barns). Additionally, it can detect fast neutrons when the gas chamber is surrounded by a moderating material like polyethylene [31], [139], [143].

Other dual-mode scintillators with PSD capabilities include inorganic scintillators like Cerium-doped cesium lithium yttrium chloride (CLYC) (gamma energy resolution 4.5–5%), NaI(Tl+Li) [130], Cerium-doped cesium lithium lanthanum chloride (CLLC) (gamma energy resolution 3.4%), and Cerium-doped cesium lithium lanthanum bromide (CLLB) (gamma energy resolution 2.9%)[4]. These scintillators can detect thermal neutrons due to their ^{6}Li content. Despite the better energy resolution of CLLB, it has inferior PSD capabilities compared to CLYC and CLLC. Additionally, CLLC and CLLB crystals exhibit self-activity due to the presence of ^{138}La [84].

RPMs with spectroscopic capabilities, utilizing NaI(Tl) and $LaBr_3$(Ce) scintillators along with separate neutron detectors, are commercially available [144], [145]. However, their higher cost compared to PVT-based RPMs limits their widespread use in ports as primary screening systems [91], [92]. To address this, efforts have been made to enhance energy resolution by impregnating plastic scintillators with high-Z elements like bismuth (e.g. Bi-loaded PVT). However, challenges such as reduced light yield and increased scintillation photon attenuation remain to be resolved. Recent advancements in semiconductors, including $TlBr$ and perovskite halide crystals, have demonstrated significant potential as high-efficiency, cost-effective solutions for spectroscopic radiation detection at room temperature [146].

A critical aspect of scintillator detection systems is the optical coupling of the scintillating crystal's output to the related light sensor. Table 3.3 compares different light sensors, ranging from conventional PMTs to the more recent SiPMs.

[4]All energy resolutions are relative to the 662 keV gamma energy.

Table 3.3: Summary of light sensors characteristics. Photosensors analysed: PMT, SiPM, APD, and P-type, Intrinsic, and N-type (PIN) diode. Adapted from [147].

Light sensor	**PMT**	**SiPM**	**APD**	**PIN diode**
Size	Big	Small	Small	Small
Bias voltage	High	Low	Medium	Low/none
Power consumption	High	Low	High	Low
Sensitivity to microphonics	No	No	Intermediate	Yes
Magnetic field influence	Yes	No	No	No

Gamma cameras offer an alternative to non-directional detection systems, providing directional capabilities for detecting and locating radioactive sources or monitoring contaminated areas. These cameras operate based on three key principles: pinhole, coded-aperture, and Compton scattering [84], [148]. Pinhole cameras employ heavy collimators to limit the entry of gamma rays, enhancing angular resolution. However, this improvement comes at the expense of detection efficiency and ease of handling. Compton cameras utilize Compton scattering kinematics for source location estimation, offering a wide field of view without the need for collimation or coded masks [149]. Coded-aperture cameras use passive or active masks to modulate gamma flux, generating images with a position-sensitive detection system [150].

3.2.3 Mobile and portable gamma-ray detection system – ground surveys

The data limitations from the Fukushima Daiichi Nuclear Power Plant (FDNPP) accident, including activity released, spatial distribution, and plume direction, severely hampered evacuation and sheltering decisions. The tsunami rendered 23 out of 24 static monitoring points inoperative, resulting in a data blackout for decision-makers [151], [152]. This highlighted the vulnerability of static monitoring systems during RN emergencies, emphasizing the need for resilient monitoring and enhanced data accessibility during disasters [153]. Environmental samples within a 20 km radius were assessed using portable car-mounted equipment, with gamma-emitting radionuclides detected through semiconductor Ge detectors. Car-borne surveys were later conducted for air dose rate mapping around Fukushima using GM counters, ionization chambers, $NaI(Tl)$, $CsI(Tl)$, HPGe, and silicon semiconductor detectors [152], [154]–[157]. This radiation monitoring was also extended to sites designated for the future deployment of NPP facilities [158]. For radiation mapping and plume tracking, $LaBr_3(Ce)$ detectors were deployed on vehicles, enhancing emergency and routine monitoring over large areas [159].

Vans are typically employed for transporting larger and heavier detection systems. For example, Baeza *et al.*[160] used a van to house a proportional counter, $NaI(Tl)$ scintillator, and HPGe detector for low-background aerosol sample measurements. Backpack-mounted systems, such as those using CZT semiconductor [161] and $NaI(Tl)$ scintillator [162], [163], provided high-spatial resolution mapping in areas inaccessible to vehicles.

Comparisons showed that while HPGe detectors are heavier, they offer lower intrinsic background, better energy resolution, and higher efficiency compared to $LaBr_3(Ce)$ and $NaI(Tl)$ detection systems.

Handheld equipment for walk surveys includes the $NaI(Tl)$ scintillator with PMT and the SiPM-based scintillators $CsI(Tl)$, $LaBr_3(Ce)$ and Cerium-doped gadolinium aluminium gallium garnet (GAGG(Ce)) [87], [147], [164]–[166]. Radiation detectors have also been connected to smartphones for use by the general public, such as Mobile Application for Radiation Intensity Assessment (MARIA) and pocket Geiger (POKEGA) [167]–[169]. These systems aim to provide widespread, low-cost, and lightweight monitoring, although challenges such as incorrect readings and user dependency have been reported.

After the Chernobyl accident, UGVs were first used for tasks too hazardous for humans due to radiation. Despite challenges like navigating through obstacles and the vulnerability of radiation-sensitive electronics, advancements have enabled the development of more compact and agile UGVs for RN emergency scenarios [24]. Examples include UGVs with rotating $LaBr_3(Ce)$ scintillators for directional gamma radiation profiles [170], and those equipped with GM counters for indoor mapping [39], [171]. Mobile robots with telescopic masts have also been used for reactor inspections under high radiation doses [172].

Despite reducing human exposure, UGVs still require advancements in autonomous navigation, mapping, exposure reduction, and communication systems.

Innovations in portable or handheld gamma cameras, such as the Safety and Security Compton Telescope (SCoTSS) Compton telescope and Volumetric Compton Imaging (VCI) systems, have enhanced source localization and mapping capabilities in nuclear Security and Safety scenarios [173]–[176]. Large coded-aperture cameras transported by ground vehicles, such as 3D Stand-Off Radiation Detection System (SORDS-3D) and Stand-Off Radiation Imaging System (SORIS), have also been developed for rapid detection and identification of radioactive sources over large areas [150], [177].

3.2.4 Mobile gamma-ray detection system – airborne surveys

After the FDNPP incident, traditional airborne radiation measurements faced significant challenges. Regulatory constraints requiring altitudes above 150 meters limited the operation of manned aircraft equipped with $NaI(Tl)$ scintillation detectors, leading to poor spatial resolution in radiation dose mapping. Although initial radiation maps of areas up to 80 km from the NPP could be generated quickly, detailed information was limited, necessitating large and expensive detection systems [152]. Manned helicopters, later equipped with $NaI(Tl)$ and $LaBr_3(Ce)$ detectors, were better suited for challenging terrains but faced similar regulatory restrictions. Additionally, the high dose rates detected raised concerns about the risks of crew radiation exposure [178], [179].

In recent years, UAVs have become increasingly popular due to their versatility, mobility, and accessibility across various sectors, including humanitarian response and Search and rescue (SAR) operations. UAVs have been deployed for diverse applications such as inspection, delivery systems, building operations, and surveillance, with significant impact on agriculture, transportation, and security [180]. They are especially valuable in SAR, providing real-time monitoring and reaching inaccessible or hazardous areas. Equipped with high-resolution imaging, thermal cameras, and LiDAR sensors, among other sensors, UAVs can collect comprehensive data, significantly enhancing situational awareness [181].

Advancements in control, motion planning, perception, and localization have enhanced UAV autonomous operations[5]. However, further research is required to achieve fully autonomous 3D collision-free navigation in extreme environments (e.g., emergency responses) and urban areas. Essential capabilities to be developed include scanning, obstacle avoidance, contour following, environment-aware return-to-home, and return-to-highest-reading functionality [182]. Current unmanned aerial vehicles require extensive human supervision, especially in urban areas, given low-altitude flights (0.3–40 m) and close proximity to structures, introducing challenges for vehicle and navigational autonomy [183], [184].

The FDNPP accident marked the first deployment of a small UAV, the Honeywell T-Hawk, used to obtain images of reactor damage and radiological measurements [182], [185]. Unmanned helicopters carrying detection systems with a payload around 10 kg, operated at lower altitudes (50-100 m) and speeds (8 m/s) than manned aircraft, improved the spatial resolution of the radiation mapping, though their shorter flight times ($\sim$ 90 minutes) and limited range (3-5 km) were notable drawbacks [40]. Fixed-wing UAVs can operate at altitudes as low as 40-60 m and at speeds of 14-18 m/s [27]. An example is the fixed-wing Unmanned Airplane for Radiation Monitoring system (UARM), although with a medium endurance (up to 6 hours) and a large-area coverage (up to 100 km) still require significant operator training and has limited payload capacity [21], [186]. However, these UAVs achieved better spatial resolution at lower costs compared to manned aircraft [25], [27].

It's worth noting that the majority of lost or stolen sources (88%) typically fall within lower activity categories (category 4 or 5)[6] [2], [187], which would make impracticable its detection at a distance of several meters. VTOL and hover capabilities of both unmanned helicopters and multirotors make them suitable for low activity sources.

The widespread use of multirotors, known for their maneuverability and ease of operation, has extended to radiation mapping and source localization. Despite limitations in payload and flight time, lightweight and compact COTS gamma radiation detection systems such as CZT and SiPM-based $CsI(Tl)$ scintillators have been successfully integrated into these platforms [21]. CZT detectors, such as the GR1 model, have proven effective

[5]Considering the mode of operation, unmanned systems can have different levels of autonomy: remotely controlled, teleoperated, semi-autonomous, and fully autonomous.

[6]According to IAEA, radioactive source can be grouped in five categories based on its potential to cause deterministic health effects and depends on the source activity and dangerous (risk). An exposure of only a few minutes to an unshielded Category 1 source may be fatal. At the lower end of the categorization system, sources in Category 5 are the least dangerous.

in radiation mapping after nuclear accidents and in monitoring NORM sites, though their small crystal size and high cost limit broader use [26], [29], [188]–[192]. Similarly, the SiPM-based 32.8 cm^3 $CsI(Tl)$ scintillator (SIGMA-50) offers a good balance of weight (300 g) and performance for UAV applications [193]. Tables 3.4 and 3.5 summarize the advantages and limitations of using multirotors for radiation measurements, as well as the recent detectors integrated into these platforms, respectively.

Table 3.4: Advantages and limitations of using multirotors for radiation measurements [21].

Advantages
- Improved spatial resolution compared to manned aircraft (lower altitudes and speed)[1] - Cost-efficiency compared to manned aircraft[2] - Flexibility and accessibility (high maneuverability allows access to difficult areas) - Easy to operate and avoid unnecessary human exposure risks - Autonomous and cooperative operation - Avoid cross contamination (compared to ground surveys) - Fast deployment to survey area
Limitations
- Flight time (flight autonomy of 30–35 min makes them less suitable for extended surveys)[3] - Compact and lightweight detectors (to increase endurance) - Weather conditions (rain and wind can impact their performance and safety)

[1] Regulatory restrictions on manned aircraft altitudes (above 150 m).
[2] Cost reduction in platform operation/maintenance and compact detectors (reduced source-detector distance).
[3] Fixed-wing UAVs offer longer flight times but may require runway.

Table 3.5: Recent gamma-ray detection systems coupled to a multirotor.

Detector	**Advantage**	**Limitation**	**Ref.**
GM counter	Low cost; lightweight; dose rate measurements	No spectroscopy	[38], [191], [194], [195]
CZT	Lightweight; high resolution	Small volume (~1 cm^3); expensive	[188]–[192], [195]–[199]
$NaI(Tl)$ with SiPMs	Compact; low power (<1 W) and compatible with strong magnetic fields	Medium resolution; Hygroscopic	[200]
$CsI(Tl)$ with SiPMs	Lightweight; low power; higher light yield than $NaI(Tl)$	Medium resolution; slightly hygroscopic	[28], [201], [202]
BGO	High sensitivity; crystal volume available (103 cm^3)	Poor energy resolution; heavy	[203]
$CdTe$	High energy resolution	Only for low-energy gamma rays	[204]
PIN Diode	Lightweight, low power consumption, and low cost	Small volume; susceptible to noise vibrations	[205]
CMOS (Timepix)	Lightweight, and low power consumption	Small volume	[206]

For higher gamma-ray detection sensitivity, larger crystals like BGO scintillators have been tested, but their weight and reduced flight time present challenges [203]. Although $LaBr_3(Ce)$ scintillator, and the semiconductors CZT and $CdTe$ detectors offer higher energy resolution, their cost and limitations in detecting low radiation fields restrict their use [131], [203]. Gamma cameras, including compact Compton cameras, have been integrated into UAVs for source localization, but challenges such as long acquisition times and limited flight duration of the aerial vehicle persist [207]–[209].

Using a fleet of unmanned vehicles, particularly UAVs, can significantly enhance the speed and effectiveness of radiation mapping and source localization. For example, fixed-wing UAVs can rapidly map large areas to identify hot spots, while multirotors can conduct detailed analyses around these hot spots. This approach, aligned with the FRIENDS project recommendations, offers redundancy and efficiency in RN emergency responses and vehicle inspections [195], [210]. The VTOL and hover capabilities of multirotors and unmanned helicopters make them suitable for low-activity source detection, especially in confined spaces or near critical infrastructures [21], [211].

3.2.5 Combination of Neutron and Gamma Detection Systems

In Security scenarios addressing the illicit trafficking of SNMs and radioactive sources, neutron detection systems are often combined with gamma spectrometers for enhanced detection capabilities. Ground vehicles, including cars, vans, and trucks, are essential for transporting large detection systems (with transversal areas of approximately 1 m^2). These vehicles are necessary due to the substantial stand-off distances required (source-detector separations of several meters) and the challenge of detecting weak, shielded, or masked sources. However, the higher cost of large detection systems, along with challenges such as deploying them in off-road locations, navigating obstacles, accessing confined spaces, and their increased sensitivity to background fluctuations, limits their applicability in certain scenarios [212], [213].

Table 3.6 highlights the use of MRDSs in Security scenarios, particularly for the monitoring, mapping, and source localization in urban environments. Notable R&D projects that integrate both gamma and neutron detection systems include Radiological multi-sensor analysis platform (Rad Map), Sistema mobile per analisi non distruttive e radiometriche (SLIMPORT), Modular Detection System for Special Nuclear Material (MODES SNM), Mobile Urban Radiation Search (MURS), and Real-time Wide Area Radiation surveillance system (REWARD). For instance, MODES SNM detection system has proven effective in scanning maritime containers at Rotterdam seaport, where it detected and identified gamma-ray sources (including NORM), neutron sources (^{252}Cf, $^{241}Am-Be$ and $^{239}Pu-Be$), SNM and the presence of hydrogenated or lead shielding [214].

The development of compact and lightweight detection systems, compatible with multirotors, is facilitated by the use of dual-mode CLYC scintillators with ^{6}Li, as explored in [223]–[226]. However, limitations on the crystal size (a CLYC scintillation crystal with

Table 3.6: Combination of mobile radiation detection systems used in Security scenarios.

Gamma-Ray Detection System	Fast/Thermal Neutron Detection System	Mobile Platform	Project/Ref.
NaI(Tl) imager; HPGe	EJ-309 liquid scintillators (fast)	Truck	Rad Map [212], [215]
NaI(Tl) ; $LaBr_3$(Ce)	NE-213 liquid scintillator (fast); ^{3}He proportional counter (thermal)	Not specified	SLIMPORT [216]
Xe scintillator	^{4}He scintillator (fast); ^{6}Li-lined ^{4}He tubes (fast and thermal)	Van	MODES SNM [214]
NaI(Tl)	^{6}LiF (thermal)	Car	MURS [217]
-	EJ-309 liquid scintillator (fast); BF_3 and ^{3}He detectors with HDPE (thermal)	Truck	[218]
Two stacked 1 cm^3 CZT	Thin planar silicon PIN diodes covered with hydrogenated plastic radiators (fast); Silicon backfilled with ^{10}B (thermal)	Not specified	REWARD [219]–[222]
CZT (1 cm^3); CLYC with ^{6}Li	CLYC with ^{6}Li (thermal)	Multirotor	[223], [224]
CLYC with ^{6}Li	CLYC with ^{6}Li (thermal)	Multirotor	[225], [226]

only 12.86 cm^3 was used) and the influence of natural background variations restrict their broader application in Security and Defence scenarios. Moreover, a network of low-cost mobile detectors with georeferenced data has been proposed for source localization in urban environments [227].

Some commercially available MRDSs suitable for Security and Safety scenarios include:

- Rapiscan-ASE's MD210, MD134, and GMS-4X4 vehicle-mounted detection systems, which detect and identify a wide range of radioactive materials and SNM. These systems can operate in stationary scan or drive-by modes, offering flexible inspection options [228];
- The Kromek D3S ID, a wearable device that continuously scans gamma and neutron radiation, provides a hands-free solution for radiation detection [229];
- Berkeley Nucleonics Model PM1703GNB and PM1703GNA PRDs, capable of detecting gamma rays and neutrons while storing and transferring gamma spectroscopic data, making it well-suited for integration into UAVs [230];
- The Mirion SPIR-Explorer Sensor, a lightweight radiation detector that can be mounted on UAVs, UGVs, or robots [231].

A recent DHS document details the essential features and selection criteria for a MRDS used in detecting, interdicting, and assessing photon and neutron radiation hazards [232].

Innovations in detection technologies have also been made. Polack *et al.* introduced a dual-particle imaging system combining Compton scattering and neutron scattering for the simultaneous detection of fast neutrons and gamma rays [233]. Al Hamrashdi *et al.* developed a portable dual-particle imager capable of detecting gamma rays, thermal neutrons, and fast neutrons. While the device has demonstrated promising results, it requires further enhancements in the discrimination between neutron and gamma-ray pulses [234]–[236].

Recent advancements in scintillator-based coded-aperture imaging systems offer potential for real-time, portable neutron localization, particularly in security and nuclear decommissioning [143], [237]. Innovations in crystal growth, such as the development of single stilbene crystals as an alternative to liquid scintillators, offer advantages like higher light output and better PSD performance [238]. Plastic scintillators like EJ-276 and EJ-276G continue to be practical options for coded-aperture imagers, with ongoing research focusing on enhancing system compactness and portability [239].

Other studies have explored the impact of angular resolution on gamma-neutron coded-aperture imagers [240], and proposed portable gamma-ray/neutron imaging systems using CLYC scintillators and coded-aperture masks for security applications [241]. Continuous research is improving the techniques, sensitivity, and overall efficiency of these advanced imaging systems.

3.3 Going beyond the state-of-the-art – challenges, hot topics, emerging issues

Several challenges in mobile radiation detection technology highlight areas requiring further research and development:

- **Detection technology.** As per the IAEA [242], future research should focus on enhancing detection probability, range, source identification, and mobility;
- **Accurate source parameters estimation.** Accurately estimating source parameters–such as position and activity–in complex nuclear environments or unknown geometries involves accounting for factors like scattering, shielding, and background radiation. This necessitates advanced mapping techniques and optimized detection path strategies [122];
- **Data fusion and sensor networks.** Integrating data from multiple sensors and using sensor networks (fixed and mobile) can improve the detection and localization of radioactive materials while reducing false alarms [21], [243];
- **Fast and accurate source detection and localization algorithms.** Future efforts should focus on improving detection algorithms for better accuracy, speed, and efficiency in identifying radioactive sources [21];
- **Fragile detection materials.** The use of fragile and expensive materials like inorganic scintillators, often experiencing cracking even with minimal exposure to shock (e.g. $NaI(Tl)$ exhibits fragility and tends to crack easily, whereas cesium $CsI(Tl)$ is more pliable and can withstand higher levels of shock). Similarly, the high machining costs and the brittle nature of stilbene (as compared to plastic scintillators) prevent the

widespread use of the single crystal. A good alternative to these detection materials are the easily machined and mechanically robust plastic scintillators [237], [244];

- **Radiation-hardened electronics.** Research into new materials and shielding combinations is vital to enhance the lifespan and operational efficiency of radiation-sensitive electronics [172], [245];
- **Navigation and environmental conditions.** Mobile radiation detection systems (MRDSs) face challenges in uncontrolled environments, both indoors (e.g., GNSS disruptions, obstacles) and outdoors (e.g., weather, terrain, urban obstacles) [246];
- **Shortage of ^{3}He gas.** The limited availability of ^{3}He gas, essential in neutron detection systems, poses a significant challenge [5], [247];
- **Autonomous vs semi-autonomous.** Currently, unmanned vehicles and robots require significant human supervision, especially in urban areas and extreme environments. Low-altitude flights (0.3–40 m) and close proximity to structures introduce challenges for aerial vehicle and navigational autonomy. Degraded GNSS signals, caused by interference from buildings and other structures, or complete unavailability in indoor environments, can significantly impact the vehicle's navigation system. Improvement of the human-machine interface for better teaming is also crucial [182], [184];
- **Photo-detectors temperature dependence.** At a fixed bias voltage, a SiPM's gain changes linearly with temperature due to the linear variation of the breakdown voltage with temperature. Thus, power supplies with built-in gain stabilization must be used [248];
- **Autonomous and cooperative source search.** Autonomous search in multi-source scenarios, and cooperative searches involving both ground and aerial vehicles [120], [121].

These challenges underline the continuous need for advancements in radiation detection technology and mobile platforms to ensure its effectiveness in Security scenarios and in response to RN accidents and emergencies.

Current hot topics include:

- **Light yield and energy resolution improvement on plastic scintillators.** Plastic scintillators generally exhibit a low light yield (around 10 photons per keV) and poor energy resolution [249]. Incorporating complex iridium fluorescents into high-Z sensitized plastic scintillators can increase light output and improve energy resolution (gamma spectroscopy [250]. Enhancing scintillation light collection can be achieved by employing a grid of smaller-volume plastic scintillators combined with a higher density of SiPM sensors. This approach is more effective than using a large plastic scintillator volume. Notably, it significantly enhances the detection of low-energy gamma-ray sources (below 60 keV), such as Am-241 [14];
- **New contextual sensors.** Visual sensors play a crucial role in mapping radiation

dispersion, particularly in tasks like decommissioning contaminated structures. Employing 3D reconstruction methods by fusing data from gamma imagers and ground-penetrating radar can improve the precision of locating radiation sources [251];
- **Networks, interoperability, and cybersecurity.** As data storage and transfer needs grow, establishing a secure, high-bandwidth network is essential to mitigate risks from cyberattacks and equipment loss during operations [243], [246].

Emerging issues related to algorithms, radiation detection systems and mobile platforms can be summarized as follows:

- **Artificial Intelligence (AI)-based algorithms.** AI, particularly deep learning techniques, shows promise for improving source detection and localization [126];
- **Cooperative navigation and unmanned vehicles.** Cooperative ranging between UAVs and UGVs in GNSS-challenged environments can improve navigation and situational awareness [252], [253];
- **Halide perovskite radiation detectors.** These detectors offer advantages like lower cost, room temperature operation, and better energy resolution compared to conventional $NaI(Tl)$ scintillators, but require further research to improve their properties [254];
- **Hybrid mobile platforms.** The use of hybrid platforms, such as unmanned fixed-wing vehicles with VTOL capabilities or hybrid plane-blimp designs, is a promising area of research [255], [256];
- **Bio-inspired robots**: Bio-inspired robots, such as quadruped or snake-like robots, are being explored for Chemical, Biological, Radiological, Nuclear, and high-yield Explosives (CBRNE) detection and safe nuclear decommissioning, offering increased mobility and reduced human risk [257], [258];
- **Contact-based inspection drones.** Drones capable of physical interaction with their environment are being developed for tasks like wall inspection and prolonged radiation measurements, offering potential for reduced power consumption during data acquisition [259]–[261];
- **Swarm robotics.** Cooperation among multiple unmanned vehicles or robots, like swarm quad-rotors for disaster response, has significant potential for expanding telecommunication coverage and performing coordinated tasks [262];
- **Machine learning and onboard AI.** The integration of AI and data fusion for real-time decision-making in robots is a key area for future improvements [263];
- **Energy storage.** Innovations like Betavolt's nuclear battery, which uses ^{63}Ni to produce long-lasting power, and hydrogen-powered drones offer new perspectives for enhancing the endurance of mobile platforms, in particular unmanned vehicles and robots [264]–[266].

4

Proposed radiation detection system and gamma-ray source localization

4.1 Current solutions

In Security and Defence scenarios, large source-detector distances, the possible presence of weak radiation sources (e.g. SNMs) or shielded/masked radioactive sources can make difficult the detection, localization and identification of the sources. Therefore, high detection efficiency and a low false alarm rate are required to detect SNM and radioactive material while maintaining the normal flow of cargo/vehicles. Existing radiation detection systems for Security and Defence scenarios are mainly based on (as described in Chapter 3):

- **Fixed or portable RPMs.** Despite their high detection efficiency, drawbacks such as the high cost, the limited speed of inspected cargo or objects and the fixed location of the detection system hinder their widespread adoption;
- **Spatially distributed detection networks (fixed networks).** For an extended area such as a seaport, a large number of gamma-ray spectrometers would be necessary, which makes this solution impracticable;
- **MRDS based on gamma-ray spectrometers carried by ground vehicles (normally carried by cars, vans or trucks).** The higher payload capability of ground vehicles allows to transport more and heavier detection systems, however the vehicles can only operate on public roads[1];
- **MRDS based on gamma-ray spectrometers carried by aerial vehicles (as described in Section 3.2.4).** Some drawbacks associated with aerial vehicles may limit the detection and localization of radioactive sources or the mapping of contaminated

[1] Additionally, ground vehicles driven in fall-out areas will also be contaminated by radioactive substances or particles in the ground.

areas. These factors include maintaining a minimum operating height or altitude to avoid ground obstacles and comply with regulatory requirements (typically 150 meters for manned aircraft), adhering to a minimum flight speed for fixed-wing aircraft, and accounting for limited operation time due to flight autonomy constraints;
- **Use of handheld or backpack radiation detection system.** Risk of radiation exposure and contamination by the human operator. For large areas monitoring can be very time consuming or impractical.

Although gamma-ray spectrometers can detect and identify the radioactive source, they are normally expensive and limited in volume and crystal shape (normally inorganic scintillators and semiconductors). Moreover, relying exclusively on gamma-ray spectrometers in ground or air-based vehicles limits the ability to detect beta-emitting radioactive sources, SNM, which are typically low-energy gamma sources, and shielded or masked gamma sources. Additionally, this approach entirely prevents the detection of neutron sources, which are essential in Security and Defence scenarios.

4.2 Objectives

In this thesis a complementary or alternative solution, based on scintillators with SiPM sensors, for the detection and localization of gamma, beta and neutron sources is proposed. The developed MRDS stands out from other detection systems typically employed in Security and Safety scenarios by virtue of its optimized geometric detection efficiency (due to its pancake-shaped design), compactness, lightweight, and low power consumption which allows seamless integration into small unmanned vehicles, such as multirotors (which often face payload restrictions). Furthermore, the incorporation of cost-effective materials such as plastic scintillators facilitates its replication and integration across various unmanned vehicles (including air, land, maritime, and hybrid vehicles). Although unmanned vehicles could be tele-operated, the semi-autonomous or autonomous operation could create the opportunity to perform automated inspections, radiation monitoring or mapping, enhancing efficiency and accuracy in radioactive source detection and localization. Deploying several unmanned vehicles (fleet) equipped with radiation detection systems and other sensors, operated individually or cooperatively, would also expand the scope of applicability beyond inspection of shipping container cargo (as proposed in this thesis) to include other infrastructures such as nuclear facilities and extensive area radiation mapping. The use of MRDS, in particular radiation detection systems integrated into unmanned vehicles could be an alternative or complement to fixed RPMs and handheld equipment used for primary and secondary inspections of stationary shipping containers respectively. Spatially distributed detector networks (fixed networks) could also be enhanced with the introduction of MRDS. This approach would improve inspection coverage, effectiveness, and flexibility. While unmanned ground vehicles can transport larger and heavier radiation detection systems, the higher maneuverability of small UAVs, such as multirotors with VTOL and hover capabilities, offers several advantages: (i) perform inspections at height, (ii) smaller and more cost-effective radiation detection systems can be used due to the reduced source-detector distance, and (iii) operation in narrow spaces, such as those between containers.

This thesis also aims to propose a two-stage method comprising:

- Rapid detection and localization of radioactive sources or materials through the utilization of cost-effective detectors integrated across diverse mobile platforms;
- Subsequent identification and quantification of radionuclides using high energy resolution detectors integrated into a mobile platform, triggered only upon detection and localization of a source. This approach streamlines the process, ensuring efficient allocation of resources while maintaining accuracy in radiation monitoring.

Although the proposed detection system envisages its deployment for Security and Defence scenarios, it can also be used for inspection and monitoring of nuclear facilities, the radiation mapping of an extended contaminated surface or the search for a lost source.

The optimization of the radiation detection system was achieved through MC modeling and simulations, corroborated by laboratory and field tests. These endeavors culminate in a proof-of-concept for inspecting maritime shipping containers, ensuring the system's efficacy and reliability in real-world scenarios.

Considering the source search method depends on both the source localization algorithm and on the path followed by the MRDS (path planning) some strategies were studied and analysed to improve the source detection and localization hidden in shipping containers.

Despite the fact that several radioactive hot spot localization algorithms are described in literature such as MLE [17], [267], radiation detector networks [43], [104], particle filter [44], and deep learning approaches [126], their application to cargo inspection remains largely unexplored. Additionally, the existing MLE algorithms are based in measurements obtained by various known detector positions (fixed positions) to localize the source.

In this thesis, an iterative MLE algorithm based on the measurements performed by a MRDS is considered, which estimates in real-time the source position at each instance considering all the radiation measurements obtained so far. Advantages of the proposed source search algorithm include:

- Estimates the source position coordinates and corresponding confidence intervals;
- When using informative path planning, the path of the radiation detection system can change in real-time according to the radiation measurements or source position estimation (updated every time a new reading is acquired).

The proposed Informative Path Planning (IPP) algorithm is based on profit functions that incorporate real-time measurements (radiation counts) or the information provided by the MLE algorithm (source position estimation), enabling dynamic path-based decisions during the inspection. Better decisions regarding how and when to change a path, can help to maximize the information gathered during the inspection process and obtain more accurate source position estimations and reduced inspection time. Although some algorithms based in IPP and profit functions have been developed in previous works, their application is limited to the use of UAVs in the localization of radioactive sources on the surface [42] or ground monitoring [268], [269].

4.3 Requirements of the radiation detection system and assumptions

The requirements considered for the development of the radiation detection system are summarized in Table 4.1.

Table 4.1: Requirements considered for the development of the radiation detection system.

- Capability to detect simultaneously gamma, beta and neutron sources
- Optimized geometric detection efficiency (using detection volumes with pancake shapes)
- Separated gamma/beta and neutron detection systems
- Low-cost scintillator material for easy replication (e.g. plastic scintillator)
- Easily integrated in a mobile platform, particularly in a multirotor, or used as a handheld equipment
- Compact and lightweight (up to 3 kg) to be integrated in a multirotor[1]
- Low power consumption (less than 5 W) and low voltage (5 V)
- Easy to change detector orientation (for multiple applications)[2]
- Neutron detection system:
•Optimized neutron detection efficiency
•Very small sensitivity to gamma rays compared to neutron detection (for low false alarm rate)
•Ability to detect both thermal and fast neutrons
•Alternative to ^3He-based detectors

[1] The detectors' size and weight was chosen according to three aims: to maximize the detection efficiency, not exceed half of the multirotor platform's maximum payload weight (6 kg) and to fit on the carbon fiber plate used to carry all the detectors, sensors and electronics.
[2] By altering detector orientation (e.g., rotating the detector by 90°), it becomes feasible to conduct not only lateral inspections of cargo or vehicles but also radiation mapping of the ground surface or searching for sources located on the ground.

For the development and testing of the radiation detection system, the following assumptions were made:

- The developed detection system will be used solely for the detection and localization of gamma and neutron sources. Source identification can be performed afterwards near the location where the hot spot was measured using a gamma spectrometer detector, which can be easily integrated into the same mobile platform (multirotor) or another one. This approach was adopted for technical reasons, as acquiring gamma-ray spectra and confirming radionuclides can take several minutes (not the focus of this thesis), significantly consuming the operational autonomy of a multirotor. This autonomy is essential for its primary task, which, in this thesis, is the inspection of the maximum number of containers to detect and localize a radioactive source;

- In the field tests it is assumed that the gamma-ray source is a ^{137}Cs source (for activity calculation). When the source is unknown, it is necessary to make the identification of the radionuclide(s) present before calculate its activity. For that it can be used a spectrometer detector such as the $CsI(Tl)$ scintillator with SiPM sensors which was also tested for comparison purposes in terms of detection efficiency;
- Although the ability to detect beta particles is crucial in Security and Defence scenarios, especially due to the potential misuse of ^{90}Sr sources in RDD, it is unlikely to detect these particles in the exterior of the shipping container due to the container's 2 mm-thick iron walls. However, the interaction of beta particles with high-Z materials can produce bremsstrahlung radiation, making it possible to detect the source. Possible contamination of the container walls exterior, due to unsealed beta source, can also be detected;
- The gamma and neutron detectors, with their larger cross-sectional areas (effective areas), were mounted vertically to maximize geometric detection efficiency during lateral inspections of shipping container cargo. During the inspection, the effective areas of the detectors were consistently kept parallel to the shipping container walls;
- To minimize costs, a single data acquisition and processing unit, the Topaz-SiPM MCA, was employed.

4.4 Proposed radiation detection system

In accordance with the requirements specified in Table 4.1, the following prototype radiation detectors were proposed. These detectors are not commercially available but were custom-built by Scionix upon request and according to the specified requirements. Their key characteristics are outlined below:

- **Gamma/beta detection system.** The EJ-200 plastic scintillator has a diameter of 110 mm, a depth of 30 mm, and a weight of 517 g (including the short cable), as shown in Figure 4.1a. A detailed detector schematic is presented in Annex I). Additional features include an ultra-thin 32 µm titanium window for improved beta particle detection efficiency, and a +5V power plug to supply power to the neutron detector. Among several commercially available plastic scintillator materials, EJ-200 was chosen for its: (i) low price, (ii) high commercial availability, (iii) long optical attenuation length (important for accommodating long detector areas), (iv) fast timing, and (v) maximum emission wavelength of 425 nm [249], which is well-suitable for coupling with SiPM sensors[2];

[2]SiPM photo-sensors have spectral sensitivities from UV to IR, peaking in the visible (400 nm - 500

- **Neutron detection system.** The thermal neutron detector is formed by two layers of EJ-426HD scintillator (with ^6Li content), each with a dimension of $25 \times 90 \times 0.32\, mm^3$, and presents a total weight of 90 g (cables included). The EJ-426HD neutron detector is shown in Figure 4.1b (a detailed detector schematic is presented in Annex II). In addition to the analog output, which also serves as a power supply line, an additional digital output was requested from the manufacturer, Scionix, to provide Transistor-Transistor-Logic (TTL) signals (5 V and 1.5 μs) corresponding to the neutron counts (neutron capture by ^6Li). For this digital output, an internally adjusted threshold above noise at 40° C was set. The choice of acquiring a neutron detector based on the EJ-426HD scintillator was related to: (i) composed by a matrix of ^6LiF (minimum ^6Li enrichment of 95% atom percent) and $ZnS : Ag$ phosphor, is highly effective in detecting thermal neutrons while exhibiting low sensitivity to gamma radiation; (ii) its very compact and lightweight (iii) the maximum emission wavelength matches the SiPM spectral sensitivities [271].

(a) EJ-200 plastic scintillator. (b) EJ-426HD scintillator.

Figure 4.1: Proposed radiation detection system based on scintillators with SiPM sensors: (a) Gamma/beta radiation detector. The titanium window of the EJ-200 detector is on the bottom of the figure (not visible); and the (b) Thermal neutron detection system.

Table 4.2 summarizes the advantages and drawbacks of the developed radiation detection system.

A third detector, a SiPM-based $CsI(Tl)$ scintillator with 51 mm of diameter and 51 mm of depth, was also considered for comparison purposes with EJ-200 plastic scintillator. The $CsI(Tl)$ scintillator presents an aluminium housing and it weights 600 g (short cable included). The schematic of the $CsI(Tl)$ scintillator is shown in Annex III).

All scintillators were produced by Scionix [273] and feature a built-in temperature-compensated bias generator and preamplifier to address the gain dependence of the SiPM sensors with temperature variations.

The following subsections detail the hardware and software architecture, along with the gamma source localization algorithm – the MLE algorithm.

nm) [270].

Table 4.2: Advantages and drawbacks of the developed MRDS [272].

Radiation detection system characteristic	**Advantages**	**Drawbacks**
Radiation detection based on plastic scintillators with SiPM[1]	Low cost, compact, low power consumption, and large detection area	Low light yield[2], detector gain temperature dependence, and no gamma spectroscopy
EJ-200 scintillator with a very thin titanium window	High sensitivity to beta particles	More fragile window and expensive.
Neutron detection system based on ^{6}Li	Compact and modular neutron moderator, alternative to ^{3}He detectors	Lower detection efficiency than ^{3}He detectors
Possible integration in a small unmanned vehicle (e.g. multirotor)[3]	Enhanced maneuverability and range, along with the avoidance of human radiation exposure	Operability of the measuring equipment depends on the availability and autonomy of the vehicle
Independent power supply and GNSS receiver	Easily integrated in any mobile platform	Electrical charge could be provided by the mobile platform's batteries[4]

[1] More details available in Tables 3.2 and 3.3.
[2] While EJ-200 scintillation efficiency is 10 photons/keV, $NaI(Tl)$ and $CsI(Tl)$ scintillators features 38 photons/keV and 54 photons/keV respectively. The lower light yield of EJ-200 scintillator limits its detection capability to low energy gamma-ray sources such as ^{241}Am sources (the most intense gamma-ray energy is 59.5 keV) [130], [249].
[3] More details available in Table 3.4.
[4] Electrical charge of the vehicle could be provided to the radiation detection system by using a DC/DC adaptor.

4.4.1 Hardware architecture

A compact and lightweight TOPAZ-SiPM MCA, developed by BrightSpec [274], was responsible for the detectors data acquisition and processing and for the supplied low voltage (5 V) to SiPM-based detectors. The dimensions and weight are 70 mm × 45 mm × 26 mm and 70 grams, respectively.

Given the availability of only one TOPAZ-SiPM MCA equipment, the proposed hardware architecture for the radiation detection system is presented in Figure 4.2.

The key functionalities of the TOPAZ-SiPM MCA and the details of its connections to the detectors and Raspberry Pi 3 model B, are described in Appendix C.

A power bank was employed to provide the necessary power supply.

To ensure continuous tracking of the detection system's position and to monitor signal quality, including metrics like satellite count and horizontal accuracy, a GNSS receiver, specifically the Beitian BS-708 receiver, was used. This receiver allows to achieve a horizontal position accuracy better than one meter, when data with a Horizontal Dilution of Precision (HDOP) lower than one is considered. The Beitian BS-708 receiver lacks an integrated Inertial Measurement Unit (IMU) and is primarily designed for accurate positioning and navigation as a standalone GNSS receiver. In contrast, GNSS receivers

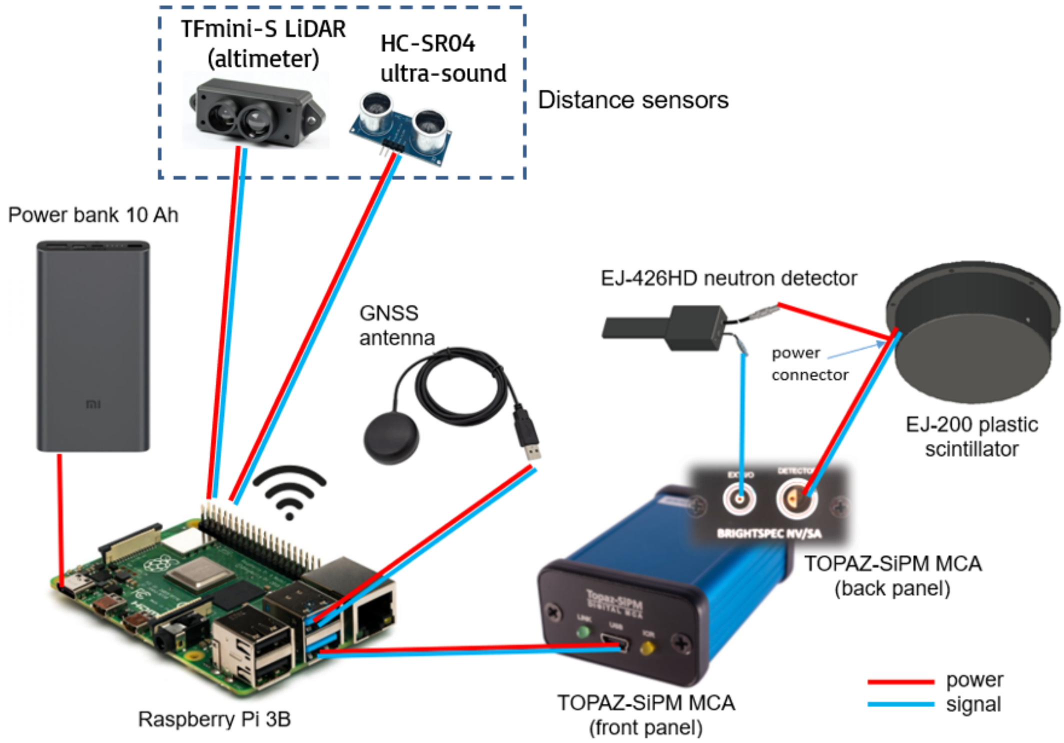

Figure 4.2: Hardware architecture of the developed radiation detection system. Equipment sizes are not at the same scale.

with integrated IMU combine GNSS and inertial data, providing superior accuracy and reliability, especially in environments where GNSS signals are weak or obstructed (which was not the case during the experimental data acquisition) [275]. Additionally, more expensive equipments, such as the Differential GNSS (DGNSS) and the Real-Time Kinematic (RTK) GNSS, offer an excellent alternative to GNSS and IMU + GNSS receivers. DGNSS enhances GNSS signal accuracy by using a network of fixed ground-based reference stations, achieving sub-meter to decimeter-level accuracy, while RTK GNSS provides centimeter-level accuracy through carrier-phase measurements and real-time corrections from a base station, making it suitable for high precision applications [276], [277].

In this thesis, the horizontal position uncertainty associated with the GNSS receiver was addressed by using only position data with an HDOP lower than one and by utilizing strategically positioned floor reference marks to provide visual guidance for the detection system's path during the inspections to shipping containers. These marks enabled adjustments to the horizontal position information obtained by the GNSS receiver relative to the shipping container, providing a ground truth for the tests. These adjustments are made during the radiation detection system's path. Trigonometry was used to adjust the initial point of the path relative to the shipping container's position and to adjust the initial direction vector of the detection system relative to the vector defined by the container side (both vectors must be parallel). Further details will be explored in the next Chapters.

A set of distance sensors was integrated in the MRDS, a LiDAR sensor (the TFmini-S from Benewake) to obtain the radiation detection system height and an ultra-sound sensor (HC-SR04 from ETC) [278] to measure the relative distance between the radiation detection system and the shipping container walls[3]. The TFMini sensor is a single-point ranging LiDAR which operates in the infrared (850 nm). Although the sensor can withstand ambient light levels up to 70 klux, it was positioned facing the ground to reduce the impact of direct sunlight exposure, which could potentially degrade performance and increase noise. The measurement range schematic diagram is shown in Figure 4.3. The referred LiDAR sensor weighs 5 g and offers a frame rate of up to 1000 Hz. It measures distances from 0.3 m to 12 m with an accuracy of 1% and has a Field of View (FOV) of 2°. The LiDAR sensor has many applications, including obstacle avoidance, vehicle/person position sensing, and UAV altimeter (e.g. altitude hold for quad-copters and terrain following) [279], [280]. In contrast, the ultrasound sensor, weighs 8.5 g, has a slower acquisition rate (40 Hz), and measures distances from 0.02 m to 4.5 m with a 15° measuring angle.The accuracy of ultrasonic distance sensors typically ranges between 1% and 3% [278]. This accuracy can be influenced by factors such as the physical characteristics of the air (temperature and humidity), ambient sound, and the presence of soft, sound-absorbing surfaces, such as those covered with cloth, or uneven targets [281].

When the distance sensors were integrated in the radiation detection system, no real shipping container was available. Therefore, the ultrasound sensor was also employed to measure the radiation detection system height, providing a redundant system. This approach explores the possibility of sensory integration or fusion. For instance, if both sensors return similar values, it is likely that the measurements are accurate. However, if the values are somewhat dissimilar, it suggests that at least one sensor may be experiencing an erroneous measurement.

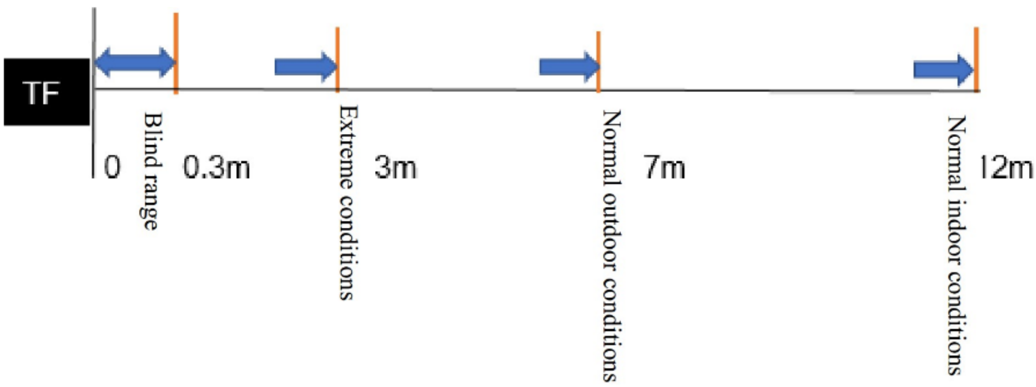

Figure 4.3: LiDAR sensor (TFMini S) measurement range schematic diagram [280].

4.4.2 Software architecture

For the correct timestamp of all sensors data accurate clock synchronization is required. This is achieved by using the Raspberry Pi clock as the reference timing.

[3] The ultrasound sensor was initially introduced to maintain a consistent distance between the detection system and the container walls.

The data acquisition and processing algorithm include the following stages:

- **Acquisition start of the GNSS receiver and distance sensors** (if applicable) [4].
- **Acquisition start of the radiation detectors.** Implemented using the Simulation Development Kit (SDK) libraries provided by the TOPAZ-SiPM MCA manufacturer. The optimized MCA settings are shown in Appendix C.
- **Data timestamp and storage.** All sensor and radiation data are timestamped using the Raspberry Pi's internal clock and securely stored in a Comma-Separated Values (CSV) file on the Raspberry Pi's memory card. Data values are displayed in real-time on the Raspberry Pi prompt window and can be accessed remotely via Wi-Fi on a connected laptop.

The radioactive source localization algorithm (MLE algorithm) is able to run online, during the data acquisition and processing (the source position and uncertainty are estimated after each radiation measurement using the data acquired so far). This is particularly important for the informative path planning algorithm (described in Chapter 7), which depends on real-time source localization estimates and their uncertainties to make informed decisions about the path of the radiation detection system.

4.5 Gamma-ray source detection and localization

In this Section it will be described all the variables necessary to estimate the gamma-ray source position using the MLE algorithm.

4.5.1 Detection system counts

In the development of the simulator, various attenuating factors were considered that influence the number of counts generated by a specific radioactive source, with a given activity, in a detector located at a certain distance. The counts recorded by a detector at a given position are determined by the following expression:

$$R = b_r A \varepsilon_g \varepsilon_i e^{-\mu_{air}(d_s - l_{cont}) - \mu_{iron} l_{cont}} + B \,, \tag{4.1}$$

where b_r is the branching fraction for ^{137}Cs decays into 662 keV gamma rays[5], A is the activity of the source, ε_g is the geometric efficiency of the detector, ε_i is the intrinsic efficiency of the detector, B is the background radiation value at that moment, which can be approximated by a Poisson distribution.

[4]The GNSS receiver was utilized only when the radiation detection equipment was in motion during measurements, while distance sensors were activated solely when adjustments in path height were needed during inspections of the shipping containers (informative path planning).

[5]The branching fraction for ^{137}Cs decays into 662 keV gamma rays is $b_r = 0.8505 \pm 0.0029$ [282]. This means that out of every 100 cesium nuclear disintegration in the source, approximately 85 will have in the final state a gamma-ray of energy 662 keV.

The attenuation effects due to material media are represented by the exponential term in (4.1), which accounts for gamma-ray attenuation in air (covering the entire gamma-ray path except the container wall) and in the container wall material [283]. Here, μ_{air} is the attenuation coefficient for air, valued at $9.867 \times 10^{-3}\ m^{-1}$ for photons with 662 keV (data extrapolated from [284]), and μ_{iron} is the attenuation coefficient for iron, valued at 60.66 m^{-1} for 662 keV photons (data extrapolated from [285]). The variable d_s represents the distance between the detector and the source.

Since the radiation detection system will conduct lateral inspections to the shipping container at a constant distance from its walls, an average wall thickness l_{cont} will be assumed for the container. The l_{cont} is obtained by the average of two thickness considering the following situations (as illustrated in Figure 4.4): (i) when the detector window is perpendicular to the source (0°), corresponding to 0.19 cm [286]; and (ii) when the detector is positioned at a 45° angle relative to the initial orientation[6].

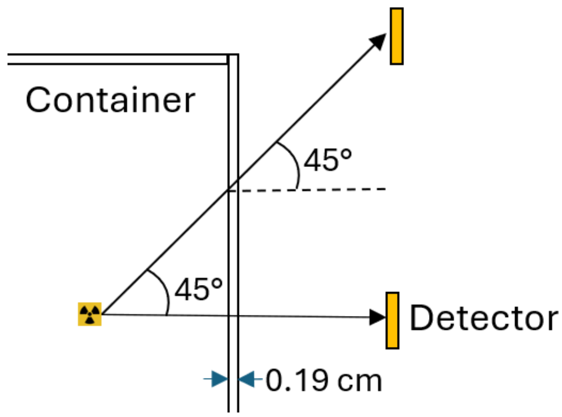

Figure 4.4: Schematic (not to scale) used to calculate the average thickness of the shipping container walls.

Thus, the average thickness of the container walls, l_{cont}, is calculated as:

$$l_{cont} = \frac{(0.19 \div cos(45°)) + 0.19}{2} \approx 0.3\ cm \tag{4.2}$$

4.5.2 Geometric detection efficiency

The geometric detection efficiency ε_g is defined as the fraction of the solid angle that the detector captures as:

$$\varepsilon_g = \frac{\Delta\Omega}{4\pi}, \tag{4.3}$$

where $\Delta\Omega$ is the solid angle subtended by a detector at a certain location to an isotropic radioactive source.

[6]This approach is based on the principle that radiation intensity decreases inversely with the square of the distance. Therefore, for higher angles (above 45°) the contribution of the source gamma-rays for the detector counts will be significantly lower.

Assuming that the detector's radius is much smaller than the distance between the detector and the source, the following simplification can be stated [52]:

$$\varepsilon_g = \frac{\Delta\Omega}{4\pi} \approx \frac{a}{4\pi d_s^2}, \tag{4.4}$$

where a is the effective area of the detector, and d_s is the distance between the detector and the source.

The detector´s effective area corresponds approximately to the area of a circle of radius r and therefore, assuming a point-like source the geometric detection efficiency becomes:

$$\varepsilon_g = \frac{\pi r^2}{4\pi d_s^2} = \frac{r^2}{4d_s^2} \tag{4.5}$$

Assuming that the detector volume has a cylindrical geometry, the effective area a depends on the orientation of the detector because, as it moves away from the central axis directly in front of the radioactive source, its projected area changes. According to [287], the effective area of a cylindrical detector can be obtained using (4.6).

$$a = a_{face}cos\theta + a_{side}sin\theta = \pi r^2 \frac{H_s}{\sqrt{H_s^2 + D_s^2}} + 2rl\frac{D_s}{\sqrt{H_s^2 + D_s^2}}, \tag{4.6}$$

and:

$$\varepsilon_g = \frac{a}{4\pi d_s^2}, \tag{4.7}$$

where a_{face} is the area of the projected face of the detector, a_{side} is the area of the projected side of the detector, θ is the incident angle of the gamma rays, r is the radius of the detector, l is its length and H_s and D_s are the vertical and lateral distances, respectively, from the detector to the source. Figure 4.5 shows a schematic representation of the situation, with the respective variables.

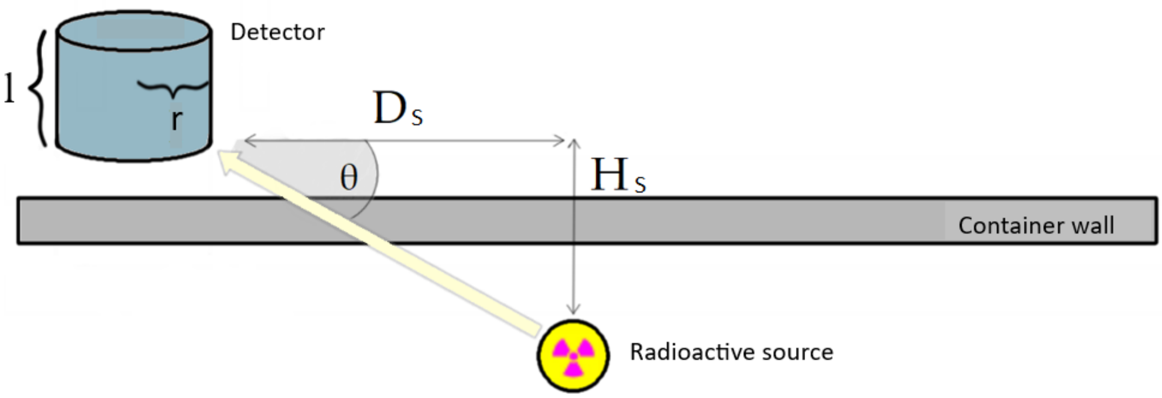

Figure 4.5: Schematic (not to scale) of the variables used to calculate the geometric detection efficiency of a cylindrical detector.

4.5.3 Intrinsic detection efficiency

The intrinsic detection efficiency ε_i can be determined either through MC simulations or experimentally by measuring the fraction of photons entering the detector that successfully generate counts:

$$\varepsilon_i = \frac{C}{R}, \tag{4.8}$$

where C is the average number of counts recorded by the detector and R is the expected number of counts for that situation according to the expression (4.1) with an intrinsic efficiency of 1.

4.5.4 Source localization – Maximum Likelihood Estimation algorithm

To estimate the position of the radioactive source within the shipping container based on the recorded detector counts, an MLE-based algorithm was used. The MLE algorithm is extensively documented in the literature for radioactive source localization, as seen in studies [38], [267]. Both studies demonstrate that the MLE algorithm yields favorable results, even for detecting multiple radioactive sources. Therefore, the same algorithm will be applied in this thesis, with a specific focus on scenarios involving only a single radioactive source.

MLE aims at estimating the parameters of an assumed probability distribution using the observed data. This involves maximizing a likelihood function, according to the assumed statistical model, to make the observed data most probable.

The chosen variable to maximize, the gamma-ray counts of the detection system at a given position, λ_i, takes a form analogous to (4.1) with the exception of background radiation, and is expressed by:

$$\lambda_i = b_r A \hat{\varepsilon}_{g,i} \hat{\varepsilon}_{int} e^{-\mu_{air}(\hat{d}_{s,i} - l_{cont}) - \mu_{iron} l_{cont}}, \tag{4.9}$$

and:

$$C_i = \lambda_i + B_i, \tag{4.10}$$

where the indices i correspond to the variables values for each detector position. $\hat{\varepsilon}_{g,i}$ represents the detector's geometric efficiency calculated for each detector-source distance $\hat{d}_{s,i}$. b_r is the branching fraction for the source radionuclide decays into the gamma rays (in this thesis it will be considered the ^{137}Cs radionuclide which decays into 662 keV gamma rays), A is the source activity, ε_{int} is the intrinsic efficiency of the detector, and B is the background radiation (a Poisson distribution was assumed).

Considering a Poisson distribution for the measured data[7], the likelihood function (probability density function) is given by [267]:

$$L(\lambda_i; C_i) = \prod_{i=1}^{N} \frac{\lambda_i^{C_i} e^{-\lambda_i}}{C_i!}, \tag{4.11}$$

[7] If the data acquisition times are much smaller compared with the half-lives of the radioisotope in the sample, it can be assumed radioactive decay follows a Poisson distribution, which impacts the radiological measurements (introducing uncertainty). Therefore, measured data also follows a Poisson distribution.

where N is the number of detector measurements and C_i represents the counts recorded by the detector in instant i.

The logarithm of (4.11), i.e., the log-likelihood function is expressed as:

$$l(\lambda_i; C_i) = \sum_{i=1}^{N} C_i \log \lambda_i - \lambda_i - \log C_i! \tag{4.12}$$

Since the last term is constant, without loss of generality, the log-likelihood function can be re-written as:

$$l(\lambda_i; C_1, ...C_N) = \sum_{i=1}^{N} C_i \log \lambda_i - \lambda_i \tag{4.13}$$

Thus, the MLE algorithm determines the optimal estimate of the source position by maximizing the log-likelihood function, as given by (4.13), based on the measured data and by adjusting the source position coordinates. In order to use the highly optimized scientific library *SciPy* from *Python*, it was decided to use the minimization of the negative of the log-likelihood function to obtain the source position estimate.

4.5.5 Source position uncertainty

To determine the uncertainties of the estimated source position coordinates, the concept "Fisher information" was utilized. The Fisher information $I(\theta)$ measures the information that an observable random variable X carries about an unknown parameter θ in a distribution modeling X [288], and is defined by the following formula:

$$[I(\theta)]_{i,j} = -E\left[\frac{\partial^2}{\partial\theta_i\partial\theta_j} L(X;\theta)\right], \tag{4.14}$$

where θ_i and θ_j represent the parameters under consideration, in this case, x, y, or z. E denotes the mean value of the distribution, and L is the likelihood function defined in (4.13).

Using the function given in (4.14), confidence intervals $\hat{\theta}_i$ for each estimated parameter can be obtained, by using:

$$\hat{\theta}_i = \theta_i \pm 1.645 \frac{1}{\sqrt{[I(\hat{\theta}_i)]_{i,i}}}, \tag{4.15}$$

where the value 1.645 defines a 90% confidence interval, and $[I(\hat{\theta}_i)]_{i,i}$ corresponds to the diagonal components of the Hessian matrix of L, as provided by the MLE algorithm.

4.5.6 Source activity calculation

Within the scope of this thesis, the calculation of the source activity was also crucial. Subsequently, based on the recorded counts and on the estimated source position, the source activity A can be calculated, according to:

$$A = \frac{C_i - B}{b_r \hat{\varepsilon}_{g,i} \hat{\varepsilon}_{int} e^{-\mu_{air}(\hat{d}_{s,i} - l_{cont}) - \mu_{iron} l_{cont}}}, \tag{4.16}$$

where B in this case represents the mean value of the background.

4.5.7 Source activity uncertainty

To quantify the uncertainty of the source activity, the following general expression was utilized:

$$\sigma_f = \sqrt{\left(\frac{\partial f}{\partial x}\right)^2 \sigma_x^2 + \left(\frac{\partial f}{\partial y}\right)^2 \sigma_y^2 + \left(\frac{\partial f}{\partial z}\right)^2 \sigma_z^2 + \ldots} \tag{4.17}$$

Here, σ_f represents the standard deviation of the function f, while σ_x, σ_y, and σ_z correspond to the standard deviations of x, y, and z, respectively.

Taking into account all uncertainties associated with the variables in (4.16) (except for the attenuation coefficients of materials), equation (4.17) can be reformulated as follows:

$$\sigma_A = \sqrt{\left(\frac{\partial A}{\partial C_i}\right)^2 \sigma_{C_i}^2 + \left(\frac{\partial A}{\partial B}\right)^2 \sigma_B^2 + \left(\frac{\partial A}{\partial b_r}\right)^2 \sigma_{b_r}^2 + \left(\frac{\partial A}{\partial \hat{\varepsilon_g}}\right)^2 \sigma_{\hat{\varepsilon_g}}^2 + \left(\frac{\partial A}{\partial \varepsilon_i}\right)^2 \sigma_{\varepsilon_i}^2 + \left(\frac{\partial A}{\partial \hat{d_s}}\right)^2 \sigma_{\hat{d_s}}^2 + \left(\frac{\partial A}{\partial l_{cont}}\right)^2 \sigma_{l_{cont}}^2} \tag{4.18}$$

The final expression for the source activity uncertainty, as well as the intermediate uncertainties, can be found in Appendix A.

The pseudocode for the source position estimation, utilizing the MLE algorithm, and the source activity calculation is presented in Algorithm 1 of Appendix B.

5

Development and optimization of the radiation detection system

5.1 Optimization of the neutron detection system

5.1.1 Monte Carlo modelling and simulation results

The state-of-the-art MC radiation-transport computer program MCNP6 was used to design, analyze and optimize the effects of various neutron moderator materials and dimensions on the EJ-426HD neutron detection efficiency. The MCNP6 can generate and transport through matter a variety of particles, including electrons, photons, neutrons, and other charged particles. This feature allows obtaining particular tallies (quantities to be scored such as the number of particles, the fluence, the energy deposition, among others) from surfaces or volumes [289]. For the MC simulations, a model of the neutron detection system (EJ-426HD scintillator and neutron moderator) and surrounding material (air) was implemented, as shown in Figure 5.1. For particle transport simulations, physics processes "mode n" was selected, which means that only neutron transport was performed.

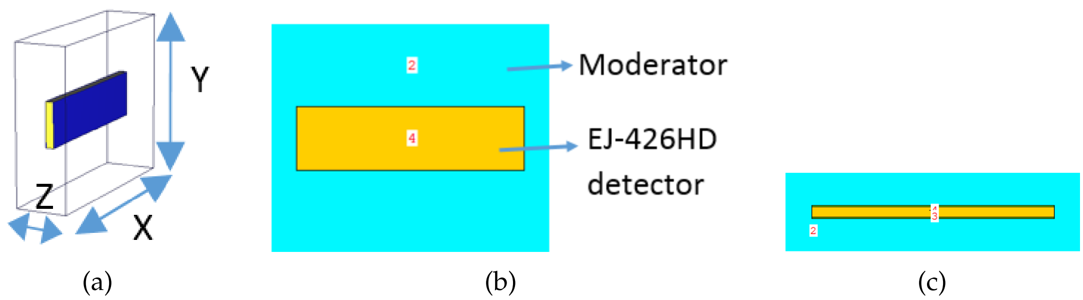

Figure 5.1: MC geometry of the neutron detector and moderator [290]. (a) 3D view. (b) XY plane view. (c) XZ plane view.

An $^{241}Am - Be$ neutron point source, with an isotropic distribution and a neutron energy spectrum as shown in Figure 2.2, was positioned at a given distance from the center of the neutron detection system.

To improve the detection efficiency of the thermal neutron detector to the $^{241}Am - Be$ source, which has a significant fast neutron component, a neutron moderator material was placed around the detector. The materials selected for the prototype neutron moderator were chosen based on their abundant hydrogen content and widespread use in various industries (thermoplastics and 3D printing). Five neutron moderator materials were simulated, the HMWPE, HDPE, Polylactic Acid (PLA), Polyethylene Terephthalate Glycol (PET-G), and nylon (also known as polyamide). HMWPE, HDPE, and nylon are commonly found in the mechanical engineering industry in the form of round rods/tubes, sheets, and parallelepiped blocks, while HMWPE and HDPE are also utilized in the food industry (e.g., hygienic cutting boards). PLA, PET-G, and nylon are popular choices as 3D printing filament materials. Details of the moderator materials' characteristics are provided in Table 5.1.

Table 5.1: Neutron moderator materials used in the MCNP6 simulations.

Material	Chemical formula	Density (g.cm^{-3})
HMWPE	CH_2	0.96 [291]
HDPE	CH_2	0.95 [291]
PLA	$(C_3H_4O_2)_n$	1.25 [292]
PET-G	$C_{14}H_{20}O_5S$	1.27 [293]
Nylon	$(C_{12}H_{22}N_2O_2)_n$	1.14 [294]

To determine the maximum neutron detection efficiency for a given moderator material, the x and y dimension was kept constant and the moderator thickness (z dimension) was varied. The neutron detection efficiency was given by the tritium production in the EJ-426HD scintillation material. Tritium production primarily occurs through thermal neutron capture in ^{6}Li, as described by (2.7). This information was obtained using tally F4 (reaction number "105"), which scores the number of (n,t) reactions per starting particle and per cubic centimeter.

In Figure 5.2, the neutron detection efficiency is illustrated as a function of various moderator materials and their thickness in the z dimension, considering a cross-sectional area (in the x and y axis) of 9×11 cm^2. Notably, PLA and PET-G exhibit inferior neutron moderator effectiveness primarily due to their lower hydrogen contents. While nylon offers values a factor of two lower than the optimum solutions, it remains a viable option for 3D printing, providing flexibility in shapes and sizes. HDPE and HMWPE yield closely aligned results, reaching the maximum detection efficiency for a moderator thickness of 7 cm. Increasing the moderator thickness beyond 7 cm will lead to the absorption of thermal neutrons by the polyethylene material (by neutron capture), thus reducing the number of neutrons detected.

After determining the best neutron moderator materials and corresponding thickness, the optimal transversal dimension of the moderator was calculated to minimize its weight. A 7 cm thick HDPE moderator material (moderator configuration with one 3.5 cm-thick

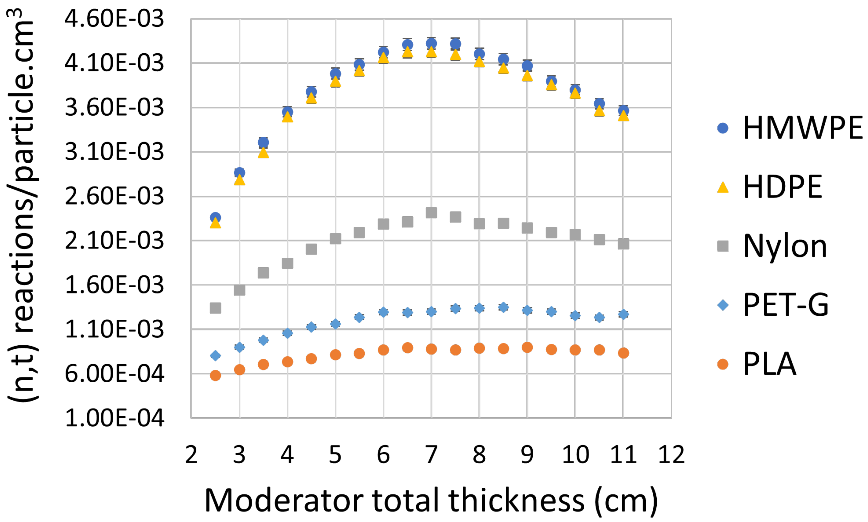

Figure 5.2: Neutron detection efficiency dependence with moderator composition and thickness, considering an $^{241}Am - Be$ source to detection system distance of 1 mm [290].

plate on each side of the EJ-426HD detector) was then used to obtain the optimal cross-sectional area of the moderator. Distances of 1 mm, 20 cm and 1 m between the $^{241}Am - Be$ source and the detection system were considered. The simulation results, depicted in Figure 5.3, illustrate that the neutron detection efficiency increases with the moderator's cross-sectional area (combined effect of increasing the X and Y dimensions), particularly evident at greater source-detector distances. However, this efficiency gain diminishes as the moderator size increases further, compounded by the substantial increase in the weight of the detection system. Consequently, it was observed that for moderator dimensions exceeding $X = 14.5\,\text{cm}$ and $Y = 11\,\text{cm}$, only minimal increments in relative detection efficiency were recorded, with a maximum increase of 2% for every additional 0.5 cm in each dimension. Furthermore, an increase of 0.5 cm in both X and Y dimensions would result in an extra 25 g of weight per moderator plate (20 mm thick HDPE). Considering four plates surrounding the detector (two on each side), this would lead to a total weight increase of 100 g for the detection system.

5.1.2 Neutron moderator prototyping

A Computer Numerical Control (CNC) milling machine was used to prototype a modular neutron moderator from commercially available HDPE (*Polystone® 300*) and HMWPE (*Polystone® 500*) sheets, measuring $60\,cm \times 30\,cm \times 20\,mm$ and $60\,cm \times 30\,cm \times 15\,mm$, respectively.[1] [291]. This process yielded four plates of 15-mm HMWPE and four plates of 20-mm HDPE, each with an optimized cross-sectional area determined by MC simulation ($14.5 \times 11\,cm^2$). An empty space was created in a pair of 15 mm and 20 mm

[1]The Polystone® material are used on the plastic fabrication (e.g. tanks and storage vessels) and food industry (e.g. used as cutting boards).

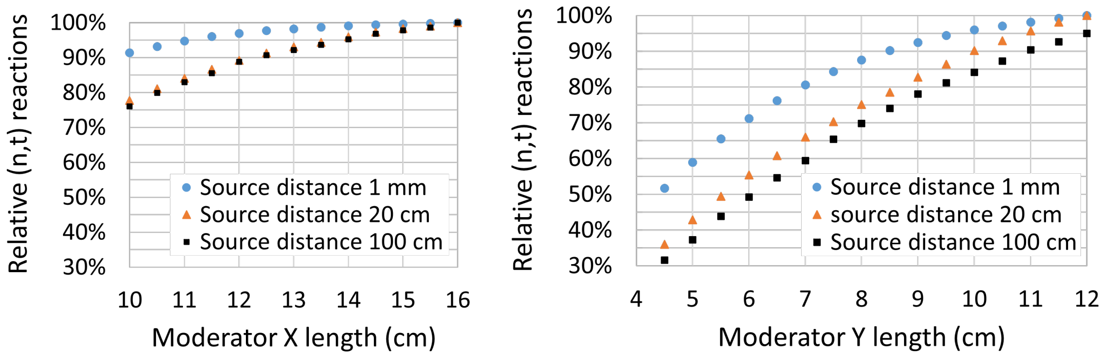

Figure 5.3: Relative neutron detection efficiency for different source-detector distances, varying moderator geometries: as a function of the X length for Y= 11 cm and Z=7 cm (left figure), and as a function of the Y length for X=9 cm and Z=7 cm (right figure) of the moderator [290].

plates, to accommodate the EJ-426HD detection system sensitive volume (0.5 cm on each plate) and the electronics box (1.5 cm on each plate) as illustrated in Figure 5.4).

The possibility of adding or removing the 15 mm and 20 mm thick neutron moderator plates on both sides of the detector makes it possible to optimise detection efficiency for specific radioactive sources, taking into account their neutron energy distribution or whether they are shielded or not (already moderated by surrounding material or not). For the sake of simplicity, a nomenclature was established for each detection system configuration. For instance, "M40R35" denotes that the detector is enveloped by a 40-mm thick polyethylene moderator on the source side (relative to the moderator) and a 35-mm thick polyethylene reflector on the opposite side of the source. The total moderator thickness along the Z-axis is 75 mm, reduced by 10 mm to accommodate the detector. Depending on the chosen configuration, the weight can vary from 0.45 kg (for configuration M15R15) to 1.65 kg (for configuration M70R40).

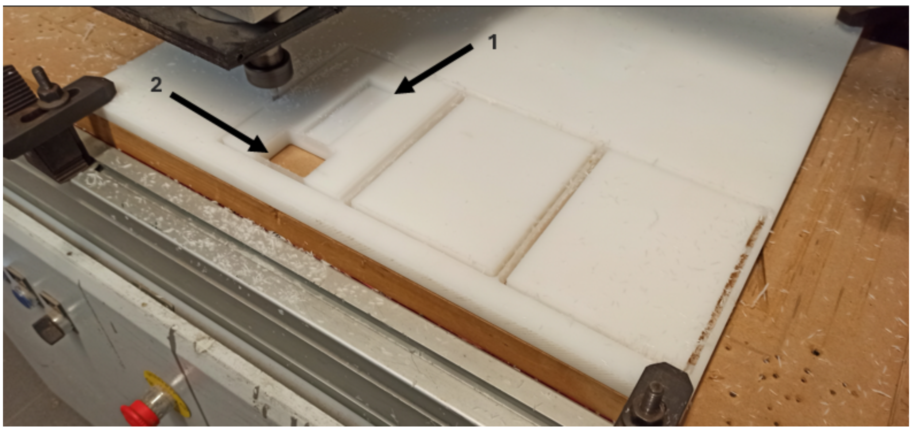

Figure 5.4: Prototyping 15 mm thick HMWPE moderator plates using a CNC milling machine. Empty space created to insert the EJ-426HD: 1- sensitive volume; 2- electronics box.

The EJ-426HD detector and the developed neutron moderator plates are shown in Figure 5.5.

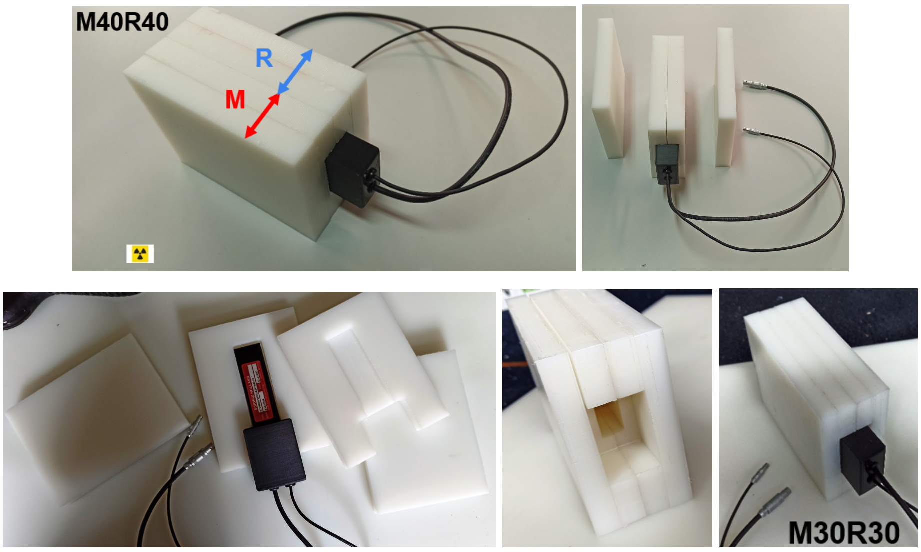

Figure 5.5: 20 mm thick HDPE moderator plates with EJ-426HD detector – M40R40 detection system configuration (top images) and 15 mm thick HMWPE moderator plates – M30R30 detection system configuration (bottom images) [290].

Figure 5.5 illustrates that the sensitive volume of the EJ-426HD detector is fully embedded within the moderator plates, with only part of the detector's electronics remaining outside. The plates are secured together using the detection system bracket, as illustrated in Section 5.3. The EJ-426HD detector is attached to the moderator plates with velcro, allowing for easy insertion and removal when the surrounding plates need to be changed. Embedding the EJ-426HD detector between a pair of plates presents the following advantages:

- **Compact and lightweight neutron detection system.** The EJ-426HD detector is supported by the moderator plates, eliminating the need for additional support materials. The parallelepiped design of the combined moderator plates optimizes geometric detection efficiency for a neutron source positioned in front of the detection system's larger cross-sectional area. This design is particularly well-suited for inspecting cargo, vehicles, or infrastructure, and it reduces weight compared to the typical spherical and cylindrical moderators used in neutron monitoring (Safety scenarios);
- **Robust detection system for integration in a mobile platform.** The EJ-426HD detector is supported all round by the moderator to prevent movement and vibrations;
- **Ensures that the center of gravity remains centered within the detection system**. Since the sensitive volume of the EJ-426HD occupies less space and therefore has more moderator material it balances the weight of the electronics which is on the opposite side of the detector. A detection system with a balanced weight distribution is crucial for its integration into the multirotor to ensure a normal flight operation.

5.1.3 Field tests and results

5.1.3.1 Experimental setup description

To validate the MC simulations and determine the optimal detection system configuration, experimental tests were performed to study the variation of the moderator geometry and configuration on the neutron detection efficiency.

Due to difficulties in obtaining an $^{241}Am-Be$ neutron source and a ^{137}Cs gamma source with the desired activities, a commercial Troxler equipment was used. The Troxler equipment is a certified surface moisture and density gauge, equipped with a 1.48 GBq (40 mCi) $^{241}Am-Be$ neutron source (which yields 70,000 neutrons per second) and a 0.3 GBq (8 mCi) ^{137}Cs gamma source. A schematic of the Troxler equipment is shown in Annex IV. When performing measurements the bottom of the equipment is placed in contact with the surface to measure and control the density and humidity of soils and pavements[2], including road surfaces (e.g. highways and aircraft runways) [295]. Due to radioactive decay, the radioactive sources had the following activities at the time of testing: 1.47 GBq (≈ 39.7 mCi) for the $^{241}Am-Be$ source (with an uncertainty of ± 10%) and 0.146 GBq (≈ 3.9 mCi) for the ^{137}Cs source (with an uncertainty of ± 10%). The neutron source is fixed at the center of the equipment, positioned just a few centimeters above the bottom of the Troxler equipment. The ^{137}Cs source can be moved from inside the Troxler equipment to the exterior using a source rod. In the safety position, the rod keeps the source inside the equipment, shielded by a tungsten sliding block at the bottom and a lead shield surrounding the sides and top. When the source rod is lowered, the tungsten block shifts to the side, exposing the source. The exposed source can then rest at the bottom surface of the Troxler (backscatter geometry) or extend a few centimeters below it. During the experiments, the ^{137}Cs source rod was in the safe position. The ^{137}Cs source rod was positioned in the backscatter geometry solely to test the neutron detection system's sensitivity to an intense gamma-ray source.

To obtain the neutron counts the EJ-426HD detector was connected to the analog input of TOPAZ-SiPM MCA, which in turn was connected to the Raspberry Pi via USB port. From radiological protection reasons, the operator kept a safe distance from the radiation source by remotely accessing the Raspberry Pi data using a laptop (via Wi-Fi hotspot). An algorithm written in C programming language was used to provide instructions to TOPAZ-SiPM MCA via Raspberry Pi, including open/close MCA, start/stop acquisition, and data storage.

The experimental setup, shown in Figures 5.6a and 5.6b, was used to obtain the neutron counts for each detection system geometry and configuration, considering the detection system at the same height and 1 meter away from the bottom of the Troxler. As shown in

[2]Scattered gamma rays are used to measure surface density, while scattered neutrons, thermalized by the ground material, are used to measure surface moisture. The scattered radiation is detected by a GM detector for gamma rays and two ^{3}He cylindrical detectors for thermal neutrons, all housed within the Troxler equipment.

Figure 5.6a the Troxler equipment was rotated 90° from its normal working position, to direct the sources´s radiation emission to the developed radiation detection system. The $^{241}Am - Be$ source, housed in the Troxler, was used to perform the measurements, with and without a neutron moderator sheet. The moderated $^{241}Am - Be$ source, as illustrated in Figure 5.6c), consist on a 5 cm-thick HDPE moderator sheet placed next to the bottom surface of the Troxler. In a real scenario, a moderated neutron source could represent an intentionally shielded source or one that is simply shielded by hydrogen-rich cargo materials inside a shipping container. A conventional 5 cm wall thick HDPE cylinder moderator was also used for comparison purposes (as shown in Figure 5.6d).

The neutron configurations that achieved the highest neutron counts, were then positioned according to the grid of points shown in Figure 5.6e, at various distances from the $^{241}Am - Be$ source, to determine the detection system's sensitivity to the source position.

5.1.3.2 Field and laboratory test results

Using the experimental setup depicted in Figures 5.6a and 5.6b, data acquisition of the neutron counts was obtained during 300 s for each detection system configuration MxRy indicated in Figures 5.7 and 5.8. A conventional cylinder moderator with 5-cm wall thick of HDPE was also used for comparison purposes.

For Figure 5.7 it was considered an $^{241}Am - Be$ source placed at 1 m from the detection system, with and without a 5 cm-thick HDPE moderator sheet. The chosen detection system configurations have an equal or higher thickness of plates in the moderator side than in the reflector side, i.e. $x \geq y$, in the MxRy configurations.

Considering Figure 5.7, the results can be summarized as follows:

- **For an unmoderated $^{241}Am - Be$ source.** The use of a cylindrical moderator yields superior detection efficiency, followed by the M40R35 and M40R40 detection system configurations. The higher detection efficiency achieved with the cylindrical moderator can be attributed to its larger cross-sectional area (224.75 cm^2) compared to the other configurations (159.5 cm^2). However, this advantage comes at the cost of increased weight: the cylindrical moderator weighs 2.2 kg, twice the weight of either M40R35 and M40R40 configurations (~ 1.1 kg);
- **For a shielded/moderated $^{241}Am - Be$ source (with a 5-cm thick HDPE moderator).** The M40R35 detection system configuration exhibits a notable reduction in neutron counts, while M40R40 maintains its performance in terms of neutron counts (and therefore detection efficiency). Furthermore, the higher neutron counts recorded for M40R40 and M40R35 compared to other configurations are in agreement with the MC simulations, indicating that the optimal moderator thickness (in Z length) is approximately 7 cm (refer to Figure 5.2).

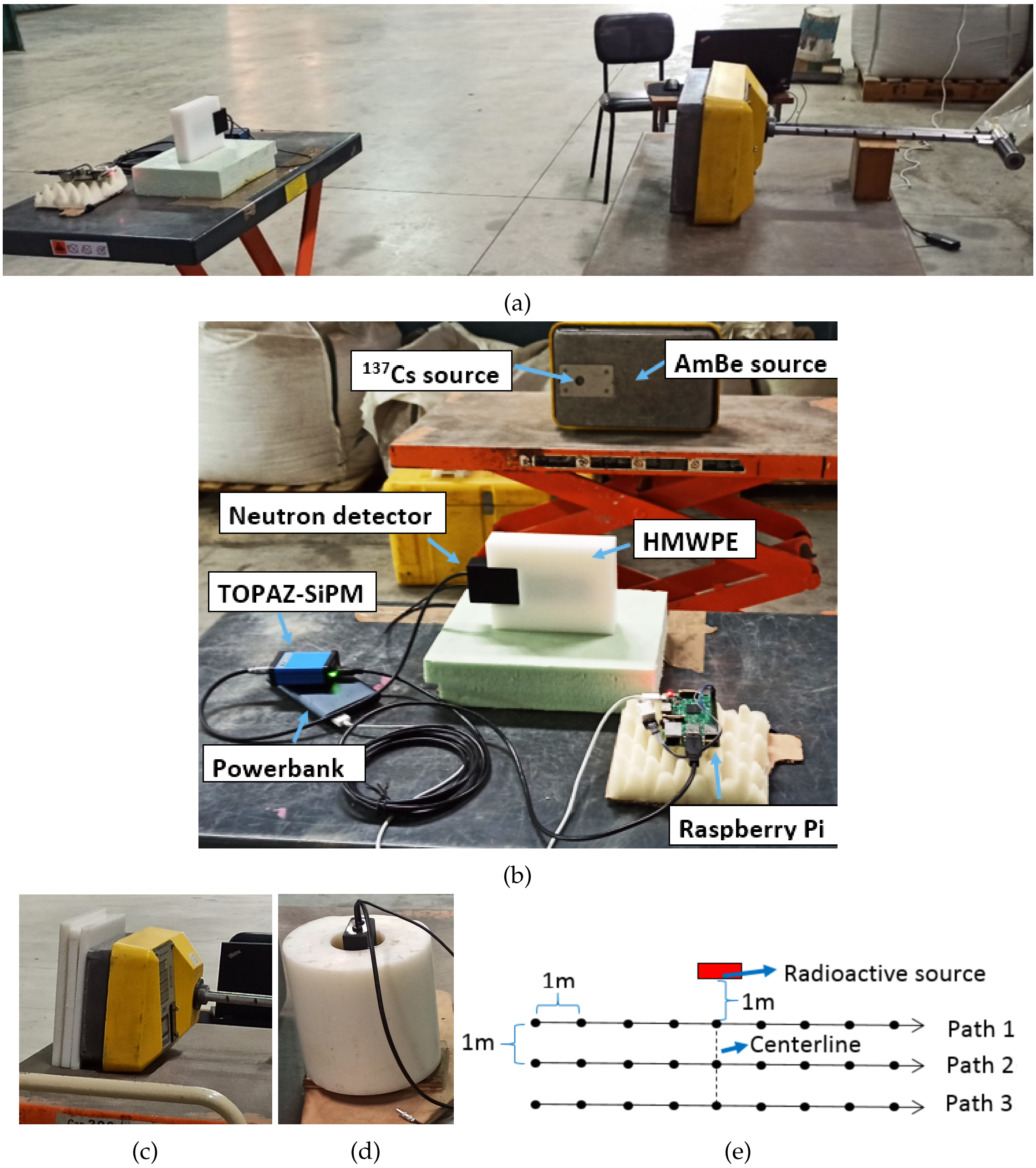

Figure 5.6: Experimental setup for source-detector distance of 1 m and equipment. (a) Setup side view. (b) Setup detail. (c) neutron source with 5 cm HDPE moderation. (d) Neutron detector inside cylindrical HDPE moderator. (e) Grid points considered for the measurements [290].

Figure 5.8 shows the results for a shielded $^{241}Am-Be$ source with a 5 cm-thick HDPE sheet placed at 1 m from the detection system, in which a rearrangement in the moderator plates was implemented. Plates initially positioned on the moderator side of the EJ-426HD detector (as in Figure 5.7) were relocated to the reflector side, excluding the central plates where the detector was situated. For instance, while the M15R15 configuration remained unchanged, the M30R15 configuration was transformed into M15R30, with no change on

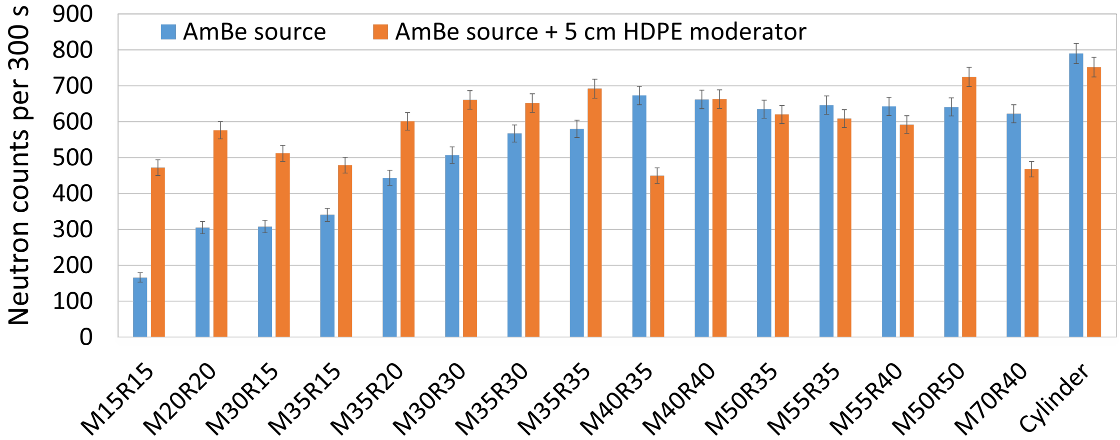

Figure 5.7: Neutron counts with varying detection system configuration (source-detector distance 1 m) considering an $^{241}Am-Be$ source only and with 5 cm-thick HDPE moderator. The cylinder features a 5-cm wall thick HDPE moderator [290].

weight. Therefore, $x \leq y$ in the considered MxRy configurations. The results, presented in Figure 5.8, reveal notable shifts, with a significant increase in the neutron counts due to the detection system configuration change. For instance, the M20R75 showed a 47% increase compared to its weight-equivalent M55R40. Generally, the enhancement in detection efficiency ranges from 12% to 79%, depending on the configuration modification.

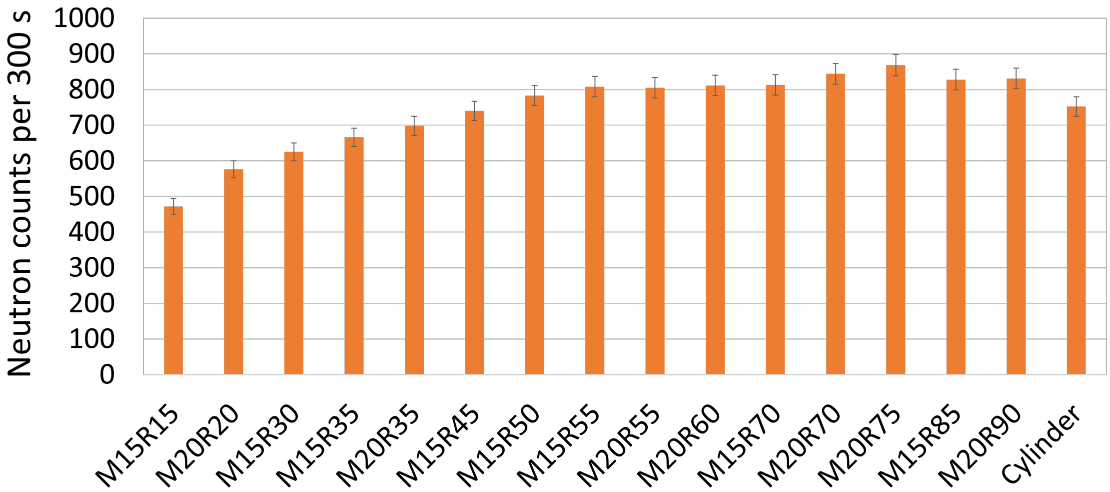

Figure 5.8: Neutron counts with varying detection system configuration (source-detector distance 1 m) considering an $^{241}Am-Be$ source with a 5 cm-thick HDPE sheet. The cylinder features a 5-cm wall thick HDPE moderator [290].

To test the sensitivity of the neutron detection system to an intense gamma-ray source, the neutron counts were collected during 300 s for the M40R35 configuration considering the $^{241}Am-Be$ source and the ^{137}Cs source unshielded in the bottom of the Troxler (source rod in the backscatter geometry). The result obtained, of 685±26 neutron counts, was similar to previous obtained result of 673±26 neutron counts obtained with the $^{241}Am-Be$

source and the shielded ^{137}Cs source (source rod at the safe position). Given the statistical uncertainties of both results, it can be concluded that the neutron detection system shows minimal sensitivity to gamma rays, even in the presence of high gamma-ray intensity.

Further investigation was conducted to determine if increasing the moderator cross-sectional area would impact significantly the neutron detection efficiency of the M4035 detection system configuration. A 1.5 cm-thick HDPE small bar was successively added to the top and side of the M4035 configuration. Neutron counts of 674±26 and 684±26 were obtained, respectively, which were consistent with the 673±26 neutron counts recorded when no additional moderator small bars were added. The results are in line with the MC simulation results (Figure 5.3), indicating that only a marginal improvement in detection efficiency can be achieved by increasing the optimized cross-sectional area of the moderator plates. In this way, a more compact and weight-efficient solution was ensured.

The grid of waypoints along the path depicted in Figure 5.6e enabled the sampling of the neutron count acquisition, with each point representing a single data acquisition of 100 s, while varying the distance to the centerline. The neutron data sampling was done using three different detection system configurations, whose data stand out in Figures 5.7 and 5.8. For the unmoderated $^{241}Am-Be$ source the M40R35, M40R40, and the "cylinder" detection system configurations were used, while for the moderated $^{241}Am-Be$ source the M20R75, M40R40, and the "cylinder" detection system configurations were used (as illustrated in Figure 5.9).

The analysis of Figure 5.9 indicates that the cylindrical moderator exhibited superior source position discrimination for path 1 when considering the unmoderated $^{241}Am-Be$ source, as shown by higher counts at the centerline position (refer to Figure 5.9a). However, for the more distant paths (path 2 and path 3), no significative difference is observed when compared with the M40R40 and M40R35 configurations (as seen in Figures 5.9b and 5.9c).

Considering a 5 cm HDPE thick moderated $^{241}Am-Be$ source, the M20R75 configuration demonstrated enhanced source position discrimination (see Figure 5.9d). Nevertheless, the differences between the detection system configurations were marginal, even for distant paths (refer to Figures 5.9e and 5.9f).

Considering the developed detection system configurations, the results and advantages of this system can be summarized as follows:

- It fulfills the Security requirements, namely:
  - High detection efficiency (comparable results to the detector with the cylindrical moderator configuration);
  - Very small sensitivity to gamma rays; and
  - Ability to detect both the thermal and fast neutron components. Adjusting the number of moderator plates on either side of the detector (modular detection system) enables the optimization of detection efficiency for various neutron sources, each with distinct neutron spectra. This flexibility also extends to detecting both shielded and unshielded sources.

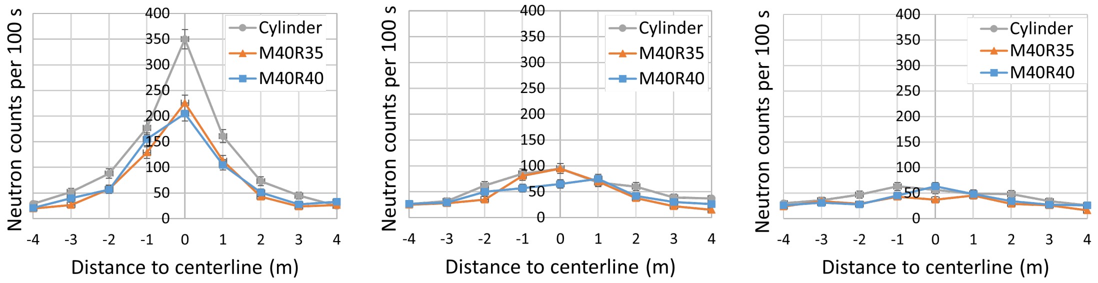

(a) Path 1 ($^{241}Am - Be$). (b) Path 2 ($^{241}Am - Be$). (c) Path 3 ($^{241}Am - Be$).

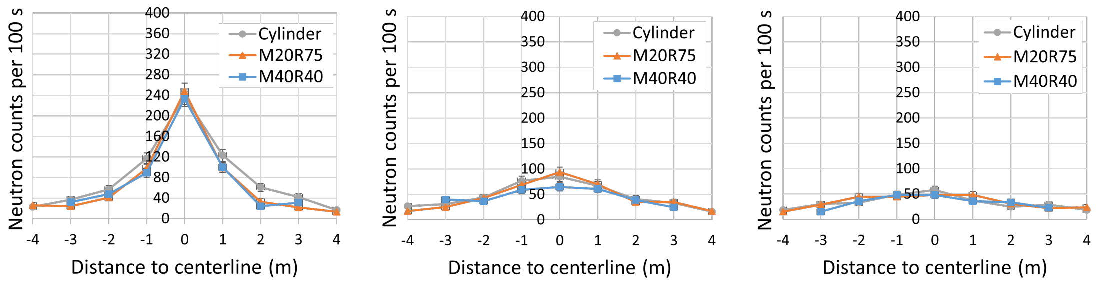

(d) Path 1 ($^{241}Am - Be$+HDPE). (e) Path 2 ($^{241}Am - Be$+HDPE). (f) Path 3 ($^{241}Am - Be$+HDPE).

Figure 5.9: Neutron counts considering an $^{241}Am - Be$ source not shielded (graphs on the top) and with a 5 cm-thick HDPE moderator (graphs on the bottom). Backgrounds acquired during 100 s: 10.0±1.3 counts (cylinder); 10.3±1.3 counts (M40R35); 9.3±1.2 counts (M40R40); 8.3±1.2 counts (M20R75) [290].

- The detection system weight, of approximately 1.2 kg (in which 1.1 kg stands for the M40R40 moderator and 0.09 kg for the EJ-426HD detector), corresponds to only 20% of the multirotor maximum payload considered in this thesis (6 kg);
- The detection system is compact, low power consumption, and it is easily integrated in a mobile platform, in particular small unmanned vehicles, due to its parallelepiped shape;
- In contrast with commercially available ^{3}He and BF$_3$ proportional counters, which normally use large and heavy cylindrical/spherical moderators, the developed detection system features a modular configuration by changing the number and/or position of the plates. This modular capability allows to optimize the detection efficiency for a given neutron source, shielded or not;
- The M40R40 detection system configuration presented high neutron detection efficiency to both moderated and non-moderated $^{241}Am - Be$ sources. This was demonstrated by the following results:
  - The M40R35 and M40R40 detection system configurations, featuring moderator thicknesses of 6.5 cm and 7 cm respectively, exhibited the highest neutron detection efficiency for an $^{241}Am - Be$ source. These results are consistent with the MC simulated values, which identify 7 cm as the optimal moderator thickness;

- When using the moderated $^{241}Am-Be$ source, the detection efficiency of the M40R40 configuration shows minimal variation, while the efficiency of the M40R35 configuration undergoes a significant decrease;
- In an analysis of detection efficiency relative to weight and volume, although M40R40 configuration demonstrated lower detection efficiency than the cylindrical configuration, a significant reduction on weight (by half) and volume was achieved.

In laboratory tests, the neutron spectrum was also obtained for the M40R40 configuration considering a 33.3 MBq (0.9 mCi) $^{241}Am-Be$ source at 2 cm distance from the neutron detection system (as shown in Figure 5.10).

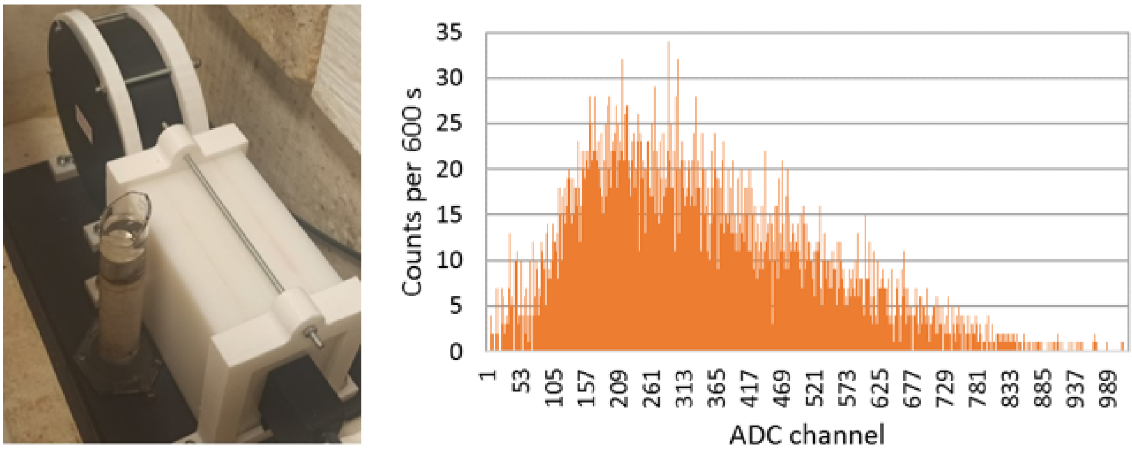

Figure 5.10: Spectrum from the EJ-426HD detector considering a 33.3 MBq (0.9 mCi) $^{241}Am-Be$ source at 2 cm distance [296].

5.2 Gamma detection system performance

5.2.1 Monte Carlo modelling and simulation results

The gamma-ray detection efficiency of both the EJ-200 plastic scintillator and the commercial CsI(Tl) scintillator were compared using MCNP6, taking into account their intrinsic and geometric detection efficiencies (by varying the source-detector distance).

The detectors feature distinct dimensions and materials, namely: (i) a 110 mm (diameter) $\times$ 30 mm (height) cylindrical EJ-200 plastic scintillator with a density of 1.023 g/cm^3; and (ii) a 51 mm (diameter) $\times$ 51 mm (height) cylindrical $CsI(Tl)$ scintillator with a density of 4.51 g/cm^3. MCNP6's tally F8 was utilized to score the pulse height distribution, providing valuable insights into the energy distribution of the detected particles. Energy thresholds were defined to account for variations in the detectors' light yields: 11 keV for the $CsI(Tl)$ scintillator[3] and 55 keV for the EJ-200 scintillator[4]. The gamma-emitter

[3]The energy threshold of the $CsI(Tl)$ scintillator was obtained experimentally through energy calibration.

[4]According to the detectors manufacturer, the EJ-200 scintillator presents an energy threshold five times higher than the one featured by the $CsI(Tl)$ scintillator.

radioactive sources used, of radionuclides ^{137}Cs and ^{241}Am, were considered separately, each being modelled as isotropic point sources centered at the detector window and emitting gamma-ray of energies of 662 keV and 59.5 keV, respectively. The simulation adopted the physics "model e" and "mode p", to perform the transport of electrons and photons. The intermediary medium was established as air.

The radiation yield must be multiplied by the F8 tally value in order to determine the detection efficiency, as the MCNP6 F8 tally provides the number of gamma rays detected per initial particle. The yield for the gamma rays of ^{137}Cs (branching fraction for the decay) at 662 keV is ~0.85, meaning that for every 100 disintegrations, about 85 gamma rays of 662 keV are released. On the other hand, the yield for the 59.5 keV gamma rays of ^{241}Am is ~0.36 [297], [298].

Table 5.2 presents the MC simulation results of the F8 tally values for both EJ-200 and $CsI(Tl)$ scintillators, considering point sources of ^{241}Am and ^{137}Cs.

Table 5.2: Comparison of the MC simulation data (F8 tally) for the EJ-200 and $CsI(Tl)$ scintillators considering point sources of ^{241}Am and ^{137}Cs at different source–detector distances [296].

Radioactive source & source-detector distance	F8 tally for EJ-200 (per starting particle)	F8 tally for CsI(Tl) (per starting particle)	F8 tally ratio between EJ-200 and CsI(Tl)
^{241}Am at 1 mm	$(1.08 \pm 0.01) \times 10^{-2}$	$(3.06 \pm 0.01) \times 10^{-1}$	0.035 ± 0.001
^{241}Am at 1 m	$(1.02 \pm 0.03) \times 10^{-5}$	$(1.33 \pm 0.01) \times 10^{-4}$	0.077 ± 0.003
^{241}Am at 5 m	$(3.8 \pm 0.2) \times 10^{-7}$	$(5.8 \pm 0.1) \times 10^{-6}$	0.066 ± 0.004
^{137} Cs at 1 mm	$(1.99 \pm 0.01) \times 10^{-1}$	$(3.23 \pm 0.01) \times 10^{-1}$	0.62 ± 0.01
^{137} Cs at 1 m	$(2.03 \pm 0.02) \times 10^{-4}$	$(1.28 \pm 0.04) \times 10^{-4}$	1.59 ± 0.06
^{137} Cs at 5 m	$(8.4 \pm 0.1) \times 10^{-6}$	$(5.7 \pm 0.1) \times 10^{-6}$	1.47 ± 0.04

The EJ-200 detection efficiency for the 59.5 keV gamma rays of ^{241}Am is considerably lower compared to the weight-equivalent $CsI(Tl)$ detector, primarily due to the higher energy threshold of the EJ-200 detector.

In scenarios where a ^{137}Cs source is in close proximity to the detector window (1 mm distance), the $CsI(Tl)$ detector exhibits a superior detection efficiency. However, at distances of 1 m and 5 m from the source, the EJ-200's detection efficiency overcomes that of $CsI(Tl)$ by factors of 1.59 and 1.47 respectively, owing to its higher geometric detection efficiency (as illustrated in Figure 5.11).

5.2.2 Laboratory results

To investigate the detector response to low-intensity radioactive sources, the ^{241}Am gamma source (the most probable energy peak is 59.5 followed by the 26.3 keV), the ^{137}Cs gamma source (the most probable peak at 662 keV), and the ^{90}Sr beta source (with a

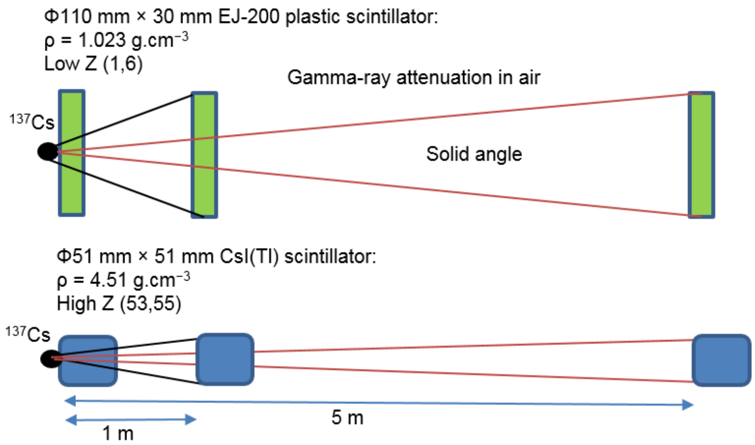

Figure 5.11: Parameters that affect the detection efficiency of EJ-200 and $CsI(Tl)$ scintillators, for different source-detector distances [296].

maximum beta energy of 0.546 MeV, however it is normally assumed the maximum beta energy of its daughter ^{90}Y of 2.284 MeV) were placed next to the entrance window of both the EJ-200 plastic scintillator (as shown in Figure 5.12) and the $CsI(Tl)$ scintillator. Subsequently, the corresponding spectra were acquired for a specific integration time.

Figure 5.12: ^{137}Cs source placed next to the EJ-200 detector window [296].

Figure 5.13 illustrates the spectrum (counts per ADC channel or Energy) recorded in both detectors in response to a ^{90}Sr source (beta emitter). Notably, owing to the very thin titanium window, the EJ-200 scintillator features a beta detection efficiency 1.68 times greater than that of the $CsI(Tl)$ scintillator.

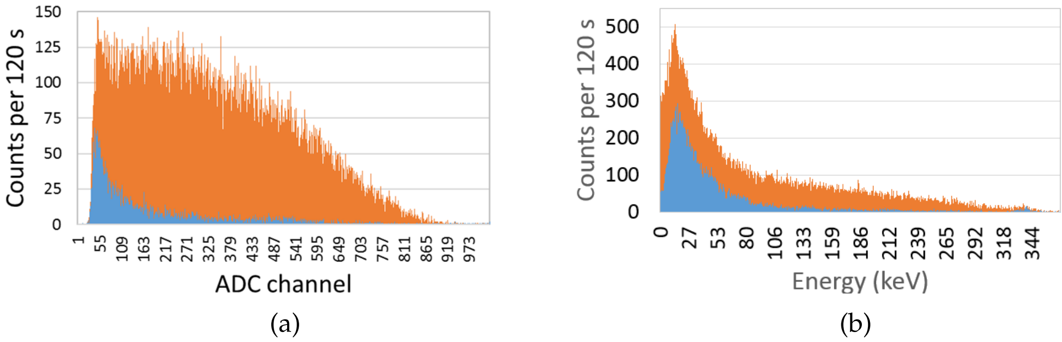

Figure 5.13: Beta spectra for a 3.3 kBq ^{90}Sr source next to the detector window (orange color) and background (blue color) obtained with the: (a) EJ-200 scintillator; and (b) $CsI(Tl)$ scintillator [296].

Given that ^{241}Am emits low energy gamma rays, with peaks at 59.5 keV and a lower intensity peak at 26.3 keV, the spectra for both detectors were acquired to assess their lower energy thresholds (see Figure 5.14). From Figure 5.14a, it is evident that the EJ-200 scintillator cannot detect the gamma rays emitted by ^{241}Am. This limitation arises due to the lower energy deposited by the gamma rays in low Z materials (due to the Compton scattering dominance)[5] and the higher energy threshold of the EJ-200 scintillator, which restricts the detection to only a small fraction of gamma rays (also susceptible to being masked by the background). In contrast, the higher gamma energy deposited in $CsI(Tl)$ crystal (due to photoelectric effect dominance)[6] and the lower threshold energy, makes it possible the detection of both the 59.5 keV and 26.3 keV peaks of ^{241}Am, as shown in Figure 5.14b.

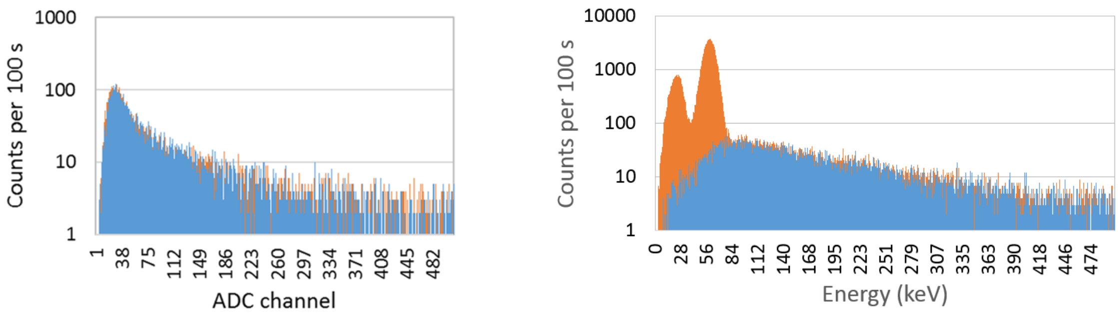

(a) (b)

Figure 5.14: Gamma-ray spectra for a 22 kBq ^{241}Am source next to the detector window (orange color) and background (blue color) obtained with the: (a) EJ-200 scintillator; and (b) $CsI(Tl)$ scintillator [296].

Figure 5.15 shows the spectra obtained with EJ-200 and $CsI(Tl)$ scintillators for a ^{137}Cs source positioned next to the detectors windows. Due to the lower intrinsic efficiency of the EJ-200 scintillator (attributed to its lower atomic number and density), it exhibits a detection efficiency approximately 0.60 times smaller than that of the $CsI(Tl)$ scintillator. This finding is consistent with the value of 0.62 ± 0.01 obtained from MC simulations (see Table 5.2). Additionally, the $CsI(Tl)$ detector features an energy resolution of 6.8% at 662 keV.

Given the EJ-200 detector's larger diameter relative to its thickness, variations in gamma-ray counts (for a given integration time) were studied by varying the angle of the ^{137}Cs source relative to the detector position while maintaining a constant source-to-detector center distance of 30 cm, as illustrated in Figure 5.16. The results are shown in Figure 5.17.

[5]For the EJ-200 plastic scintillator, rich in hydrogen (Z=1) and carbon (Z=6) atoms, the 59.5 keV gamma rays will interact mainly through Compton scattering.

[6]The photoelectric effect is dominant considering the gamma-ray energy range and the high atomic number (Z) of the material's constituent atoms: 55 for cesium and 53 for iodine.

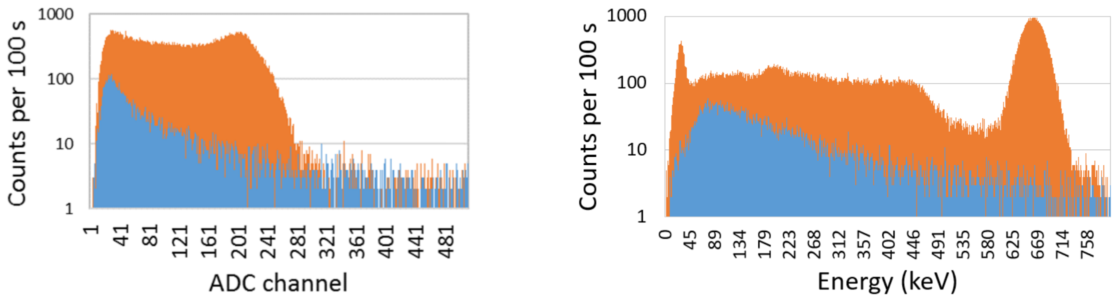

(a) (b)

Figure 5.15: Gamma-ray spectra for a 8.5 kBq ^{137}Cs source next to the detector window (orange color) and background (blue color) obtained with the: (a) EJ-200 scintillator; and (b) $CsI(Tl)$ scintillator [296].

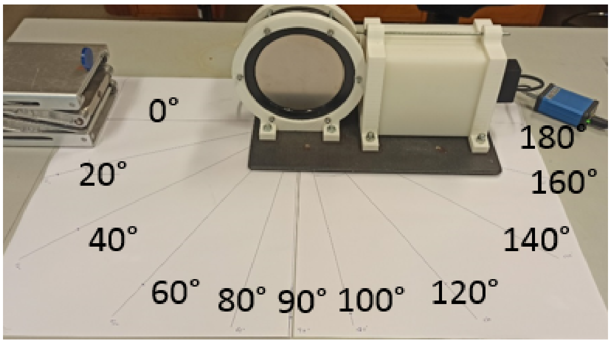

Figure 5.16: Experimental setup used to obtain the EJ-200 response to a ^{137}Cs source by varying the source-detector angle [296].

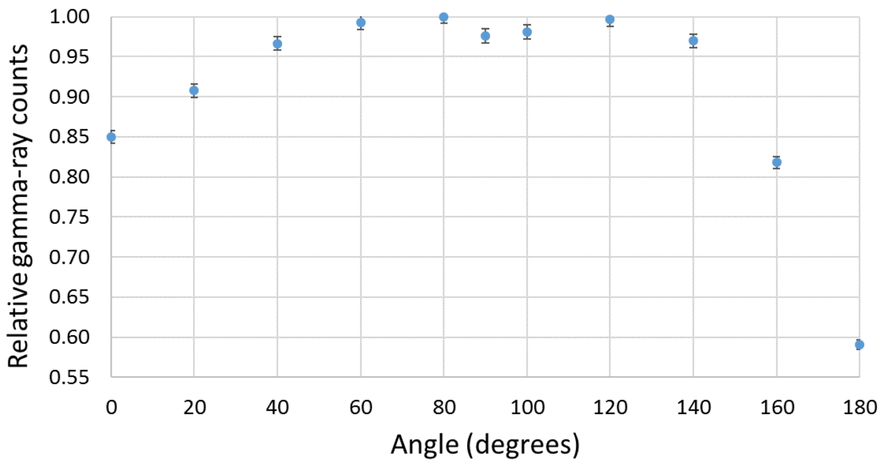

Figure 5.17: Gamma-ray detection efficiency as a function of the angle between the source and detector, for a 0.11 MBq (2.86 µCi) ^{137}Cs source and a EJ-200 scintillator (source-detector distance is kept constant) [296].

When the neutron detection system was positioned between the source and the EJ-200 scintillator, detection efficiency decreased by approximately 10% and 25% at angles of 160° and 180°, respectively, compared to the symmetrical angles of 20° and 0° (as seen in Figure

5.17). However, since the EJ-200 detection system will conduct lateral inspections of the shipping containers with its detector window parallel to the container walls, the difference in detection efficiency at angles nearly parallel to the system's movement direction will have no significant impact on the results. Therefore, no mitigation of the variation in detection efficiency is necessary for inspecting shipping containers.

5.2.3 Field test and results

The gamma-ray detection efficiency of $CsI(Tl)$ and EJ-200 scintillators was compared by measuring both background and count rates at various source-detector distances ranging from 1 to 5 meters, with a ^{137}Cs source positioned at a fixed height of 12 cm (coincident with the height of the detectors center). Figure 5.18 shows the Signal-to-Noise Ratio (SNR) results. Even though $CsI(Tl)$ scintillator has a higher intrinsic detection efficiency, the EJ-200 detector exhibits an SNR that is nearly three times higher than $CsI(Tl)$ for source-detector distances ranging from 1 to 5 m.

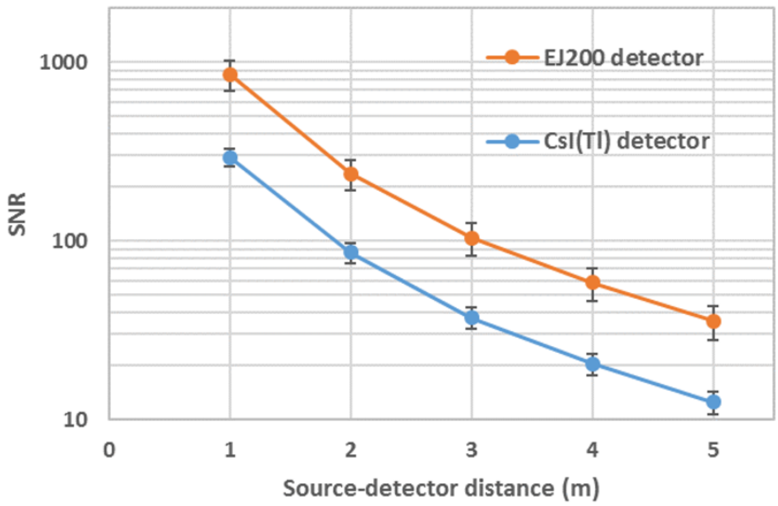

Figure 5.18: SNR for $CsI(Tl)$ and EJ-200 scintillators, for a source-detector distance between 1 and 5 meters.

5.3 Radiation detection system assembly

After determining the optimal neutron detection system configuration, the M40R40 (as described in subsection 5.1.3.1), it was necessary to develop supports for the neutron and gamma detection systems. To transport the detection system as a handheld equipment or to facilitate its integration into mobile platforms, lightweight and compact supports were designed and manufactured. The 3D geometry of the supports was optimized using *SolidWorks®* software and then prototyped through 3D printing with PLA filament, as shown in Figure 5.19. A carbon fiber sandwich plate measuring 30 cm (lenght) $\times$ 20 cm (width) $\times$ 4 mm (thickness) was also manufactured to carry the radiation detection system, sensors and associated electronics. To achieve a balanced payload, an even weight distribution of the detectors on the carbon fiber plate was carefully considered.

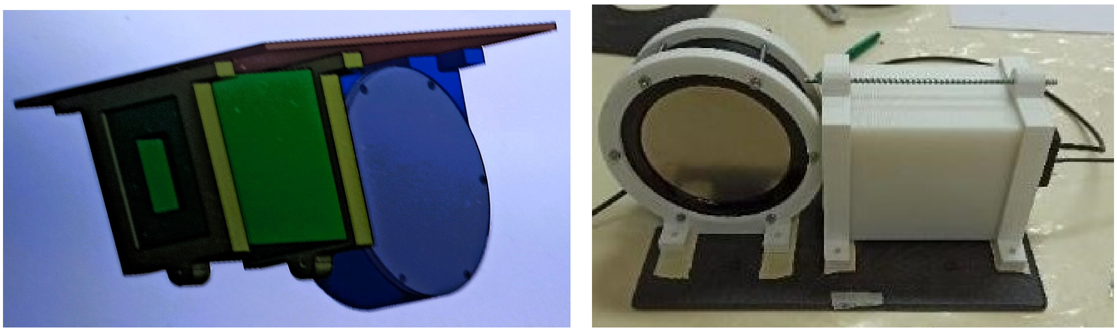

Figure 5.19: 3D printed detector supports and carbon fiber plate developed for detector integration on a mobile platform. SolidWorks® drawn (left image) and developed prototype (right image).

The handheld configurations of the radiation detection system without and with distance sensors is shown in Figures 5.20 and 5.21 respectively.

Figure 5.20: Radiation detection system – Handheld configuration without distance sensors. Front side view (left image) and back side view (right image).

Figure 5.21: Radiation detection system – Handheld configuration with distance sensors. Front side view (left image) and back side view (right image).

The developed radiation detection system weighs 2.8 kg (including the carbon fiber plate, associated electronics, and supports) and was also integrated into a DJI Matrice 600 Pro (Figure 5.22), a hexacopter that can take off with a maximum weight of 15.5 kg (with a maximum payload of 6 kg) [299]. Since an uneven weight distribution of the payload could cause one or two rotors to overload, a weight balance of the multirotor[7] was performed by repositioning the radiation detection system electronics (placed on top of the carbon fiber sandwich plate) till the desired center of gravity was achieved. The fast installation and removal of the payload from the multirotor is achieved by only four screws. The total cost of the radiation detection system, along with its associated electronics, was estimated to be approximately 7,400.00 €[8], while the cost of the multirotor platform was around 7,000.00 € (including two battery packs and one charger)[9].

5.4 Discussion and conclusions

This Chapter outlines the development and optimization of an innovative radiation detection system tailored for Security and Defence applications. The system, evaluated through MC simulations, laboratory experiments, field tests, and practical prototyping, overcomes the limitations of current technologies, particularly for detecting weak or shielded radiation sources at large distances.

The MRDS features a compact, pancake-shaped design that enhances geometric detection efficiency while remaining lightweight, making it ideal for mobile platforms like multirotors. Its use of cost-effective materials, including plastic scintillators and low-power SiPM sensors, reduces costs and simplifies deployment. Integrating the MRDS into an unmanned vehicle enables autonomous and cooperative inspections using multiple vehicles. The system employs a two-stage detection method–initial rapid detection followed by radionuclide identification–improving operational efficiency. The developed MRDS offers a practical alternative or complement to fixed radiation portal monitors and handheld systems, particularly where mobility, rapid deployment, and extensive inspection coverage are needed. It also has the potential to enhance existing detection networks by providing better coverage and adaptability to dynamic operational conditions.

Section 4.4 outlines the development of a portable and accurate radiation detection system with integrated sensors to enhance data reliability. The hardware includes a compact TOPAZ-SiPM MCA for data acquisition, a standalone GNSS receiver to obtain the system's horizontal position, and a LiDAR sensor for accurate vertical distance measurements. For improved positional accuracy and reliability, particularly in challenging GNSS

[7]Mass and balance of an aircraft (the weight and the location of its center of gravity) is a vital procedure for a normal flight operation.

[8]The costs were as follows: 3,250.00 € for the Topaz SiPM MCA device, 2,565.00 € for the EJ-200 plastic scintillator, 1,295.00 € for the EJ-426HD neutron detector, 110.00 € for the 3D-printed supports and carbon fiber plate, 30.00 € for the moderator plates, and 150.00 € for the distance sensors, Raspberry Pi, and power bank.

[9]The battery packs and chargers can also be rented, reducing costs.

environments, future research should consider advanced solutions like GNSS receivers with integrated IMU or higher-precision sensors such as DGNSS and RTK GNSS. The software architecture enables precise data synchronization and flexible processing for both real-time and offline source localization.

The optimization of the neutron detection system through MC simulations and practical prototyping is presented in Section 5.1. Simulations revealed that HDPE and HMWPE were the most effective moderators for neutron detection, with a 7 cm thickness achieving peak efficiency. The modular design, incorporating CNC-milled HDPE and HMWPE plates, proved effective for adjustable configurations, balancing weight and performance. Field tests validated the simulation results, with the M40R40 configuration demonstrating high efficiency and portability. It was concluded that the modular approach offers significant advantages over traditional designs, providing a compact, lightweight, and adaptable neutron detection system.

Section 5.2 explored the performance of the EJ-200 gamma-ray detection system in comparison with a weight equivalent CsI(Tl) scintillator. MC simulations, validated by laboratory and field tests, highlighted the CsI(Tl) scintillator's superior efficiency for detecting gamma-ray sources at close distances (1 mm), compared to the EJ-200 scintillator. At longer distances (above 1 m), the EJ-200 scintillator exhibited higher efficiency due to its geometric detection advantages. In contrast with CsI(Tl) scintillator, the low light yield of EJ-200 scintillator makes impraticable the detection of low energy gamma rays (bellow 60 keV), such as the gamma rays emitted by the ^{241}Am source. As outlined in Section 3.3, the low light yield and limited gamma energy resolution of plastic scintillators can be improved through several approaches. Using high-Z sensitized plastic scintillators or employing a grid of smaller scintillator volumes with a high density of SiPM sensors, rather than a single large volume, can optimize scintillation light collection and gamma-ray energy discrimination. Furthermore, Section 3.2.1.1 highlights that applying techniques such as EW, LSF, and SAM for spectrum analysis can effectively discriminate between NORM, SNM, and other radionuclides, and facilitate the identification of various radioisotopes, including ^{137}Cs, ^{241}Am and ^{99m}Tc.

Finally, the assembly and integration of the detectors into a carbon fiber plate was demonstrated, enabling seamless integration with mobile platforms. The radiation detection system offers three configurations: (i) a handheld unit without distance sensors for inspections at a fixed height; (ii) a multirotor-based radiation detection system for versatile, airborne applications (distance sensors were not available yet); and (iii) a handheld unit with distance sensors for variable path height inspections (considered in the measurement campaign described in Chapter 8).

Figure 5.22: Radiation detection system integrated in the DJI Matrice 600 Pro multirotor (top image) and detail view of the screws used to attach the carbon fiber plate to the multirotor structure (bottom image).

6 Source detection and localization using predefined paths – proof-of-concept and field tests

6.1 Experimental setup and methods

The developed radiation detection system was first tested in a proof-of-concept scenario consisting on the inspection of a 20 ft long shipping container with the internal dimensions of 5.94 m (length) × 2.34 m (width) × 2.39 m (height). Both the handheld equipment and the radiation detection system integrated into the multirotor were used for the detection and localization of neutron and gamma sources within the container (without distance sensors – not available yet). Two types of radioactive sources were used in the experiment: i) ten equal sources of ^{137}Cs with a total activity of ~4 MBq (0.11 mCi)[1], were positioned at the geometric center (as shown in Figure 6.1a) or at the bottom corner of the container (as shown in Figure 6.1b), and ii) a Troxler equipment, oriented at 90° positioned at the geometric center (as illustrated in Figure 6.1c) or at the bottom corner of the container.

The Troxler equipment houses a 1.45 GBq (39.2 mCi) $^{241}Am-Be$ neutron source (with an activity uncertainty of ±10%) and a 215 MBq (5.81 mCi) ^{137}Cs gamma source (with an activity uncertainty of ±10%) were employed.

For the field tests the radiation detection system performed predefined paths:

- Along the length of the container – inspection to only one container side for radioactive source detection;
- Around the container (full laps) to enhance radioactive source detection and localization.

During the container inspection the detection system was maintained parallel to the container walls to improve the detection efficiency.

[1] Since the ten ^{137}Cs sources are used together in this thesis, they can be regarded as a single ^{137}Cs source.

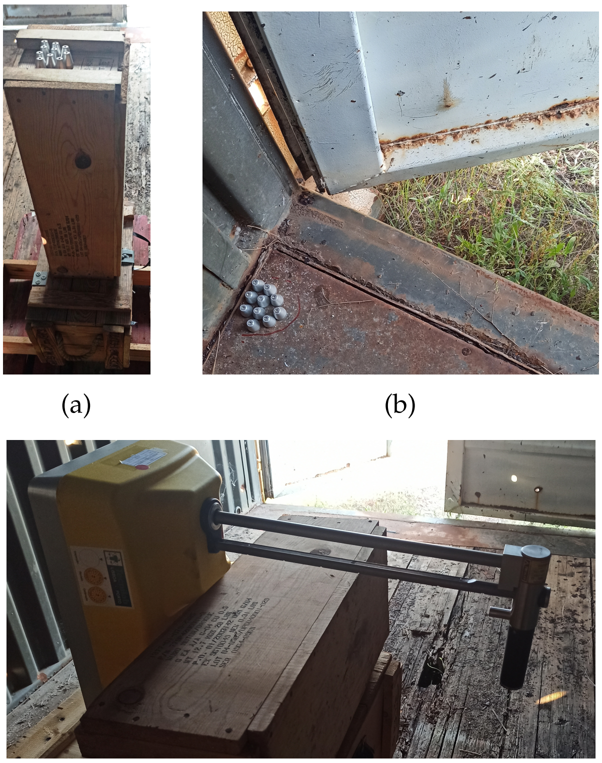

(a) (b)

(c)

Figure 6.1: Radioactive sources used in the field tests: (a) ^{137}Cs sources centered in the container. (b) ^{137}Cs sources at the corner of the container. (c) Troxler equipment oriented 90° centered in the container [296].

Different path heights were considered, namely one-third of the container height (0.864 m ≈ 0.86 m), half the container height (∼ 1.3 m), and two-thirds of the container height (∼ 1.73 m). Figure 6.2 shows the different path heights considered and source positions. To validate the data, the experiment was repeated five times for each different type of path (one side only or full lap), path height, and source position.

For the gamma-ray source localization, the MLE algorithm was used to estimate the source position (single source), as described in Section 4.5. During these field tests, only predefined paths at a constant height were considered, and no LiDAR sensor was available for height measurements; therefore, the MLE algorithm estimated only the horizontal source position (the x and y coordinates). In the initial field tests, the spherical approximation of the EJ-200 scintillator was utilized[2].

For detecting a gamma-ray source, if the EJ-200 detector counts exceed a decision threshold, it signals that further inspection is needed to confirm the source's presence. This decision threshold is calculated as the sum of the background mean and 1.645 times the Standard Deviation (SD) of the background values [300].

When employing the handheld configuration of the detection system without distance sensors (as shown in Figure 5.20), the radiation detection system moved at an approximate

[2]However, in the next Chapters it will be used the cylindrical approximation for the EJ-200 scintillator.

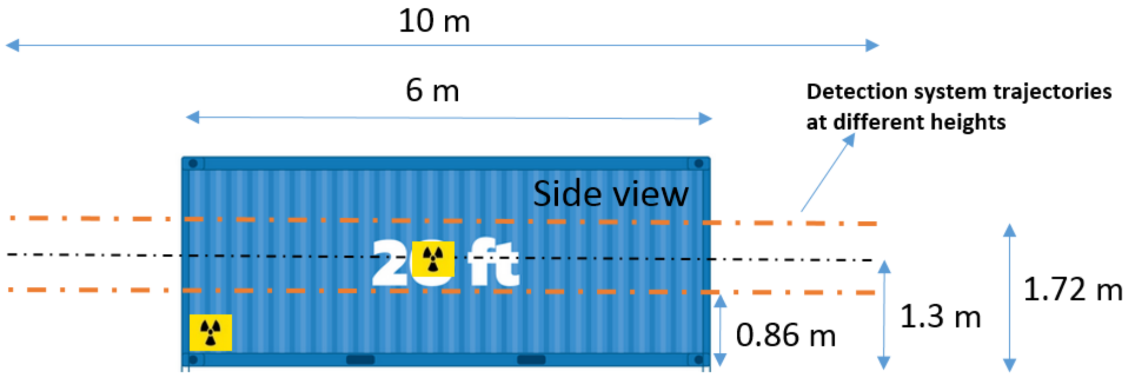

Figure 6.2: Mobile radiation detection system paths performed during the lateral wall inspections of the cargo shipping container cargo (blue rectangle) [296].

speed of 0.33 m/s, maintaining a constant distance of 1 m from the shipping container's lateral walls. A lower speed of approximately 0.2 m/s was considered when using the radiation detection system integrated into the multirotor. Since the multirotor was manually operated and it was difficult to keep a constant distance between the multirotor and the container walls (for safety reasons and wind conditions), the reduced speed allowed to keep the required radiation sensitivity during the inspections.

The radiation detection system measurements were conducted on different days, initially using the handheld equipment and subsequently with the system integrated into the multirotor. Figure 6.3 illustrates the equipment used during the manual inspection campaign, including the gamma-ray sources box, the portable radiation detection system, an LCD monitor for real-time data acquisition visualization, and a Bluetooth keyboard for direct interaction with the Raspberry Pi, if necessary. Additionally, a laptop was available for Wi-Fi connection with the Raspberry Pi.

Figure 6.3: Equipment used during the manual inspections of the shipping container.

Figure 6.4 shows the van used to support the measurement campaign with the radiation detection system coupled to the multirotor. Five battery packs and two battery pack charger were used to ensure nearly uninterrupted operation of the multirotor. Inside the van, a laptop provided remote access (via a dedicated Wi-Fi router) to the Raspberry Pi connected to the detection system. A gasoline generator powered the laptop and the multirotor's battery chargers.

Figure 6.4: Support van and multirotor with the integrated radiation detection system.

Figure 6.5 illustrates the inspection of the shipping container cargo using the developed radiation detection system integrated into the multirotor. With the payload installed, the multirotor achieved a flight time autonomy between 17 and 22 minutes, depending on the platform's flight paths and the battery pack used.

Figure 6.5: Multirotor with developed radiation detection system screening the shipping container cargo [296].

6.2 Field tests results

While both the EJ-200 plastic scintillator and the EJ-426HD neutron detection system conducted measurements concurrently, for clarity and organization of data, the results and corresponding discussions are presented separately for each detection system.

6.2.1 Neutron detection system

Before initiating experimental tests for radioactive source detection and localization, the neutron background count rate was determined. Multiple measurements were conducted around the shipping container in the absence of any source. Each measurement point had an average integration time of 80 s, yielding a neutron background mean of 0.07 ± 0.03 Counts per second (cps) (as shown in Figure 6.6).

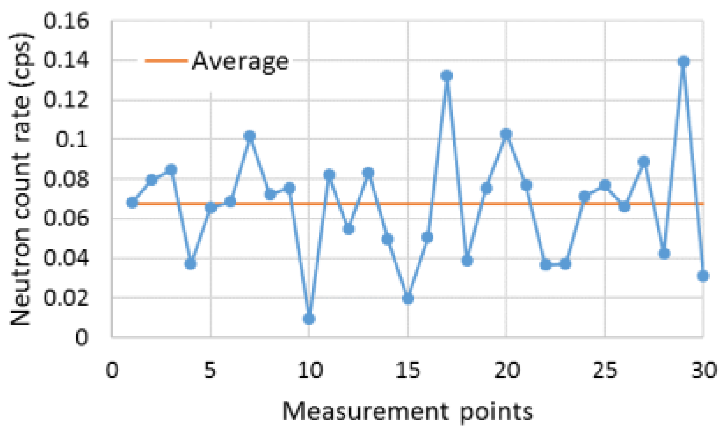

Figure 6.6: Neutron background count rate (cps) in the vicinity of the shipping container [296].

The 1.45 GBq $^{241}Am - Be$ source (which is inside the Troxler equipment referred in Section 6.1 with the ^{137}Cs source rod at the safe position–shielded ^{137}Cs source), was then placed inside the shipping container. The radiation detection system integrated into the multirotor was used to obtain the total neutron counts during the inspections to the lateral side only and for the full lap performed around the container at different heights. The neutron count rate of the inspections are shown in Table 6.1 and Table 6.2 for the source positioned at the center and at the bottom corner of the container respectively. The values shown correspond to the average value of the five measurements performed for each situation and the corresponding standard deviation.

When the source was placed at the container's center (as shown in Table 6.1), the neutron count rate increased nearly three to fourfold compared to the natural background count rate, providing us with a robust signal for confidently detecting the neutron source. Additionally, the highest neutron count rate value was registered on the paths performed at 1.3 m (half the container height) providing us an indication that the $^{241}Am - Be$ source is approximately located at the center of the container.

Table 6.1: Neutron count rates and standard deviations obtained with the EJ-426HD detection system integrated into the multirotor, for the Troxler equipment placed at the center of the shipping container [296].

Path height (m)	Neutron count rate (cps) for a single-side inspection	Neutron count rate (cps) for a full lap inspection
0.86	0.26 ± 0.05	0.24 ± 0.05
1.3	0.27 ± 0.06	0.26 ± 0.01
1.73	0.24 ± 0.08	0.22 ± 0.03

For the $^{241}Am - Be$ source positioned at the corner (as detailed in Table 6.2), the neutron count rate obtained was 4 to 6.6 times the natural background level. Once more, the highest neutron count rate was observed on the paths performed at 0.86 m (equivalent to one-third of the container's height), strongly suggesting that the $^{241}Am - Be$ source is likely situated at the container's floor.

Table 6.2: Neutron count rates and standard deviations obtained with the EJ-426HD detection system integrated into the multirotor, for the Troxler equipment placed at the bottom corner of the shipping container [296].

Path height (m)	Neutron count rate (cps) for a single-side inspection	Neutron count rate (cps) for a full lap inspection
0.86	0.45 ± 0.13	0.46 ± 0.09
1.3	0.34 ± 0.09	0.28 ± 0.03
1.73	0.37 ± 0.05	0.30 ± 0.06

As a result, an approximate neutron source localization (source at the top, middle or bottom of the container) can be obtained from a shipping container inspection carried out at three distinct path heights, increasing likewise the confidence in the source detection.

In general, the longer integration times used to obtain neutron counts during a full lap inspection, compared to a single-side inspection, resulted in lower SD values, as anticipated. Differences in the SD values obtained for a given radioactive source position and inspection type (full lap and single-side inspection) can be justified by the contribution of the background variation, which presents a SD value equal to 0.03 cps.

6.2.2 Gamma-ray detection system

For the detection of gamma rays, the radiation detection system considered was both handheld equipment and integrated into the multirotor.

The handheld equipment allowed to perform the first tests with the gamma-ray detection system (EJ-200 plastic scintillator) to study the effect of different sampling/integration times in the source detection and localization. For that, the ^{137}Cs sources with a total activity of 4 MBq were positioned at the center and at the corner of the container. The handheld equipment performed full laps around the container at half the container's height. After all points were acquired the MLE algorithm was used to estimate the horizontal coordinates of the source position (performed offline). The estimated-to-real source distance D (localization error) and the standard deviation of the five measurements considered for each integration time and source position are shown in Table 6.3.

Despite the improvement in localization estimation with extended sampling times, non-central source placement leads to a loss of data points, hindering the algorithm's ability to accurately estimate the source position. This is evident from the marginal difference in the estimated-to-real distances obtained with the integration times of 2 s and 4 s for the sources positioned at the center, and with no difference in the estimated-to-real distances for the sources positioned at the corner. To maintain comparable effectiveness without losing data points, we opted for a 1 s integration time [3] and reduced the survey speed from approximately 0.33 m/s (the speed used for handheld configuration measurements) to 0.2 m/s for the multirotor-coupled detection system. Although higher estimated-to-real distance values were obtained for the source positioned at the corner, these values are still below the minimum internal dimension of the container (2.34 m).

Table 6.3: Average and SD of the distance (D) between the MLE estimated position and the real sources position using the EJ-200 scintillator and considering ^{137}Cs sources with a total activity of 4 MBq placed at the center and at the bottom corner of the shipping container. Results displayed for three sampling/integration time values (1, 2 and 4 seconds) [296].

Sampling/integration time (s)	D (m)—Sources at the center	D (m)—Sources at the corner
1	0.84 ± 0.31	1.3 ± 0.3
2	0.44 ± 0.22	1.1 ± 0.4
4	0.47 ± 0.07	1.1 ± 0.1

Figures 6.7 and 6.8 show some examples of the gamma-ray count rate obtained with the handheld equipment using different integration times, when performing full laps around the container with ^{137}Cs sources positioned at the center and at the corner of the shipping container, respectively. The real and estimated source positions are shown, along with the estimated-to-real distances.

[3] The 1 s integration time allows improved spatial resolution and is also used by other sensors such as the GNSS receiver.

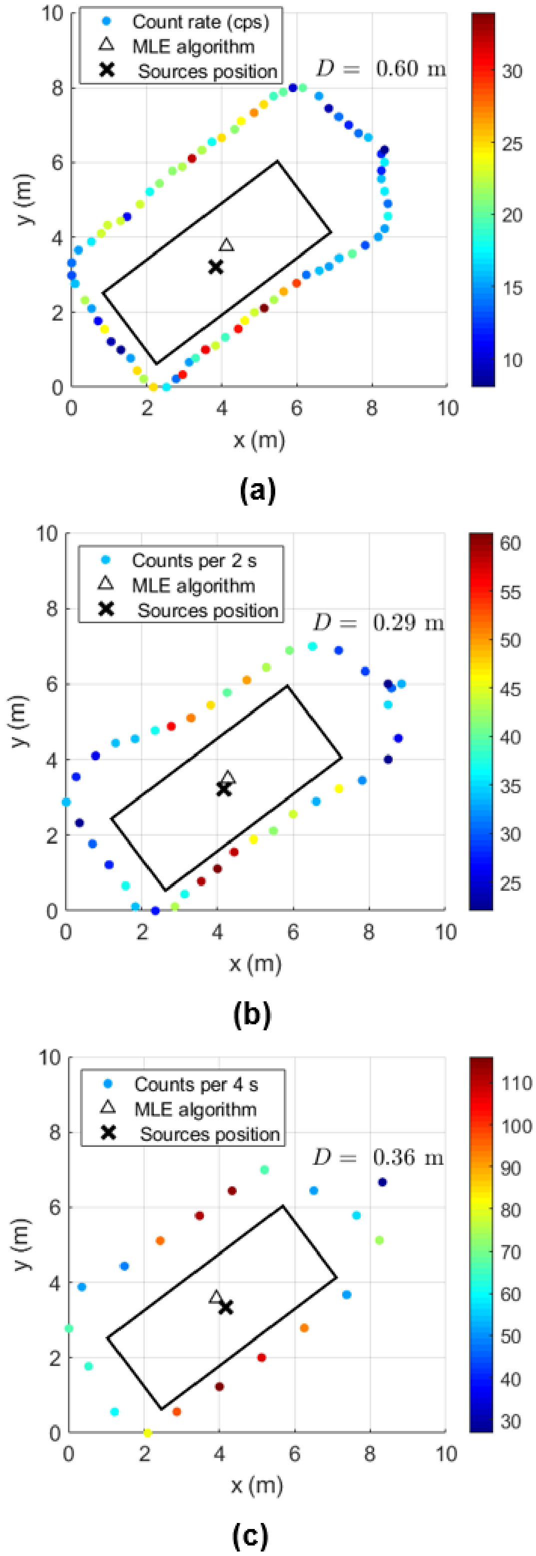

Figure 6.7: EJ-200 scintillator gamma-ray count rate (cps) measurements obtained using the developed handheld equipment considering ^{137}Cs sources of 4 MBq positioned at the center of the container. Sampling/integration times (dwell times) considered for the same total duration of the path: (a) 1 s. (b) 2 s. (c) 4 s [296].

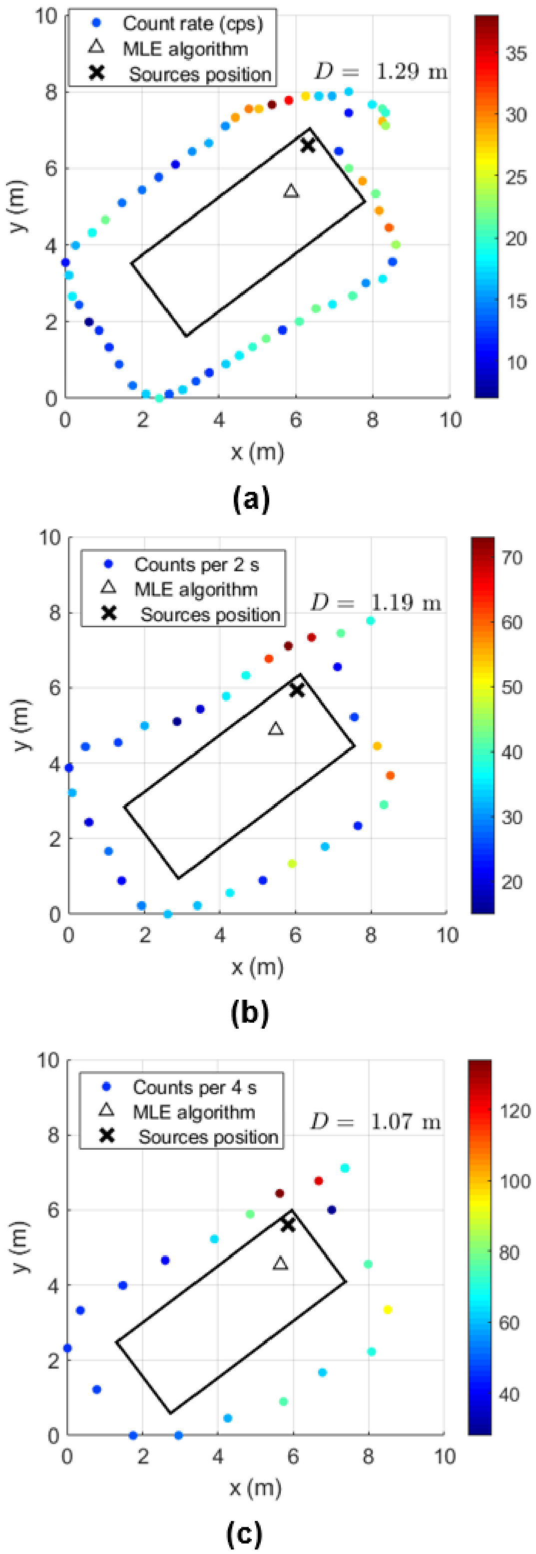

Figure 6.8: EJ-200 scintillator gamma-ray count rate (cps) measurements obtained using the developed handheld equipment considering ^{137}Cs sources with a total activity of 4 MBq positioned at the bottom corner of the container. Sampling/integration times (dwell times) considered for the same total duration of the path: (a) 1 s. (b) 2 s. (c) 4 s [296].

The estimated-to-real source distance D and the corresponding standard deviation (for the five measurements performed) were also obtained for the radiation detection system integrated into the multirotor, as shown in Table 6.4. In this case, the multirotor performed predefined paths around the container at different heights. While the estimated-to-real source distance was lower than one meter for the ^{137}Cs sources positioned at the center of the container (examples of the paths are shown in Figure 6.9), for the same sources positioned at the corner of the container the estimated-to-real source distance values were considerable higher (2 times higher for the path heights 0.86 m, 2.5 times higher for path height 1.3 m, and 6 times higher for the path height 1.73 m). This increase on the estimated-to-real source distances for higher path heights can be partially attributed to the source's non-central position and the higher impact of the GNSS receiver's positioning uncertainties during inspections when using the multirotor, as shown in Figure 6.10. The greater vertical distance between the path height and the real source position positioned at the corner (0.1 m above the ground), compounded by the fact that the MLE algorithm utilized in these tests did not consider the estimation of the z-coordinate (vertical component), further contributes to these results. Additionally, the higher standard deviation (SD=0.99 m) recorded for the source positioned at the corner and at a path height of 1.3 m (as shown in Table 6.4), indicates greater dispersion in the estimated source position values due to higher uncertainties in the radiation detection system's positioning during the inspections, as illustrated in Figure 6.10b. Conversely, the lower SD value (SD=0.13 m) observed for the source placed at the center and at a path height of 1.73 m indicates lower uncertainties in the radiation detection system's positioning during the inspections. This scenario also corresponds to the most accurate source position estimate, with a distance D = 0.41 m.

Consequently, as elaborated in the subsequent Sections, it becomes imperative to incorporate a MLE algorithm capable of estimating all three coordinates of the source, a procedure to mitigate the uncertainties of the GNSS receiver positioning, along with an informative path planning strategy. The informative path planning ensures the optimization of the initial path to gather comprehensive data for refining the accuracy of the source position estimation.

Table 6.4: Average and SD values for the estimated-to-real source distances using EJ-200 detector and considering ^{137}Cs sources of 4 MBq placed at the center and at the bottom corner of the shipping container [296].

Path height (m)	**D (m)—Sources Centered**	**D (m)—Sources at the Corner**
0.86	0.76 ± 0.39	1.56 ± 0.28
1.3	0.90 ± 0.46	2.22 ± 0.99
1.73	0.41 ± 0.13	2.54 ± 0.36

Despite efforts to keep the multirotor close to the container walls during inspections (maintaining the detection system 1 m away), variations of up to 1.5 m were observed, with the distance increasing due to manual adjustments and wind conditions.

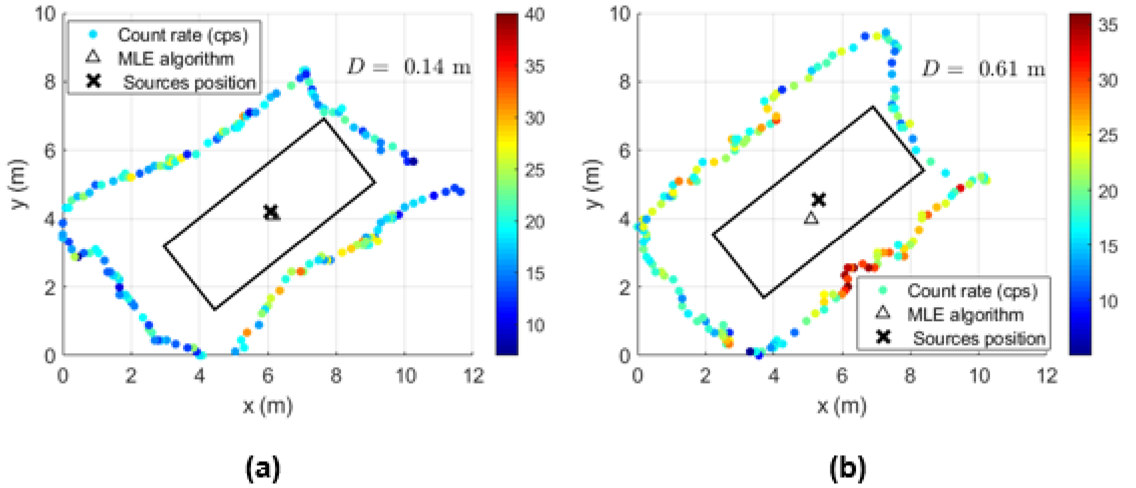

Figure 6.9: EJ-200 scintillator gamma-ray count rate (cps) measurements obtained using the detection system integrated into the multirotor considering ^{137}Cs sources with a total activity of 4 MBq positioned at the center of the container. Multirotor paths were performed at: (a) one-third the container height. (b) half the container height [296].

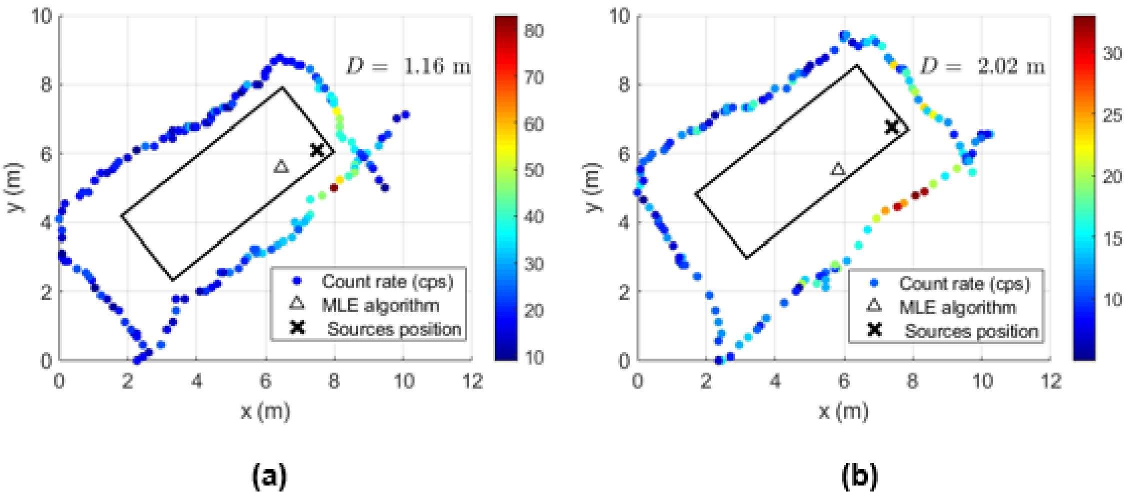

Figure 6.10: Examples of the EJ-200 scintillator gamma-ray count rate (cps) measurements obtained using the detection system integrated into the multirotor considering ^{137}Cs sources with a total activity of 4 MBq positioned at the bottom corner of the container. Multirotor paths were performed at: (a) one-third the container height. (b) half the container height [296].

Due to the storage layout of containers at seaports, typically only one or, at most, two lateral sides of most containers are available for primary inspection. Therefore, decision was made to utilize the radiation detection system integrated into the multirotor to perform single-side inspections (along the length of the container) at various heights. The registered gamma-ray counts were compared with the decision threshold (background mean + 1.645 × SD), as referred in Section 6.1.

Figures 6.11 and 6.12 show the count rates recorded during single-side inspections of the shipping container at various heights. The ^{137}Cs sources, with a total activity of 4 MBq, were positioned at the center and bottom corner of the container, respectively. The abscissa axis represents the time elapsed since the start of the container side inspection. For each source position and path height it was performed five inspections (indicated by different colors).

Despite the considerable source-detector distances (up to 3 m for the sources at the center), along with the iron shielding of the container walls and a 1-second sampling time, the ^{137}Cs sources were detectable when positioned at the center of the container in most of the measurements (Figure 6.11). Nearly all data points exceeded the decision threshold. However, for path heights of 0.86 m and 1.3 m, not all measurements triggered an alarm, indicating that probably the Minimum Detectable Activity (MDA) was reached for this inspection configuration. The MDA is influenced by factors such as the source activity, source-detector distances, mobile platform speed, and sampling time.

When the ^{137}Cs sources were placed at the bottom corner of the container[4], a high confidence detection was achieved (Figure 6.12). In this case, all inspections performed (measurement datasets) showed a significant number of points above the decision threshold. The peak observed at approximately 15 seconds, particularly noticeable in the screening conducted at one-third the container's height, corresponds to the moment when the multirotor is closest to the source during its passage.

It is important to note that if the cargo material inside the container were considered, it would result in increased attenuation of both gamma rays and neutrons, depending on the material's density and atomic number. This attenuation would reduce the counting rate measured externally and, consequently, impact both the MDA and the accuracy of radiation source localization.

[4]The ^{137}Cs sources were placed in the corner of the container, facing the inspection side.

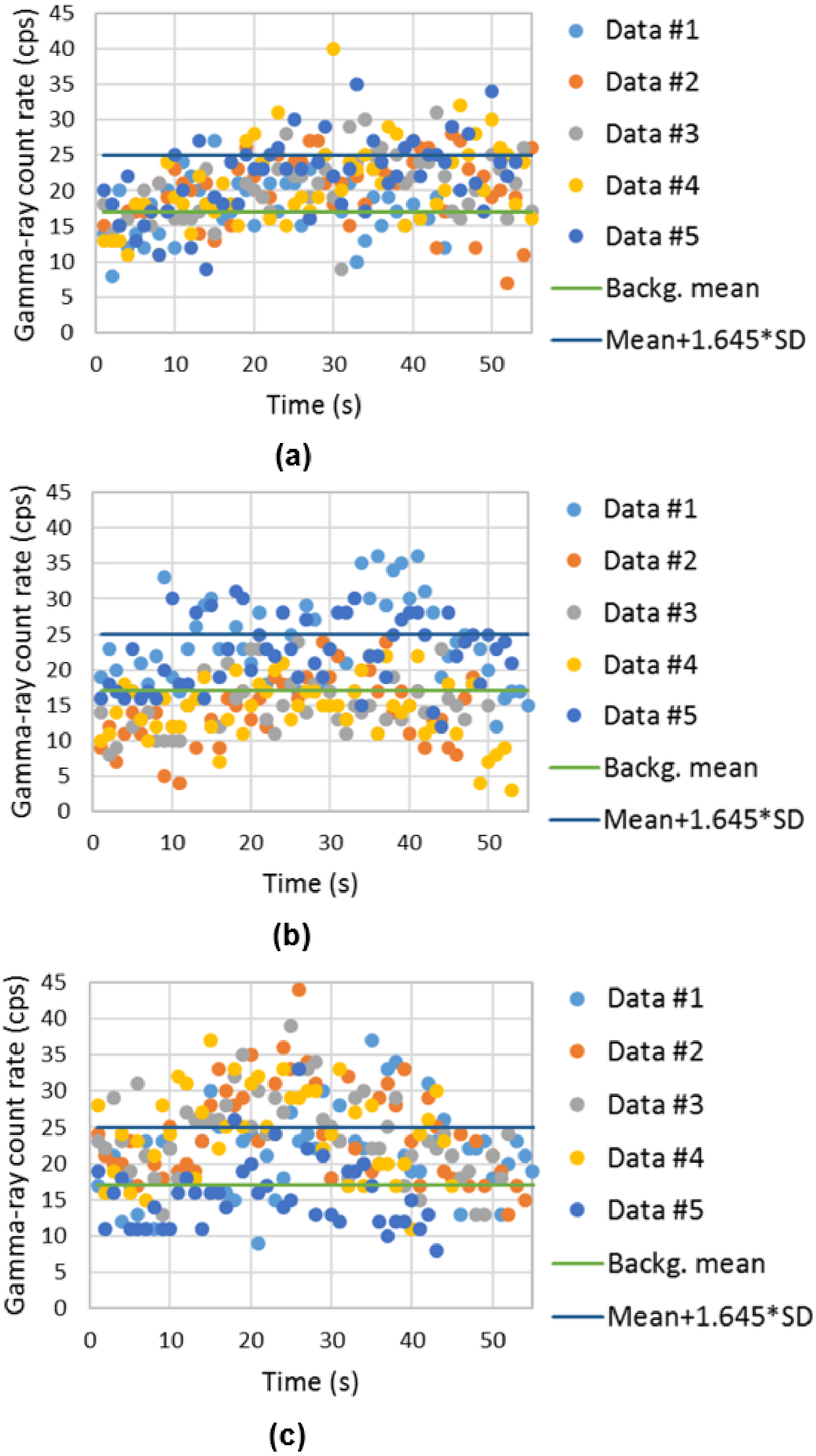

Figure 6.11: EJ-200 scintillator gamma-ray count rate (cps) measurements obtained using the detection system integrated into the multirotor considering ^{137}Cs sources with a total activity of 4 MBq positioned at the center of the container. Multirotor paths were performed at: (a) one-third the container height. (b) half the container height. (c) two-thirds the container height. The five data sets correspond to the five inspections carried out and corresponding measurements [296].

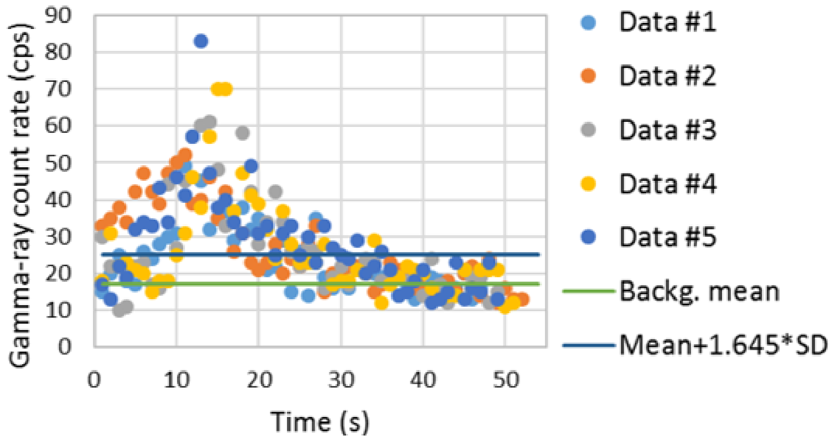

(a)

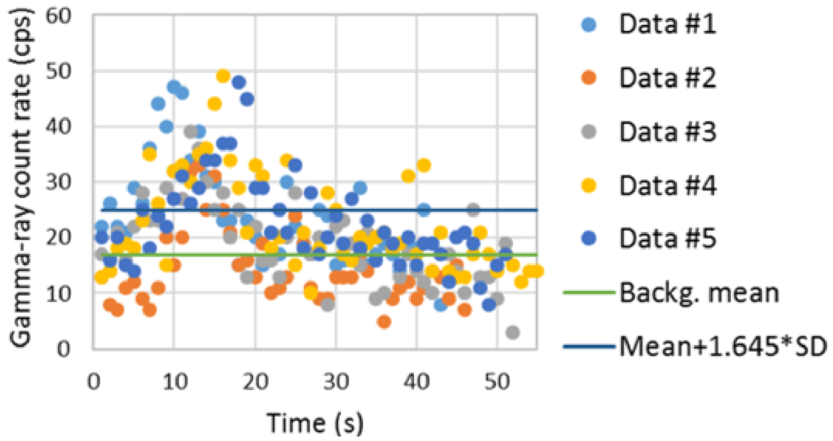

(b)

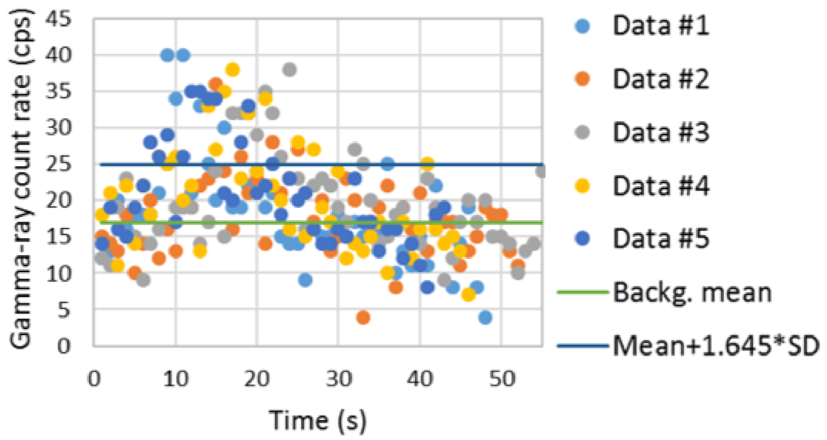

(c)

Figure 6.12: EJ-200 scintillator gamma-ray count rate (cps) measurements obtained using the detection system integrated into the multirotor considering ^{137}Cs sources with a total activity of 4 MBq positioned at the bottom corner of the container. Multirotor paths were performed at: (a) one-third the container height. (b) half the container height. (c) two-thirds the container height. The five data sets correspond to the five inspections carried out and corresponding measurements [296].

To assess the detection and localization of the $^{241}Am - Be$ source and the shielded 215 MBq ^{137}Cs source (Troxler equipment oriented 90° in the safe position), the gamma-ray count rate for full laps around the container at half its height was obtained (an example is shown in Figure 6.13). The higher gamma-ray count rate values observed in only one container side suggests that a possible gamma-ray leakage exist on the top of the Troxler equipment[5]. The asymmetric gamma-ray count rate registered around the container walls led to an estimated-to-real source distance above one meter (1.32 ±0.47 m), reinforcing that a non-uniform distribution of counts, in this case due to an uneven shielding around the source (which causes a certain degree of collimation in the source), can lead to a poorer estimation of the source's position.

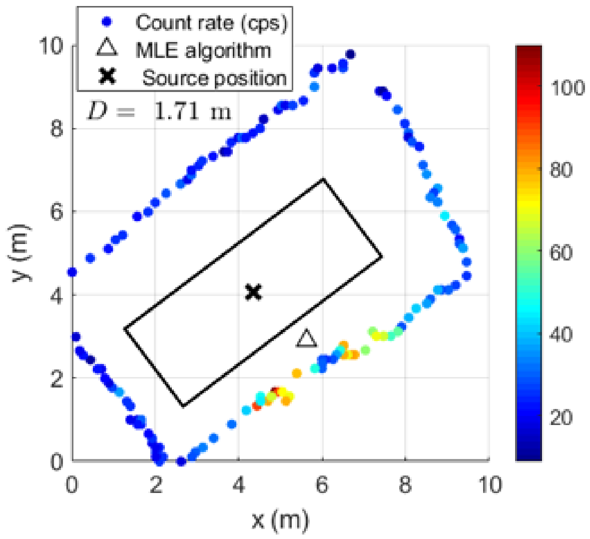

Figure 6.13: EJ-200 scintillator gamma-ray count rate (cps) measurements with detection system coupled with the multirotor considering the Troxler equipment oriented 90° (shielded 215 MBq ^{137}Cs source—safe position) in the center of the shipping container. The distance "D" between the real source position and the estimated position (MLE algorithm) is also given [296].

Figure 6.14 depicts the single-side inspection (along the length of the container) at half the container's height, with the Troxler equipment in the safe position[6]. Despite all the five inspections performed showed count rates above the decision threshold, no significant gamma-ray peak was observed. Furthermore, due to the potential for gamma attenuation by the cargo material, the Troxler equipment would likely remain undetected with a gamma-ray detection system alone. However, the simultaneous use of a neutron detection system, as discussed in Section 6.2.1, would ensure the clear detection of neutrons emitted by the $^{241}Am - Be$ source.

[5]Top of the Troxler equipment is turned in the direction of the container wall which registered higher gamma-ray count rate values.

[6]The inspection was performed in the opposite side where it was registered the gamma-ray leakage of the Troxler.

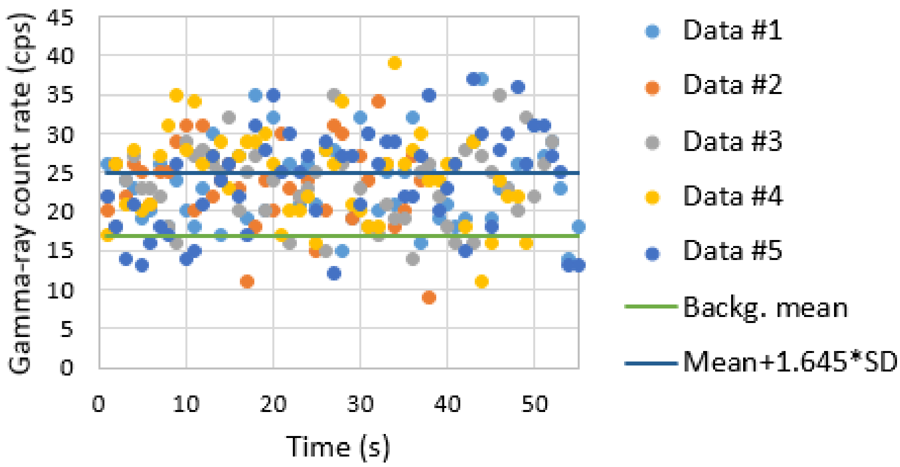

Figure 6.14: EJ-200 scintillator gamma-ray count rate (cps) measurements performed along the container length with detection system coupled with the multirotor considering the Troxler equipment oriented 90° (shielded 215 MBq ^{137}Cs source—safe position) positioned at the center of the shipping container. Multirotor path was performed at half the container height [296].

Concerning the use of the $^{241}Am - Be$ source and the unshielded 215 MBq ^{137}Cs source (Troxler equipment in the backscatter geometry), due to radiation safety reasons, only radiation measurements performed with the multirotor were considered. Figure 6.15 shows the gamma-ray count rate measured around the container at various heights. Because of the higher source activity of the 215 MBq ^{137}Cs source, in comparison to the ^{137}Cs sources with a total activity of 4 MBq, detection is feasible even when the multirotor is several meters away from the lateral wall where the collimated radiation is incident.

Since the 215 MBq ^{137}Cs source is heavily collimated by tungsten and lead shielding (on the lateral and top sides of the equipment, respectively), an asymmetric radiation distribution is obtained. Consequently, the MLE algorithm provides misleading information about the source position. The estimated-to-real source distance can reach almost 3 m (as shown in Table 6.5), exceeding the smaller internal dimension of the container (2.34 m). Examples of source localization estimation can be found in Figure 6.15.

Table 6.5: Average and SD values for the estimated-to-real source distances using the EJ-200 scintillator gamma-ray count rate measurements considering the Troxler equipment oriented 90° (collimated 215 MBq ^{137}Cs source unshielded–first notch after safe position) in the center of the shipping container [296].

Path height (m)	D (m)—Source Centered
0.86	2.96 ± 0.37
1.3	2.93 ± 0.20
1.73	2.77 ± 0.19

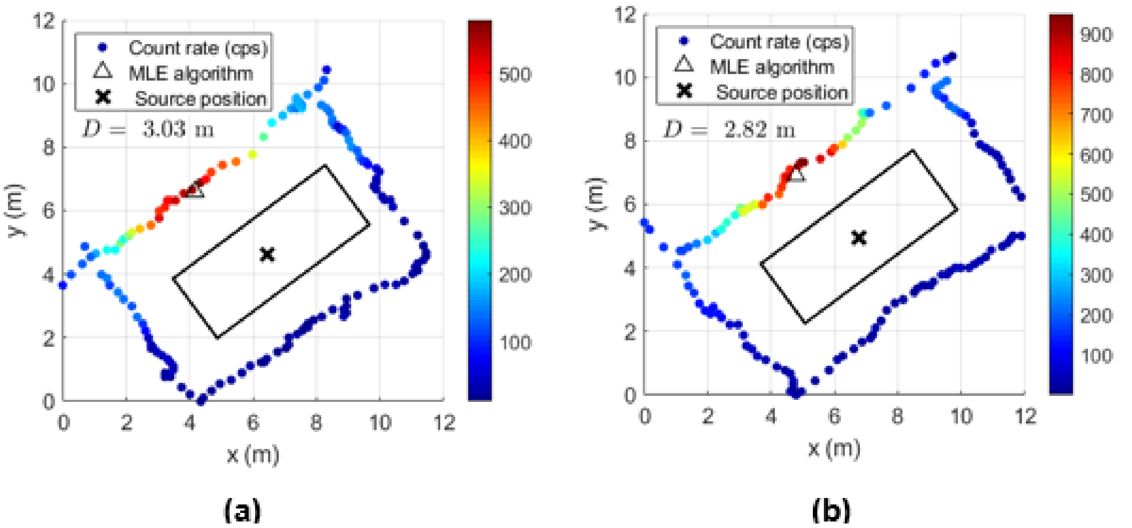

Figure 6.15: EJ-200 scintillator gamma-ray count rate (cps) measurements with detection system coupled with the multirotor considering the Troxler equipment oriented 90° (collimated 215 MBq ^{137}Cs source exposed—first notch after safe position) in the center of the shipping container. Distance “D” between the sources position and the MLE calculated position is also shown. Multirotor paths were performed at: (a) one-third the container height; and (b) half the container height [296].

The integration of georeferenced radiation data from full laps around the container obtained at different heights can yield a three-dimensional view of the shipping container inspection. Figures 6.16 and 6.17 show the gamma-ray count rate obtained in full laps for the ^{137}Cs sources with a total activity of 4 MBq and for the collimated 215 MBq ^{137}Cs source (Troxler equipment in the backscatter geometry – ^{137}Cs source unshielded) respectively. To enhance visualization of the count rate observed at different heights, different scaling was used for the z-axis compared to x and y axis.

The 3D visualization of the full laps obtained at different heights can be used to obtain a rough estimation of the source localization (top, middle or bottom, and center/corner of the container).

For the ^{137}Cs sources with 4 MBq positioned at the center of the container (top image of Figure 6.16), the slightly higher gamma-ray count rate on one lateral side compared to the opposite side at a height of 1.3 m can be attributed to several factors:

- Closer path of the multirotor to the lateral wall on a given container side(s);
- Variations in multirotor speed across different regions of the lateral wall, as maintaining an exact constant speed was not always feasible;
- Statistical fluctuations affecting the gamma-ray count rate, which is comparable to the background level.

Figure 6.17 reveals the presence of a collimated gamma-ray source and the direction of the gamma rays. This information proves invaluable for radiation experts in scenarios necessitating further analysis, such as container inspection, or for delineating a safe perimeter around the container. Additionally, the higher count rate observed on the path performed at a height of 1.3 m allows for an approximate inference of its location, likely at the center of the container.

6.3 Discussion and conclusions

The developed radiation detection system was evaluated for detecting and localizing neutron and gamma-ray sources within a 20 ft long shipping container. The system, consisting of handheld equipment and a multirotor-integrated setup, was tested with neutron and gamma-ray sources placed at different locations inside the container.

The neutron detection system effectively identified the presence and approximate location of a 1.45 GBq $^{241}Am - Be$ neutron source within the shipping container. The system detected significant increases in neutron count rates when the source was centrally located or placed at the container's bottom corner. The results indicate that inspecting at different heights can reliably determine whether a neutron source is located at the top, middle, or bottom of the container.

The gamma-ray detection system performed well in detecting and localizing the ^{137}Cs sources with a total activity of 4 MBq centrally positioned at the container. However, the localization accuracy decreased when the sources were placed in the container's corners, highlighting the limitations of the MLE algorithm used, which did not estimated the vertical position (z-coordinate) of the source. Despite these challenges, the EJ-200 scintillator detected gamma rays effectively even at distances of up to 3 m.

The inspection of the shipping container with a Troxler equipment inside and the 215 MBq ^{137}Cs source shielded, revealed asymmetries in gamma-ray distribution due to potential leakage and collimation effects. These asymmetries resulted in higher localization errors, especially when the gamma source was unshielded.

The integration of georeferenced radiation data at three different path heights enabled 3D visualization, allowing rough estimates of the source's vertical position and the direction of collimated gamma rays. This 3D view is crucial for detailed analysis and establishing safety perimeters.

The system proved effective but highlighted the need for improvements, including a 3D MLE algorithm for better localization and strategies to mitigate GNSS uncertainties during multirotor operations. Future work should aim to enhance the reliability and accuracy of the radiation detection system's positioning, particularly through improvements to the standalone GNSS receiver. Additionally, further research should explore scenarios involving shielded or collimated sources, and the system's performance should be thoroughly tested in shipping containers loaded with typical cargo materials.

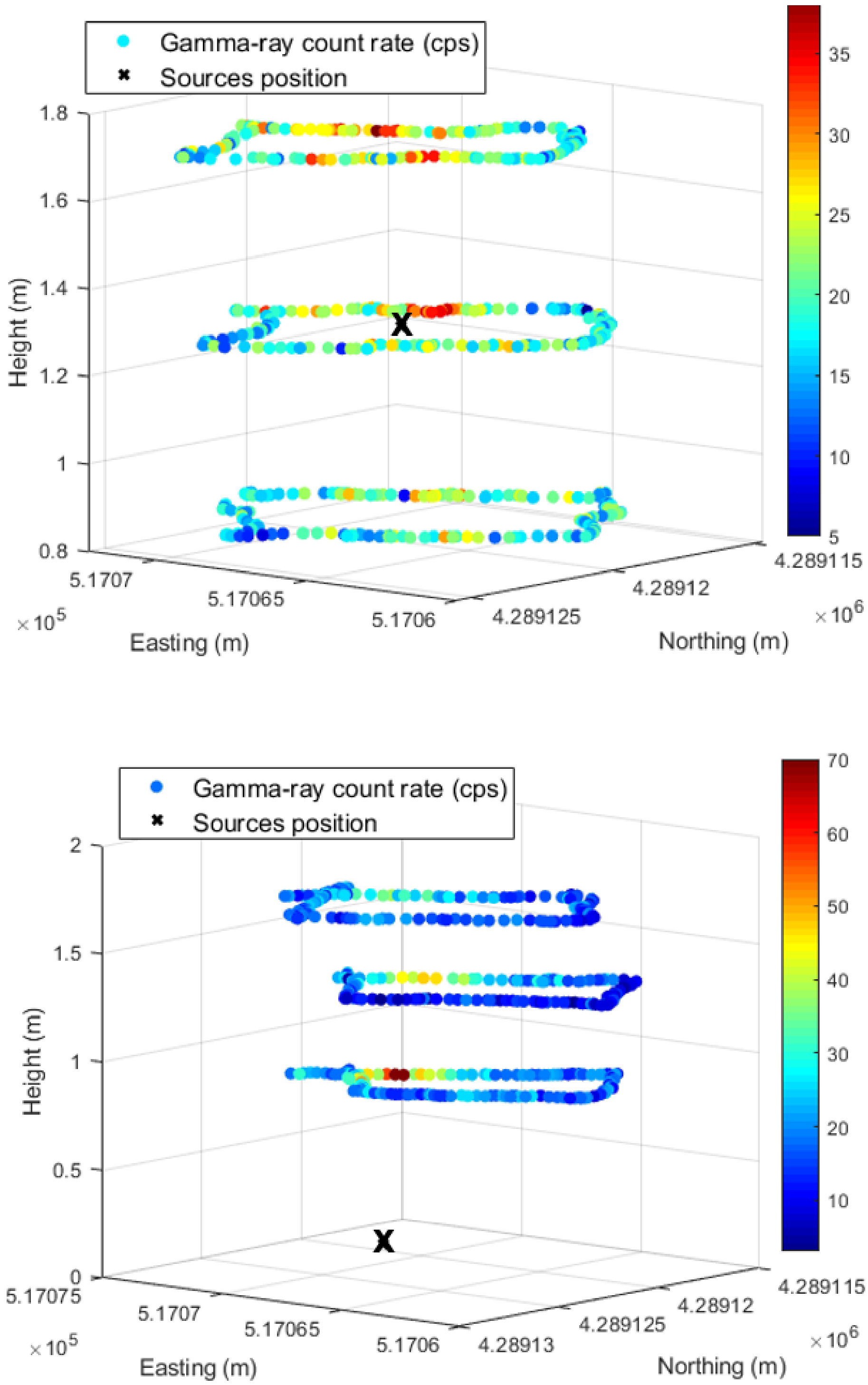

Figure 6.16: A 3D view of the EJ-200 scintillator gamma-ray count rate (cps) measurements considering the ^{137}Cs sources of 4 MBq at the center (top image) and at the bottom corner (bottom image) of the shipping container. The actual sources position is indicated by an "x" mark [296].

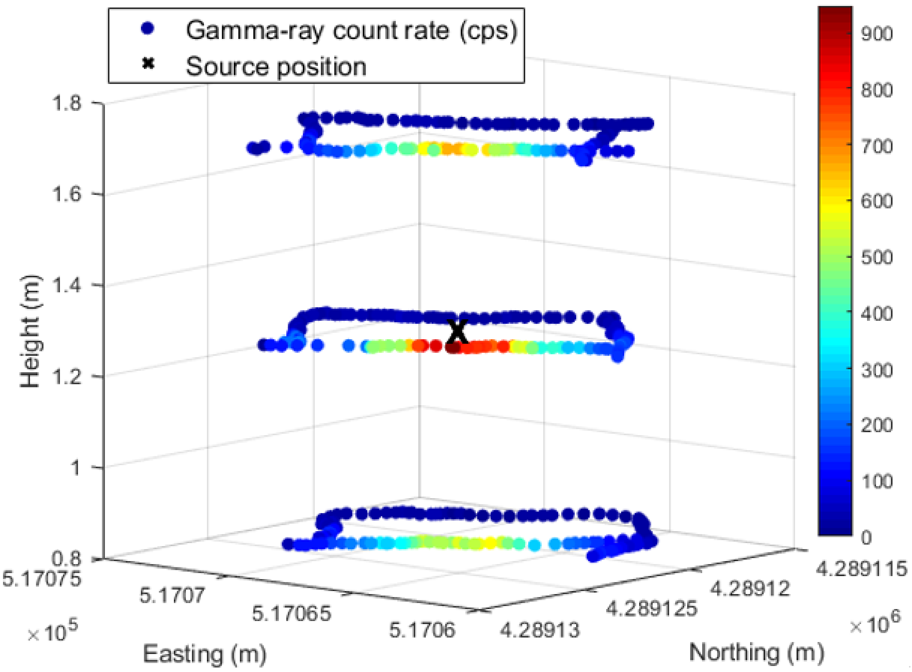

Figure 6.17: 3D view of the EJ-200 scintillator gamma-ray count rate (cps) measurements considering the Troxler equipment (collimated 215 MBq ^{137}Cs source—first notch after the safe position) at the center of the container. The actual source position is indicated by an “x” [296].

7

Gamma-ray source detection and localization – simulation

7.1 Simulator description

This Section describes the development from scratch of a computer simulator program, written in *Python* programming language, to study how the path followed by the mobile radiation detection system can improve the detection and localization of a gamma-ray source hidden inside a maritime shipping container. Various paths around the container were studied, in order to ascertain the impact of radiation detection system counts and source position estimates on the path followed (informative path planning), aiming at the improvement of the source localization accuracy.

The MLE algorithm described in Section 4.5.4 was also used to estimate the three coordinates of the source position at each radiation data point obtained during the path performed around the shipping container.

To determine optimal path adjustments for the radiation detection system, an informative path planning algorithm based on profit functions was implemented. The resulting paths were then compared with predefined paths, evaluating both source localization accuracy and path duration. The profit functions principle involves analyzing the measured data and estimated parameters (such as source position and uncertainties provided by the MLE algorithm) to determine whether to maintain the current path or alter it. The goal is to maximize the information gathered along the path, enhancing source position accuracy while minimizing the required inspection time.

This Section provides a brief overview of the simulator's functionality and assumptions, followed by a discussion of the profit functions considered in this thesis. Key concepts such as baseline, critical and detection limits, and exit conditions will also be introduced. Finally, the simulation results will be presented and analyzed.

The developed simulation environment aims at replicating the inspection of a maritime shipping container to detect and localize a gamma-ray source hidden inside the container.

This involves a mobile radiation detection system moving along one or more predefined paths at constant path height or using informative path planning to decide how and when the path height is changed in order to improve the accuracy of the source position estimation and reduce the inspection time. All paths assume a constant distance between the detector and the container walls (rectangular path around the container).

Due to their availability in field tests, ^{137}Cs sources were chosen for the simulation. The branching fraction for ^{137}Cs decays into 662 keV gamma rays is $b_r = 0.8505 \pm 0.0029$ [282]. Although other gamma-ray sources can be simulated, it is necessary to determine the intrinsic efficiency of the detector for each specific radionuclide, as they may emit gamma rays of different energies with specific branching fractions. The MLE algorithm described in Section 4.5 was considered for the source position estimation, and the cylindrical approximation was used to obtain the geometric detection efficiency of the EJ-200 plastic scintillator. The MLE algorithm and the calculation of the geometric detection efficiency run at each new position of the radiation detection system.

To calculate the radiation detection system counts at each detector position, it was first necessary to define some input parameters on the simulator, including the:

- Source position (in the center or corner of the container);
- Source activity (ranging from 3 MBq[1] to 1 GBq);
- Mobile platform speed (0.2 m/s);
- EJ-200 detector geometry (cylindrical volume, with a diameter of 11 cm and a depth of 3 cm);
- Detector integration and sampling time (1 s);
- Dimensions of the shipping container to be analyzed (standard dimensions for a 20 ft long maritime shipping container, with internal dimensions of 5.94 m (length) × 2.34 m (width) × 2.39 m (height) [301];
- Number of paths to be performed (one or two);
- Path height (1/3, 1/2 or 2/3 of the container's height);
- A detection system to container wall distance of 0.5 m (physical distance between the MRDS and the shipping container walls to avoid collision)[2];
- EJ-200 intrinsic detection efficiency equal to 0.23 (obtained experimentally);
- Background radiation, which considers a Poisson distribution with a mean value of 26 cps (obtained experimentally).

A ^{137}Cs source activity of 1 MBq positioned at the geometric center of the container was considered as an initial guess for all the simulations.

The simulator assumptions are summarized in Table 7.1.

[1] Although the simulator indicates that the ^{137}Cs source can be detected at activities as low as 1 MBq (MDA with the source placed at the center of the container), it was not possible to localize the source below 3 MBq due to high uncertainties.

[2] A shorter detector-to-container wall distance was selected compared to Section 6) (previously 1 m) to improve the gamma-ray count statistics during the upcoming container inspections in field, given the available ^{137}Cs sources with a total activity of 4 MBq.

Table 7.1: Simulator assumptions.

Scenario
- A single radioactive source inside a 20 ft long shipping container.
Path followed by the radiation detection system
- The radiation detection system performs lateral inspection to one or more sides of the shipping container at a constant speed and with a fixed safety distance to the container walls.
Radioactive source
- Point source with isotropic emission. - Gamma-ray source that emits an average number of photons according to its activity and branching fraction. - The source activity is assumed to be constant, given that the radioactive source's half-life is significantly longer than the measurement time.
Radiation detection system
- EJ-200 plastic scintillator. For calculating the geometric detection efficiency, a cylindrical volume with a diameter of 11 cm and a thickness of 3 cm was used. - The number of detected particles follows a Poisson distribution. - A radiation detection system dwell time of 1 second (acquisition time) was considered. - Gamma-ray counts are calculated on the intermediate point between time instant t and $t-1$.
Radiation attenuation and scattering
- Homogeneous media, consisting of air and iron (for the container walls) characterized by attenuation coefficients μ_{air} and μ_{iron} respectively, were considered. - It is assumed that the only obstacle between the detector and the source is the container wall. - Compton scattering and backscattering of gamma rays by the shipping container walls (shielding) were not considered.

The pseudocode of the developed simulator program, written in *Python*, is presented in Algorithm 2 in Appendix B. Figure 7.1 displays the (x,y,z) coordinates reference frame considered in the simulations and shows an example of a path followed by the radiation detection system around the shipping container at a constant height.

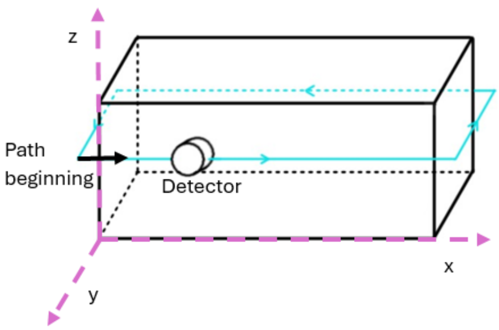

Figure 7.1: Schematic of the path followed by the radiation detection system around the container at a constant height, along with the chosen reference frame.

7.2 Informative path planning

To improve source localization accuracy and reduce inspection time, informative path planning was considered and compared with predefined paths. For informative path planning, profit functions were used to determine how and when to adjust the initially defined path. These profit functions utilize the radiation detection system data acquired during the path, as well as the source localization estimate, to modify the path and gather more information about the source position.

7.2.1 Profit functions

The profit function serves as a tool to evaluate the effectiveness of specific actions within a system, using metrics to determine whether the associated costs–in this thesis, to adjust the detection system's path during the container inspection–are advantageous. In this context, the profit function dictates when and how the MRDS should adjust its path to maximize source detection probability and enhance localization accuracy. This adaptive approach assumes that path adjustments closer to the source are more beneficial, considering parameters like increased detector counts. The goals of the profit function include: i) improving source position estimation (achieving a smaller estimated-to-actual source distance); ii) reducing the source position uncertainty (narrowing confidence intervals); and iii) minimizing the time for source detection and localization.

Therefore, to enhance gamma source detection and localization accuracy while reducing the duration of container cargo inspections, three profit functions were proposed and studied. Developed in this PhD thesis, these profit functions introduce a novel and innovative approach specifically tailored for radiological inspections. Although designed for detecting hidden radioactive sources in shipping containers, they can be adapted for the inspection of other infrastructures and vehicles. A brief description of the profit functions is as follows [302], [303]:

- ***Step* profit function.** The radiation detection system initially follows a path along the container at half the container's height with a horizontal velocity of 0.2 m/s. If, at a given moment during its path, the estimated z-component of the source position deviates from the path height, a vertical velocity component (0.1 m/s) is introduced for downward or upward movement. This adjustment allows the radiation detection system to modify its height, ensuring that it aligns with the z-component of the estimated source position;
- **Up and Down (UD) profit function.** The detection system begins its path along the container at one-third of the container's height with a horizontal velocity of 0.2 m/s. Upon detecting a gamma-ray count peak, the system halts its horizontal movement and initiates an up-and-down movement. The peaks are identified by the *FindPeak* function of *Python*, and only if the peak maximum number of counts c surpass a predefined threshold l times the baseline counts b ($c > l \times b$) the up-and-down movement is performed. This up-and-down movement is performed at a vertical velocity of 0.1 m/s and it aims at identifying a gamma-ray count peak in the vertical direction[3]. If a peak is found, the detection system resumes horizontal movement

[3]The vertical velocity of 0.1 m/s allows the detection system to acquire enough data points to accurately determine the position of the measured count peak in the vertical direction.

around the container at the peak height (as illustrated in Figure 7.2a). If another peak is detected during horizontal movement, the procedure is repeated;

- **Step + Up and Down (STUD) profit function.** The detection system starts its path at half the container's height with a horizontal velocity of 0.2 m/s. If the current number of counts c surpass a predefined threshold l times the baseline counts b ($c > l \times b$), the MRDS performs a sinusoidal path. The amplitude of this path is determined by the maximum and minimum height values specified for the container sweep, which are 20 cm above the top of the container and a minimum height of 50 cm, respectively (as illustrated in Figure 7.2b). After completing one period of sinusoidal movement, the MRDS resumes its forward path until it reaches another face of the container, at which point the process is repeated [303].

While the *Step* profit function relies on the estimated z coordinate of the radioactive source (source height) at each instance to adjust the height of the radiation detection system's path, aligning the path height with the estimated source height, the UD and STUD profit functions directly depend on the gamma-ray counts recorded at each instance to determine whether to modify the previous path.

The baseline b, considered for the UD and STUD profit functions, is defined as the average number of counts obtained by the detector when stationary for a specific time at an initial distance from the source (or the container if the source is closest to the detector). This criterion ensures that the MRDS alters its path only when in proximity to the source, optimizing the search. The value of l varies depending on the profit function and the application, tailored to the type of source being targeted (considering the activity interval). The baseline count b is obtained during a 5-second interval at a distance of 2.5 m from the shipping container before the inspection takes place. Predefined thresholds l of 2.5 and 4 were considered for the UD and STUD profit functions respectively. These threshold values ensure that the *up and down* movement (for the UD profit function) and the sinusoidal movement (for the STUD profit function) are initiated in the right timing, and were optimized for the source activity range considered in this thesis (between 3 MBq and 1 GBq).

The pseudocodes for the UD and STUD profit function algorithms are detailed in Algorithms 3 and 4, respectively, in Appendix B.

Figure 7.2 illustrates the UD and STUD profit functions functioning.

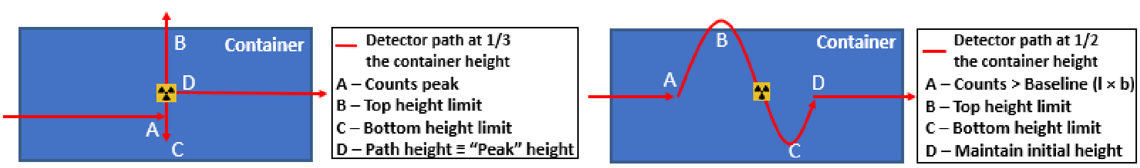

(a) UD profit function.

(b) STUD profit function.

Figure 7.2: Informative path planning based on: a UD profit function (left image) and a STUD profit function (right image) [303].

Figure 7.3 illustrates the source search algorithm functioning using an informative path planning based on a profit function. During the radiation detection system movement around the container, the developed simulator calculates the count rates registered in the detector and provides this information and the corresponding detector positions to the MLE algorithm. With this information the MLE algorithm estimates the source position coordinates and the confidence intervals (using the Fisher information). The MLE algorithm only initiates the source position estimation after at least four radiation data points exceed the decision threshold, which is defined by the critical level L_c [300]:

$$L_c = 1.645\sqrt{2{s^2}_B} = 2.33s_B\,, \tag{7.1}$$

where s_B is the standard deviation of the background counts.

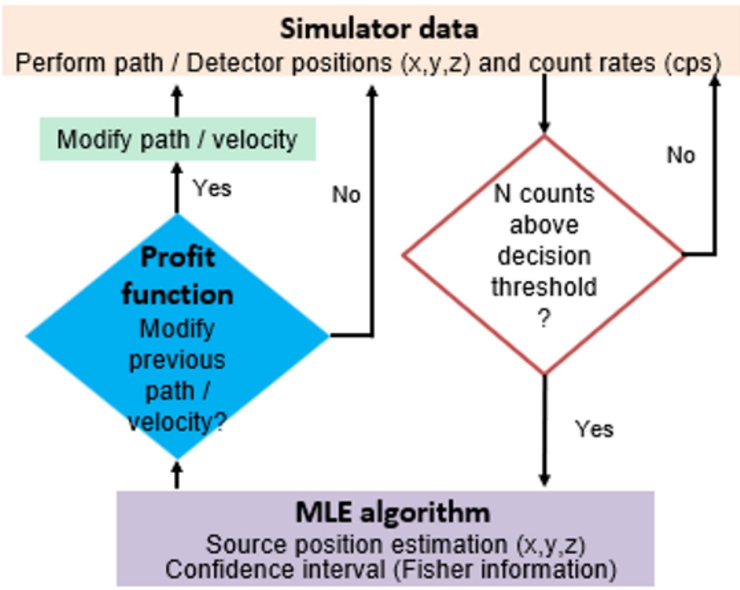

Figure 7.3: Schematic diagram of the source search algorithm using an informative path planning based in a profit function [302].

7.2.2 Exit condition

When containers are awaiting shipment at a seaport, they are typically stacked in large clusters, limiting access for primary inspection by MRDS to only one or two sides of each container.

If an RPM initially triggers an alarm, the MRDS can be deployed for a secondary inspection to confirm the presence of a radioactive source. In such cases, where all sides of the container may be accessible, a swift inspection becomes essential to minimize disruptions to the normal flow of containers and reduce the associated costs–particularly in large seaports, where delays can have significant economic impacts.

To reduce the inspection time of the container(s), an exit condition was implemented in the informative path planning algorithm. This exit condition allows for obtaining the distance d between the estimated and the actual source positions as soon as the required accuracy of the source position estimation is achieved. For comparison purposes, the final estimated-to-actual source distance d_F, obtained after the radiation detection system completes a full lap around the container, will also be presented.

Thus, the exit condition ensures the algorithm successfully detects and localizes the source within the shipping container with the required accuracy and is contingent upon meeting the following criteria [303]:

1. The average net counts that surpass the critical level L_C (given by (7.1)) must be above the detection limit L_D given by (7.2), which ensures a 95% confidence that a radioactive source has been detected [300]. This allows to exclude possible statistical fluctuations originated by the background radiation and detector counts uncertainty[4];
$$L_D = 3 + 4.65 s_B \tag{7.2}$$
2. The confidence intervals for each estimated source position coordinate x, y and z must be within 10% of the smallest dimension of the analyzed container;
3. The Mean Squared Deviation (MSD) values for the uncertainties in each source position parameter must not deviate by more than 10% from the values established for criterion 2.

Criterion 1 establishes the minimum requirement for calculating the source position estimate, while criteria 2 and 3 are used to ensure minimal uncertainty in the estimated source coordinates and to verify convergence between successive estimations, respectively.

The flowchart of Figure 7.4 illustrates the proposed source search method, which is valid for both simulated data and experimental measurements. At the end of the source search some important outputs can be obtained: i) the source presence confirmation; ii) the estimated source position and the corresponding confidence intervals; and iii) the MRDS path adjustment parameters if using informative path planning. These path adjustment parameters can then be sent to a mobile platform operator or directly to an unmanned vehicle, allowing for semi-autonomous or fully autonomous source search.

7.3 Simulation data results

The simulation data presented in this Section is important to study the impact of the radiation detection system path in the source localization accuracy and inspection time.

Three profit functions were proposed for the informative path planning, and the results were compared with predefined paths.

[4]The effect of the uncertainties (detector counts and detection system position) on the source localization accuracy will be considered in the subsection 7.3.2.2.

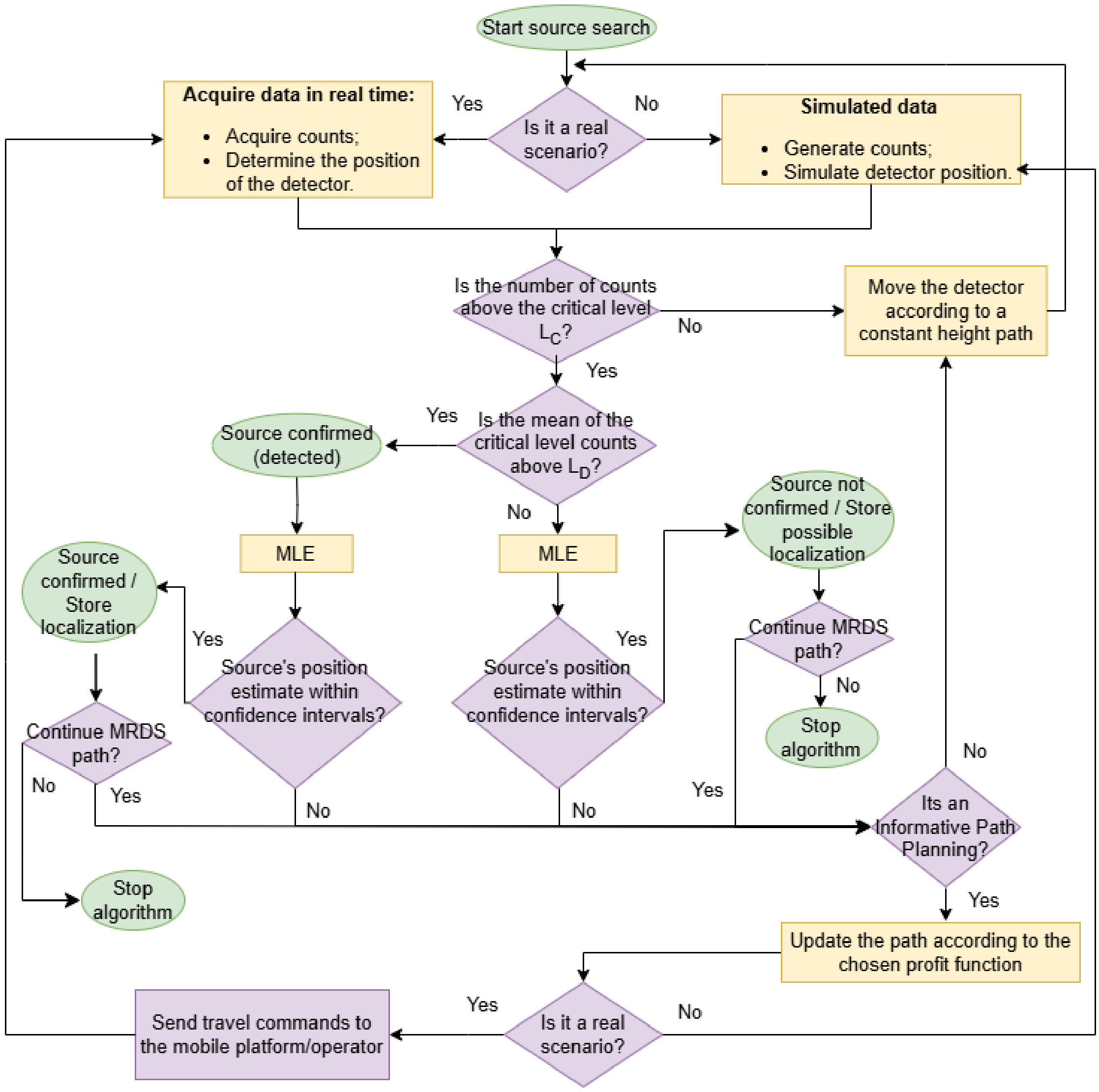

Figure 7.4: Flowchart summarizing the proposed radioactive source search [303].

The influence of the uncertainty of some parameters on the estimation of the source's position will also be analyzed, namely the:

- **Background radiation variation.** A random number following a Poisson distribution, with an average value of 26 counts (value obtained experimentally) was considered;
- **Detector position uncertainty.** A random number within the range f, where f represents the considered uncertainty, has been added to the x, y and z positions of the detector;
- **Detector counts uncertainty.** A random number following a Poisson distribution, with a mean value equal to the detector counts calculated by the simulator.

The results will consider different source activities and the effect of the exit condition on the source localization accuracy and inspection time.

7.3.1 Informative path planning – *Step* profit function vs *Up and Down* profit function

Due to the significant difference in the informative path planning based on the *Step* and UD profit functions, the benefits and drawbacks of their operating principles will be analyzed. As was described in Section 7.2.1 the *Step* profit function relies on the source z-coordinate estimate obtained at each MLE algorithm iteration to decide whether to change the radiation detection system path, while the UD profit function (as well as the STUD profit function) depends on the gamma-ray counts obtained at each radiation data point to decide a path change. The results obtained with the *Step* and UD profit functions will be compared with one or two predefined paths performed around the shipping container.

In these simulations only background variation and a 4 MBq ^{137}Cs source placed at the center and at the corner of the container were considered. This ^{137}Cs source has the same source activity as the source considered in the experimental tests described in Chapter 6. To account for statistical variations due to background fluctuations (Poisson distribution), five complete simulations were performed for each path and source position considered.

The source position estimation was first obtained for predefined paths, considering one or two full laps around the container at different heights (no exit condition was considered). The single lap was conducted at one-third of the container's height, while the double lap was performed at one-third and two-thirds of the container's height.

Tables 7.2 and 7.3 summarize the estimated mean values for the source position coordinates considering single or double predefined paths respectively. According to Table 7.3, the z-component estimation of the source position improves with two full laps compared to a single full lap (as shown in Table 7.2), as the latter lacks information along the z-axis. However, two laps take twice as long compared to a single path inspection (206 s vs. 103 s). Therefore, to reduce the inspection time, the improvement in the information gathered by the detection system during a single path inspection is essential [302].

Table 7.2: Simulated values for a single path (one-third the container height) around the container – Predefined path [302].

Estimated parameters	Source at the center[a]	Source at the corner[b]
x (m)	2.97 ± 0.02	0.13 ± 0.01
y (m)	-1.17 ± 0.01	-0.14 ± 0.01
z (m)	0.80 ± 0.05	0.80 ± 0.02
d (m)	0.395 ± 0.05	0.70 ± 0.02

[a](x=2.97 m, y=-1.17 m, z=1.195 m). [b](x=0.1 m, y=-0.1 m, z=0.1 m).

Table 7.3: Simulated values for two paths (one-third and two-thirds the container height) around the container – Predefined paths [302].

Estimated parameters	Source at the center[a]	Source at the corner[b]
x (m)	2.97 ± 0.01	0.13 ± 0.01
y (m)	-1.17 ± 0.01	-0.13 ± 0.01
z (m)	1.20 ± 0.05	0.19 ± 0.01
d (m)	0.01 ± 0.05	0.10 ± 0.01

[a](x=2.97 m, y=-1.17 m, z=1.195 m). [b](x=0.1 m, y=-0.1 m, z=0.1 m).

Figure 7.5 illustrates examples of predefined paths performing a single lap and a double lap.

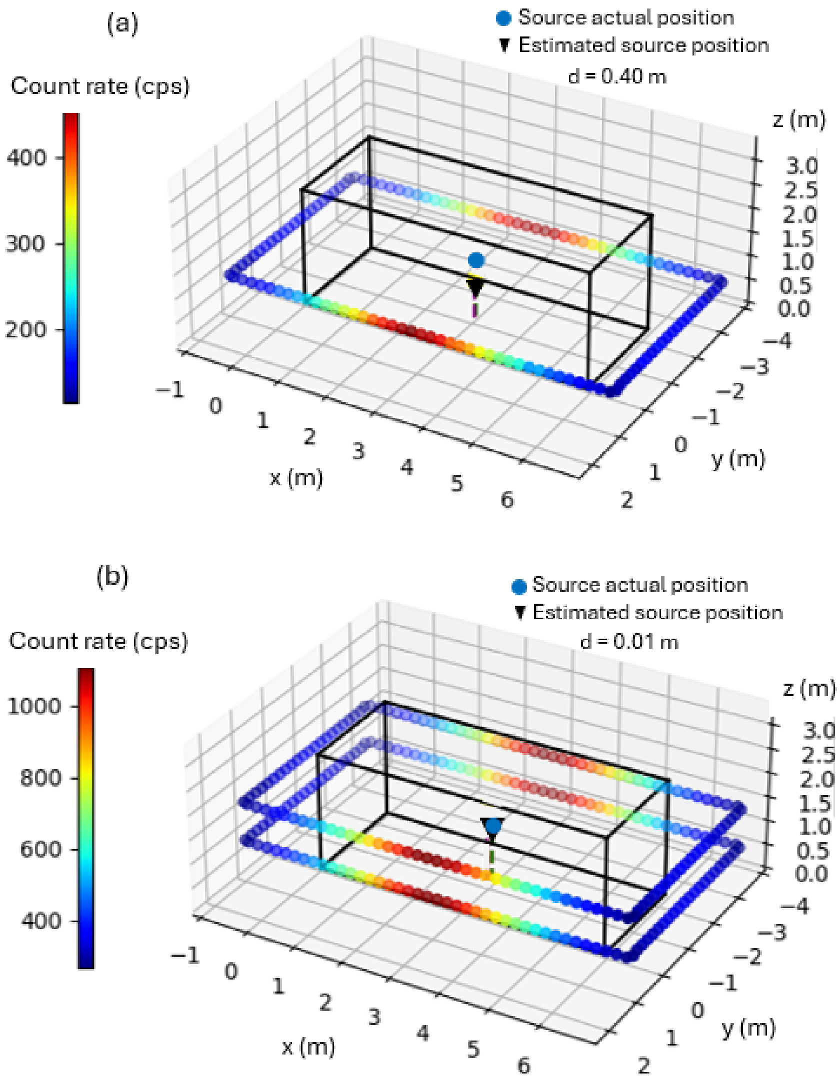

Figure 7.5: Simulation data for the gamma-ray count rate considering a 4 MBq ^{137}Cs source at the container center using: (**a**) a single predefined path; (**b**) two predefined paths [302].

Tables 7.4 and 7.5 displays the estimated mean values for the source position coordinates considering the informative path planning based on the *step* and UD profit functions respectively.

Table 7.4: Simulated values for a *step* profit function path [302].

Estimated parameters	Source at the center[a]	Source at the corner[b]
x (m)	2.98 ± 0.02	0.15 ± 0.01
y (m)	-1.17 ± 0.01	-0.16 ± 0.01
z (m)	1.25 ± 0.03	0.53 ± 0.01
d (m)	0.06 ± 0.03	0.44 ± 0.01

[a](x=2.97 m, y=-1.17 m, z=1.195 m). [b](x=0.1 m, y=-0.1 m, z=0.1 m).

Table 7.5: Simulated values for a UD profit function path [302].

Estimated parameters	Source at the center[a]	Source at the corner[b]
x (m)	2.97 ± 0.02	0.12 ± 0.01
y (m)	-1.18 ± 0.01	-0.13 ± 0.01
z (m)	1.22 ± 0.03	0.22 ± 0.01
d (m)	0.03 ± 0.03	0.13 ± 0.01

[a](x=2.97 m, y=-1.17 m, z=1.195 m). [b](x=0.1 m, y=-0.1 m, z=0.1 m).

Using the informative path planning based on the *Step* profit function, the detection system maintains a constant velocity around the container, resulting in the same inspection time as the single predefined path (103 s). In contrast, when using the UD profit function the path takes 137 s for a source placed at the center and 145 s for a source placed at the corner of the container. The longer path duration of the UD profit function is due to the system stopping at gamma-ray count peak positions to vertically scan the z-axis. Despite the longer time required by the UD profit function path, it significantly improved the source position estimation (lower distance d and an estimated z-component closer to the actual source z-coordinate) compared to a single predefined path and the path based on the *Step* profit function.

Although two predefined paths yielded the best source position estimation, informative path planning based on the UD profit function achieved a high accuracy in source position estimation, completing the inspection in less time (approximately one minute less for the source placed at the center and 20 s less for the source placed at the corner).

While the *Step* function is faster than the UD profit function, implementing it practically on a mobile platform may result in numerous unnecessary movements. This is because it relies solely on source position estimates at a given instance, rather than considering the gamma-ray counts registered at each moment. Consequently, the z component estimations of the source position can vary significantly from one point to another, potentially causing the detection system movement to be out of step and eventually miss positions with more information (higher counts).

Figures 7.6 and 7.7 shows some examples of informative path planning based on the *Step* and UD profit functions respectively.

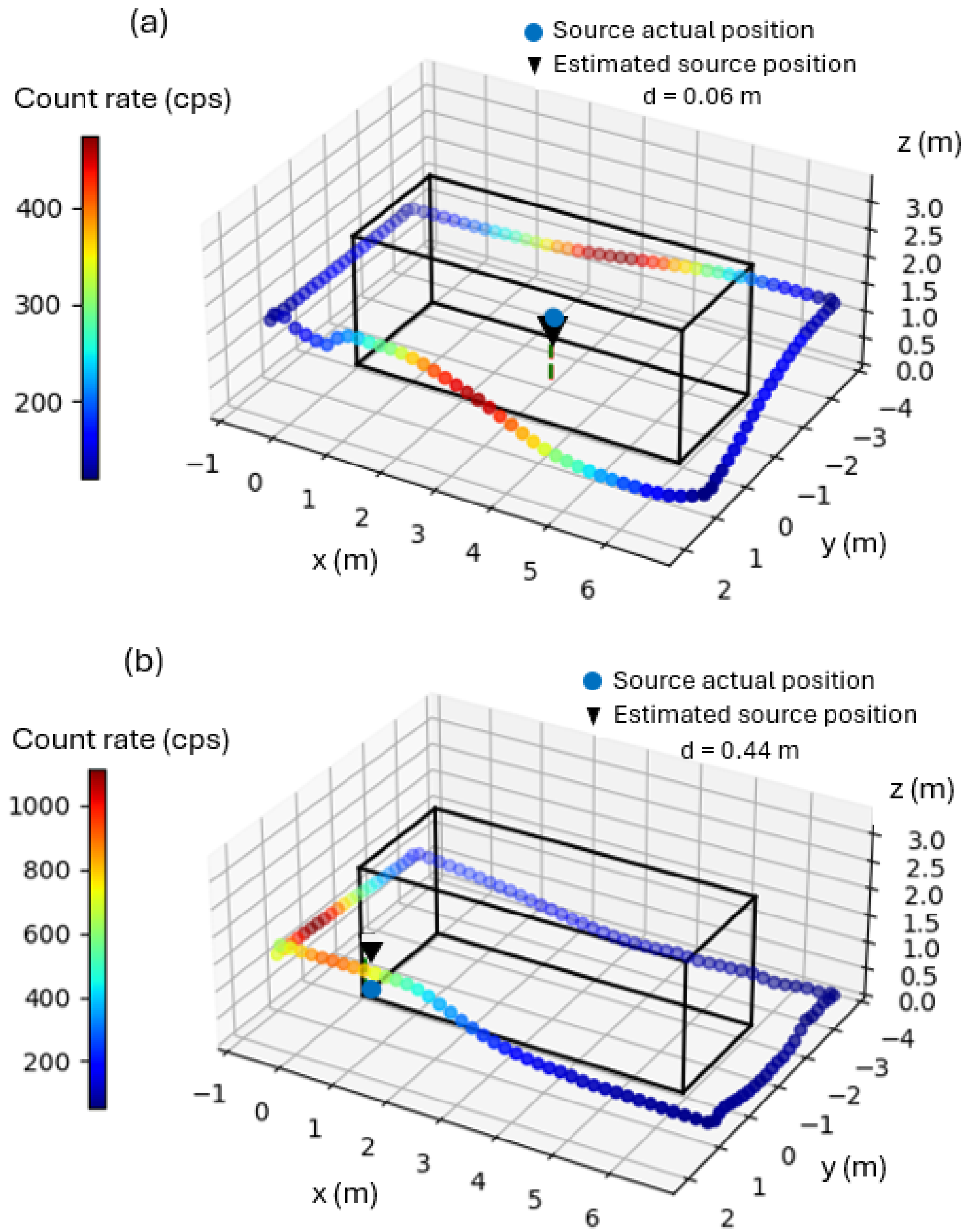

Figure 7.6: Simulation data for the gamma-ray count rate considering a path based on a *Step* profit function and a 4 MBq ^{137}Cs source positioned at the: (**a**) container center; (**b**) bottom left corner of the container [302].

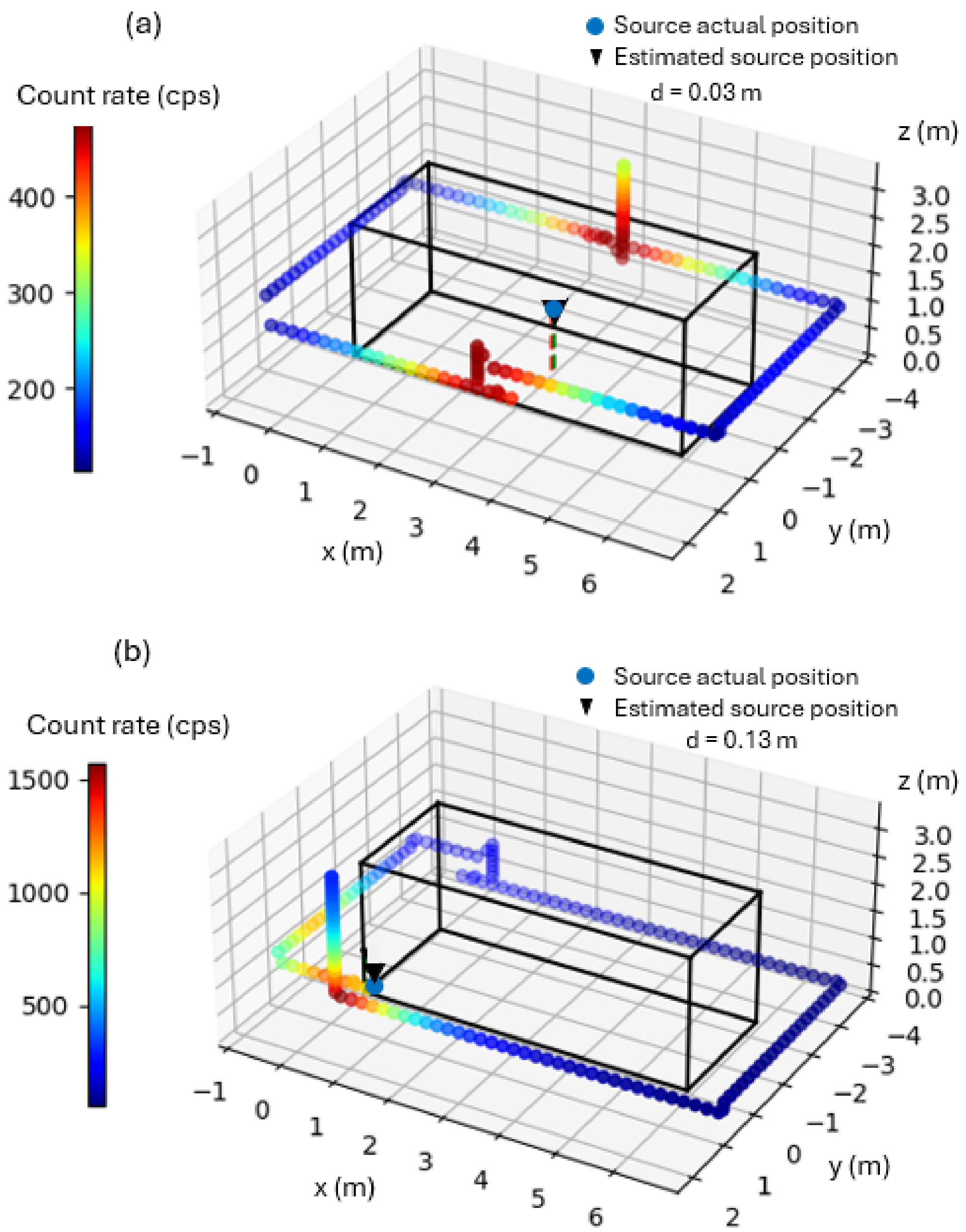

Figure 7.7: Simulation data for the gamma-ray count rate considering a path based on a UD profit function and a 4 MBq ^{137}Cs source positioned at the: (**a**) container center; (**b**) bottom left corner of the container [302].

7.3.2 Informative path planning – *Up and Down* profit function vs *STUD* profit function

To optimize both the accuracy of source position estimation and inspection time, a third informative path planning method based on a STUD profit function will be analyzed in this Section and compared with both the UD profit function and a single predefined path (at one-third the container height). An exit condition will also be introduced to obtain the source position estimation with the required accuracy before completing the full lap, thereby reducing inspection time. Different uncertainties in the radiation detection position and detector counts will be considered to analyse their impact on the accuracy of the source position estimation and on the inspection time. Additionally, a wider range of source activities and positions within the container will be examined. To mitigate the impact of statistical fluctuations arising from the uncertainties considered, 100 simulations will be conducted for each case.

7.3.2.1 Estimated-to-actual source distance and path duration

The simulation results, summarizing the average values obtained for the estimated-to-actual source distance d (after exit condition is accomplished) and d_F (after full lap), as well as the time required for radiation source localization t (until reaching exit condition) and t_F (full lap) along different paths, are presented in Figure 7.8 for the ^{137}Cs source positioned at the center of the container. The average values shown refer to the 100 simulations carried out for each type of path in order to take into account the statistical fluctuations of the background variation. Error bars on distance and time represent the standard deviations of the 100 simulations performed. These results consider source activities of 3 MBq[5], 4 MBq (source activity used in the experimental tests described in Section 6), 10 MBq, 100 MBq and 1000 MBq (1 GBq). The comparison includes predefined paths and paths based on UD and STUD profit functions (informative path planning).

The key results for the estimated-to-actual source distances and path times, considering the source centered in the shipping container (as seen in Figure 7.8), can be summarized as follows:

- Figures 7.8a and 7.8b clearly show that informative path planning significantly improved source position estimation, with average estimated-to-actual source distances below 0.3 m. Additionally, informative path planning with an exit condition yields very accurate distance d results, indicating that no significant gain in accuracy is achieved by completing the entire lap. In contrast, predefined paths require complete laps around the container to achieve significantly lower estimated-to-actual source distances (d vs. d_F values);
- Although the UD profit function achieves slightly better d distances compared to the STUD profit function, UD profit function-based paths take significantly longer due to the need to stop horizontal movement to perform a z-scan. Consequently, STUD profit function-based paths are more time-efficient;
- Despite predefined paths yielded lower distances d for activities of 3 MBq and 4 MBq compared to 10^7 Bq (as seen in Figure 7.8a), the significantly higher uncertainties prevent any definitive conclusions about a reduction in distance d at lower activity levels;

[5]Minimum source activity to obtain a source localization using this setup and the MLE algorithm.

- For the UD profit function, t_F values are significantly higher for source activities of 10^8 Bq and 10^9 Bq compared to lower activities (as shown in Figure 7.8d). This is because higher source activities trigger four vertical scans during full lap inspection—one for each side of the container—whereas lower source activities only prompt two vertical scans (on the long sides of the container).

For the source placed at the bottom right of the container (as shown in Figures 7.9a and 7.9b), the informative path planning combined with the exit condition allowed to obtain better or similar accuracy in the source localization for sources with 10^7 Bq or less, than considering the full lap. For source activities of 10^8 Bq and 10^9 Bq a little improvement in the source localization accuracy occurs for the informative path planning using full lap. In contrast, for predefined paths and for sources with 10^7 Bq or less a significant improvement exist when performing full laps, while for the higher source activities the distance increases for full laps. However, the significantly higher uncertainties for the distances d and d_F prevent any definitive conclusions about the increase/decrease of the distance with or without exit condition for the predefined paths. The STUD profit function-based paths continue to be more time-efficient than predefined paths (for t, and equal t_F values) and UD profit function-based paths (for both t and t_F), as seen in Figures 7.9c and 7.9d.

The situation where the source is placed in the bottom left corner of the container was also analyzed (as shown in Figure 7.10). In this case, since the source is very close to the starting point of the path, the sinusoidal movement begins very close to the position of the source, causing the detection system to move away from the source as it passes it, thus losing some significant counts, as shown in Figure 7.11 for a source of 4 MBq. This issue is more pronounced for sources with low activity (3 and 4 MBq), where the distance values d and d_F are significantly greater than those obtained for the right bottom corner. One way to mitigate this, and improve the accuracy of the source's location, is to move the path beginning point further back from the container, from the current value of 0.5 m to 1.5 m backward. This adjustment ensures that the STUD profit function's path as the necessary number of points to begin effectively.

Some examples of simulation data output are shown in Figure 7.12, obtained with a 4 MBq ^{137}Cs source (activity equal to the one considered in Section 6) positioned at the center and at the corner of the container, considering predefined and informative path planning. Interestingly, for UD and STUD profit functions-based paths, the final estimated-to-actual source distance d_F typically exceeds the estimated-to-actual source distance d achieved when the exit condition is met. This contrasts with the results from predefined paths.

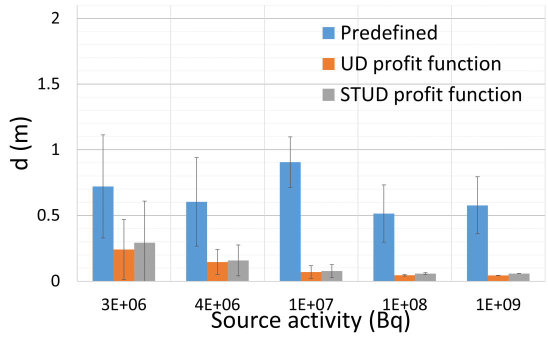

(a)

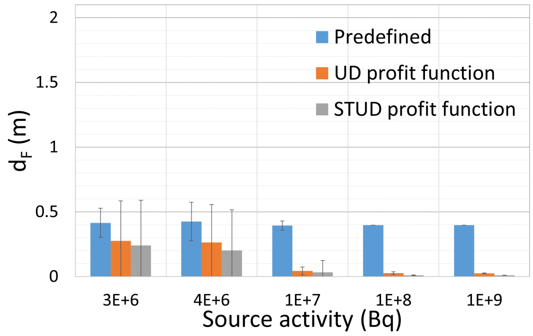

(b)

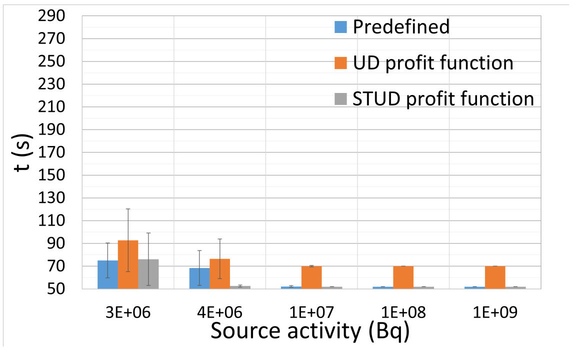

(c)

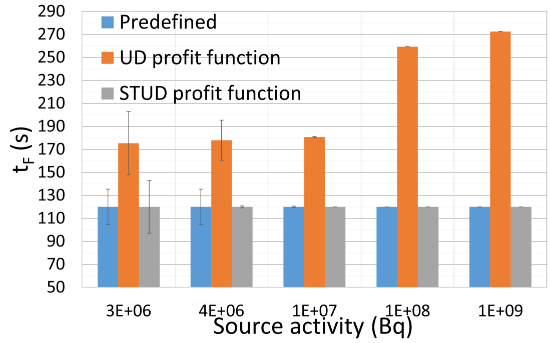

(d)

Figure 7.8: Estimated-to-actual distances and path time duration using predefined paths and informative path planning, considering a ^{137}Cs source with different activities placed at the center of the shipping container.

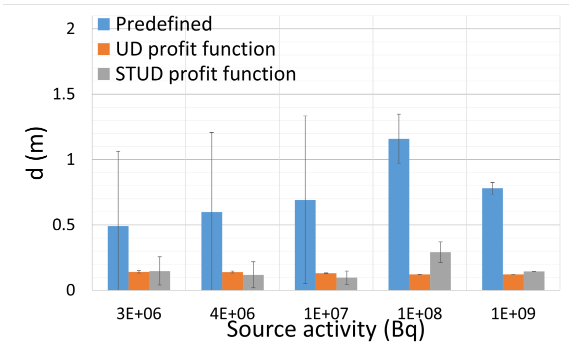

(a)

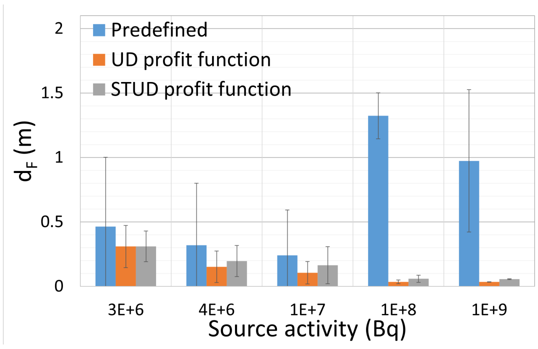

(b)

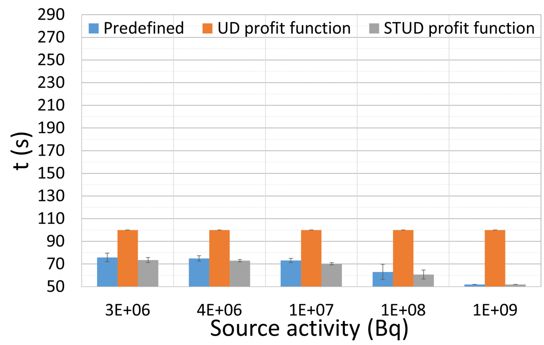

(c)

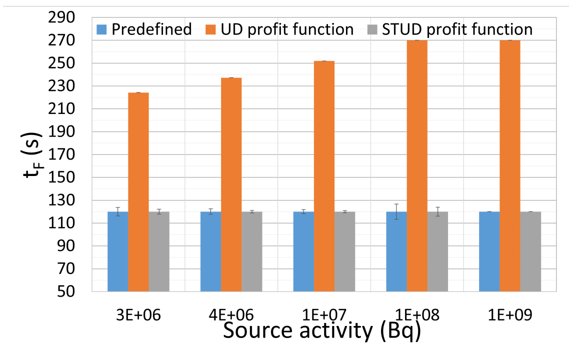

(d)

Figure 7.9: Estimated-to-actual distances and path time duration using predefined paths and informative path planning, considering a ^{137}Cs source with different activities placed at the bottom right corner of the shipping container.

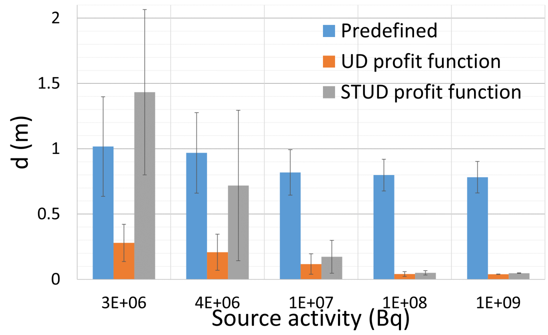

(a)

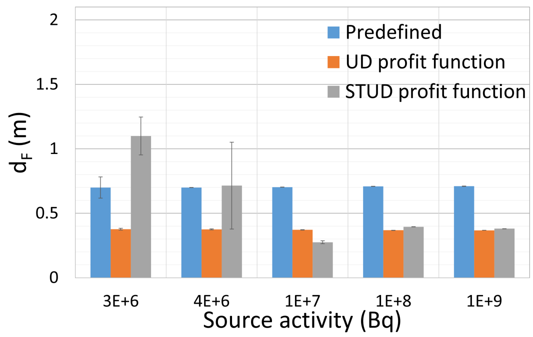

(b)

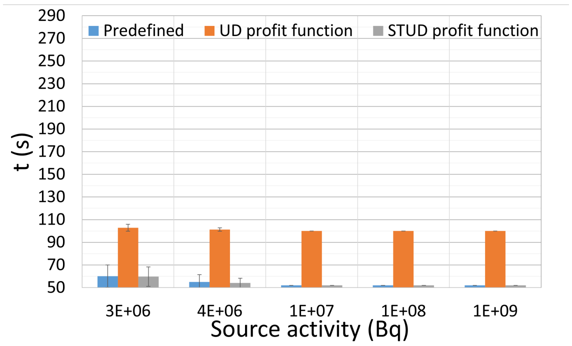

(c)

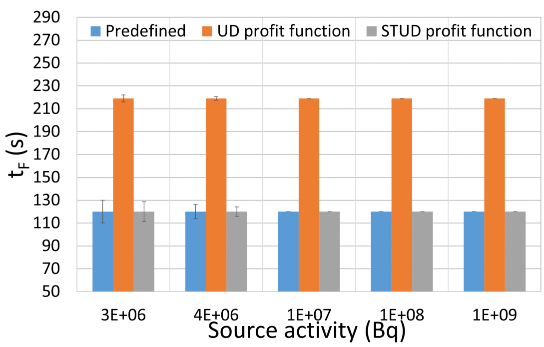

(d)

Figure 7.10: Estimated-to-actual distances and path time duration using predefined paths and informative path planning, considering a ^{137}Cs source with different activities placed at the bottom left corner of the shipping container.

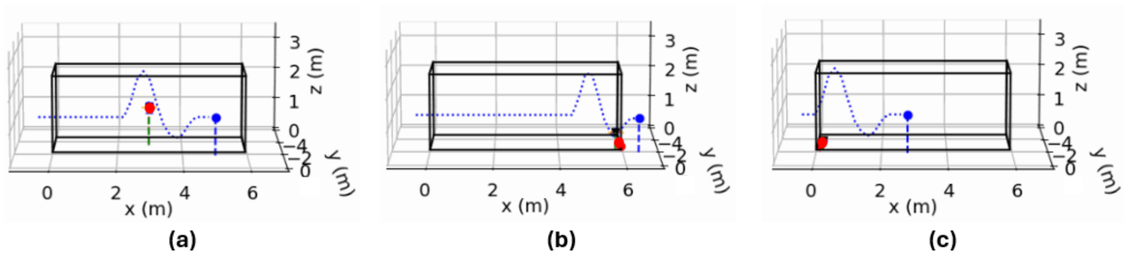

Figure 7.11: STUD profit function based path considering a 4 MBq ^{137}Cs source positioned at: (**a**) Center of the container. (**b**) Right bottom corner of the container. (**c**) Left bottom corner of the container.

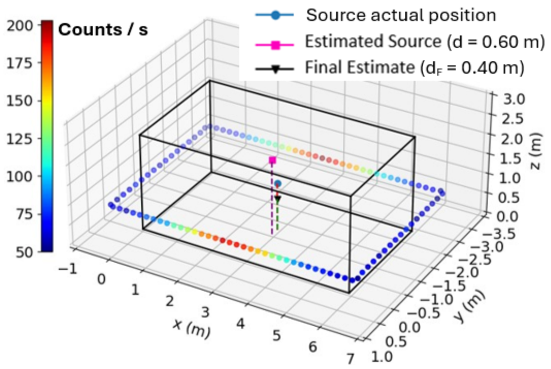

(a) Predefined path (source centered).

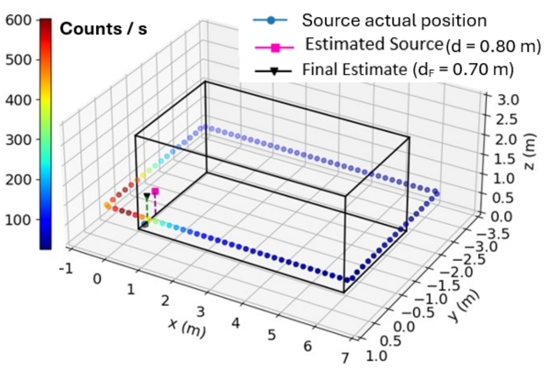

(b) Predefined path (source at corner).

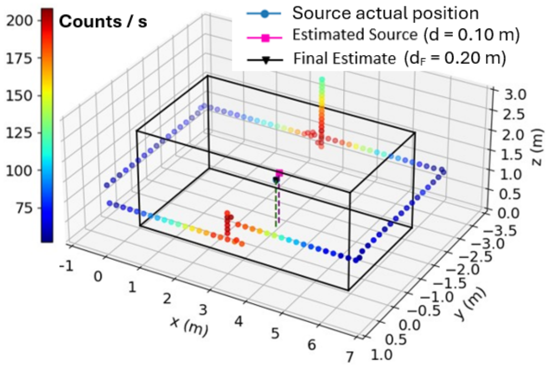

(c) UD-based path (source centered).

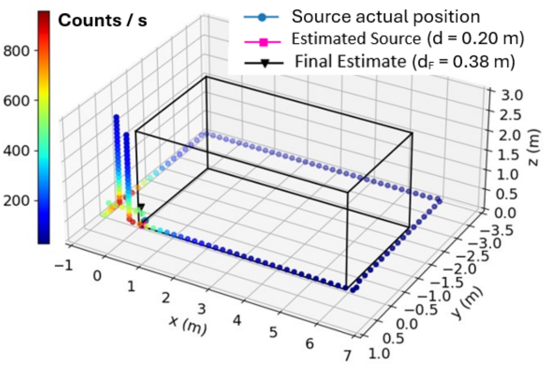

(d) UD-based path (source at corner).

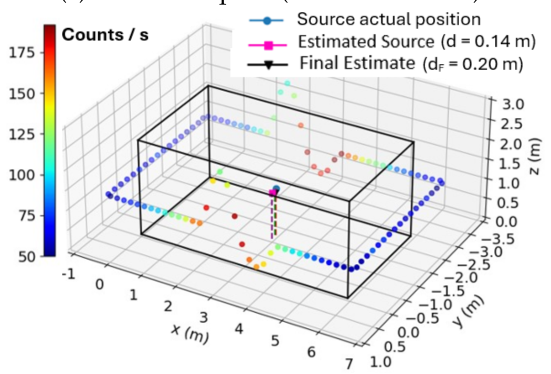

(e) STUD-based path (source centered).

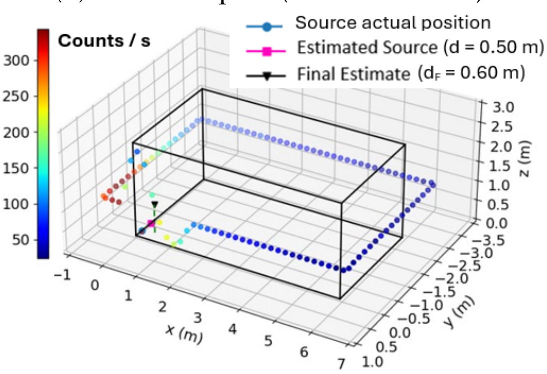

(f) STUD-based path (source at corner).

Figure 7.12: Localization of a 4 MBq ^{137}Cs source placed at the center and corner of a shipping container using predefined paths and informative path planning [303].

7.3.2.2 Uncertainties on the detector position and counts

Table 7.6 summarizes the various combinations of uncertainties considered in this thesis to analyze the impact of detector position uncertainty and detector count uncertainty on the accuracy of the source localization.

Table 7.6: Combinations of uncertainties considered in the simulations: detector position uncertainty ("UP") and detector count uncertainty ("UC"). Background variation modeled by a Poisson distribution.

Uncertainties	Description
UP none; UC none	No uncertainties considered
UP none; UC yes	Only uncertainty in the detector counts
UP 0.1 m; UC yes	Detector position uncertainty of ±0.1 m and detector counts uncertainty
UP 0.25 m; UC yes	Detector position uncertainty of ±0.25 m and detector counts uncertainty
UP 0.5 m; UC yes	Detector position uncertainty of ±0.5 m and detector counts uncertainty

The chosen uncertainty values for the detector's position were based on the following rationale: A maximum uncertainty of 0.5 m was selected because it matches the distance between the detection system and the container walls. An uncertainty exceeding this value would suggest that the detector's position could be inside the container, which is unrealistic. Therefore, 0.5 m is the maximum allowable uncertainty. Intermediate and minimum uncertainties were set at 0.25 m and 0.1 m, respectively, to provide a range of potential scenarios.

Figure 7.13 summarizes the simulation results of the estimated-to-actual distances d considering different uncertainties and varying the path type and the source position.

The difference in the results between the path types lies primarily in their response to detector position uncertainty and its impact on the distance d. Predefined paths show high sensitivity to detector position uncertainty, resulting in significant increases in d values for uncertainties as low as 0.1 m. The UD profit function exhibits less sensitivity, with d values doubling only for uncertainties exceeding 0.25 m, although larger uncertainties of 0.5 m can lead to substantial increases in d, particularly with higher source activities. On the other hand, the STUD profit function generally yields lower d distances but experiences significant increases with a detector position uncertainty of 0.5 m. Therefore, maintaining the detector position uncertainty below 0.5 m is crucial for achieving accurate source localization when using informative path planning.

Figure 7.14 illustrates the simulation results for UD and STUD profit functions-based paths, comparing detector position uncertainties of 0.25 m and 0.5 m, highlighting the notable increase in distances d with higher uncertainty. In this scenario, source position accuracy is only improved by performing a full lap, which results in lower d_F distances but has the drawback of increasing the inspection time.

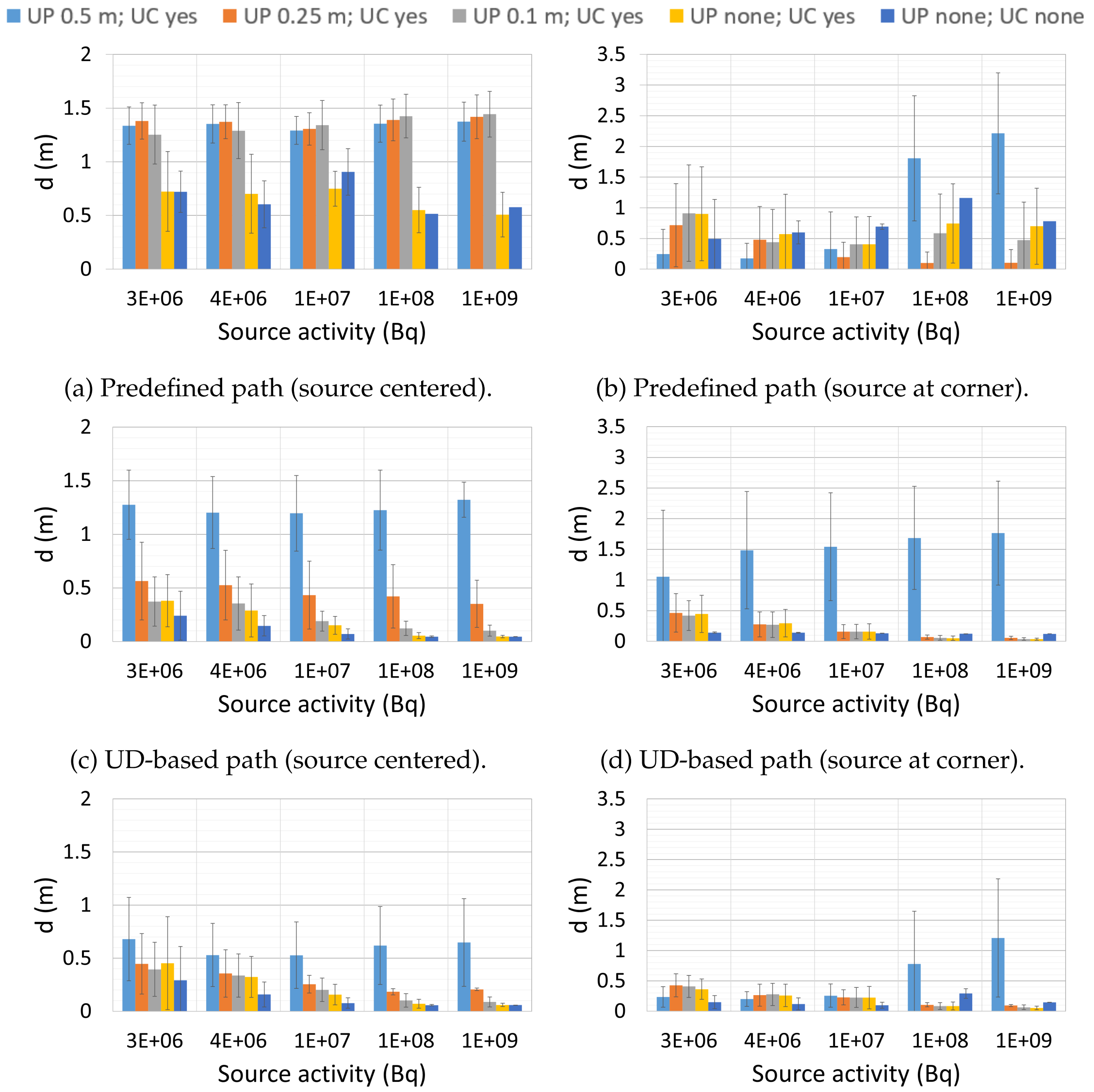

(a) Predefined path (source centered).

(b) Predefined path (source at corner).

(c) UD-based path (source centered).

(d) UD-based path (source at corner).

(e) STUD-based path (source centered).

(f) STUD-based path (source at corner).

Figure 7.13: Estimated-to-actual distances d considering different uncertainties in the detector position and counts, varying the path type and source position.

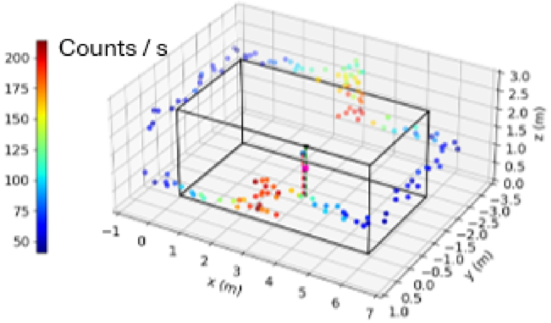

d=0.396 m; t=72 s; d_F=0.22 m; t_F=173 s

(a) UD profit function (UP=0.25; UC=yes).

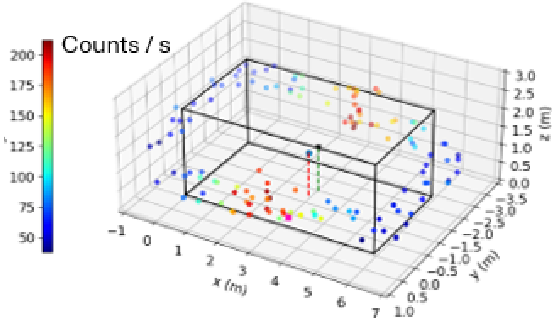

d=1.482 m; t= 71 s; d_F= 0.274 m; t_F=159 s

(b) UD profit function (UP0.50; UC=yes).

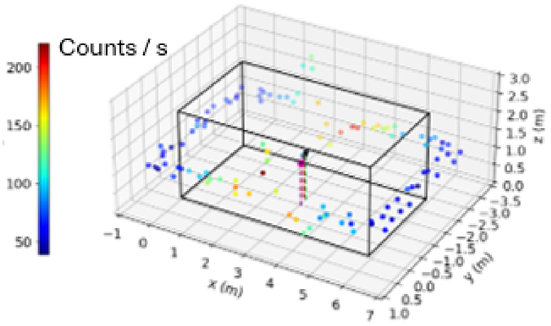

d=0.31 m; t=55 s; d_F=0.111 m; t_F=120 s

(c) STUD profit function (UP=0.25; UC=yes).

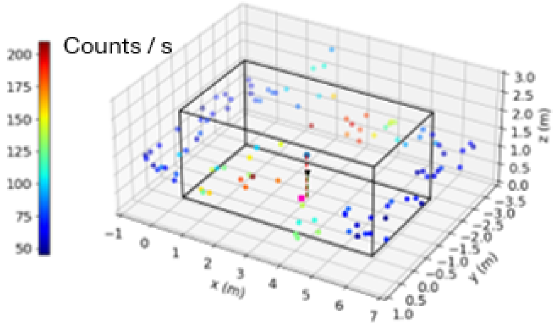

d=1.202 m; t=58 s; d_F=0.516 m; t_F=120 s

(d) STUD profit function (UP=0.50; UC=yes).

Figure 7.14: Impact of the detector position and counts uncertainties on the source localization accuracy using informative path planning, considering a 4 MBq ^{137}Cs source positioned at the center of the container.

7.4 Discussion and conclusions

The development of a computer simulator program to enhance gamma-ray source detection and localization within maritime shipping containers has shown considerable promise in optimizing inspection processes. The simulation, which tested various paths for the MRDS, used an iterative MLE algorithm to estimate the gamma-ray source position at each radiation data point. By evaluating three profit functions for informative path planning, the study demonstrated that adaptive paths–where the MRDS's path is dynamically adjusted in real-time based on source position estimation or radiation data (detector counts)–outperforms predefined paths by improving localization accuracy and reducing inspection times.

The *Step* profit function, which adjusts the path based on estimated source height, achieves improved localization accuracy compared to predefined paths with a single full lap. However, its dependence on position estimates can result in inefficient path adjustments and missed opportunities for detecting higher gamma-ray counts.

In contrast, the UD profit function, which modifies the path based on gamma-ray counts, improves localization accuracy significantly, especially in terms of the z-coordinate. However, this comes at the cost of increased inspection time due to the vertical scanning involved.

The STUD profit function, incorporating sinusoidal movements based on gamma-ray counts, provides a trade-off between source position accuracy and inspection time while performing efficiently with increased uncertainties in detector positions (0.25 m) and counts. It achieves high localization accuracy with reduced time compared to the UD function, particularly when using an exit condition. This approach is particularly advantageous in high-traffic environments, such as large seaports, where minimizing inspection times are critical.

Simulation results showed that the choice of profit function and uncertainties considered (detector position and counts) had a greater impact on localization accuracy and inspection time than the source activity level, which had minimal effect on both performance and duration. Profit functions proved especially advantageous for detecting low-activity sources or those positioned at the corner of the container, where detection is more difficult.

The simulator operated under several key assumptions, including a homogeneous medium of air and iron and the exclusion of Compton scattering effects. While these assumptions simplified the model, they also introduced certain limitations.

Finally, the results indicate that using real-time data and profit functions for informative path planning significantly improves inspection efficiency and accuracy, presenting a practical solution for enhancing security in international shipping. Future work should focus on refining the simulation assumptions, integrating more complex radiation interaction models (e.g. MC-based simulations), and validating results with real-world experimental data.

8 Gamma source detection and localization - Field tests using Informative Path Planning

Field tests were conducted using the portable radiation detection system–a handheld device equipped with distance sensors (as shown in Figure 5.21)–to inspect a simulated shipping container containing a ^{137}Cs source[1]. The primary objectives of these tests were:

- Validate the simulator described in Chapter 7;
- Estimate the ^{137}Cs source position and compare results using predefined paths and informative path planning based on the UD and STUD profit functions;
- Obtain the ^{137}Cs source activity and uncertainty.

For the experimental results presented in this Chapter, both the multirotor and the maritime shipping container were unavailable. Although the use of the multirotor and shipping container would not alter the main conclusions of this thesis–specifically, the effects of using predefined paths and informative path planning on the source localization accuracy and inspection time–it would have allowed a more realistic scenario (e.g. account for the attenuation of gamma radiation by the container walls) and the testing of the ultrasound distance sensor (to monitor the distance between the radiation detection system and the container wall).

Given the use of handheld equipment, the first batch of tests was limited to predefined paths and the UD profit function, as these paths were easier to execute manually. However, during the second field tests, it was also possible to incorporate the STUD profit function-based paths for comparison. In the first batch, experimental data was collected and stored on a Raspberry Pi memory card. After applying an outlier filter and confirming the data's reliability through offline analysis, the source position was estimated

[1]Although 10 identical ^{137}Cs radioactive sources were used, their close proximity led to the assumption that a single radioactive source was concealed within the shipping container.

using the MLE algorithm. The development of a source search algorithm, based on the flowchart in Figure 7.4, which integrates various components—including data acquisition, the MLE algorithm, informative path planning, detector position unit conversion, and outlier filtering—enabled real-time source detection and localization. This means that source detection confirmation, along with the estimated source coordinates and associated uncertainties, was provided to the system operator as soon as the data became available during the inspections.

8.1 Field Tests Methodology

The field tests involved placing ten identical ^{137}Cs radioactive sources (collectively referred to as the ^{137}Cs source), with a total activity of approximately 3.94 ± 0.46 MBq, inside a simulated 20 ft long maritime shipping container. The container's internal length and width boundaries were simulated using a cord on the floor. During the inspections, the detector's window was kept parallel to the container boundaries, maintaining a constant distance of 0.5 m from the container boundaries by using marks on the floor. The container boundaries and the horizontal path followed by the radiation detection system, as well as the ^{137}Cs source different positions are shown in Figures 8.1 and 8.2.

In a predefined path the detection system completes a full lap around the container at a specific height (one-third or two-thirds of the container height). In the UD profit function-based path, the radiation detection system path starts at a constant height (one third the container height) and finish when the required accuracy is achieved (exit condition)– coincident with a estimated-to-real source distance lower than 0.5 m. This approach also ensures that a complete container side is inspected from the beginning of the process[2].

Both predefined paths and UD profit function-based paths were performed manually by a person (as shown in Figure 8.3). To allow the detection system operator to focus on navigating around the container, a second person, with remote access to the sensor data, was responsible for the monitoring and alerts. The proximity of a few meters between the two individuals allowed for rapid transmission of information, which was crucial given the frequency of data acquisition every second. This setup ensured that the key parameters were consistently maintained and that specific procedures were carried out promptly [304], namely:

- Constant path height during inspection (using LiDAR information);
- Indication of gamma-ray count peaks (to perform the UD profit function) and the moment to start performing the sinusoidal movement (for the STUD profit function);
- Indication of when the exit condition was satisfied;
- Travel speed of approximately 0.2 m/s (controlled with a chronograph).

[2]A source localization accuracy of 0.5 m is the minimum acceptable distance considering the proposed methodology and position sensors uncertainties)

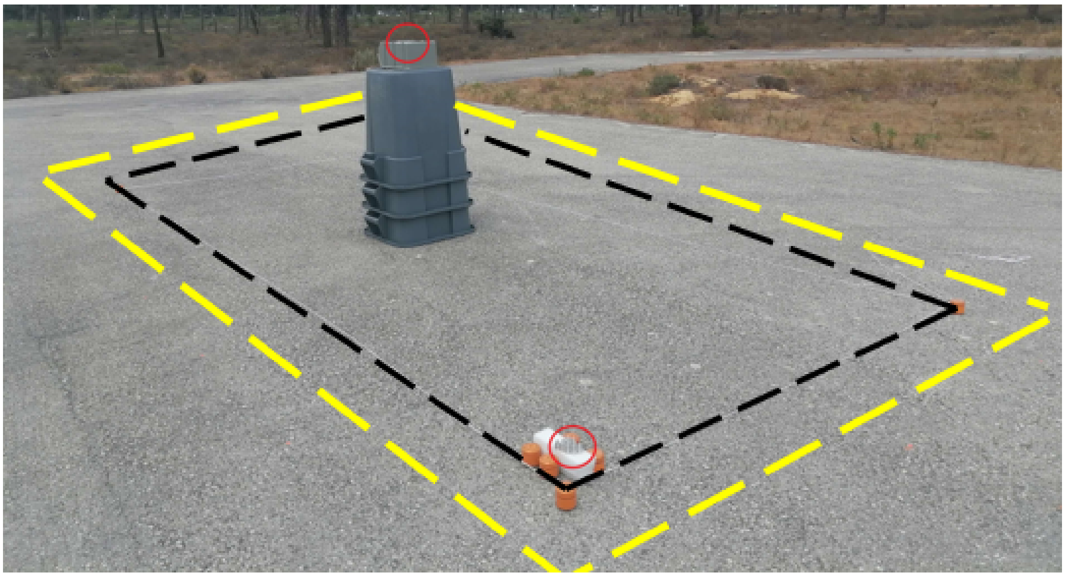

Figure 8.1: ^{137}Cs sources locations: at the center or at the corner of a simulated container. Container boundaries marked with a black dashed line and the radiation detection system path marked with a yellow dashed line.

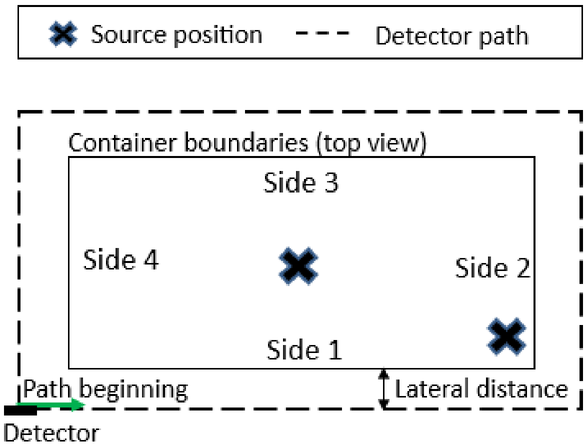

Figure 8.2: Path performed by the EJ-200 plastic scintillator around a simulated shipping container (top view), considering the ^{137}Cs sources centered and at the corner of the container [304].

8.2 Simulator validation using experimental data

The simulator was validated by acquiring and analyzing real data of the EJ-200 detector when performing predefined paths at one-third and two-thirds of the container's height. The ^{137}Cs source was placed at the center and at the corner of the shipping container. The simulated data were obtained as described in Chapter 7, and the cylindrical approximation for the EJ-200 scintillator was considered. Four experimental data sets and their mean values were compared with the simulated data[3], considering a time window of 60 s (for

[3]Five simulations were performed for each path type and source position. Simulation results correspond to their mean values.

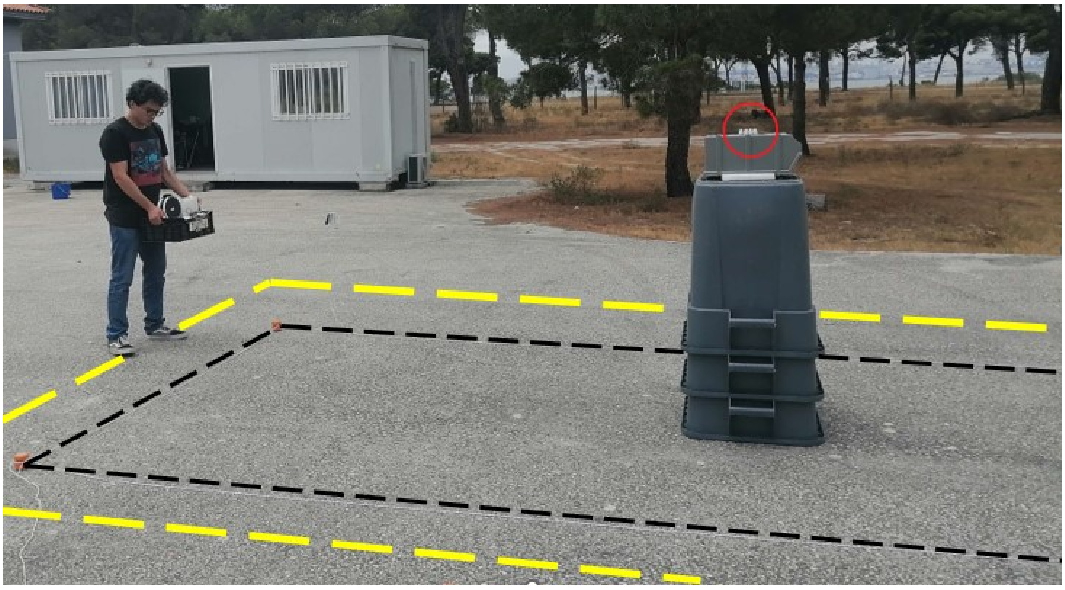

Figure 8.3: Data acquisition for the ^{137}Cs source localization (source centered) using the detection system (manual inspection) [304].

greater detail), for the source centered and at the corner, as shown in Figure 8.4 and Figure 8.5 respectively. The peak maximum observed in Figure 8.4 occurs when the radiation detection system passes directly in front of the source. In Figure 8.5, with the source positioned at the corner (where side 1 and side 2 of the container intersect), the detection system registers two overlapping peaks as it approaches and then moves away from the source on each side. The comparison between experimental and simulated data is summarized as follows:

- All the peaks maxima of the simulated and experimental data coincide;
- The experimental data peaks are generally broader than the simulated ones. This difference can be explained by the fact that the simulator does not account for scattered and backscattered gamma rays from the container walls. This difference becomes more pronounced when the source is placed at the corner, where increased iron shielding in the vicinity of the source leads to more backscattering events;
- For the predefined paths at one-third of the container's height, the peak maxima of the experimental mean curve are significantly lower than those in the simulated data. For instance, the maximum experimental mean value (165 counts) is 0.72 times lower than the maximum value obtained for the simulated data (230 counts). These discrepancies can be attributed to: (i) small variations in the path speed (variations up to ±0.05 m/s for a speed of 0.2 m/s), as indicated by the time shifts between the data sets; and (ii) The uncertainties on the radiation detection system position (position errors of the GNSS receiver).

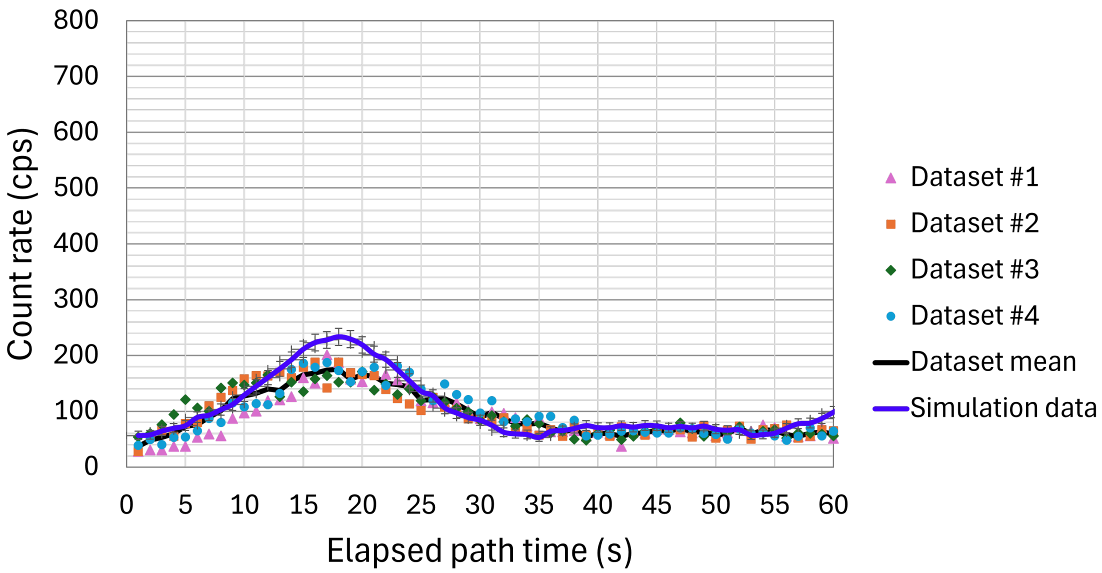

(a) Predefined path at one third the container height.

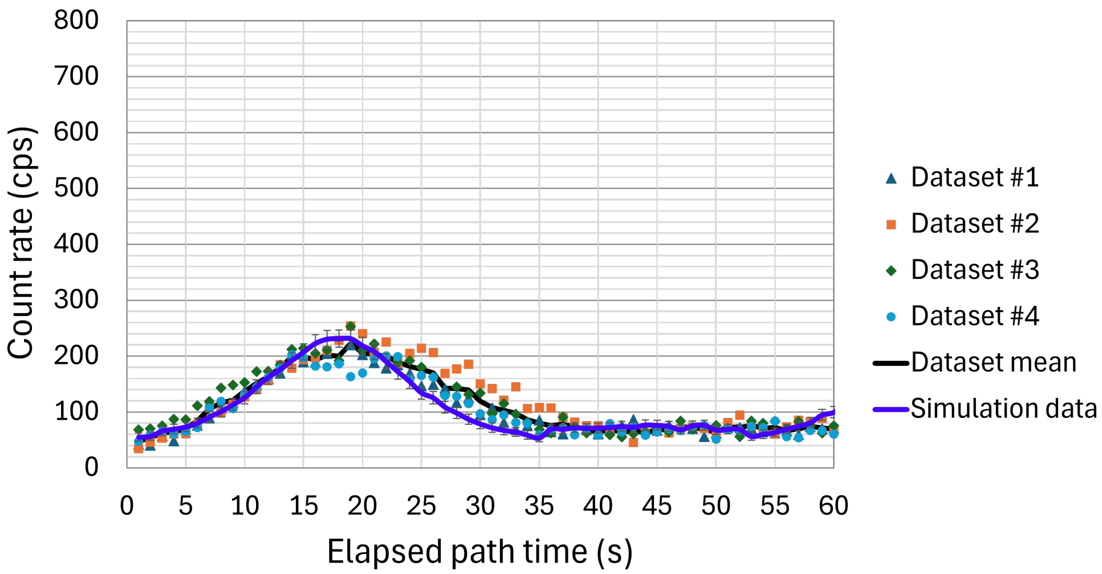

(b) Predefined path at two thirds the container height

Figure 8.4: Comparison of the experimental and simulated data gamma-ray count rate for the EJ-200 scintillator performing predefined paths around side 1 and 2 of the shipping container with the ^{137}Cs source placed at the center.

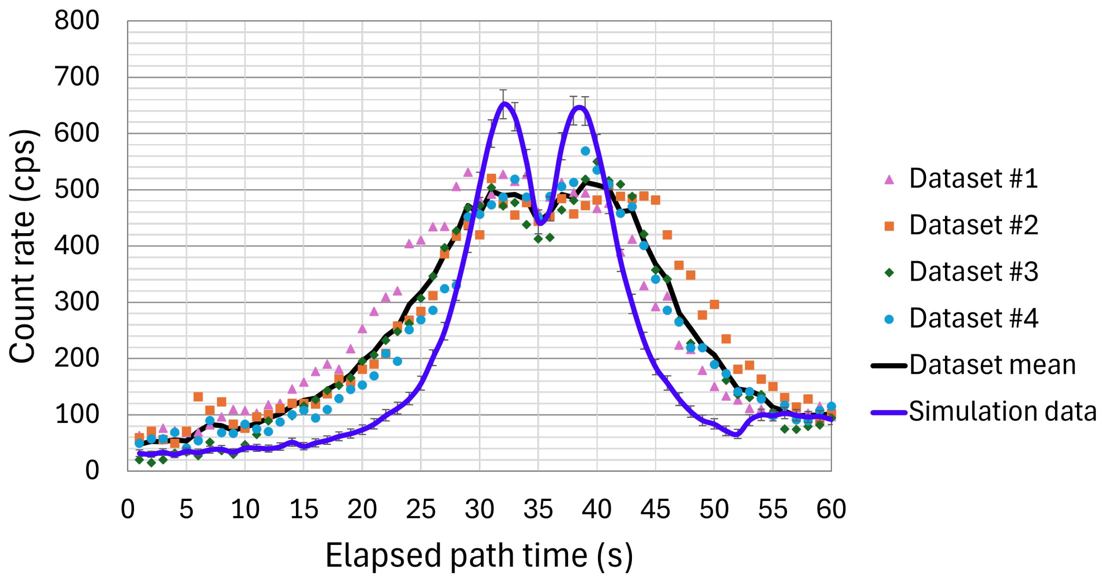

(a) Predefined path at one third the container height.

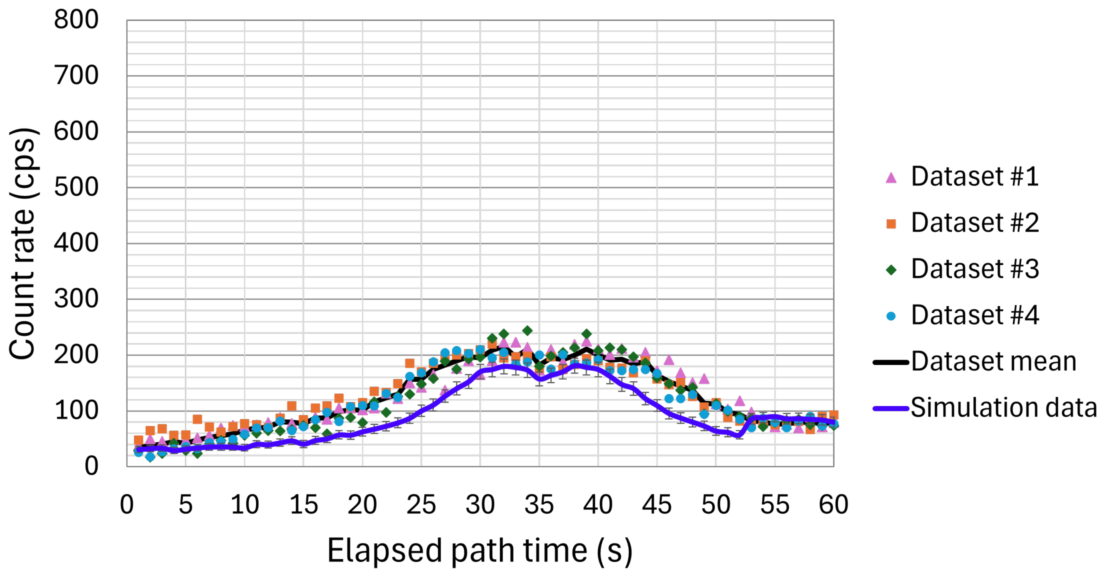

(b) Predefined path at two thirds the container height.

Figure 8.5: Comparison of the experimental and simulated data gamma-ray count rate for the EJ-200 scintillator performing predefined paths around side 1 and 2 of the shipping container with the ^{137}Cs source placed at the corner.

Although there are some differences between the experimental and simulated results, primarily due to simplifications considered in the simulator, radiation detection system speed variations and uncertainties in the radiation detection system's position, the simulator's results remain valid for its intended purpose: comparing data from different paths and source positions in terms of source localization accuracy and inspection times.

8.3 Source position estimation and activity calculation results – data analysis performed offline

In accordance with Section 4.4.2, the experimental data was acquired and processed. To proceed with the offline data analysis and convert the detector position data into the relative units required by the MLE algorithm, a rotation and translation of the detector position points (provided in relative easting and northing) was required to align them with the container boundaries defined within the algorithm (as depicted in Figure 8.6). While the rotation of the points allowed to align the direction vector of the detection system path[4] with the container's side direction (coincident with the x axis), the translation allowed to perform small adjustments in the detector position point at the path beginning to coincide with the accurate known position (from ground true). These adjustments allowed to correct some systematic errors of the GNSS receiver using the ground truth of the marks placed on the floor. As a result, we achieved a horizontal position accuracy for the radiation detection system better than 0.5 m.

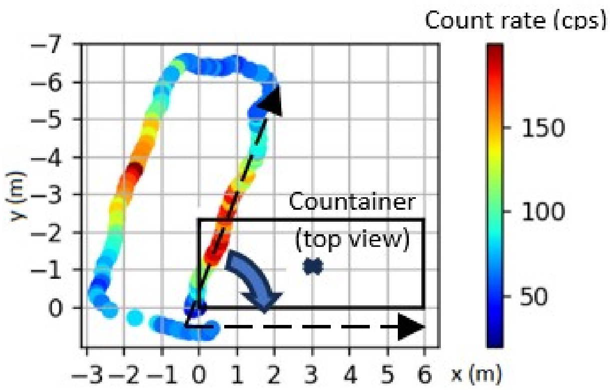

Figure 8.6: Example of the EJ-200 count rate measured points located using relative easting and northing coordinates. Desired rotation between the direction path vector (arrow) and the container reference frame is also indicated [304].

The LiDAR sensor measured the detection system height every second, while the ultrasound sensor served as a backup to identify and correct any erroneous data.

Since only ^{137}Cs gamma-ray sources were available, only the gamma-ray detection system was used in this tests. At each second, a timestamp of the data was recorded including

[4]The direction vector of the detection system's path was determined by performing a linear regression on the first 20 points of the path. The direction is represented by the slope of the resulting best-fit line, which captures the overall trend of the detection system's movement.

the gamma-ray counts, detection system height, and horizontal position (provided by the GNSS receiver). This information, along with the background radiation counts (previously measured), was then used by the MLE algorithm to estimate the three coordinates of the source position and corresponding uncertainties. A cylindrical approximation of the EJ-200 scintillator was used to calculate the geometric detection efficiency at each acquired data point. After four gamma-ray counts exceeding the critical level (minimum number of points necessary to estimate the source position), the MLE algorithm began to estimate the source position coordinates and corresponding confidence intervals (Fisher information) for each entry in the CSV file, considering all data acquired up to that point, using the equations described in Section 4.5.4.

The estimation of the ^{137}Cs source position and the calculation of the corresponding activity were conducted using predefined paths and informative path planning around the simulated container. Two initial path heights were considered, at one-third and two-thirds of the container's height. The ^{137}Cs sources were positioned either at the center or at the bottom corner of the container (as shown in Figures 8.1 and 8.2). Although five measurements were conducted for each combination of path and source configuration, only four measurements were further considered in the data analysis to ensure data integrity and results quality.

While for predefined paths only full lap inspection was considered, the informative path planning based on the UD profit function was performed with exit condition. As previously explained, the exit condition allows to finish the inspection as long as the required source localization accuracy is obtained meeting the criteria defined in Section 7.2.2. To meet the exit condition, it was typically sufficient to inspect only "side 1" of the container for the source positioned at the center, and "sides 1 and 2" for the source located at the bottom right corner, which allowed to achieve a source localization accuracy better than 0.5 meters when IPP algorithm was used (as shown in Figure 8.7)[5].

Figure 8.7 compares the average estimation results of the ^{137}Cs sources position for predefined paths (full laps) and for paths based on the UD profit function (informative path planning) with exit condition. In this plot, uncertainties are represented by the standard deviation of all four measurements obtained for each situation.

From Figure 8.7, higher estimated-to-real source distances d are observed using predefined paths (up to 1.3 meters when the source is positioned at the center and 0.8 meters when at the corner). The larger standard deviations for predefined paths also indicate greater uncertainty in the source position estimation.

For all initial path height and source position configurations, the use of informative path planning yielded more accurate results. Estimated-to-real source distances d of up to

[5] Although the baseline count b (parameter of the informative path planning) was measured as outlined in Section 7.2.1, the low source activity and the considerable source-detector distance during measurement led to baseline count b being considered approximately equal to the background counts rate (obtained from a 5-minute measurement conducted in the absence of any sources). Baseline count b was considered equal to 26 cps (average of background counts rate).

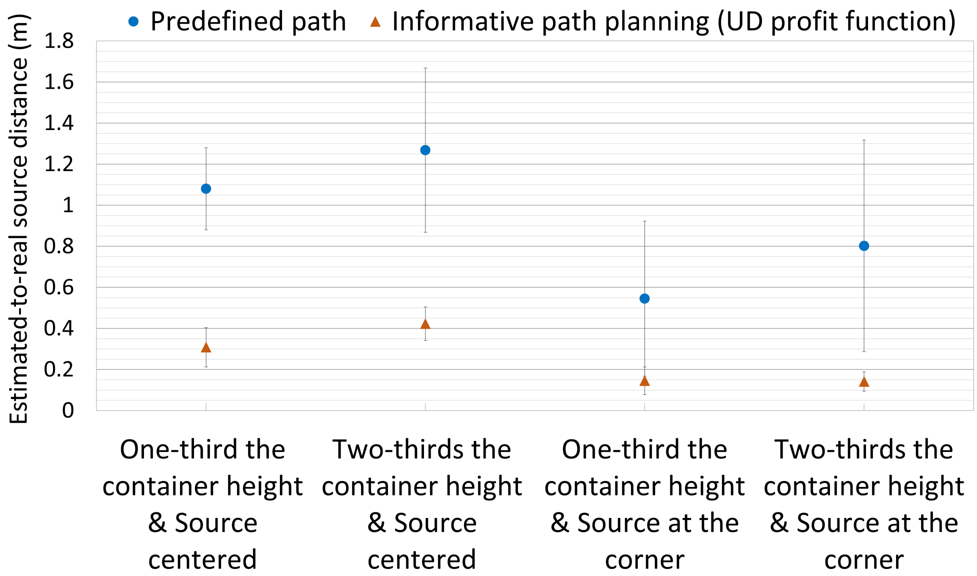

Figure 8.7: Estimated-to-real source distances for predefined paths and for paths based on UD profit function (informative path planning) with exit condition, considering different initial path heights (one-third and two-thirds the container height) and source positions (centered and at the corner) within the simulated container [304].

0.4 m for the source at the center and 0.15 m for the source at the corner of the container were achieved, representing a 3 to 6 fold improvement compared to predefined paths.

Additionally, compared to previously work published in [296], which only considered predefined paths for the inspection of containers and where reported estimated-to-real source distances of up to 2.5 meters were obtained, the use of an informative path planning and an iterative 3-D MLE algorithm significantly improved source localization accuracy. Clearly, the UD profit function allowed the radiation detection system to gather more information during the path, improving the source localization accuracy by performing a z-scan in the vicinity of the source.

The different components of the estimated-to-real source distance d_x, d_y and d_z for the predefined paths and for the UD profit function-based paths are shown in Figures 8.8 and 8.9 respectively. Figure 8.8 highlights the limitations of the MLE algorithm in accurately estimating the z-component of the source position when the radiation detection system performs predefined paths. These estimation difficulties stem from the insufficient radiation data on the z-component near the hot spot. This is evident from the average d_z value exceeding one meter when the source is centered, along with the high standard deviations in d_z values when the source is positioned at the corner.

As shown in Figure 8.9, significant improvement in estimating the source position is achieved through informative path planning, with the average d_z distances consistently below half a meter for all scenarios. A significant reduction in the standard deviation of the d_z values for the source positioned at the corner was also observed. Similar to predefined paths, d_z is notably lower when the source is positioned at the corner of the container.

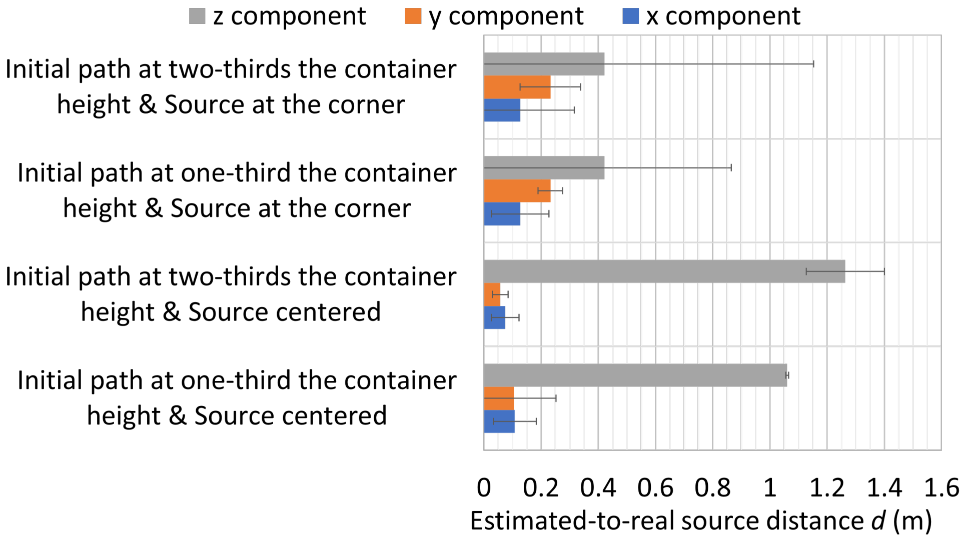

Figure 8.8: Estimated-to-real source distance components (d_x, d_y and d_z) for predefined paths considering different initial path heights (one-third and two-thirds the container height) and source positions inside the simulated container [304].

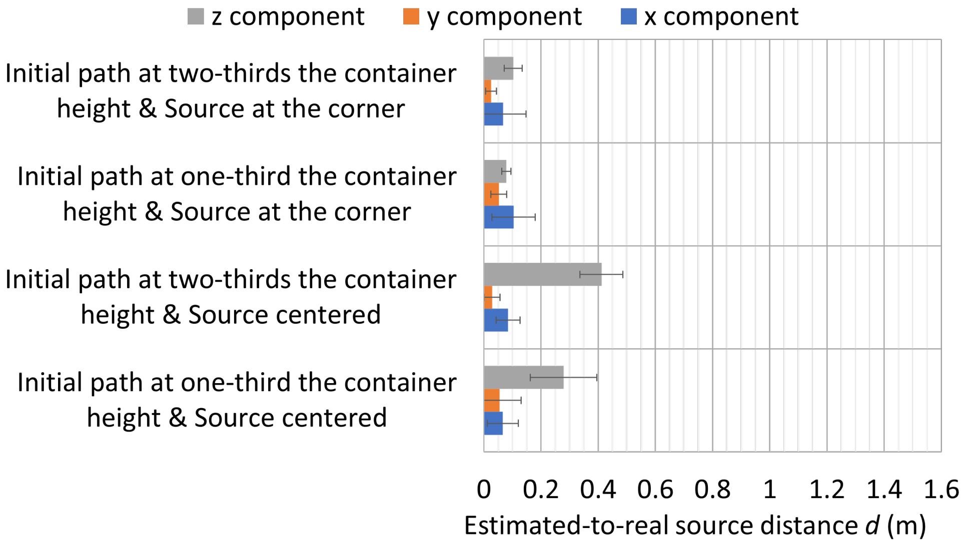

Figure 8.9: Estimated-to-real source distance components (d_x, d_y and d_z) for informative path planning based on the UD profit function, considering different initial path heights (one-third and two-thirds the container height) and source positions inside the simulated container [304].

Examples of the EJ-200 scintillator count rate during predefined and UD profit function-based paths, considering different initial path heights and source positions inside the shipping container, are shown in Figures 8.10, 8.11, 8.12 and 8.13. These figures also present the distance d between the estimated and real source positions. To mitigate errors from the GNSS receiver and LiDAR sensor, outliers were removed from some measurements (performed offline). Therefore, if gamma-ray source localization is intended to be performed in real time, an outlier filter should be implemented.

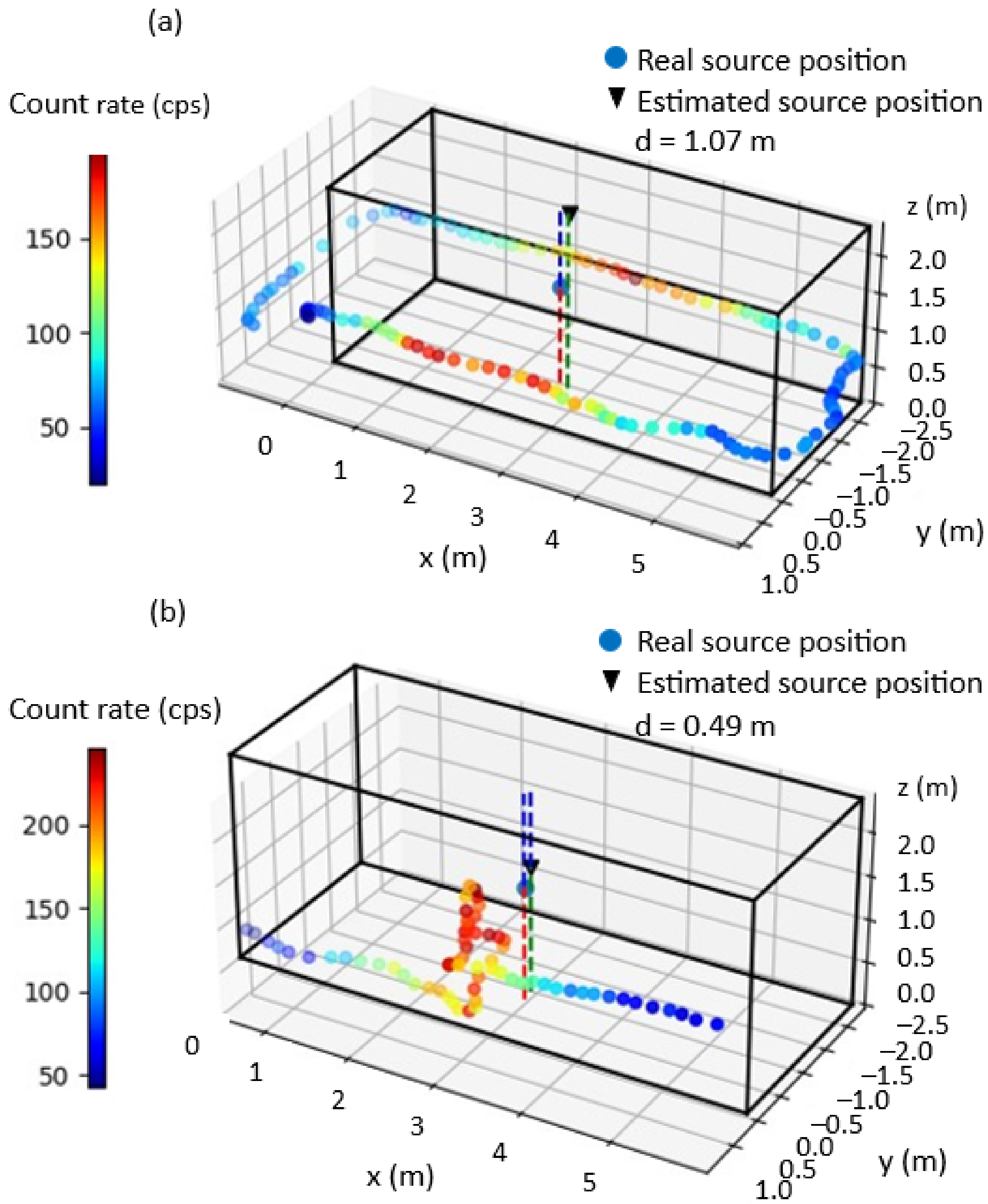

Figure 8.10: Example of the ^{137}Cs sources position estimation (using MLE algorithm) for an initial path of one-third the container height and the sources centered at the simulated container considering: (a) a predefined path (b) path based on the UD profit function [304].

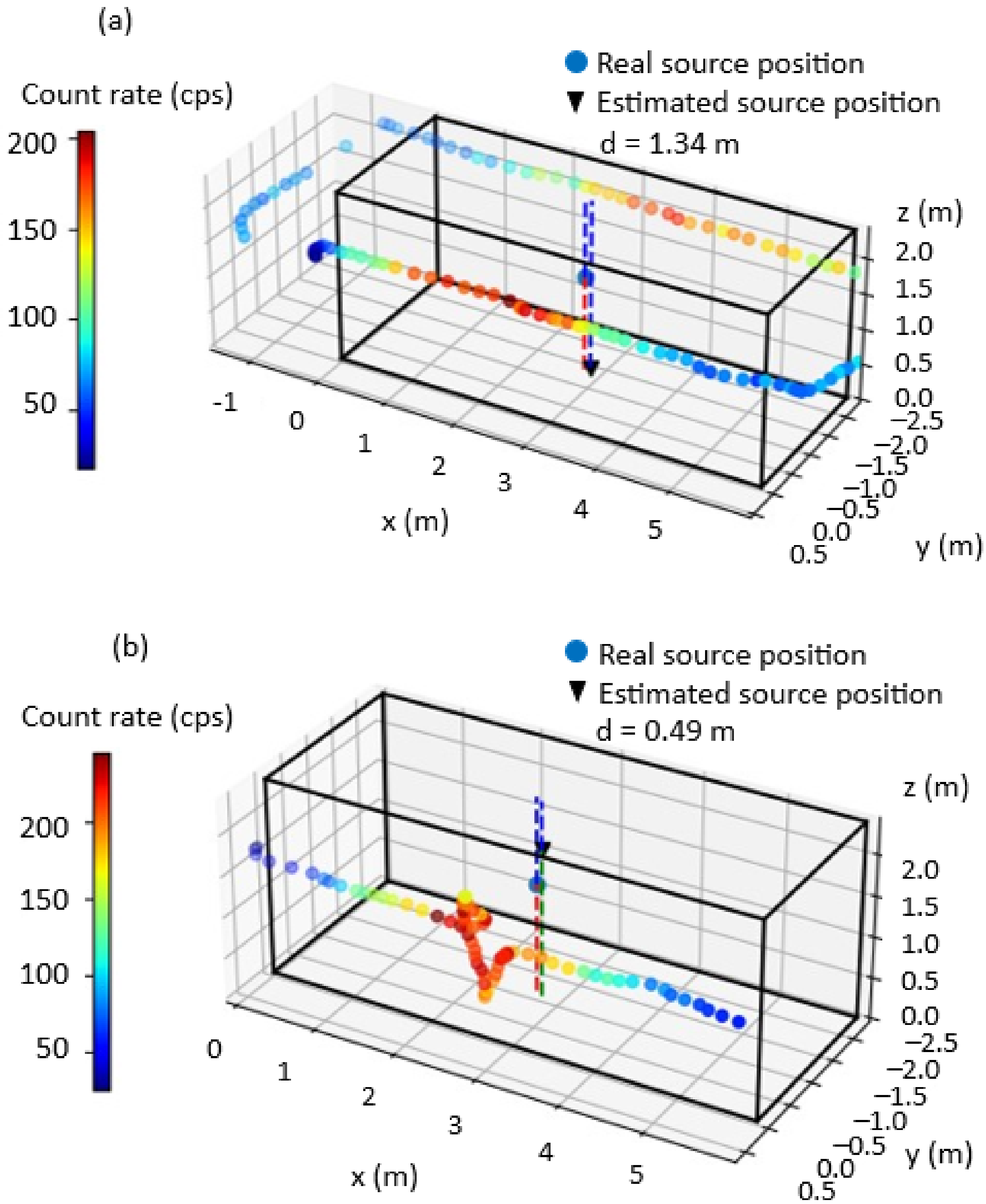

Figure 8.11: Example of the ^{137}Cs sources position estimation (using MLE algorithm) for an initial path of two-thirds the container height and the sources centered within the simulated container considering: (a) a predefined path (b) UD profit function based path [304].

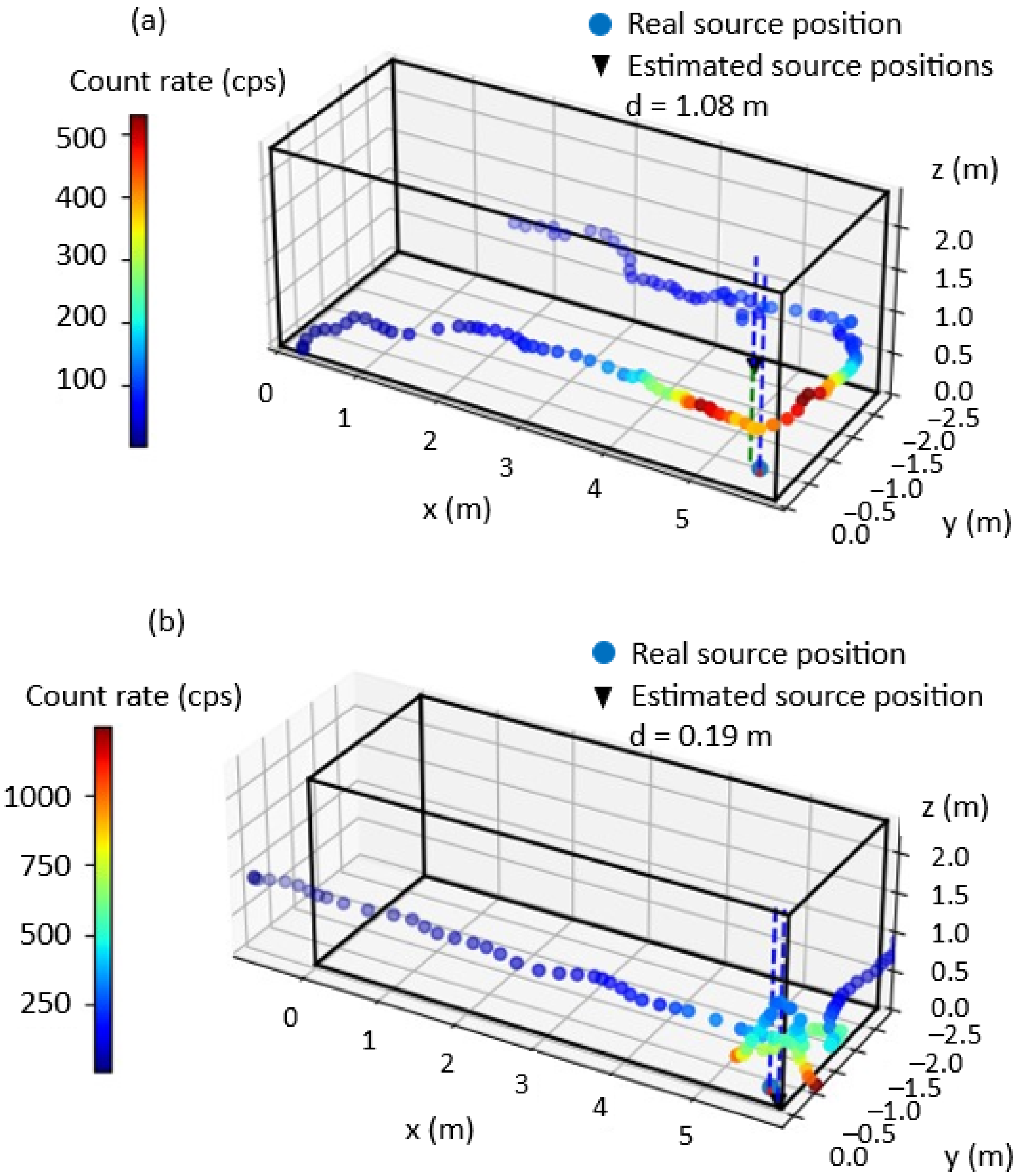

Figure 8.12: Example of the ^{137}Cs sources position estimation (using MLE algorithm) for an initial path of one-third the container height and the sources placed at the corner of the simulated container considering: (a) a predefined path (b) UD profit function based path [304].

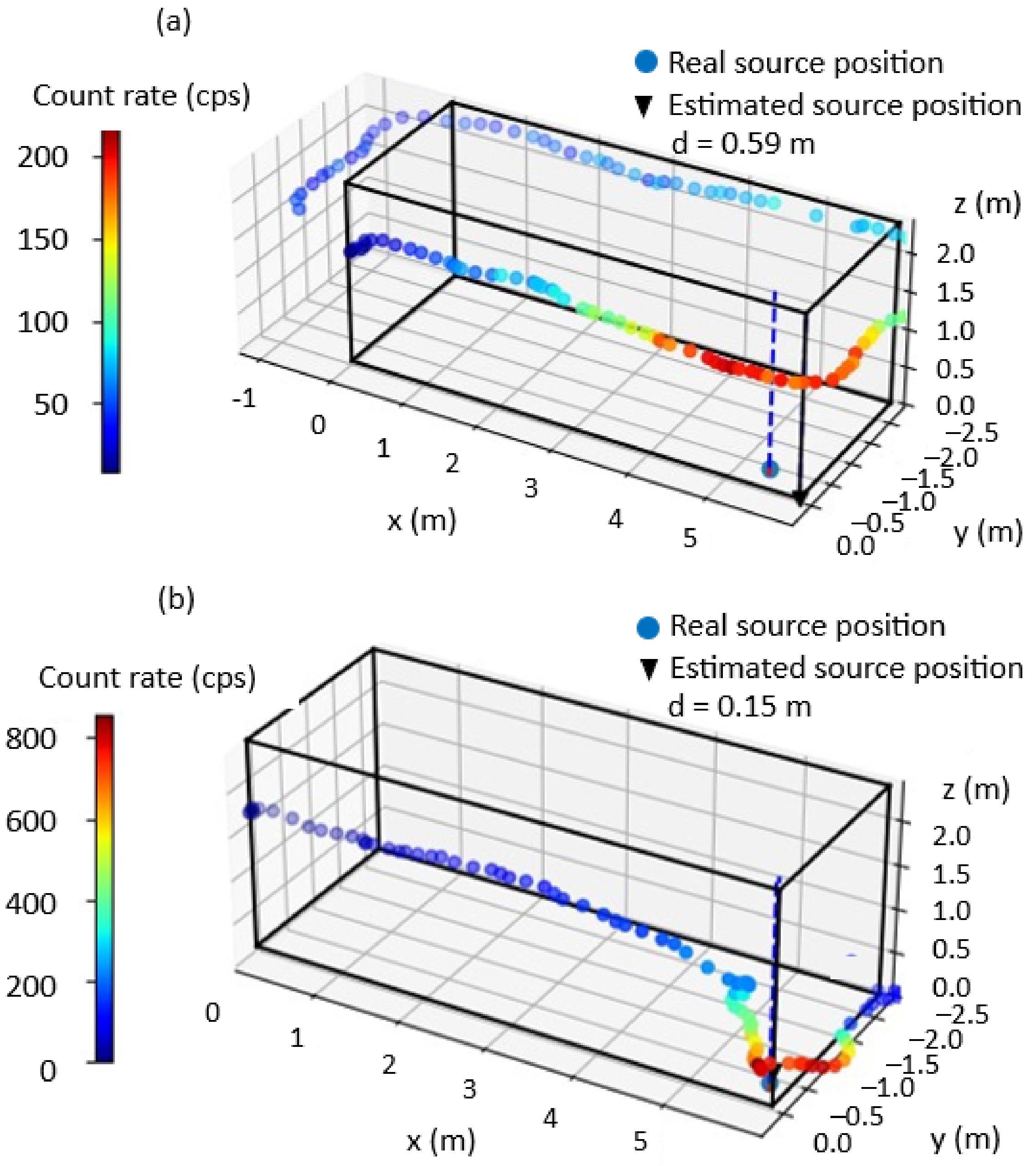

Figure 8.13: Example of the ^{137}Cs sources position estimation (using MLE algorithm) for an initial path of two-thirds the container height and the sources placed at the corner of the simulated container considering: (a) a predefined path (b) UD profit function based path [304].

Figure 8.14 illustrates the average time required to complete both predefined paths and UD profit function-based paths. Although the UD profit function required the radiation detection system to halt horizontal movement and perform a z-scan near the source–a time-consuming process–the use of an exit condition allowed the inspection to end once the desired source localization accuracy was achieved. This significantly reduced the inspection time compared to predefined paths.

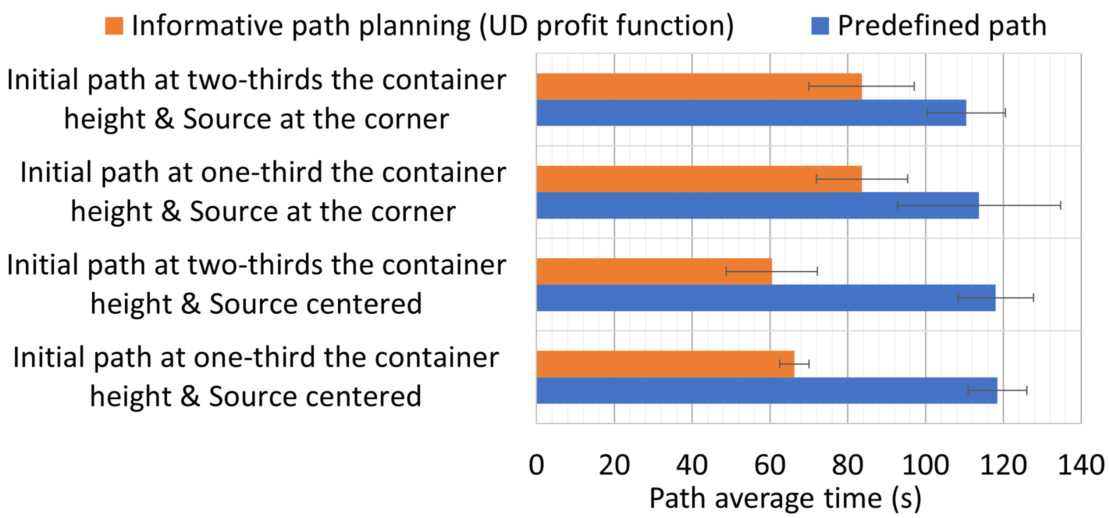

Figure 8.14: Average time required to complete the predefined paths and paths based on informative path planning, along with their corresponding standard deviations [304].

The radioactive source activity was calculated after estimating the source position, specifically considering a ^{137}Cs point-like source with an isotropic emission. If the gamma-ray source was unknown, it would be necessary first identify the radionuclide to use the correct intrinsic detection efficiency, which depend on the gamma rays energy, and the appropriate branching ratio for the specific gamma rays emitted by the source. If the radionuclide present in the lost or hidden radioactive source is known, one simply needs to adjust the intrinsic detection efficiency and the branching fraction parameters to obtain the accurate source activity.

Another important aspect is the presence of shielding material between the source and the detection system. If the shielding is unknown or not accounted for, the calculation of source activity may be inaccurate, typically leading to an underestimation. This underestimation occurs because shielding reduces the detected radiation, making the source appear weaker than it actually is. In the simulation and experimental data, only the air and the container walls were considered; however, in a real scenario, additional materials such as cargo or shielding around the source (e.g., shielded transport and storage containers) could further attenuate the radiation, exacerbating this underestimation. For example, the experimental results presented in Chapter 6 illustrate the challenges in detecting a shielded 215 MBq (5.81 mCi) ^{137}Cs source housed within the Troxler equipment.

The attenuated gamma rays were barely detectable, nearly blending with background radiation. In contrast, the neutrons emitted by the $^{241}Am - Be$ source, also present in the Troxler equipment, were clearly detected.

However, in the activity calculations presented below, the focus is not on analyzing the effects of shielding material on the absolute value of the calculated source activity. Instead, the key objective is to compare how closely the values obtained using predefined paths and IPP align with the actual source activity under consistent shielding conditions.

Therefore, using the recorded gamma counts and the estimated source position, the source activity A and corresponding uncertainty was calculated according to (4.16) and (4.17) respectively. Table 8.1 presents the uncertainties of the variables considered in the source activity calculation.

Table 8.1: Uncertainties considered on the ^{137}Cs source activity calculation [304].

Variable	**Description**	**Uncertainty**
z_d	z-coordinate of the detector's position	0.01 m[a]
x_d, y_d	x, y coordinate of the detector's position	0.5 m[b]
x_s,y_s,z_s	Coordinates of the source's position	Fisher information
r,l	Detector radius and thickness	0.0003 m[c]
C_i	Detector counts	$\sqrt{C_i}$
B	Background averaged value (B=26 counts)[d]	$\sqrt{B}$
b_r	Branching fraction of the 662 keV gamma rays	0.0029
ε_i	Detector intrinsic efficiency (ε_i = 0.23)[d]	0.04

[a]LiDAR uncertainty.
[b]Integration of information from GNSS receiver and ground marks.
[c]Provided by the manufacturer.
[d]Obtained experimentally.

Figure 8.15 shows the ratio between the experimental source activities and the real source activity for each path type and source position. When an informative path planning is considered, all the experimental activity values closely align with the actual source activity (with a ratio closer to one). In contrast, experimental activities obtained using predefined paths deviate by up to three times the actual activity, with wider uncertainty intervals observed. This highlights that a more accurate estimation of the source position, as achieved with an informative path planning, contributes to enhancing the accuracy of the obtained source activity.

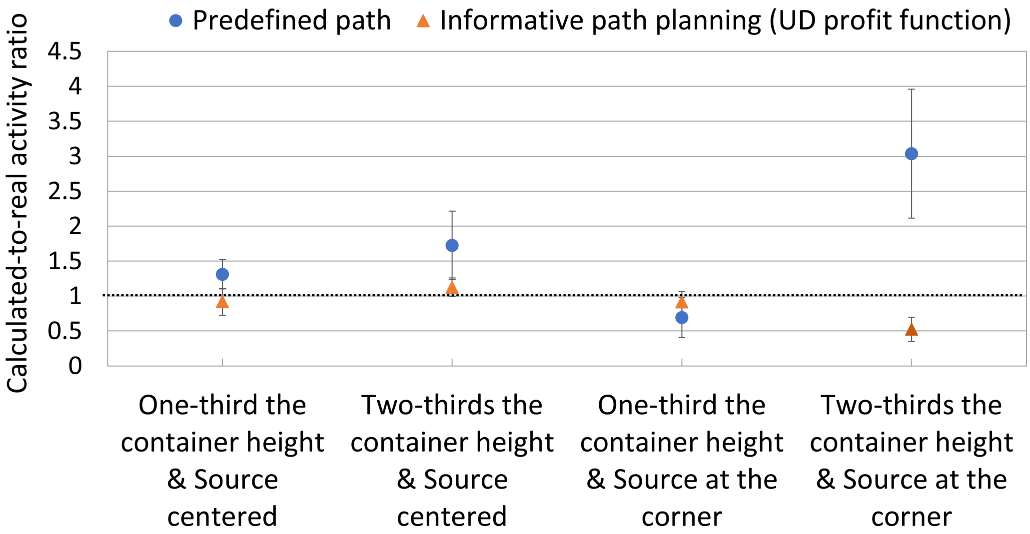

Figure 8.15: Comparison of the ratios between the experimentally calculated activity values and the real activity value considering predefined paths and informative path planning (UD profit function) with different initial path heights and source positions inside the simulated container [304].

8.4 Source position estimation and activity calculation results – real-time data analysis

A second series of field tests was conducted using both predefined paths and informative path planning techniques. The objectives of these tests were: (i) to detect and localize gamma-ray sources in real-time, and (ii) to compare the outcomes of using predefined paths versus informative path planning, based on the UD and STUD profit functions.

To enable real-time source detection and localization, an outlier filter was implemented to address anomalies before the measured data is processed by the MLE algorithm. The most significant anomaly encountered during data acquisition, which affected the accuracy of the source localization results, was the occurrence of LiDAR measurements registering as zero. Since variations in LiDAR values are minimal (with a maximum expected variation of 10 cm between consecutive points), any instance where the LiDAR returns a zero value was handled by replacing it with the previous valid measurement.

Six measurements were conducted for each scenario outlined in Table 8.2. The initial path height for both the predefined paths and those based on the UD profit function was set at one-third of the container's height. In contrast, the initial path height for the STUD profit function was set at half the container's height.

The algorithm used for the detection and localization of the gamma source was based on the flowchart of Figure 7.4. According to the flowchart, the algorithm can provide three different outputs: (i) Source not confirmed and no localization is provided; (ii) Source not confirmed but a possible source localization is provided; and (iii) Source confirmed and

Table 8.2: Field tests performed with EJ-200 scintillator considering ^{137}Cs sources inside a simulated shipping container – Predefined paths vs. Informative path planning.

Path type	Source position	Exit condition / Full laps
Predefined	No source	Full laps
Predefined	Centered	Full laps
Predefined	Centered	Exit condition
Predefined	At the corner	Exit condition
UD profit function	Centered	Exit condition
UD profit function	At the corner	Exit condition
STUD profit function	Centered	Exit condition
STUD profit function	At the corner	Exit condition

source localization information is provided.

The source confirmation occurs if the mean of the counts that surpass critical level are above the detection limit, as given by (7.1) and (7.2) respectively, while localization of the source is provided if four points are above the critical level –minimum number of points considered for the MLE algorithm perform the source localization estimation.

Before starting the tests a background radiation measurement was obtained during 5 minutes, obtaining a mean value of 28 cps.

The algorithm's ability to confirm the presence of a source was validated through measurements conducted with and without ^{137}Cs sources inside the simulated container. As shown in Figure 8.16, when no source was present within the simulated container, no count rate exceeding the detection limit was observed, and as expected, the algorithm correctly did not confirm the presence of a source. During the predefined path tests with ^{137}Cs sources placed at the center and the corner of the simulated container–illustrated in Figures 8.17 and 8.18, respectively–the gamma-ray counts quickly surpassed the detection limit, triggering an alarm that confirmed the presence of the source.

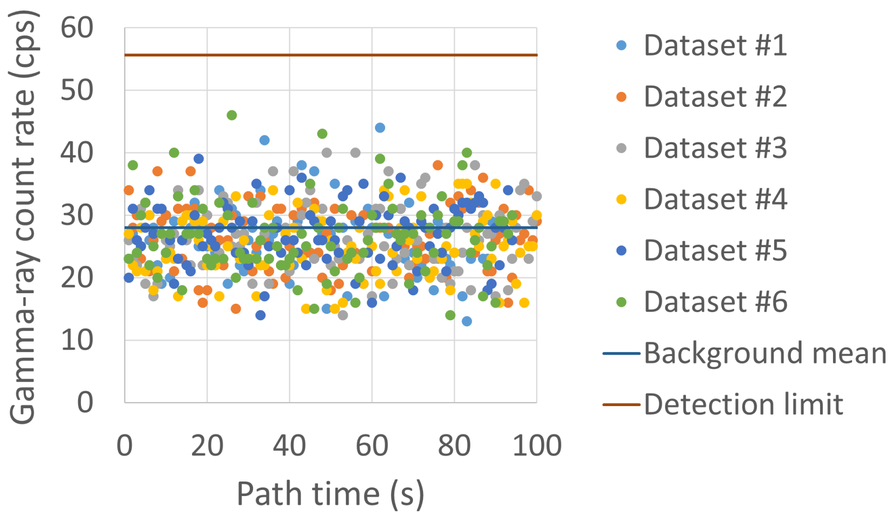

Figure 8.16: EJ-200 count rates obtained for six data sets considering predefined path (full lap) and no source inside the simulated container.

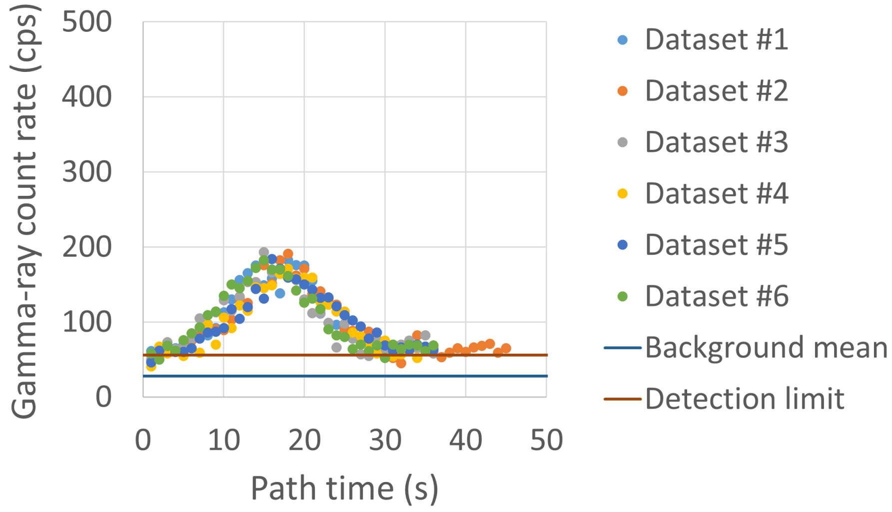

Figure 8.17: EJ-200 count rates obtained for six data sets considering predefined path (with exit condition) and ^{137}Cs sources at the center of the simulated container.

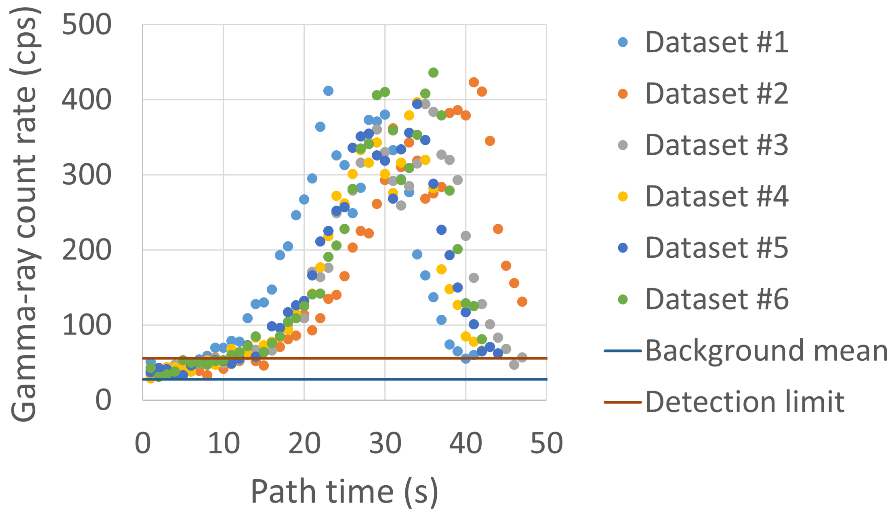

Figure 8.18: EJ-200 count rates obtained for six data sets considering predefined path (with exit condition) and ^{137}Cs sources at the corner of the simulated container.

Figure 8.19 shows the comparison of the estimated-to-real source distances d (with exit condition) for predefined paths and for paths based on UD and STUD profit functions (informative path planning)[6]. As discussed in Section 8.3, the profit function UD resulted in significantly lower distances d-approximately half the distance-compared to predefined paths. Notably, the STUD profit function produced even lower d distances than the UD profit function, which can be attributed to its greater resilience to uncertainties, particularly the uncertainty of the detector's position, as demonstrated in Section 7.3.2.2.

[6]Baseline count b was considered equal to 28 cps (the average of background counts rate).

For the predefined paths, the estimated-to-real source distances considering full laps d_F were also measured for the source positioned at the center, allowing for comparison with the distances d under the exit condition. A smaller distance of $d_F = 1.18 \pm 0.14$ m was observed, compared to $d = 1.68 \pm 0.20$ m. This finding underscores the importance of completing the full lap to enhance the accuracy of source localization when using predefined paths.

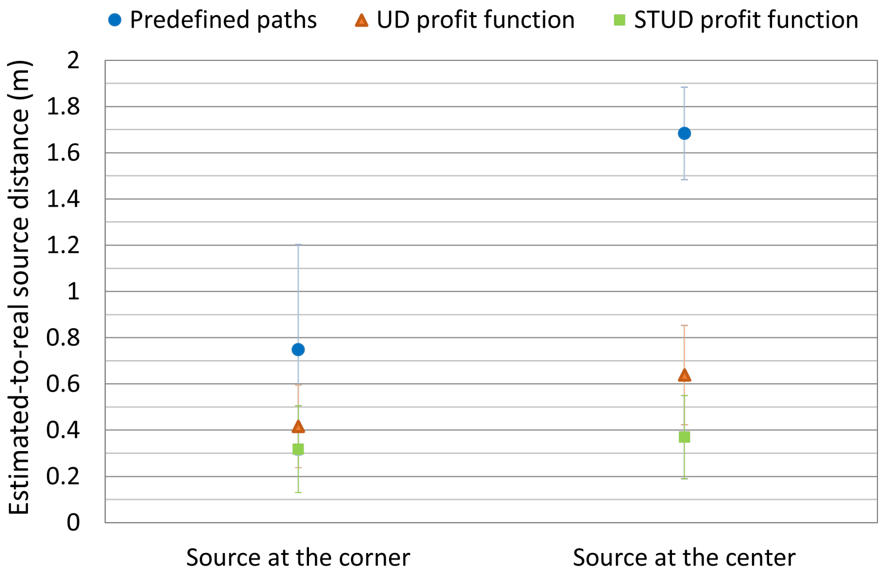

Figure 8.19: Estimated-to-real source distances for predefined paths and for paths based on UD and STUD profit functions (informative path planning), with exit condition applied to all paths. The analysis includes ^{137}Cs sources at the corner and at the center of the simulated container.

Figures 8.20 and 8.21 depict the individual components of the estimated-to-real source distances—d_x, d_y, and d_z—for paths using informative path planning compared to predefined paths, with sources positioned at the corner and center of the simulated container, respectively. When using predefined paths with the source positioned at the center, the MLE algorithm shows difficulties in accurately estimating the source height—the z component—as discussed in Section 8.3. Additionally, it struggles with the y coordinate and, to a lesser extent, the x coordinate. These issues may be attributed to the higher susceptibility of source position estimates to uncertainties when using predefined paths. For the UD profit function, the distance d_z is observed to be higher compared to the STUD profit function for both sources position.

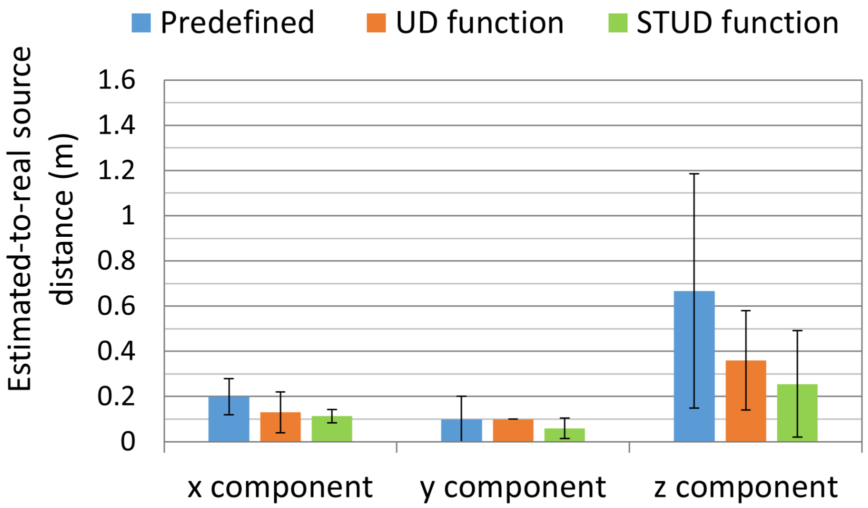

Figure 8.20: Estimated-to-real source distance components (d_x, d_y and d_z) for predefined paths and paths based on informative path planning (both with exit condition) considering the ^{137}Cs sources positioned at the corner of the simulated container.

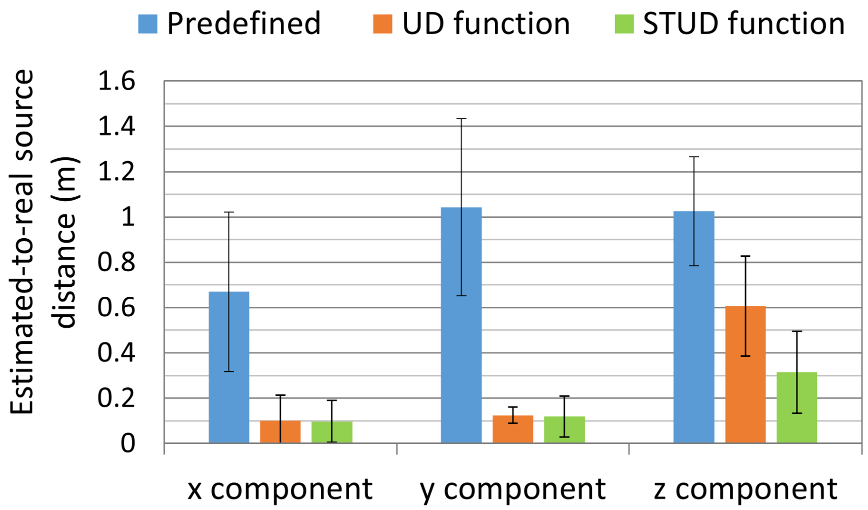

Figure 8.21: Estimated-to-real source distance components (d_x, d_y and d_z) for predefined paths and paths based on informative path planning (both with exit condition) considering the ^{137}Cs sources positioned at the center of the simulated container.

Examples of the EJ-200 scintillator count rate during predefined, UD and STUD profit function-based paths, for ^{137}Cs sources positioned at the corner and at the center of the simulated container are shown in Figures 8.22 and 8.23 respectively. These figures also present the distance d values between the estimated and real source positions.

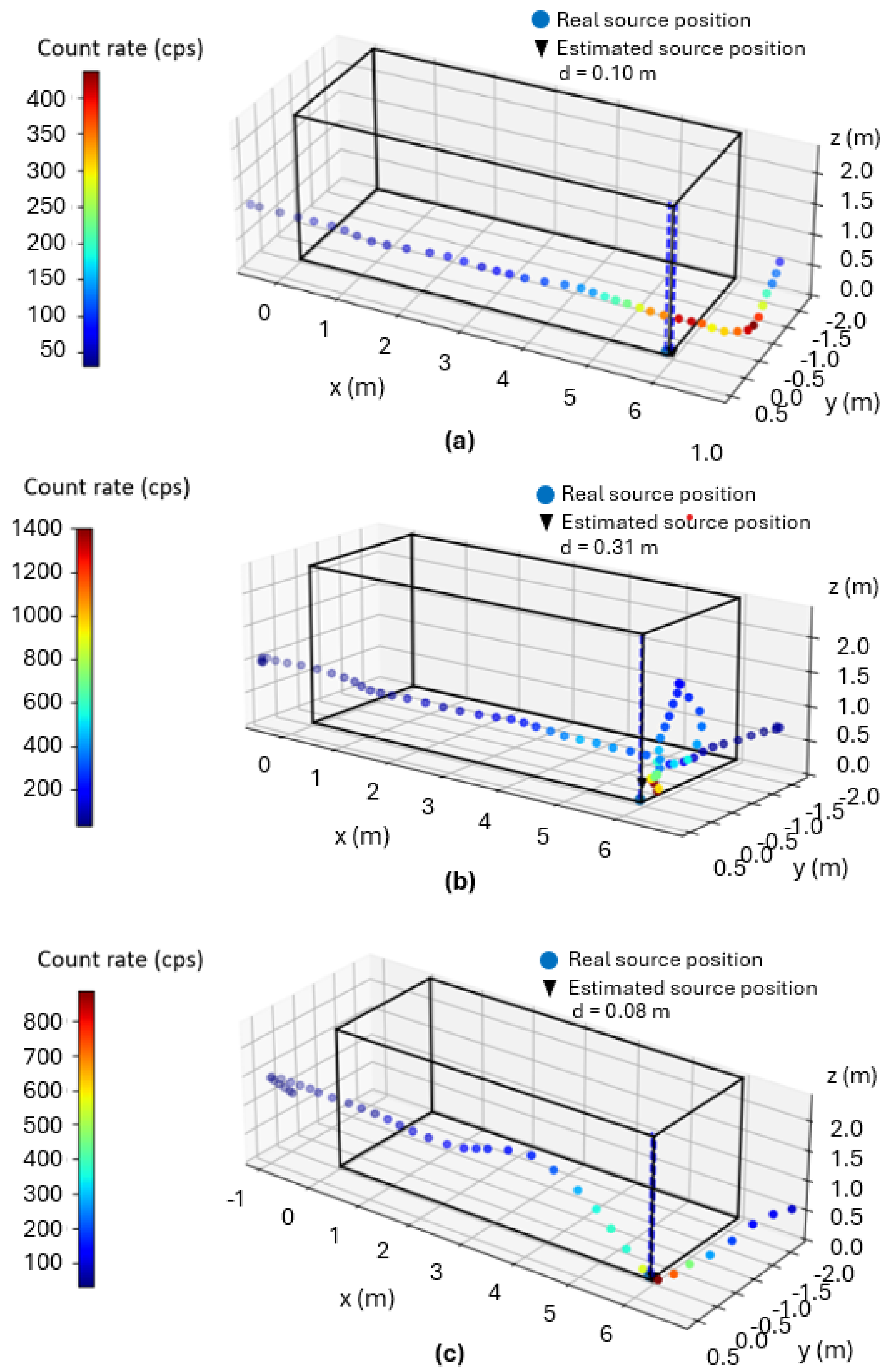

Figure 8.22: Example of the ^{137}Cs sources position estimation (MLE algorithm) –^{137}Cs sources at the corner– considering: (a) a predefined path (b) UD profit function-based path (c) STUD profit function-based path.

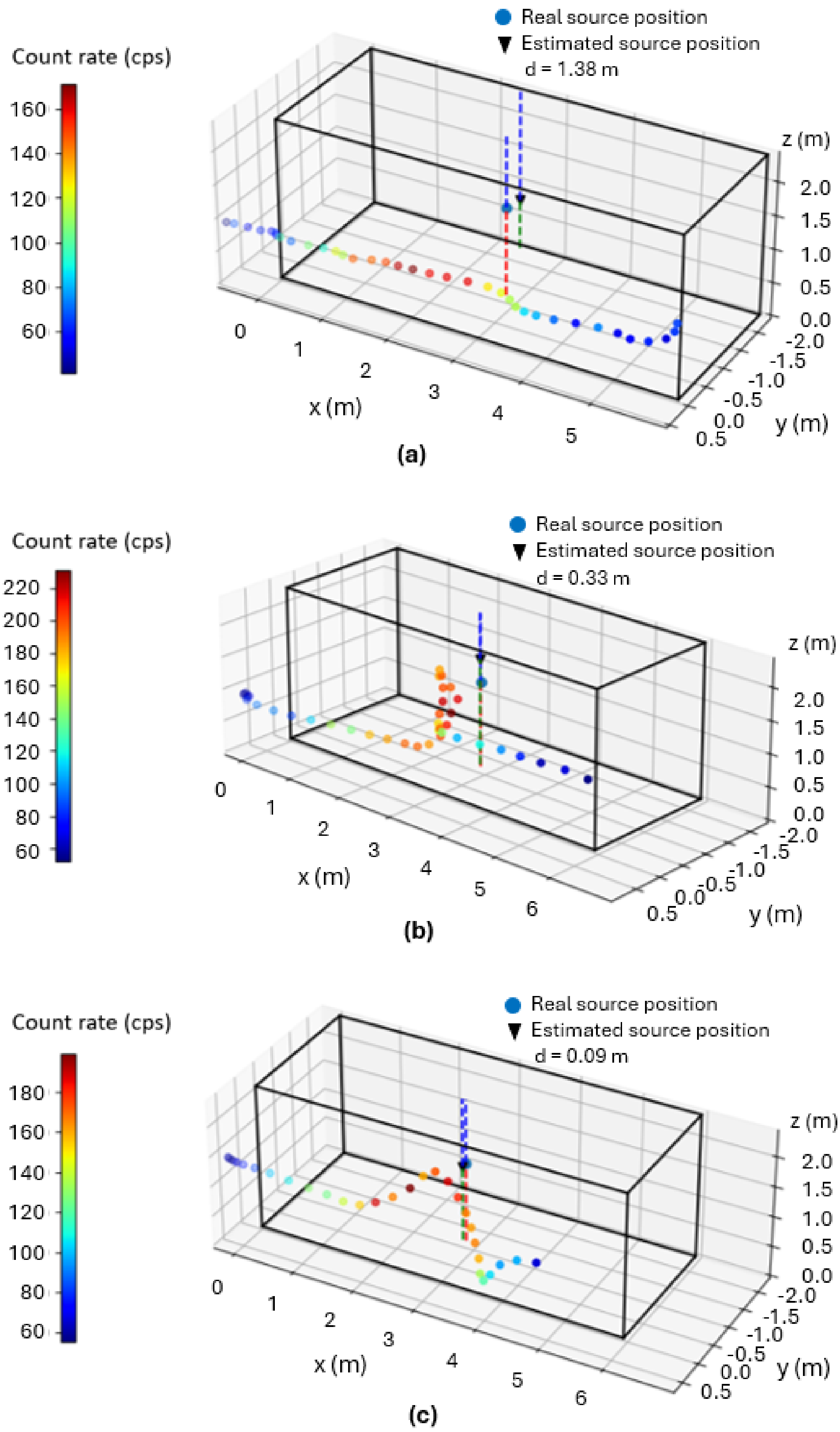

Figure 8.23: Example of the ^{137}Cs sources position estimation (MLE algorithm) –^{137}Cs sources at the center– considering: (a) a predefined path (b) UD profit function-based path (c) STUD profit function-based path.

Figure 8.24 shows the average path time for the different path types and ^{137}Cs sources position. As expected from previous results, the UD profit function takes longer to perform the sources localization, while the predefined paths and the STUD profit function-based paths (both with exit condition) showed similar average path times.

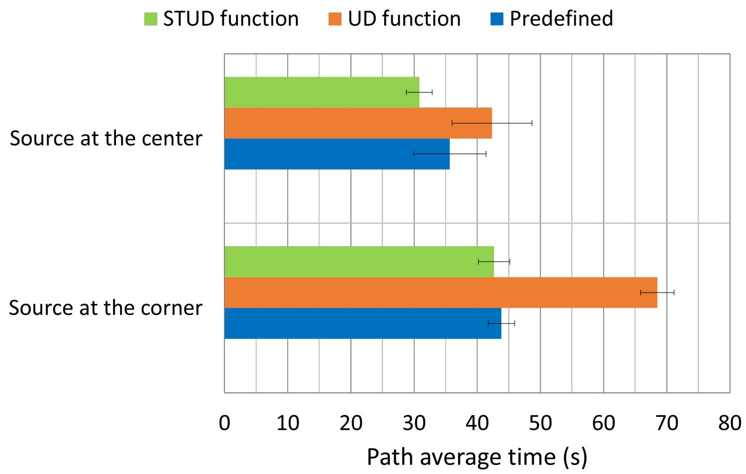

Figure 8.24: Average path time of the predefined paths and paths based on informative path planning (both with exit condition), along with their corresponding standard deviations.

Finally, the activity of the ^{137}Cs sources was calculated, as depicted in Figure 8.25, showing that the STUD profit function yielded values closer to the true activity. The UD profit function produced results comparable to those from predefined paths for the source located at the corner, while more accurate results were obtained for the source positioned at the center.

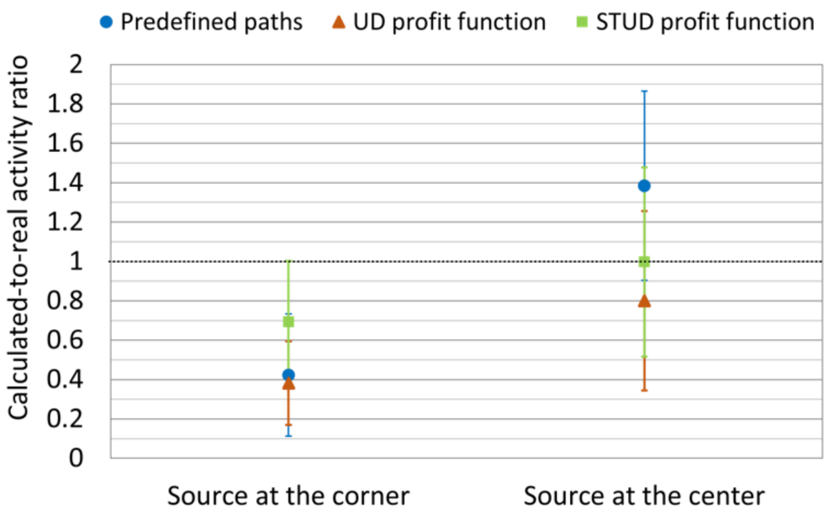

Figure 8.25: Comparison of the ratios between the experimentally calculated activity values and the real activity value considering predefined paths and paths based on informative path planning (both with exit condition), for ^{137}Cs sources positioned at the corner and at the center of the simulated container.

8.5 Discussion and conclusions

The field tests were designed to evaluate the effectiveness of informative path planning, using UD and STUD profit functions, compared to predefined paths for detecting and localizing a ~ 4 MBq ^{137}Cs source within a simulated maritime shipping container. The primary objective was to validate the simulator, comparing the simulated with experimental data. Although some discrepancies between the simulated and experimental data were observed, primarily due to the simulator not accounting for gamma-ray scattering and backscattering present in the experimental setup, the simulator effectively supports comparative studies of different path planning strategies.

The results from the field tests can be summarized as follows:

- Informative path planning based on the UD profit function provided more accurate source localization compared to predefined paths. Estimated-to-real source average distances were significantly lower with informative path planning, reaching 0.64 m for a source at the center and 0.42 m for a source at the corner of the container, compared to approximately 1.2 m and 0.8 m obtained with predefined paths (full laps) respectively. However, because the UD profit function-based path requires a pause for a vertical scan before resuming movement around the container, it results in a longer average inspection time compared to both predefined paths and the STUD profit function-based path (when exit condition are considered for all paths);
- The STUD profit function's superior tolerance to uncertainties, particularly in detector position, enabled it to achieve the best source localization accuracy compared to predefined paths and UD profit function-based paths, obtaining an estimated-to-real source average distances of 0.37 m for the source at the center and 0.32 m for the source at the corner. Additionally, it achieved the shortest average path/inspection time (lower than 45 seconds) when the exit condition was applied;
- The calculated source activity using the informative path planning yielded values significantly closer to the real source activity, in contrast to predefined paths, which exhibited deviations of up to three times.

The findings highlight that informative path planning is superior to predefined paths for source localization and activity estimation. The path adjustments increased data collection efficiency near the source, improving the source localization accuracy and ultimately reducing inspection time to less than one minute (with the use of the exit condition). In this thesis, comparable source localization accuracies were achieved relative to fixed detector networks. For instance, Sharma et al. [17] achieved a source position accuracy of approximately 0.53 m for a 189 kBq ^{137}Cs source within a $5\,m \times 5\,m \times 5\,m$ volume using five $NaI(Tl)$ detectors over a measuring time of 3 minutes. However, this fixed-detector approach is impractical for large areas like seaports. This thesis presents a more flexible solution by proposing a compact and low-cost MRDS for inspecting stationary shipping containers, emphasizing the significance of these results and encouraging further development of the proposed solution for Security and Defence applications. The integration of the radiation detection system into a mobile platform, in particular an UAV, combined with the developed source search algorithm presents a viable alternative or complement to traditional RPMs, fixed detector networks and manual inspections (normally used for secondary inspections – source confirmation). For instance, the use of informative path planning, in particular the STUD profit function with an exit condition can significantly improve source localization accuracy within a container, while also reducing the time required for secondary inspections at seaports, which currently rely on portable equipment without a source localization algorithm and can take up to 20 minutes to complete. Future research should address the shielding limitations and explore further improvements in path planning algorithms for diverse operational scenarios. Since the largest contributor to the uncertainty in source localization and activity calculation is the uncertainty in the detection system's position at any given moment, it would be recommended to use in the future a more advanced GNSS position sensor with improved accuracy.

9 Conclusions

During the Fukushima NPP accident, the absence of advanced mobile radiation detection and measurement technology, particularly unmanned vehicles, resulted in limited data collection on critical parameters such as the activity released by the radionuclides and the spatial distribution and direction of the radioactive plume. This deficiency significantly hindered effective sheltering and evacuation decisions as well as other RN emergency response countermeasures. The Fukushima NPP accident and its aftermath marked the first use of UAVs which significantly improved the spatial resolution of contaminated area mapping (essential for identifying no-go zones), and the effectiveness of monitoring and remediation measures. Additionally, new technologies, such as compact portable radiation sensors and advanced unmanned vehicles, have emerged, enabling efficient radiation detection and contributing to reduce human exposure to ionizing radiation. These innovations are nowadays crucial for responding to radiological and nuclear accidents and paramount to combating transnational threats involving radionuclides. To combat nuclear terrorism and the smuggling of SNM and other radioactive materials, it is essential to focus on preventing illicit trafficking.

Illicit trafficking of SNM and radioactive materials poses a global threat, as these materials can be used in RDDs, REDs, and improvised nuclear devices INDs. While INDs can cause massive casualties, RDDs and REDs can lead to significant social and economic disruption. Detection primarily relies on static RPMs at certain border crossings, airports, and maritime ports, including shipping container terminals. Radionuclides of potential concern in Security and Defence scenarios include those that emit gamma, alpha, beta, and neutron radiation. Due to the short range of alpha particles in the air (up to 4 cm) and their ability to be easily stopped by a sheet of paper, the detection systems normally used in fixed and portable RPMs, as well as mobile radiation detection systems that operate at distances in the order of a meter, do not take into account the detection of alpha particles. However alpha emitters can emit other types of radiation, such as gamma rays and, less commonly, neutrons.

RPMs typically consist of large sheets of PVT scintillators for gamma-ray detection and ^{3}He proportional counters for neutron detection, inspecting vehicles cargo as they pass through at controlled speeds. Considering that approximately 80% of global trade is conducted by sea, it is crucial to monitor the goods arriving at seaports, particularly those transported in standard maritime containers (20 ft and 40 ft-long). However, the RPMs high cost limits their widespread deployment across all seaports. Furthermore, their placement at seaport entry and exit points prevents the inspection of many containers that are transshipped from one vessel to another. Additionally, due to the global shortage of ^{3}He gas, developing alternative technologies for neutron detection is crucial. Neutron detection systems allows to identify neutron sources such as ^{252}Cf, $^{241}Am-Be$, and SNM like plutonium and HEU. Although $^{241}Am-Be$ and SNM also emit characteristic gamma rays, their low energy and the ease of shielding, concealing or masking by using NORM make them difficult to detect. Additionally, the limited number of commercial neutron sources and the lower natural background of neutrons compared to gamma rays make neutron detection a clear indicator of the presence of these radioactive materials. Therefore, integrating neutron detection systems alongside gamma-ray detection is essential in Security and Defence scenarios.

Although mobile radiation detection systems are available, their considerable weight and size, necessary for efficiently detecting distant sources, typically require transportation by cars and vans, limiting their flexibility and efficiency. Compact and lightweight gamma-ray detection systems with spectrometry capabilities, such as semiconductor CZT or inorganic scintillators coupled to SiPMs (e.g., $CsI(Tl)$ scintillator), can be deployed on small unmanned aerial vehicles (e.g., multirotors). However, their high cost and limited sensitive volume restrict their widespread use in Defence and Security scenarios.

Despite the fact that fixed detector networks being described in the literature can be deployed as an alternative to RPMs and portable/mobile radiation detection systems, their large-scale implementation in a seaport is impractical due to the vast number of detectors required for adequate coverage. Fixed detector networks utilize algorithms such as Particle Filter and MLE for radioactive source detection and localization.

Gamma source localization algorithms using mobile radiation detection systems are also described in literature, however they are normally applied for source search in the surface (e.g. hot spots localization on the ground).

9.1 Novel concept of a mobile radiation detection system proposed in this thesis

In this thesis a novel concept of a mobile radiation detection system to perform inspections to maritime shipping containers cargo is proposed, its design is studied and optimized and its performance is assessed. Several key considerations were addressed to ensure this system is particularly effective for Security and Defence applications, enabling the simultaneous detection and localization of hidden neutron and gamma-ray/beta sources, namely:

- **Gamma/beta detection system.** The use of a EJ-200 plastic scintillator with a diameter of 110 mm, a depth of 30 mm, and a weight of 517 g for gamma rays detection. Other features include the use of: SiPM sensors, a ultra-thin titanium window (32 µm) for improved beta particles detection (allowing detection of beta sources such as ^{90}Sr), and an additional +5V power plug to support the neutron detection system (to allow the use of a single Topaz-SiPM MCA device). Compared to semiconductors and inorganic scintillators, plastic scintillators features the following advantages: low-cost, fast response, large volumes and different shapes are available, and good physical and chemical properties featuring robust and non-hygroscopic characteristics (more resistant to material cracking and requires lighter detector housings). Monte Carlo simulations of the detection efficiency of the EJ-200 scintillator compared with a weight equivalent $CsI(Tl)$ scintillator were performed and compared with laboratory and field tests;
- **Neutron detection system.** The use of a scintillator composed by two $25 \times 90 \times 0.32\,mm^3$ layers of EJ-426HD scintillation material (with ^6Li content) and SiPM sensors, for the thermal neutron detection (weight: 90 g). In addition to the analog output, it has a digital output which provides TTL signals corresponding to the neutron counts for General-Purpose Input/Output (GPIO) port connection. The neutron detector was combined with polyethylene moderator plates to increase detection efficiency to neutron sources such as plutonium, ^{252}Cf or $^{241}Am - Be$ (which have a significant fast neutron component in the energy spectrum). Monte Carlo simulations, validated with laboratory and field tests, were used to optimize the neutron detection system configuration to an $^{241}Am - Be$ neutron source (moderated or not);
- **The use of SiPM sensors.** In contrast with traditional PMTs, SiPM enables a more compact, lightweight, and energy-efficient detection system. SiPM sensors are also immune to magnetic fields, making them ideal for the inspection and monitoring of fusion reactors or particle accelerator facilities;
- **Radiation detection system integration into a multirotor platform.** The use of robust, compact and low-cost radiation sensitive materials (scintillators with SiPM), low power consumption detectors (0.1 W, 20 mA @ 5V), the use of a single acquisition and processing unit (Topaz-SiPM MCA), and the use of an independent GNSS receiver and power supply batteries allowed the easy integration into a multirotor platform. These characteristics also enable seamless integration with various mobile platforms (aerial, maritime, terrestrial, or hybrid) and make the system easily replicable for deployment in a fleet of unmanned vehicles;
- **Gamma-ray source localization algorithm.** To achieve an efficient and accurate gamma-ray source position estimation an MLE algorithm was used;
- **Data acquisition and processing algorithm**. Radiation detectors and other sensors

data (GNSS receiver and distance sensors) were synchronized to generate a timestamped information at every second, allowing simultaneous gamma and neutron source detection;

- **Radiological inspection of a maritime shipping container.** Field tests of the radiation detection system, used as a handheld equipment or integrated into a multirotor, were performed to detect a hidden 4 MBq ^{137}Cs radioactive source and a 1.45 GBq $^{241}Am-Be$ neutron source. To be able to detect and localize the radiation sources predefined paths around a shipping container at a constant speed (0.33 m/s or 0.2 m/s) and at a fixed distance from the container walls (1 m) were considered;
- **Informative path planning.** An informative path planning algorithm, based on three different profit functions, was implemented to determine how and when to adjust the path height during the container inspections, to enhance source localization accuracy. The *Step* profit function adjusts the path height based on the source position estimate at a given instant (obtained using the MLE algorithm), while the UD and STUD profit functions utilize real-time data to perform either a vertical scan of the container or a sinusoidal path near the hot spot, respectively;
- **Computer simulator.** The radiological inspection for detecting and localizing a gamma source hidden in a shipping container was simulated using a Python program developed from scratch. To assess the performance of informative path planning compared to predefined trajectories, the simulation accounted for key physical phenomena, including radiation attenuation by container walls and air, source emission characteristics, and the path followed by the EJ-200 detector, with counts recorded per second using a cylindrical approximation. During the simulation, each radiation data point was analyzed using the MLE algorithm to estimate the source position and its associated uncertainties. The simulated results were validated through field tests, both of which utilized a constant speed of 0.2 m/s and maintained a fixed 0.5 m distance from the container walls to maximize radiation sensitivity;
- **Radiation source search.** The radiation source search algorithm integrates all the described algorithms, providing real-time results to the radiation detection system operator. These results include: (i) detection of neutron sources based on counts exceeding background levels; (ii) confirmation of gamma-ray source presence with 95% confidence; (iii) numerical and graphical estimation of the gamma-ray source position, along with the calculated activity and corresponding uncertainty.

The proposed radiation detection system demonstrated significant improvements in radioactive source localization accuracy and inspection time when using informative path planning compared to predefined paths. The proposed method represents an alternative or complement to RPMs, fixed detector networks and mobile radiation detection systems based on expensive radiation detection systems such as semiconductors and inorganic scintillators (which are normally sensitive to only gamma-ray radiation). The Monte Carlo simulation results were validated by laboratory and field tests which confirmed the system's effectiveness and efficiency to detect and provide an approximate location of a neutron source, and to detect, localize and quantify a gamma-ray source, validating the theoretical models and algorithms. Despite some limitations related to detection system position uncertainty, the findings provide a robust foundation for further advancements in UAV-based radiation detection technology.

9.2 Main results and contributions

The main components and results of this Ph.D. thesis work and associated research were as follows:

Development of a portable neutron detection system for Security and Defence applications. Utilizing the EJ-426HD scintillator with SiPM sensors, a lightweight (1.2 kg with four 20-mm thick HDPE moderator plates) and compact neutron detection system was built, featuring:

- **Optimized neutron efficiency to both thermal and fast neutrons.** Due to the high thermal neutron cross section of ^6Li (940 barns) and by introducing polyethylene moderator plates around the EJ-426HD detector;
- **Low gamma-ray sensitivity.** No significant variation in neutron counts was registered when a 3.9 mCi ^{137}Cs source was placed one meter away; and
- **Low power consumption (0.1 W).**

Through MC simulations, the geometry and materials of the neutron moderator were optimized in terms of detection efficiency. The moderator plates were then prototyped and tested using different detection system configurations. Compared to a common cylindrical moderator found in radiological protection applications, the developed neutron moderator plates presents the following advantages:

- **Lightweight and compact.** The incorporation of moderator plates reduced the system's overall size while halving the weight compared to the cylindrical moderator;
- **Modular configuration.** By changing the number and position of moderator plates relative to the EJ-426HD scintillator the detection efficiency can be optimized to different neutron sources (with different energy spectrum) and to moderated (shielded) sources. The developed M40R40 detection system configuration, which means that the EJ-426HD detector is surrounded by 40-mm thick polyethylene moderator plates (where "M" stands for moderator side and "R" for reflector side), showed a high detection efficiency to both moderated and unmoderated $^{241}Am-Be$ source, along with an effective source position discrimination. Moving moderator plates to the reflector side increased detection efficiency by 12% to 79%, with the M20R75 configuration achieving the highest efficiency for the moderated $^{241}Am-Be$ source.

EJ-200 plastic scintillator comparison with a commercial and weight equivalent CsI(Tl) inorganic scintillator. MC simulations were performed to both detectors to obtain the detection efficiency, which were then validated by experimental and field tests. Despite the higher intrinsic gamma-ray detection efficiency of the $CsI(Tl)$ scintillator, the EJ-200 presented a SNR and consequently a total detection efficiency approximately three times higher than $CsI(Tl)$ for a ^{137}Cs source placed at 1 to 5 m distance. This significant difference in total detection efficiency is due to the higher geometric detection efficiency of EJ-200 (with a pancake shape), thus presenting the best efficiency per weight. The EJ-200 scintillator also showed better detection efficiency to beta particles (1.68 higher) than $CsI(Tl)$. The higher energy threshold of EJ-200 prevented it to detect ^{241}Am gamma rays (with energies bellow ≈ 60 keV).

Although plastic scintillators have poor energy resolution and low light yield–limitations that generally hinder their ability to identify radionuclides and detect low-energy gamma rays (below 60 keV)–several approaches outlined in the literature can help mitigate these inherent drawbacks and improve their performance in radiation detection applications, namely:

- The use of high-Z sensitized plastic scintillators;
- The use of smaller plastic scintillator volumes with a higher density of SiPM sensors for improved scintillation light collection;
- The use of spectrum analysis algorithms, such as EW methods, to enable the discrimination between threat radiation sources and NORM.

Deployment of a neutron and gamma-ray detection system coupled to a multirotor for screening shipping container cargo. The EJ-426HD neutron detection system, configured with the M40R40 moderator, and the EJ-200 detection system were deployed simultaneously to detect and localize a gamma and neutron source within a 20 ft-long shipping container (with internal dimensions of 5.94 m × 2.34 m × 2.39 m) using predefined paths. The key results are summarized as follows:

- The high maneuverability of the multirotor enabled the radiation detection system to perform measurements from a distance of at least one meter from the shipping container. This capability significantly enhanced overall detection efficiency compared to other mobile platforms such as cars or vans. Depending on the multirotor's path and battery pack used, a flight time of 17-22 minutes was achieved using the multirotor with the radiation detection system. Additionally, the multirotor's vertical takeoff, landing, and hovering capabilities enable inspections at elevated heights, such as tall infrastructures or stacked shipping containers up to 13 meters high. Although the multirotor was tele-operated in this thesis, it can also be operated semi-autonomously or fully autonomously, allowing for automated inspections and continuous monitoring;

- The radiation detection system successfully detected a Troxler equipment, equipped with a 1.45 GBq (39.2 mCi) $^{241}Am-Be$ neutron source and a shielded 215 MBq (5.81 mCi) ^{137}Cs source (with the source rod in the safe position), inside the shipping container. Although the EJ-200 scintillator struggled to detect the shielded ^{137}Cs source, the EJ-426HD detection system confidently detected the neutrons emitted by the $^{241}Am-Be$ source;
- By following predefined paths at three different heights, the system could approximate the neutron source's location within the container, identifying whether it was positioned at the top, middle, or bottom;
- The EJ-200 detection system's ability to accurately locate a $\sim$ 4 MBq (0.11 mCi) ^{137}Cs radioactive source was demonstrated by performing predefined paths around the container using both handheld equipment and the multirotor-integrated radiation detection system (proof-of-concept). During manual inspections, average estimated-to-real distances ranged from 0.5 m to 0.8 m for centrally positioned sources and up to 1.3 m for sources located in the container's corners. In contrast, multirotor-based inspections showed average distances between 0.4 m and 0.9 m for centrally positioned sources, with distances reaching up to 2.5 m for sources positioned at the corner.

Simulation results for the detection and localization of a ^{137}Cs gamma-ray source placed inside a shipping container using the EJ-200 scintillator. A software/computer simulation program ("simulator") was developed from scratch to analyze the benefits of using informative path planning on the source localization accuracy. This approach was used to improve the information gathered by the radiation detection system during the path around the shipping container. Profit functions based on the source position estimation obtained at each data point and based on real-time detector counts were proposed and compared with predefined paths. Uncertainties were added to the detector position and counts registered to assess their impact on the localization accuracy. The combined use of an informative path planning with an exit condition allowed to improve the source position accuracy and reduce the inspection time, compared to predefined paths. Although the UD profit function demonstrated superior accuracy in source localization, the inspection time is significantly longer compared to the STUD profit function and predefined paths, due to the need to halt horizontal movement to conduct vertical scans. While paths based on STUD profit function allowed to improve the source localization accuracy (compared to predefined paths), it showed the lowest inspection time and a greater resilience to uncertainties (detector position and counts variation). For manual inspection, the path based on the UD profit function is easier to execute; however, to ensure accurate source localization, the detector position uncertainty must be maintained below 0.5 m.

Gamma source localization using informative path planning (manual inspection). Field tests were performed with the radiation detection system (handheld equipment) for the detection and localization of a ~ 4 MBq ^{137}Cs source concealed inside a simulated shipping container. In these tests, neither a shipping container nor a multirotor was available. Instead, the handheld configuration was used, with a simulated container defined by floor markings to represent its boundaries. Both predefined paths and informative path planning were tested, with key findings as follows:

- By analyzing the detection system's path around a simulated container, the informative path planning based on the UD and STUD profit functions showed improvements on the source localization accuracy to better than approximately 0.6 m and 0.4 m, respectively, compared to predefined paths (source position accuracy up to approximately 1.2 m using full laps). Additionally, the STUD profit function demonstrated greater tolerance to uncertainties, such as detector position inaccuracies. This represents a substantial improvement over both predefined paths and the UD profit function;
- Thanks to the improved source position estimates, informative path planning enabled more accurate calculations of the radioactive source's activity;
- The results also demonstrated that the use of informative path planning with an exit condition, which allowed to conclude the inspection when certain criteria were fulfilled, consistently resulted in shorter time intervals for accurately locating the radioactive source across various initial path heights and source position configurations. For instance, using the STUD profit function inspection times lower than 45 seconds were obtained.

These outcomes emphasize the effectiveness of the informative path planning in enhancing the accuracy of radioactive source localization using a mobile radiation detection system. The source localization accuracy in this study is comparable to the results obtained by Sharma et al. [17], who achieved an accuracy better than 0.6 m for a 189 kBq ^{137}Cs source using a fixed detector networks. While the source activity used in their study was lower than in this thesis, the higher number of detection systems (five $NaI(Tl)$ scintillators) and the extended measurement time (3 minutes) needed to reach that accuracy underscore the effectiveness of both approaches. Therefore, the integration of the radiation detection system with a mobile platform, such as a UAV, and utilizing the developed source search algorithm offers a viable alternative or complement to traditional RPMs, fixed detector networks, and manual inspections used for secondary source confirmation. For instance, employing informative path planning–particularly the STUD profit function with an exit condition–can greatly enhance source localization accuracy within containers and reduce secondary inspection times at seaports. Currently, these inspections, which use portable equipment without source localization algorithms, can take up to 20 minutes. Additionally, if a secondary inspection is inconclusive a tertiary inspection may be needed, requiring unpacking the container's contents, which is time-intensive and laborious (a team of five people and three hours work is normally necessary to inspect a 40 ft long shipping container). Therefore, an accurate and efficient source detection and localization are essential to avoid delays and ensure the normal flow of cargo at seaports.

The research also highlighted the potential of using the EJ-200 plastic scintillator and the EJ-426HD neutron detection system with SiPM sensors for inspecting critical infrastructures beyond maritime containers, such as nuclear facilities, due to their cost-effectiveness and ease of integration onto compact platforms.

The key contributions of this Ph.D. thesis include:

- **A comprehensive review of state-of-the-art radiation detection systems.** The thesis begins by thoroughly examining the current radiation detection system technologies used in various Security and Safety scenarios. This review provides a solid foundation for understanding the limitations and potential improvements in existing detection systems and mobile platforms and was published in an international journal with peer-reviewing;
- **The development of a portable radiation detection system.** A novel radiation detection system based on EJ-200 and EJ-426HD scintillators with SiPM sensors was developed. This system is capable of detecting gamma radiation, beta particles, and neutrons. Unlike previous approaches that primarily used inorganic scintillators and semiconductors, this system offers enhanced geometric detection efficiency due to the use of larger volumes and pancake-like shapes;
- **Monte Carlo modelling and simulation.** To optimize the detection system, MC simulations using the MCNP6 were conducted. These simulations were validated through laboratory and field tests, ensuring the accuracy and reliability of the detection system;
- **The development of an innovative neutron detection system.** Addressing the global shortage of ^{3}He, the thesis introduces a neutron detection system based on ^{6}Li and a modular neutron moderator. This modular design allows for the optimization of detection efficiency and flexibility in detecting various neutron sources and both shielded and unshielded sources;
- **Integration of SiPM sensors.** The use of SiPM sensors instead of traditional PMTs significantly reduced the size and weight of the detection system, enhancing its feasibility for integration into small mobile platforms with payload constraints;
- **A proposal for a two-stage detection/localization and identification methodology.** The proposed methodology entails the swift detection and localization of radionuclides using cost-effective radiation detection systems, such as those employing EJ-200 and EJ-426HD scintillator materials. This is followed by identification and quantification with detection systems that offer high energy resolution, such as inorganic scintillators or semiconductor detectors;
- **Deployment, custom mounting and integration of the neutron and gamma/beta radiation detection systems into a multirotor using 3D-printed, lightweight mounts**

and a carbon fiber sandwich plate. This design allows for easy installation and removal, facilitating its use across different platforms;

- **Algorithms development.** Custom algorithms for data processing, synchronization, and real-time remote data access were developed, enabling the detection system to operate independently or as part of various mobile platforms;
- **The implementation of an informative path planning.** A novel approach for path planning based on profit functions and an exit condition was introduced, where the detection system modifies its path according to the source position estimation or real-time measurements. Compared to predefined paths, this method enhances the accuracy of radioactive source localization and reduces inspection time. Exhaustive simulation tests were performed, validated by field tests;
- **Proof-of-concept for shipping container cargo inspection.** A successful demonstration validated the radiation detection system's capability to inspect shipping containers using a highly maneuverable UAV (multirotor). The system efficiently detected and localized both gamma-ray and neutron sources, offering a cost-effective alternative or complement to traditional RPM systems, manual inspections, and fixed detector networks, while enhancing flexibility and expanding the coverage area.

9.3 Limitations of the study

The MDA can be influenced by multiple variables (multiparametric problem), including path speed, the distance between the detection system and the container walls, the sampling or integration time of the detection system, and the detection system physical characteristics itself. Due to the complexity of accounting for all these factors, the source activity was fixed to isolate and observe the effects of the other variables, thereby facilitating the derivation of conclusive results for the developed radiation detection system. On the other hand, the difficulty in finding ^{137}Cs radioactive sources with activities above 4 MBq (a value close to the MDA), also hindered the possibility of conducting tests with other activity levels. Similarly, the availability of additional neutron sources with varying activities, beyond the 1.45 GBq $^{241}Am - Be$ source, would have been beneficial. For the purpose of radioactive source localization during the radiological inspection of the shipping container, a single isotropically emitting gamma-ray point source was assumed.

9.4 Future work

Some improvements and recommendations for future research include:

- Enhancement of the system's robustness to detector position uncertainty, possibly through the integration of an IMU or more advanced GNSS technologies such as

RTK-GNSS or differential GNSS to mitigate the limitations posed by a standalone GNSS receiver;
- Exploration of the integration of this technology with other sensor systems (e.g. chemical and/or biological sensors) to provide a more comprehensive situational awareness platform for Chemical, Biological, Nuclear, and Radiological (CBRN) teams;
- Evaluation of the impact of cargo materials and nearby containers on source localization and source activity estimation, with respect to radiation shielding and scattering effects;
- Analyze how changes in the desired minimum detectable activity affect inspection parameters, including path speed, detection system sampling/integration time, proximity of the detection system to the container, and the required system characteristics (e.g., effective area and thickness);
- Consideration of a scenario consisting of multiple radioactive sources hidden inside the shipping container or other suspect object/vehicle;
- Perform field tests with other radiation sources such as ^{252}Cf, with a neutron spectrum more similar to plutonium.

The long-term goal is to develop a fully autonomous fleet of unmanned vehicles for mobile radiation detection, capable of operating independently or cooperatively to provide continuous monitoring and inspection. This vision includes advancements in UAV technology (e.g. lightweight and long-lasting batteries), AI-driven data analysis, collision-free navigation and real-time communication networks.

Beyond shipping container inspection, this system could be adapted to perform inspections to nuclear facilities (e.g. to ensure regulatory compliance and early detection of potential leaks) or to provide a surface mapping in RN accidents and emergencies. Environmental monitoring around industrial sites or nuclear forensics are others promising applications.

Bibliography

[1] United States Government Accountability Office, "Radiation portal monitors DHS's fleet is lasting longer than expected, and future acquisitions focus on operational efficiencies accessible", Tech. Rep., 2016 (cit. on pp. 1, 2).

[2] International Atomic Energy Agency, "IAEA Incident and Trafficking Database (ITDB)", International Atomic Energy Agency, Tech. Rep., 2023 (cit. on pp. 2, 34, 48).

[3] International Atomic Energy Agency, "Combating illicit trafficking in nuclear and other radioactive material", International Atomic Energy Agency, Vienna, Tech. Rep. 6, 2008 (cit. on pp. 2, 32, 34, 35).

[4] United States Government Accountability Office, "Combating nuclear smuggling dhs has made progress deploying radiation detection equipment at U.S. ports-of entry, but concerns remain", Tech. Rep., 2010 (cit. on pp. 2, 3).

[5] R. T. Kouzes, J. H. Ely, L. E. Erikson, *et al.*, "Neutron detection alternatives to ^{3}He for national security applications", *Nuclear Instruments and Methods in Physics Research Section A: Accelerators, Spectrometers, Detectors and Associated Equipment*, vol. 623, no. 3, pp. 1035–1045, 2010. DOI: 10.1016/j.nima.2010.08.021 (cit. on pp. 2, 7–9, 53).

[6] G. Aloise, "Combating nuclear smuggling dhs's cost-benefit analysis to support the purchase of new radiation detection portal monitors was not based on available performance data and did not fully evaluate all the monitors' costs and benefits.", eng, Washington, DC, Tech. Rep., 2006 (cit. on pp. 2, 3).

[7] K. Bodewig, "Motorways of the sea detailed implementation plan of the european coordinator", European Commission, Tech. Rep., 2022 (cit. on p. 2).

[8] R. Downes, C. Hobbs, and D. Salisbury, "Combating nuclear smuggling? exploring drivers and challenges to detecting nuclear and radiological materials at maritime facilities", *Nonproliferation Review*, vol. 26, pp. 83–104, 1-2 2019-01. DOI: 10.1080/10736700.2019.1610256 (cit. on p. 2).

[9] International Atomic Energy Agency, "Safety of radiation sources and security of radioactive materials", ser. Proceedings Series, Vienna: International Atomic Energy Agency, 1999, ISBN: 92-0-101499-6 (cit. on p. 2).

[10] Hsu, Spencer S., "U.S. weighs how best to defend against nuclear threats", *Washington Post*, 2006. DOI: 10.1063/PT.5.020026 (cit. on p. 2).

[11] R. Mackenzie, T. Twomey, D. Upp, S. Hitch, and R. Keyser, "High resolution detection systems for interdiction of nuclear material trafficking", ORTEC, Tech. Rep. [Online]. Available: https://www.ortec-online.com/-/media/ametekortec/technical-papers/homeland-security-applications-and-chemical-weapons-assay-pins/high-resolution-detection-systems-interdiction-nuclear-material-trafficking.pdf?la=en&revision=4e003fd5-2696-4434-9596-cd50c720dc9f&hash=D876513FE8CC28B8D7FF8502FB07B6FE (cit. on p. 2).

[12] National Urban Security Technology Laboratory, "Portable radiation portal monitors market survey report", Tech. Rep., 2015, Accessed: 2023-09-30. [Online]. Available: https://www.dhs.gov/sites/default/files/publications/PortRadPortalMons-MSR_0315-508.pdf (cit. on p. 3).

[13] Global Security, *Homeland Security – Mobile Radiation Portal Monitors (RPM)*, https://www.globalsecurity.org/security/systems/mobile-rpm.htm, Accessed: 2023-09-30 (cit. on p. 3).

[14] Arktis, *Mobile radiation monitoring system*, https://www.arktis-detectors.com/de/products/mobile-radiation-monitoring-system/, Accessed: 2023-09-30 (cit. on pp. 3, 53).

[15] S.-W. Kwak, S.-S. Chang, and H.-S. Yoo, "Radiation detection system for prevention of illicit trafficking of nuclear and radioactive materials", *Journal of Radiation Protection*, vol. 35, 2010-01 (cit. on p. 3).

[16] N. S. Rao, S. Sen, M. L. Berry, *et al.*, "Datasets for radiation network algorithm development and testing", 2016-01. [Online]. Available: https://www.osti.gov/biblio/1327710 (cit. on pp. 3, 39–41).

[17] M. Sharma, A. Alajo, and H. Lee, "Three-dimensional localization of low activity gamma-ray sources in real-time scenarios", *Nuclear Instruments and Methods in Physics Research Section A Accelerators Spectrometers Detectors and Associated Equipment*, vol. 813, pp. 132–138, 2016-03. DOI: 10.1016/j.nima.2016.01.001 (cit. on pp. 3, 9, 39, 40, 42, 57, 161, 170).

[18] E. L. Connolly and P. G. Martin, "Current and prospective radiation detection systems, screening infrastructure and interpretive algorithms for the non-intrusive screening of shipping container cargo: A review", *Journal of Nuclear Engineering*, vol. 2, no. 3, pp. 246–280, 2021. DOI: 10.3390/jne2030023 (cit. on pp. 3, 40–42).

[19] R. Coogan and C. Marianno, "A strategic analysis of stationary radiation portal monitors and mobile detection systems in border monitoring", *Nuclear Engineering and Technology*, vol. 52, 2019-08. DOI: 10.1016/j.net.2019.08.010 (cit. on pp. 3, 35).

[20] Cleveland containers, *How high can shipping containers be stacked?*, https://www.clevelandcontainers.co.uk/news-and-blog/how-high-can-shipping-containers-be-stacked, Accessed: 2023-09-30 (cit. on p. 3).

[21] L. Marques, A. Vale, and P. Vaz, "State-of-the-art mobile radiation detection systems for different scenarios", *Sensors*, vol. 21, no. 4, 2021. DOI: 10.3390/s21041051 (cit. on pp. 3, 5, 6, 8, 31, 35, 37, 42, 48–50, 52).

[22] M. Harbaugh, "Unmanned aerial systems (UAS) for intelligence, surveillance, and reconnaissance (ISR)", Defense Systems Information Analysis Center, Tech. Rep., 2018 (cit. on p. 5).

[23] J. R. Centre, I. for Reference Materials, Measurements, *et al.*, *Possible scenarios for radiation measurements and sampling using unmanned systems*. Publications Office, 2014. DOI: 10.2788/60148 (cit. on p. 6).

[24] R. R. Murphy, *Disaster Robotics*. The MIT Press, 2017 (cit. on pp. 6, 47).

[25] Y. Sanada, T. Orita, and T. Torii, "Temporal variation of dose rate distribution around the Fukushima Daiichi nuclear power station using unmanned helicopter", *Applied Radiation and Isotopes*, vol. 118, pp. 308–316, 2016. DOI: 10.1016/j.apradiso.2016.09.008 (cit. on pp. 6, 48).

[26] A. Vale, R. Ventura, J. Corisco, N. Catarino, N. Veiga, and S. Sargento, "Heterogeneous drone fleet for radiological inspection", in *Unmanned Aerial Vehicles Applications: Challenges and Trends*, M. Abdelkader and A. Koubaa, Eds. Cham: Springer International Publishing, 2023, pp. 127–168, ISBN: 978-3-031-32037-8. DOI: 10.1007/978-3-031-32037-8_4 (cit. on pp. 6, 49).

[27] D. T. Connor, K. Wood, P. G. Martin, *et al.*, "Radiological mapping of post-disaster nuclear environments using fixed-wing unmanned aerial systems: A study from Chornobyl", *Frontiers in Robotics and AI*, vol. 6, 2020. DOI: 10.3389/frobt.2019.00149 (cit. on pp. 7, 48).

[28] D. Connor, P. Martin, H. Pullin, *et al.*, "Radiological comparison of a FDNPP waste storage site during and after construction", *Environmental Pollution*, vol. 243, pp. 582–590, 2018. DOI: 10.1016/j.envpol.2018.08.099 (cit. on pp. 7, 49).

[29] Kromek, *What is CZT?*, https://www.kromek.com/czt/, Accessed: 2023-09-30 (cit. on pp. 7, 43, 49).

[30] O. Šálek, M. Matolín, and L. Gryc, "Mapping of radiation anomalies using UAV mini-airborne gamma-ray spectrometry", *Journal of Environmental Radioactivity*, vol. 182, pp. 101–107, 2018. DOI: 10.1016/j.jenvrad.2017.11.033 (cit. on p. 7).

[31] G. F. Knoll, *Radiation Detection and Measurement*. 2010 (cit. on pp. 8, 18, 20, 21, 24, 25, 29, 44, 45).

[32] A. Stoykov, J.-B. Mosset, U. Greuter, M. Hildebrandt, and N. Schlumpf, "A SiPM-based ZnS:6LiF scintillation neutron detector", *Nuclear Instruments and Methods in Physics Research Section A: Accelerators, Spectrometers, Detectors and Associated Equipment*, vol. 787, pp. 361–366, 2015, New Developments in Photodetection NDIP14. DOI: 10.1016/j.nima.2015.01.076 (cit. on p. 8).

[33] A. Osovizky, K. Pritchard, Y. Yehuda-Zada, *et al.*, "Selection of silicon photomultipliers for a 6LiF:ZnS(Ag) scintillator based cold neutron detector", *Journal of Physics Communications*, vol. 2, no. 4, p. 045 009, 2018-04. DOI: 10.1088/2399-6528/aab381 (cit. on p. 8).

[34] Y. Yehuda-Zada, K. Pritchard, J. Ziegler, *et al.*, "Optimization of 6LiF:ZnS(Ag) scintillator light yield using GEANT4", *Nuclear Instruments and Methods in Physics Research Section A: Accelerators, Spectrometers, Detectors and Associated Equipment*, vol. 892, pp. 59–69, 2018. DOI: 10.1016/j.nima.2018.02.099 (cit. on p. 8).

[35] D. Serini, P. De La Torre Luque, L. Di Venere, *et al.*, "Characterization of plastic scintillators equipped with SiPM for the next generation of satellites for the study of cosmic radiation", *Nuovo Cimento C*, vol. 43, no. 2-3, p. 100, 2020. DOI: 10.1393/ncc/i2020-20100-x. [Online]. Available: https://cds.cern.ch/record/2766505 (cit. on p. 8).

[36] J. Benito, M. García-Díez, V. Sánchez-Tembleque, L. Fraile, and J. M. Udías, "Performance study of plastic scintillators coupled to sipm for fast-timing measurements", in *2021 IEEE Nuclear Science Symposium and Medical Imaging Conference (NSS/MIC)*, 2021, pp. 1–3. DOI: 10.1109/NSS/MIC44867.2021.9875794 (cit. on p. 8).

[37] D. Grzonka, P. Bergmann, T. Hahnraths von der Gracht, *et al.*, "A large area efficient trigger scintillator with SiPM read out", *Nuclear Instruments and Methods in Physics Research Section A: Accelerators, Spectrometers, Detectors and Associated Equipment*, vol. 1041, p. 167 410, 2022. DOI: 10.1016/j.nima.2022.167410 (cit. on p. 8).

[38] Y. Brouwer, A. Vale, D. Macedo, B. Gonçalves, and H. Fernandes, "Radioactive hot-spot detection using unmanned aerial vehicle surveillance", *EPJ Web Conf.*, vol. 225, p. 06 005, 2020. DOI: 10.1051/epjconf/202022506005 (cit. on pp. 9, 41, 42, 49, 67).

[39] A. H. Zakaria, Y. M. Mustafah, J. Abdullah, N. Khair, and T. Abdullah, "Development of autonomous radiation mapping robot", *Procedia Computer Science*, vol. 105, pp. 81–86, 2017, 2016 IEEE International Symposium on Robotics and Intelligent Sensors, IRIS 2016, 17-20 December 2016, Tokyo, Japan. DOI: 10.1016/j.procs.2017.01.203 (cit. on pp. 9, 41, 42, 47).

[40] J. Towler, B. Krawiec, and K. Kochersberger, "Radiation mapping in post-disaster environments using an autonomous helicopter", *Remote Sensing*, vol. 4, no. 7, pp. 1995–2015, 2012, ISSN: 2072-4292. DOI: 10.3390/rs4071995 (cit. on pp. 9, 42, 48).

[41] T. Kishimoto, H. Woo, R. Komatsu, *et al.*, “Path planning for localization of radiation sources based on principal component analysis”, *Applied Sciences*, vol. 11, no. 10, 2021. DOI: `10.3390/app11104707` (cit. on pp. 9, 42).

[42] Y. Brouwer, A. Vale, and R. Ventura, “Informative path planner with exploration–exploitation trade-off for radiological surveys in non-convex scenarios”, *Robotics and Autonomous Systems*, vol. 136, p. 103 691, 2021. DOI: `10.1016/j.robot.2020.103691` (cit. on pp. 9, 42, 58).

[43] C. Q. Wu, M. L. Berry, K. M. Grieme, *et al.*, “Network detection of radiation sources using localization-based approaches”, *IEEE Transactions on Industrial Informatics*, vol. 15, no. 4, pp. 2308–2320, 2019. DOI: `10.1109/TII.2019.2891253` (cit. on pp. 9, 41, 57).

[44] J. Cook, R. C. Smith, C. Ramirez, and N. S. V. Rao, *Particle filtering convergence results for radiation source detection*, 2020. arXiv: `2004.08953` (cit. on pp. 9, 40–42, 57).

[45] IAEA, *What are radioactive sources?*, `https://www.iaea.org/newscenter/news/what-are-radioactive-sources`, Accessed: 2024-01-05 (cit. on pp. 17, 18).

[46] Ionactive, *Radioactivity - the becquerel (Bq)*, `https://ionactive.co.uk/resource-hub/guidance/radioactivity-the-becquerel-bq`, Accessed: 2024-08-01 (cit. on p. 17).

[47] K. S. Krane, *Introductory Nuclear Physics*. New York: Wiley, 1987 (cit. on pp. 17, 18, 21).

[48] Australian Radiation Protection and Nuclear Safety Agency, *Other types of radioactive decay*, `https://www.arpansa.gov.au/understanding-radiation/what-is-radiation/ionising-radiation/radiation-decay`, Accessed: 2024-01-22 (cit. on p. 18).

[49] G. Scharff-Goldhaber and G. S. Klaiber, “Spontaneous emission of neutrons from uranium”, *Phys. Rev.*, vol. 70, pp. 229–229, 3-4 1946-08. DOI: `10.1103/PhysRev.70.229.2` (cit. on p. 18).

[50] K. Iniewski, *Radiation Effects in Semiconductors*. CRC Press, 2018 (cit. on p. 18).

[51] Harvard University, *Lecture Demonstrations*, `https://sciencedemonstrations.fas.harvard.edu`, Accessed: 2024-04-01 (cit. on p. 18).

[52] N. Tsoulfanidis and S. Landsberger, *Measurement and Detection of Radiation*. CRC Press, 2021 (cit. on pp. 18–20, 25, 66).

[53] University of Missouri, *Radionuclide data sheet strontium–90*, `https://ehs.missouri.edu/sites/ehs/files/pdf/isotopedata/sr-90.pdf`, Accessed: 2024-01-05 (cit. on p. 19).

[54] R. M. Keyser and T. R. Twomey, "Detector resolution required for accurate identification in common gamma-ray masking situations", *Journal of Radioanalytical and Nuclear Chemistry*, vol. 282, pp. 841–847, 3 2009-12, ISSN: 02365731. DOI: 10.1007/s10967-009-0233-1 (cit. on p. 21).

[55] N. power, *Neutron cross-section*, https://www.nuclear-power.com/neutron-cross-section/, Accessed: 2024-02-17 (cit. on p. 22).

[56] M. F. L'Annunziata, "1 - Nuclear radiation, its interaction with matter and radioisotope decay", in *Handbook of Radioactivity Analysis (Second Edition)*, M. F. L'Annunziata, Ed., Second Edition, San Diego: Academic Press, 2003, pp. 1–121, ISBN: 978-0-12-436603-9. DOI: https://doi.org/10.1016/B978-012436603-9/50006-5 (cit. on p. 22).

[57] A. Furrer, "Neutron sources", in *Encyclopedia of Condensed Matter Physics*, F. Bassani, G. L. Liedl, and P. Wyder, Eds., Oxford: Elsevier, 2005, pp. 69–75, ISBN: 978-0-12-369401-0. DOI: 10.1016/B0-12-369401-9/00633-1 (cit. on p. 22).

[58] International Atomic Energy Agency, "Neutron monitoring for radiation protection", International Atomic Energy Agency, Vienna, Tech. Rep. 115, 2023. [Online]. Available: https://www.iaea.org/publications/15007/neutron-monitoring-for-radiation-protection (cit. on pp. 23, 28, 30).

[59] Mirion, *Neutron detection and counting*, https://www.mirion.com/discover/knowledge-hub/articles/education/nuclear-measurement-fundamental-principle-neutron-detection-and-counting, Accessed: 2023-09-30 (cit. on pp. 23, 24).

[60] R. T. Kouzes, E. R. Siciliano, J. H. Ely, P. E. Keller, and R. J. McConn, "Passive neutron detection for interdiction of nuclear material at borders", *Nuclear Instruments and Methods in Physics Research Section A: Accelerators, Spectrometers, Detectors and Associated Equipment*, vol. 584, no. 2, pp. 383–400, 2008. DOI: 10.1016/j.nima.2007.10.026 (cit. on pp. 24, 33).

[61] P. Peerani and A. Tomanin, "Surrogates of plutonium for detection equipment testing", *Nuclear Instruments and Methods in Physics Research Section A: Accelerators, Spectrometers, Detectors and Associated Equipment*, vol. 654, no. 1, pp. 613–620, 2011. DOI: 10.1016/j.nima.2011.04.065 (cit. on p. 24).

[62] J. Flamanc and C. Rozsa, "Compact LaBr3:Ce gamma ray detector with Si-APD readout", *AIP Conference Proceedings*, vol. 1099, 2009-03. DOI: 10.1063/1.3120159 (cit. on p. 26).

[63] H. Spieler, "Analog and digital electronics for detectors", 2006. [Online]. Available: https://api.semanticscholar.org/CorpusID:7807414 (cit. on pp. 26, 27).

[64] D. Reilly, N. Ensslin, H. J. Smith, and S. Kreiner, “Passive nondestructive assay of nuclear materials”, Nuclear Regulatory Commission, Tech. Rep. NUREG/CR-5550, 1991 (cit. on p. 28).

[65] Massachusetts Institute of Technology, *Neutron interactions and applications*, `https://ocw.mit.edu/courses/22-106-neutron-interactions-and-applications-spring-2010/pages/lecture-notes/`, Accessed: 2023-06-05 (cit. on p. 28).

[66] U. of Alberta, *Table of isotopic masses and natural abundances*, `https://www.chem.ualberta.ca/~massspec/atomic_mass_abund.pdf`, Accessed: 2024-02-13 (cit. on p. 29).

[67] N. N. D. Center, *ENDF/B-VII.1 Evaluated Nuclear Data Library*, `https://www.nndc.bnl.gov/endf-b7.1/`, Accessed: 2022-02-17 (cit. on p. 29).

[68] G. Kemmerling and S. Jaksch, “Solid-state neutron detector sonde”, Forschungszentrum Jülich, Jülich Research Centre, Tech. Rep. D1.2 Materials Report, 2015, `https://arxiv.org/ftp/arxiv/papers/1707/1707.08679.pdf` (cit. on p. 29).

[69] H. Kato, Y. Onda, and M. Teramage, “Depth distribution of 137Cs, 134Cs, and 131I in soil profile after Fukushima Daiichi Nuclear Power Plant Accident”, *Journal of Environmental Radioactivity*, vol. 111, pp. 59–64, 2012, Environmental Impacts of the Fukushima Accident (Part I). DOI: `10.1016/j.jenvrad.2011.10.003` (cit. on p. 32).

[70] S. Hardie and I. McKinley, “Fukushima remediation: Status and overview of future plans”, *Journal of Environmental Radioactivity*, vol. 133, pp. 75–85, 2014, Environmental Radioactivity: Implications for Human and Environmental Health - International Symposium at Plymouth University, UK. DOI: `10.1016/j.jenvrad.2013.08.002` (cit. on p. 32).

[71] P. G. M. D. Connor and T. B. Scott, “Airborne radiation mapping: Overview and application of current and future aerial systems”, *International Journal of Remote Sensing*, vol. 37, no. 24, pp. 5953–5987, 2016. DOI: `10.1080/01431161.2016.1252474` (cit. on p. 32).

[72] International Atomic Energy Agency, “Decommissioning after a nuclear accident: Approaches, techniques, practices and implementation considerations”, International Atomic Energy Agency, Vienna, Tech. Rep. NW-T-2.10, 2019 (cit. on p. 32).

[73] O. Masson, G. Steinhauser, D. Zok, *et al.*, “Airborne concentrations and chemical considerations of radioactive ruthenium from an undeclared major nuclear release in 2017”, *Proceedings of the National Academy of Sciences*, vol. 116, no. 34, pp. 16 750–16 759, 2019. DOI: `10.1073/pnas.1907571116` (cit. on p. 32).

[74] E. Cazalas, “Defending cities against nuclear terrorism: Analysis of a radiation detector network for ground based traffic”, *Homeland Security Affairs*, vol. 14, 10 2018 (cit. on pp. 32, 35).

[75] J. Medalia, “Dirty bombs: Technical background, attack prevention and response, issues for congress”, Congressional Research Service, Tech. Rep. R41890, 2011-06 (cit. on p. 32).

[76] J. Peterson, M. Macdonell, L. Haroun, and F. Monette, *Radiological and chemical fact sheets to support health risk analyses for contaminated areas*, `https://remm.hhs.gov/ANL_ContaminantFactSheets_All_070418.pdf`, Accessed: 2024-02-03 (cit. on pp. 32–34).

[77] International Atomic Energy Agency, “Nuclear security systems and measures for the detection of nuclear and other radioactive material out of regulatory control”, International Atomic Energy Agency, Vienna, Tech. Rep. 21, 2013 (cit. on p. 33).

[78] C. L. Morris, C. C. Alexander, J. D. Bacon, *et al.*, “Tomographic imaging with cosmic ray muons”, *Science & Global Security*, vol. 16, no. 1-2, pp. 37–53, 2008. DOI: `10.1080/08929880802335758` (cit. on p. 33).

[79] International Atomic Energy Agency, “Prevention of the inadvertent movement and illicit trafficking of radioactive materials”, International Atomic Energy Agency, Vienna, Tech. Rep. 1311, 2002 (cit. on p. 33).

[80] Verification Research, Training and Information Centre, *Illicit trafficking of nuclear and other radioactive material*, `https://www.vertic.org/media/assets/Publications/ITR_WEB.pdf`, Accessed: 2024-02-03, 2012 (cit. on p. 34).

[81] The Guardian, *Spain: Call for return of stolen kit containing radioactive material*, `https://www.theguardian.com/world/2022/mar/15/spain-call-for-return-of-stolen-kit-containing-radioactive-material`, Accessed: 2024-02-03 (cit. on p. 34).

[82] The Guardian, *Search stepped up for potentially deadly radioactive capsule lost in western australia*, `https://www.theguardian.com/australia-news/2023/jan/29/new-technology-deployed-in-search-for-tiny-potentially-deadly-missing-radioactive-capsule`, Accessed: 2024-02-03 (cit. on p. 34).

[83] International Atomic Energy Agency, “Response to events involving the inadvertent movement or illicit trafficking of radioactive materials”, International Atomic Energy Agency, Vienna, Tech. Rep. 1313, 2002 (cit. on p. 35).

[84] S. Ihantola, O. Tengblad, H. Toivonen, *et al.*, “European reference network for critical infrastructure protection: Novel detection technologies for nuclear security”, no. KJ-NA-29270-EN-N, 2018, ISSN: 1831-9424. DOI: `10.2760/703301` (cit. on pp. 35, 45, 46).

[85] Organisation for Economic Co-operation and Development, *R&D and Innovation Needs for Decommissioning Nuclear Facilities*. 2014. DOI: `10.1787/9789264222199-en` (cit. on p. 36).

[86] International Atomic Energy Agency, "Decommissioning of particle accelerators", International Atomic Energy Agency, Vienna, Tech. Rep. NW-T-2.9, 2020 (cit. on p. 36).

[87] N. N. Garba, A. T. Ramli, M. A. Saleh, S. M. Sanusi, and H. T. Gabdo, "Radiological mapping of Kelantan, Malaysia, using terrestrial radiation dose rate", *Isotopes in Environmental and Health Studies*, vol. 52, no. 3, pp. 214–218, 2016. DOI: 10.1080/10256016.2016.1095189 (cit. on pp. 36, 47).

[88] R. O'Brien and M. Cooper, "Technologically enhanced naturally occurring radioactive material (NORM): Pathway analysis and radiological impact", *Applied Radiation and Isotopes*, vol. 49, no. 3, pp. 227–239, 1998, Naturally Occurring Radioactive Material in the Environment, ISSN: 0969-8043. DOI: 10.1016/S0969-8043(97)00244-3 (cit. on p. 36).

[89] R. Kouzes, J. Ely, B. Geelhood, *et al.*, "Naturally occurring radioactive materials and medical isotopes at border crossings", in *2003 IEEE Nuclear Science Symposium. Conference Record (IEEE Cat. No.03CH37515)*, vol. 2, 2003, 1448–1452 Vol.2. DOI: 10.1109/NSSMIC.2003.1351967 (cit. on p. 36).

[90] H. Rosoff and D. von Winterfeldt, "A risk and economic analysis of dirty bomb attacks on the ports of los angeles and long beach", *Risk Analysis*, vol. 27, 2007. DOI: 10.1111/j.1539-6924.2007.00908.x (cit. on p. 38).

[91] B. Milbrath, A. Peurrung, M. Bliss, and W. Weber, "Radiation detector materials: An overview", *Journal of Materials Research*, vol. 23, pp. 2561–2581, 2008. DOI: 10.1557/JMR.2008.0319 (cit. on pp. 38, 44, 45).

[92] R. T. Klann, J. Shergur, and G. Mattesich, "Current state of commercial radiation detection equipment for homeland security applications", *Nuclear Technology*, vol. 168, no. 1, pp. 79–88, 2009. DOI: 10.13182/NT09-A9104 (cit. on pp. 38, 45).

[93] D. Stromswold, J. Darkoch, J. Ely, *et al.*, "Field tests of a nai(tl)-based vehicle portal monitor at border crossings", in *IEEE Symposium Conference Record Nuclear Science 2004.*, vol. 1, 2004, 196–200 Vol. 1. DOI: 10.1109/NSSMIC.2004.1462180 (cit. on p. 38).

[94] RadTech, *AT2329 Radiation Portal Monitor*, https://www.radtech.it/it/modelli?p_id=177, Accessed: 2024-09-02 (cit. on p. 38).

[95] J. Ely, R. Kouzes, J. Schweppe, E. Siciliano, D. Strachan, and D. Weier, "The use of energy windowing to discriminate SNM from NORM in radiation portal monitors", *Nuclear Instruments and Methods in Physics Research Section A: Accelerators, Spectrometers, Detectors and Associated Equipment*, vol. 560, no. 2, pp. 373–387, 2006. DOI: 10.1016/j.nima.2006.01.053 (cit. on p. 39).

[96] R. Hevener, M.-S. Yim, and K. Baird, “Investigation of energy windowing algorithms for effective cargo screening with radiation portal monitors”, *Radiation Measurements*, vol. 58, pp. 113–120, 2013. DOI: `10.1016/j.radmeas.2013.08.004` (cit. on p. 39).

[97] T. Grisa and D. Sas, “On the ratio distribution of energy windowing algorithms for radiation portal monitors”, *Applied Radiation and Isotopes*, vol. 132, pp. 195–199, 2018. DOI: `10.1016/j.apradiso.2017.12.005` (cit. on p. 39).

[98] M. G. Paff, M. L. Ruch, A. Poitrasson-Riviere, A. Sagadevan, S. D. Clarke, and S. Pozzi, “Organic liquid scintillation detectors for on-the-fly neutron/gamma alarming and radionuclide identification in a pedestrian radiation portal monitor”, *Nuclear Instruments and Methods in Physics Research Section A: Accelerators, Spectrometers, Detectors and Associated Equipment*, vol. 789, pp. 16–27, 2015. DOI: `10.1016/j.nima.2015.03.088` (cit. on p. 39).

[99] M. G. Paff, A. Di Fulvio, S. D. Clarke, and S. A. Pozzi, “Radionuclide identification algorithm for organic scintillator-based radiation portal monitor”, *Nuclear Instruments and Methods in Physics Research Section A: Accelerators, Spectrometers, Detectors and Associated Equipment*, vol. 849, pp. 41–48, 2017. DOI: `10.1016/j.nima.2017.01.009` (cit. on p. 39).

[100] H. C. Lee, W.-G. Shin, H. J. Park, *et al.*, “Validation of energy-weighted algorithm for radiation portal monitor using plastic scintillator”, *Applied Radiation and Isotopes*, vol. 107, pp. 160–164, 2016. DOI: `10.1016/j.apradiso.2015.10.019` (cit. on p. 39).

[101] H. C. Lee, H. J. Choi, B. T. Koo, *et al.*, “Dynamic radionuclide identification using energy weighted algorithm with commercialized radiation portal monitor based on plastic scintillators”, *Radiation Physics and Chemistry*, vol. 170, p. 108 645, 2020. DOI: `10.1016/j.radphyschem.2019.108645` (cit. on p. 39).

[102] N. S. V. Rao, C. Y. T. Ma, and D. K. Y. Yau, “On performance of individual, collective and network detection of propagative sources”, in *2012 15th International Conference on Information Fusion*, 2012, pp. 247–254 (cit. on p. 39).

[103] S. Brennan, A. Mielke, D. Torney, and A. Maccabe, “Radiation detection with distributed sensor networks”, *Computer*, vol. 37, no. 8, pp. 57–59, 2004. DOI: `10.1109/MC.2004.103` (cit. on p. 39).

[104] N. S. Rao, S. Sen, N. J. Prins, *et al.*, “Network algorithms for detection of radiation sources”, *Nuclear Instruments and Methods in Physics Research Section A: Accelerators, Spectrometers, Detectors and Associated Equipment*, vol. 784, pp. 326–331, 2015, Symposium on Radiation Measurements and Applications 2014 (SORMA XV). DOI: `10.1016/j.nima.2015.01.037` (cit. on pp. 40, 57).

[105] B. Ristic, S. Arulampalam, and N. Gordon, *Beyond the Kalman Filter: Particle Filters for Tracking Applications*. Boston, MA, USA: Artech House, 2004 (cit. on p. 40).

[106] "American National Standard for Performance Criteria for Spectroscopy-Based Portal Monitors Used in Homeland Security", *ANSI N42.38-2015 (Revision of ANSI N42.38-2006)*, pp. 1–59, 2016. DOI: 10.1109/IEEESTD.2016.7394937 (cit. on p. 41).

[107] J. Ely, E. Ashbaker, M. Batdorf, *et al.*, "Spreader-bar radiation detection system enhancements", Pacific Northwest National Lab. (PNNL), Richland, WA, USA, Tech. Rep., 2012 (cit. on p. 41).

[108] M. Grypp, C. Marianno, J. Poston, and G. Hearn, "Design of a spreader bar crane-mounted gamma-ray radiation detection system", *Nuclear Instruments and Methods in Physics Research A*, vol. 743, pp. 1–4, 2014. DOI: 10.1016/j.nima.2014.01.015 (cit. on p. 41).

[109] K. M. Chandy, J. Bunn, and A. H. Liu, "Models and algorithms for radiation detection", in *Modeling and Simulation Workshop for Homeland Security*, 2010 (cit. on pp. 41, 42).

[110] Topcoder, *Detecting radiological threats in urban areas*, https://www.topcoder.com/challenges/d616d145-d7e7-4d62-9323-9c558b216b40, Accessed: 2024-02-28 (cit. on p. 41).

[111] M. D. Porter and A. Akakpo, "Detecting, identifying, and localizing radiological material in urban environments using scan statistics", in *2019 IEEE International Symposium on Technologies for Homeland Security (HST)*, 2019, pp. 1–6. DOI: 10.1109/HST47167.2019.9032931 (cit. on p. 41).

[112] Defense Advanced Research Projects Agency, *Advanced radioactive threat detection system completes first large-scale citywide test*, https://www.darpa.mil/news-events/2016-10-11, Accessed: 2024-02-28 (cit. on p. 41).

[113] J. Zhao and C. J. Sullivan, "Detection and parameter estimation of radioactive sources with mobile sensor networks", *Radiation Physics and Chemistry*, vol. 155, pp. 265–270, 2019, IRRMA-10. DOI: 10.1016/j.radphyschem.2018.06.018 (cit. on pp. 41, 42).

[114] D. Hochbaum and B. Fishbain, "Nuclear threat detection with mobile distributed sensor networks", *Ann Oper Res*, vol. 187, pp. 45–63, 2011. DOI: 10.1007/s10479-009-0643-z (cit. on pp. 41, 42).

[115] I. F. Vis and R. de Koster, "Transshipment of containers at a container terminal: An overview", *European Journal of Operational Research*, vol. 147, no. 1, pp. 1–16, 2003. DOI: 10.1016/S0377-2217(02)00293-X (cit. on p. 41).

[116] Carvalho, Henrique, Vale, Alberto, Marques, Rúben, Ventura, Rodrigo, Brouwer, Yoeri, and Gonçalves, Bruno, "Remote inspection with multi-copters, radiological sensors and SLAM techniques", *EPJ Web Conf.*, vol. 170, p. 07014, 2018. DOI: 10.1051/epjconf/201817007014 (cit. on p. 41).

[117] T. Lazna, P. Gabrlik, T. Jilek, and L. Zalud, "Cooperation between an unmanned aerial vehicle and an unmanned ground vehicle in highly accurate localization of gamma radiation hotspots", *International Journal of Advanced Robotic Systems*, vol. 15, no. 1, p. 1 729 881 417 750 787, 2018. DOI: 10.1177/1729881417750787 (cit. on p. 41).

[118] B. Ristic, M. Morelande, and A. Gunatilaka, "Information driven search for point sources of gamma radiation", *Signal Processing*, vol. 90, no. 4, pp. 1225–1239, 2010, Special Section: Ethnic Music Audio Documents: From the Preservation to the Fruition. DOI: 10.1016/j.sigpro.2009.10.006 (cit. on pp. 42, 43).

[119] J. Zhao, Z. Zhang, and C. J. Sullivan, "Identifying anomalous nuclear radioactive sources using Poisson kriging and mobile sensor networks", *PLOS ONE*, vol. 14, no. 5, e0216131, 2019. DOI: 10.1371/journal.pone.0216131 (cit. on p. 43).

[120] J. Huo, M. Liu, K. A. Neusypin, H. Liu, M. Guo, and Y. Xiao, "Autonomous search of radioactive sources through mobile robots", *Sensors*, vol. 20, no. 12, 2020. DOI: 10.3390/s20123461 (cit. on pp. 43, 53).

[121] R. B. Anderson, M. Pryor, A. Abeyta, and S. Landsberger, "Mobile Robotic Radiation Surveying with Recursive Bayesian Estimation and Attenuation Modeling", *IEEE Transactions on Automation Science and Engineering*, vol. 19, no. 1, pp. 410–424, 2022. DOI: 10.1109/TASE.2020.3036808 (cit. on pp. 43, 53).

[122] Y. Xiao, C. Zhang, J. Luo, C. Yang, and C. Liu, "Integrating the radiation source position into a grid map of the environment using a mobile robot", *Nuclear Instruments and Methods in Physics Research Section A: Accelerators, Spectrometers, Detectors and Associated Equipment*, vol. 976, p. 164 253, 2020. DOI: 10.1016/j.nima.2020.164253 (cit. on pp. 43, 52).

[123] M. Gomez-Fernandez, K. Higley, A. Tokuhiro, K. Welter, W.-K. Wong, and H. Yang, "Status of research and development of learning-based approaches in nuclear science and engineering: A review", *Nuclear Engineering and Design*, vol. 359, p. 110 479, 2020. DOI: 10.1016/j.nucengdes.2019.110479 (cit. on p. 43).

[124] M. Medhat, "Artificial intelligence methods applied for quantitative analysis of natural radioactive sources", *Annals of Nuclear Energy*, vol. 45, pp. 73–79, 2012. DOI: 10.1016/j.anucene.2012.02.013 (cit. on p. 43).

[125] B. Jeon, Y. Lee, M. Moon, J. Kim, and G. Cho, "Reconstruction of Compton Edges in Plastic Gamma Spectra Using Deep Autoencoder", *Sensors*, vol. 20, no. 10, p. 2895, 2020. DOI: 10.3390/s20102895 (cit. on p. 43).

[126] F. Mendes, M. Barros, A. Vale, and B. Gonçalves, "Radioactive hot-spot localisation and identification using deep learning", *Journal of Radiological Protection*, vol. 42, no. 1, p. 011 516, 2022. DOI: 10.1088/1361-6498/ac1a5c (cit. on pp. 43, 54, 57).

[127] G. Skinner, "Practical gamma-ray spectrometry: G. Gilmore and J.D. Hemingway, John Wiley, Chichester, UK, 1995", *Spectrochimica Acta Part A: Molecular and Biomolecular Spectroscopy*, vol. 52, no. 3, p. 379, 1996. DOI: 10.1016/S0584-8539(96)90113-0 (cit. on p. 43).

[128] J. Ely, E. Siciliano, and R. Kouzes, "Comparison of NaI(Tl) scintillators and high purity germanium for vehicle portal monitor applications", in *IEEE Symposium Conference Record Nuclear Science 2004.*, vol. 3, 2004, 1584–1587 Vol. 3. DOI: 10.1109/NSSMIC.2004.1462543 (cit. on p. 43).

[129] UKRSPEC systems, *Gamma-Radiation CdZnTe Micro Spectrometer - Specifications*, http://www.ritec.lv/html/uspec.html#specs, Accessed: 2024-01-28 (cit. on p. 43).

[130] Saint-Gobain, *Scintillation crystal materials*, https://www.crystals.saint-gobain.com/products/crystal-scintillation-materials, Accessed: 2020-07-01 (cit. on pp. 44, 45, 61).

[131] M. Lowdon, P. G. Martin, M. Hubbard, *et al.*, "Evaluation of scintillator detection materials for application within airborne environmental radiation monitoring", *Sensors*, vol. 19, no. 18, 2019. DOI: 10.3390/s19183828 (cit. on pp. 44, 50).

[132] P. Sibczynski, A. Broslawski, A. Gojska, *et al.*, "Characterization of some modern scintillators recommended for use on large fusion facilities in γ-ray spectroscopy and tomographic measurements of γ-emission profiles", *Nukleonika*, vol. 62, no. 3, pp. 223–228, 2017. DOI: doi:10.1515/nuka-2017-0032 (cit. on p. 44).

[133] Advatech, *BGO–Bismuth Germanate Scintillator Crystal*, https://www.advatech-uk.co.uk/bgo.html, Accessed: 2020-07-01 (cit. on p. 44).

[134] Kinheng Crystal, *NaI(TI) Scintillator Detectors*, http://www.kinheng-crystal.com/scintillation-crystal/csi-tl-scintillator-csi-tl-scintillation-crystal.html, Accessed: 2020-07-01 (cit. on p. 44).

[135] Epic Crystal, *CsI(Tl) Scintillation Crystal*, http://www.epic-crystal.com/others/nai-tl-scintillator-detectors.htm, Accessed: 2020-07-01 (cit. on p. 44).

[136] Omega Piezol, *BGO and LYSO crystals*, https://www.omegapiezo.com/crystal-scintillators/, Accessed: 2020-07-01 (cit. on p. 44).

[137] B. Seitz, N. Rivera, and A. Stewart, "Energy Resolution and Temperature Dependence of Ce:GAGG Coupled to Silicon Photomultipliers", *IEEE Transactions on Nuclear Science*, vol. 63, pp. 503–508, 2016-04. DOI: 10.1109/TNS.2016.2535235 (cit. on p. 44).

[138] Saint-Gobain, *Product comparisons*, https://www.luxiumsolutions.com/sites/default/files/2021-11/Product-Comparisons-Inorganic-Organic-Gas-Flow-Porportional-Counters.pdf, Accessed: 2024-02-12 (cit. on pp. 44, 45).

[139] C. Dujardin, E. Auffray, E. Bourret-Courchesne, *et al.*, "Needs, trends, and advances in inorganic scintillators", *IEEE Transactions on Nuclear Science*, vol. 65, no. 8, pp. 1977–1997, 2018. DOI: `10.1109/TNS.2018.2840160` (cit. on pp. 44, 45).

[140] I. Pawelczak, A. Glenn, H. Martinez, M. Carman, N. Zaitseva, and S. Payne, "Boron-loaded plastic scintillator with neutron-γ pulse shape discrimination capability", *Nuclear Instruments and Methods in Physics Research Section A: Accelerators, Spectrometers, Detectors and Associated Equipment*, vol. 751, pp. 62–69, 2014. DOI: `10.1016/j.nima.2014.03.027` (cit. on p. 44).

[141] U. Shirwadkar, E. van Loef, G. Markosyan, *et al.*, "Low-cost, multi-mode detector solutions", *Nuclear Instruments and Methods in Physics Research Section A: Accelerators, Spectrometers, Detectors and Associated Equipment*, vol. 954, p. 161 289, 2020, Symposium on Radiation Measurements and Applications XVII. DOI: `10.1016/j.nima.2018.09.124` (cit. on p. 44).

[142] Eljen Technology, *Neutron/Gamma PSD EJ-301, EJ-309*, `https://eljentechnology.com/products/liquid-scintillators/ej-301-ej-309`, Accessed: 2024-02-01 (cit. on p. 44).

[143] A. Hamrashdi, Hajir, Monk, S. D., and D. Cheneler, "Passive gamma-ray and neutron imaging systems for national security and nuclear non-proliferation in controlled and uncontrolled detection areas: Review of past and current status", *Sensors*, vol. 19, no. 11, 2019. DOI: `10.3390/s19112638` (cit. on pp. 45, 52).

[144] R. Kouzes, J. Ely, B. Milbrath, J. Schweppe, E. Siciliano, and D. Stromswold, "Spectroscopic and non-spectroscopic radiation portal applications to border security", in *IEEE Nuclear Science Symposium Conference Record, 2005*, vol. 1, 2005, pp. 321–325. DOI: `10.1109/NSSMIC.2005.1596262` (cit. on p. 45).

[145] I. Yaar and I. Peysakhov, "A multiple-detector Radioactive Material Detection Spectroscopic (RMDS) portal", *Nuclear Instruments and Methods in Physics Research Section A: Accelerators, Spectrometers, Detectors and Associated Equipment*, vol. 712, pp. 62–74, 2013. DOI: `10.1016/j.nima.2013.01.040` (cit. on p. 45).

[146] A. Datta, P. Becla, and S. Motakef, "Novel Electrodes and Engineered Interfaces for Halide-Semiconductor Radiation Detectors", *Scientific Reports*, vol. 9, p. 9933, 2019. DOI: `10.1038/s41598-019-46360-z` (cit. on p. 45).

[147] A. Osovizky, D. Ginzburg, A. Manor, *et al.*, "SENTIRAD—An innovative personal radiation detector based on a scintillation detector and a silicon photomultiplier", *Nuclear Instruments and Methods in Physics Research Section A: Accelerators, Spectrometers, Detectors and Associated Equipment*, vol. 652, no. 1, pp. 41–44, 2011, Symposium on Radiation Measurements and Applications (SORMA) XII 2010. DOI: `10.1016/j.nima.2011.01.027` (cit. on pp. 46, 47).

[148] J. Jiang, K. Shimazoe, Y. Nakamura, *et al.*, "A prototype of aerial radiation monitoring system using an unmanned helicopter mounting a GAGG scintillator Compton camera", *Journal of Nuclear Science and Technology*, vol. 53, no. 7, pp. 1067–1075, 2016. DOI: `10.1080/00223131.2015.1089796` (cit. on p. 46).

[149] J. Kataoka, A. Kishimoto, T. Nishiyama, *et al.*, "Handy Compton camera using 3D position-sensitive scintillators coupled with large-area monolithic MPPC arrays", *Nuclear Instruments and Methods in Physics Research Section A: Accelerators, Spectrometers, Detectors and Associated Equipment*, vol. 732, pp. 403–407, 2013, Vienna Conference on Instrumentation 2013. DOI: `10.1016/j.nima.2013.07.018` (cit. on p. 46).

[150] R. Penny, W. Hood, R. Polichar, *et al.*, "A dual-sided coded-aperture radiation detection system", *Nuclear Instruments and Methods in Physics Research Section A: Accelerators, Spectrometers, Detectors and Associated Equipment*, vol. 652, no. 1, pp. 578–581, 2011, Symposium on Radiation Measurements and Applications (SORMA) XII 2010. DOI: `10.1016/j.nima.2011.01.161` (cit. on pp. 46, 47).

[151] A. Omoto, "The accident at TEPCO's Fukushima-Daiichi Nuclear Power Station: What went wrong and what lessons are universal?", *Nuclear Instruments and Methods in Physics Research Section A: Accelerators, Spectrometers, Detectors and Associated Equipment*, vol. 731, pp. 3–7, 2013. DOI: `10.1016/j.nima.2013.04.017` (cit. on p. 46).

[152] P. P. Povinec, K. Hirose, and M. Aoyama, "5 - Fukushima Radioactivity Impact", in *Fukushima Accident*, P. P. Povinec, K. Hirose, and M. Aoyama, Eds., Boston: Elsevier, 2013, pp. 131–275, ISBN: 978-0-12-408132-1. DOI: `10.1016/B978-0-12-408132-1.00005-X` (cit. on pp. 46, 47).

[153] F. N. A. I. I. Commission, *The official report of the Fukushima Nuclear Accident Independent Investigation Commission*, `https://www.nirs.org/wp-content/uploads/fukushima/naiic_report.pdf`, 2012 (cit. on p. 46).

[154] M. Tanigaki, R. Okumura, K. Takamiya, N. Sato, H. Yoshino, and H. Yamana, "Development of a car-borne γ-ray survey system, KURAMA", *Nuclear Instruments and Methods in Physics Research A*, vol. 726, pp. 162–168, 2013-10. DOI: `10.1016/j.nima.2013.05.059` (cit. on p. 46).

[155] S. Tsuda, T. Yoshida, M. Tsutsumi, and K. Saito, "Characteristics and verification of a car-borne survey system for dose rates in air: KURAMA-II", *Journal of Environmental Radioactivity*, vol. 139, pp. 260–265, 2015. DOI: `10.1016/j.jenvrad.2014.02.028` (cit. on p. 46).

[156] S. Kobayashi, T. Shinomiya, H. Kitamura, *et al.*, "Radioactive contamination mapping of northeastern and eastern Japan by a car-borne survey system, Radi-Probe", *Journal of Environmental Radioactivity*, vol. 139, pp. 281–293, 2015. DOI: `10.1016/j.jenvrad.2014.07.026` (cit. on p. 46).

[157] M. Takeishi, M. Shibamichi, A. Malins, *et al.*, "Using two detectors concurrently to monitor ambient dose equivalent rates in vehicle surveys of radiocesium contaminated land", *Journal of Environmental Radioactivity*, vol. 177, pp. 1–12, 2017. DOI: 10.1016/j.jenvrad.2017.05.010 (cit. on p. 46).

[158] Y.-Y. Ji, K. Chung, and M. Kang, "Assessment of dose rate of detected gamma emitting nuclides using a carborne survey with a large volume NaI(Tl) detector", *Progress in Nuclear Energy*, vol. 123, p. 103 272, 2020-05. DOI: 10.1016/j.pnucene.2020.103272 (cit. on p. 46).

[159] E. Prieto, E. Jabaloyas, R. Casanovas, C. Rovira, and M. Salvadó, "Set up of a gamma spectrometry mobile unit equipped with LaBr3(Ce) detectors for radioactivity monitoring", *Radiation Physics and Chemistry*, vol. 168, p. 108 600, 2020. DOI: 10.1016/j.radphyschem.2019.108600 (cit. on p. 46).

[160] A. Baeza, J. Corbacho, and J. Miranda Carpintero, "Design and implementation of a mobile radiological emergency unit integrated in a radiation monitoring network", *Nuclear Science, IEEE Transactions on*, vol. 60, pp. 1400–1407, 2013-04. DOI: 10.1109/TNS.2013.2245511 (cit. on p. 46).

[161] P. Martin, O. Payton, Y. Yamashiki, D. Richards, and T. Scott, "High-resolution radiation mapping to investigate FDNPP derived contaminant migration", *Journal of Environmental Radioactivity*, vol. 164, pp. 26–35, 2016. DOI: 10.1016/j.jenvrad.2016.06.025 (cit. on p. 46).

[162] M. Andoh, H. Yamamoto, T. Kanno, and K. Saito, "Measurement of ambient dose equivalent rates by walk survey around Fukushima Dai-ichi Nuclear Power Plant using KURAMA-II until 2016", *Journal of Environmental Radioactivity*, vol. 210, p. 105 812, 2019, Special issue on Five years of Fukushima. DOI: 10.1016/j.jenvrad.2018.09.010 (cit. on p. 46).

[163] P. G. Martin, C. Hutson, L. Payne, *et al.*, "Validation of a novel radiation mapping platform for the reduction of operator-induced shielding effects", *Journal of Radiological Protection*, vol. 38, no. 3, p. 1097, 2018-08. DOI: 10.1088/1361-6498/aad5f2 (cit. on p. 46).

[164] K. N. Shokhirev, D. Konno, T. M. Schmit, V. Ziskin, and B. R. Cosofret, "Man-portable radiation detector based on advanced source detection, identification, and localization algorithms", in *2015 IEEE Nuclear Science Symposium and Medical Imaging Conference (NSS/MIC)*, 2015, pp. 1–5. DOI: 10.1109/NSSMIC.2015.7581756 (cit. on p. 47).

[165] D. Celeste, A. Curioni, A. Fazzi, M. Silari, and V. Varoli, "B-RAD: a radiation survey meter for operation in intense magnetic fields", *Journal of Instrumentation*, vol. 14, no. 05, T05007, 2019-05. DOI: 10.1088/1748-0221/14/05/T05007 (cit. on p. 47).

[166] H. M. Park and K. S. Joo, "Development and performance characteristics of personal gamma spectrometer for radiation monitoring applications", *Sensors*, vol. 16, no. 6, 2016. DOI: 10.3390/s16060919 (cit. on p. 47).

[167] IPFN, *Mobile Application for Radiation Intensity Assessment (MARIA)*, https://www.ipfn.tecnico.ulisboa.pt/MARIA/, Accessed: 2024-02-13 (cit. on p. 47).

[168] Y. Ishigaki, Y. Matsumoto, R. Ichimiya, and K. Tanaka, "Development of mobile radiation monitoring system utilizing smartphone and its field tests in Fukushima", *IEEE Sensors Journal*, vol. 13, no. 10, pp. 3520–3526, 2013. DOI: 10.1109/JSEN.2013.2272734 (cit. on p. 47).

[169] K. Fukuoka, S. Awai, and S. Markon, "A mobile cloud-based radiation monitoring system for citizens", in *2015 IEEE Region 10 Humanitarian Technology Conference (R10-HTC)*, 2015, pp. 1–5. DOI: 10.1109/R10-HTC.2015.7391857 (cit. on p. 47).

[170] A. Miller, R. Machrafi, and A. Mohany, "Development of a semi-autonomous directional and spectroscopic radiation detection mobile platform", *Radiation Measurements*, vol. 72, pp. 53–59, 2015. DOI: 10.1016/j.radmeas.2014.11.009 (cit. on p. 47).

[171] W. Khan, C. He, Y. Cao, R. Khan, and W. Yang, "A detector system for searching lost γ-ray source", *Nuclear Engineering and Technology*, vol. 52, no. 7, pp. 1524–1531, 2020. DOI: 10.1016/j.net.2019.12.021 (cit. on p. 47).

[172] H. Shin, C.-H. Kim, Y.-C. Seo, H.-S. Eom, Y. Choi, and M. Kim, "Aerial working environment monitoring robot in high radiation area", in *2014 14th International Conference on Control, Automation and Systems (ICCAS 2014)*, 2014, pp. 474–478. DOI: 10.1109/ICCAS.2014.6988048 (cit. on pp. 47, 53).

[173] L. Sinclair, P. Saull, D. Hanna, H. Seywerd, A. MacLeod, and P. Boyle, "Silicon Photomultiplier-Based Compton Telescope for Safety and Security (SCoTSS)", *IEEE Transactions on Nuclear Science*, vol. 61, no. 5, pp. 2745–2752, 2014-10. DOI: 10.1109/tns.2014.2356412 (cit. on p. 47).

[174] L. E. Sinclair, A. McCann, P. R. Saull, *et al.*, "End-user experience with the SCoTSS Compton imager and directional survey spectrometer", *Nuclear Instruments and Methods in Physics Research Section A: Accelerators, Spectrometers, Detectors and Associated Equipment*, vol. 954, p. 161 683, 2020-02. DOI: 10.1016/j.nima.2018.11.142 (cit. on p. 47).

[175] R. Barnowski, A. Haefner, L. Mihailescu, and K. Vetter, "Scene data fusion: Real-time standoff volumetric gamma-ray imaging", *Nuclear Instruments and Methods in Physics Research Section A: Accelerators, Spectrometers, Detectors and Associated Equipment*, vol. 800, pp. 65–69, 2015. DOI: 10.1016/j.nima.2015.08.016 (cit. on p. 47).

[176] A. Haefner, R. Barnowski, P. Luke, M. Amman, and K. Vetter, "Handheld real-time volumetric 3-D gamma-ray imaging", *Nuclear Instruments and Methods in Physics Research Section A: Accelerators, Spectrometers, Detectors and Associated Equipment*, vol. 857, pp. 42–49, 2017. DOI: 10.1016/j.nima.2016.11.046 (cit. on p. 47).

[177] S. Zelakiewicz, R. Hoctor, A. Ivan, *et al.*, "SORIS—A standoff radiation imaging system", *Nuclear Instruments and Methods in Physics Research Section A: Accelerators, Spectrometers, Detectors and Associated Equipment*, vol. 652, no. 1, pp. 5–9, 2011, Symposium on Radiation Measurements and Applications (SORMA) XII 2010. DOI: 10.1016/j.nima.2011.02.068 (cit. on p. 47).

[178] Y. Sanada, T. Sugita, Y. Nishizawa, A. Kondo, and T. Torii, "The aerial radiation monitoring in Japan after the Fukushima Daiichi nuclear power plant accident", *Progress in Nuclear Science and Technology*, vol. 4, pp. 76–80, 2014-01. DOI: 10.15669/pnst.4.76 (cit. on p. 47).

[179] J. Hirouchi, Y. Nishizawa, Y. Urabe, K. Shimada, Y. Sanada, and M. Munakata, "Development and application of a method for discriminating the influence of radon progenies in air from aerial radiation monitoring data", *Applied Radiation and Isotopes*, vol. 141, pp. 122–129, 2018. DOI: 10.1016/j.apradiso.2018.08.027 (cit. on p. 47).

[180] UNICEF, *UAVs: The Next Game-Changer in Development?*, https://www.unicef.org/innovation/drones/the-next-game-changers-development, Accessed: 2024-01-28 (cit. on p. 48).

[181] A. Balova, *Geospatial Intelligence 101: AI Drones vs Satellites*, https://www.ramboll.com/galago/geospatial-intelligence-101-ai-drones-vs-satellites, Accessed: 2024-01-28 (cit. on p. 48).

[182] B. A. Duncan and R. R. Murphy, "Autonomous capabilities for small unmanned aerial systems conducting radiological response: Findings from a high-fidelity discovery experiment", *Journal of Field Robotics*, vol. 31, no. 4, pp. 522–536, 2014. DOI: 10.1002/rob.21503 (cit. on pp. 48, 53).

[183] T. Elmokadem and A. V. Savkin, "Towards Fully Autonomous UAVs: A Survey", *Sensors*, vol. 21, no. 18, 2021. DOI: 10.3390/s21186223 (cit. on p. 48).

[184] J. Scanlan, D. Flynn, D. Lane, R. Richardson, T. Richardson, and A. Sóbester, *Extreme Environments Robotics: Robotics for Emergency Response, Disaster Relief and Resilience* (UK-RAS White Papers), English. UK-RAS Network, 2017-06 (cit. on pp. 48, 53).

[185] Army technology, *Army Technology: Honeywell T-Hawk Micro Air Vehicle (MAV)*, https://www.army-technology.com/projects/honeywell-thawk-mav-us-army/, Accessed: 2024-02-16 (cit. on p. 48).

[186] JAXA, *Unmanned Airplane for Radiation Monitoring System (UARMS)*, `https://www.aero.jaxa.jp/eng/research/star/uas/uarms/`, Accessed: 2024-02-19 (cit. on p. 48).

[187] International Atomic Energy Agency, "Categorization of radioactive sources", International Atomic Energy Agency, Vienna, Tech. Rep. RS-G-1.9, 2005 (cit. on p. 48).

[188] J. MacFarlane, O. Payton, A. Keatley, *et al.*, "Lightweight aerial vehicles for monitoring, assessment and mapping of radiation anomalies", *Journal of Environmental Radioactivity*, vol. 136, pp. 127–130, 2014. DOI: `10.1016/j.jenvrad.2014.05.008` (cit. on p. 49).

[189] P. Martin, O. Payton, J. Fardoulis, D. Richards, Y. Yamashiki, and T. Scott, "Low altitude unmanned aerial vehicle for characterising remediation effectiveness following the FDNPP accident", *Journal of Environmental Radioactivity*, vol. 151, pp. 58–63, 2016. DOI: `10.1016/j.jenvrad.2015.09.007` (cit. on p. 49).

[190] P. Martin, S. Kwong, N. Smith, *et al.*, "3D unmanned aerial vehicle radiation mapping for assessing contaminant distribution and mobility", *International Journal of Applied Earth Observation and Geoinformation*, vol. 52, pp. 12–19, 2016. DOI: `10.1016/j.jag.2016.05.007` (cit. on p. 49).

[191] J. Borbinha, Y. Romanets, P. Teles, *et al.*, "Performance Analysis of Geiger–Müller and Cadmium Zinc Telluride Sensors Envisaging Airborne Radiological Monitoring in NORM Sites", *Sensors*, vol. 20, no. 5, 2020. DOI: `10.3390/s20051538` (cit. on p. 49).

[192] P. Martin, O. Payton, J. Fardoulis, D. Richards, and T. Scott, "The use of unmanned aerial systems for the mapping of legacy uranium mines", *Journal of Environmental Radioactivity*, vol. 143, pp. 135–140, 2015. DOI: `10.1016/j.jenvrad.2015.02.004` (cit. on p. 49).

[193] Mirion technologies, *SIGMA Compact CsI Scintillation Spectrometer*, `https://www.mirion.com/products/technologies/spectroscopy-scientific-analysis/gamma-spectroscopy/detectors/scintillation-czt-detectors-accessories/sigma-compact-csl-scintillation-spectrometer`, Accessed: 2024-02-17 (cit. on p. 49).

[194] Lüley, Jakub, Vrban, Branislav, Čerba, Štefan, Osuský, Filip, and Nečas, Vladimír, "Unmanned radiation monitoring system", *EPJ Web Conf.*, vol. 225, p. 08 008, 2020. DOI: `10.1051/epjconf/202022508008` (cit. on p. 49).

[195] L. R. Pinto, A. Vale, Y. Brouwer, *et al.*, "Radiological scouting, monitoring and inspection using drones", *Sensors*, vol. 21, no. 9, 2021. DOI: `10.3390/s21093143` (cit. on pp. 49, 50).

[196] P. Royo, E. Pastor, M. Macias, R. Cuadrado, C. Barrado, and A. Vargas, "An Unmanned Aircraft System to Detect a Radiological Point Source Using RIMA Software Architecture", *Remote Sensing*, vol. 10, no. 11, 2018. DOI: 10.3390/rs10111712 (cit. on p. 49).

[197] Y. Verbelen, P. G. Martin, K. Ahmad, S. Kaluvan, and T. B. Scott, "Miniaturised low-cost gamma scanning platform for contamination identification, localisation and characterisation: A new instrument in the decommissioning toolkit", *Sensors*, vol. 21, no. 8, 2021. DOI: 10.3390/s21082884 (cit. on p. 49).

[198] J. Aleotti, G. Micconi, S. Caselli, *et al.*, "Detection of Nuclear Sources by UAV Teleoperation Using a Visuo-Haptic Augmented Reality Interface", *Sensors*, vol. 17, no. 10, 2017. DOI: 10.3390/s17102234 (cit. on p. 49).

[199] Z. Cook, M. Kazemeini, A. Barzilov, and W. Yim, "Low-altitude contour mapping of radiation fields using UAS swarm", *Intelligent Service Robotics*, vol. 12, pp. 219–230, 2019. DOI: 10.1007/s11370-019-00277-8 (cit. on p. 49).

[200] M. Carminati, D. Di Vita, G. Morandi, I. D'Adda, and C. Fiorini, "Handheld magnetic-compliant gamma-ray spectrometer for environmental monitoring and scrap metal screening", *Sensors*, vol. 22, no. 4, 2022. DOI: 10.3390/s22041412 (cit. on p. 49).

[201] A. Chierici, A. Malizia, D. Di Giovanni, R. Ciolini, and F. d'Errico, "A high-performance gamma spectrometer for unmanned systems based on off-the-shelf components", *Sensors*, vol. 22, no. 3, 2022. DOI: 10.3390/s22031078 (cit. on p. 49).

[202] E. L. Connolly, P. G. Martin, and E. Woodbridge, "Passive radiological inspection of shipping containers at seaports using UAV-based detectors with the method of spectral comparison ratios", in *2023 IEEE Nuclear Science Symposium, Medical Imaging Conference and International Symposium on Room-Temperature Semiconductor Detectors (NSS MIC RTSD)*, 2023, pp. 1–1. DOI: 10.1109/NSSMICRTSD49126.2023.10338318 (cit. on p. 49).

[203] O. Šálek, M. Matolín, and L. Gryc, "Mapping of radiation anomalies using uav mini-airborne gamma-ray spectrometry", *Journal of Environmental Radioactivity*, vol. 182, pp. 101–107, 2018. DOI: 10.1016/j.jenvrad.2017.11.033 (cit. on pp. 49, 50).

[204] P. P. Falciglia, L. Biondi, R. Catalano, G. Immè, S. Romano, and F. G. A. Vagliasindi, "Preliminary investigation for quali-quantitative characterization of soils contaminated with 241Am and 152Eu by low-altitude unmanned aerial vehicles (UAVs) equipped with small size γ-ray spectrometer: detection efficiency and minimum detectable activity (MDA) concentration assessment", *Journal of Soils and Sediments*, vol. 18, pp. 2399–2409, 2018. DOI: 10.1007/s11368-017-1720-6 (cit. on p. 49).

[205] C. Cai, B. Carter, M. Srivastava, J. Tsung, J. Vahedi-Faridi, and C. Wiley, "Designing a radiation sensing UAV system", in *2016 IEEE Systems and Information Engineering Design Symposium (SIEDS)*, 2016, pp. 165–169. DOI: 10.1109/SIEDS.2016.7489292 (cit. on p. 49).

[206] T. Baca, M. Jilek, P. Manek, *et al.*, "Timepix radiation detector for autonomous radiation localization and mapping by micro unmanned vehicles", in *2019 IEEE/RSJ International Conference on Intelligent Robots and Systems (IROS)*, 2019, pp. 1129–1136. DOI: 10.1109/IROS40897.2019.8968514 (cit. on p. 49).

[207] S. Mochizuki, J. Kataoka, L. Tagawa, *et al.*, "First demonstration of aerial gamma-ray imaging using drone for prompt radiation survey in Fukushima", *Journal of Instrumentation*, vol. 12, no. 11, P11014, 2017-11. DOI: 10.1088/1748-0221/12/11/P11014 (cit. on p. 50).

[208] Y. Sato, S. Ozawa, Y. Terasaka, *et al.*, "Remote radiation imaging system using a compact gamma-ray imager mounted on a multicopter drone", *Journal of Nuclear Science and Technology*, vol. 55, no. 1, pp. 90–96, 2018. DOI: 10.1080/00223131.2017.1383211 (cit. on p. 50).

[209] Y. Sato, S. Ozawa, Y. Terasaka, *et al.*, "Remote detection of radioactive hotspot using a Compton camera mounted on a moving multi-copter drone above a contaminated area in Fukushima", *Journal of Nuclear Science and Technology*, vol. 57, no. 6, pp. 734–744, 2020. DOI: 10.1080/00223131.2020.1720845 (cit. on p. 50).

[210] IPFN, *Fleet of drones for radiological inspection, communication, and rescue*, https://www.ipfn.tecnico.ulisboa.pt/FRIENDS/, Accessed: 2024-02-17 (cit. on p. 50).

[211] B. Li, Y. Zhu, Z. Wang, C. Li, Z.-R. Peng, and L. Ge, "Use of multi-rotor unmanned aerial vehicles for radioactive source search", *Remote Sensing*, vol. 10, no. 5, 2018. DOI: 10.3390/rs10050728 (cit. on p. 50).

[212] M. S. Bandstra, B. J. Quiter, J. C. Curtis, *et al.*, "Attribution of gamma-ray background collected by a mobile detector system to its surroundings using panoramic vide", *Nuclear Instruments and Methods in Physics Research Section A: Accelerators, Spectrometers, Detectors and Associated Equipment*, vol. 954, no. 1, p. 161 126, 2020. DOI: 10.1016/j.nima.2018.08.085 (cit. on pp. 50, 51).

[213] K. Borozdin, A. Klimenko, W. Priedhorsky, *et al.*, "Optimized strategies for smart nuclear search", vol. 2, 2006-12, pp. 926–928. DOI: 10.1109/NSSMIC.2006.355998 (cit. on p. 50).

[214] D. Cester, M. Lunardon, L. Stevanato, *et al.*, "Commissioning and Field Tests of a Van-Mounted System for the Detection of Radioactive Sources and Special Nuclear Material", *IEEE Transactions on Nuclear Science*, vol. 63, no. 2, pp. 1314–1322, 2016. DOI: 10.1109/TNS.2016.2528163 (cit. on pp. 50, 51).

[215] M. S. Bandstra, T. J. Aucott, E. Brubaker, *et al.*, "RadMAP: The Radiological Multi-sensor Analysis Platform", *Nuclear Instruments and Methods in Physics Research Section A: Accelerators, Spectrometers, Detectors and Associated Equipment*, vol. 840, pp. 59–68, 2016. DOI: `10.1016/j.nima.2016.09.040` (cit. on p. 51).

[216] D. Cester, G. Nebbia, L. Stevanato, *et al.*, "Special nuclear material detection with a mobile multi-detector system", *Nuclear Instruments and Methods in Physics Research Section A: Accelerators, Spectrometers, Detectors and Associated Equipment*, vol. 663, no. 1, pp. 55–63, 2012. DOI: `10.1016/j.nima.2011.10.011` (cit. on p. 51).

[217] J. C. Curtis, R. J. Cooper, T. H. Joshi, *et al.*, "Simulation and validation of the Mobile Urban Radiation Search (MURS) gamma-ray detector response", *Nuclear Instruments and Methods in Physics Research Section A: Accelerators, Spectrometers, Detectors and Associated Equipment*, vol. 954, p. 161 128, 2020, Symposium on Radiation Measurements and Applications XVII. DOI: `https://doi.org/10.1016/j.nima.2018.08.087` (cit. on p. 51).

[218] A. L. Hutcheson, B. F. Phlips, E. A. Wulf, L. J. Mitchell, and R. S. Woolf, "Standoff detection of thermal and fast neutrons", in *2015 IEEE International Symposium on Technologies for Homeland Security (HST)*, 2015, pp. 1–6. DOI: `10.1109/THS.2015.7225336` (cit. on p. 51).

[219] S. Kuehn, "The REWARD project: Real Time Wide Area Radiation Surveillance with semiconductor detectors", in *2013 IEEE Nuclear Science Symposium and Medical Imaging Conference (2013 NSS/MIC)*, 2013, pp. 1–4. DOI: `10.1109/NSSMIC.2013.6829630` (cit. on p. 51).

[220] M. Dambacher, A. Fauler, C. Disch, *et al.*, "Evaluation of various Coplanar Grid (Cd,Zn)Te detector concepts for the application in gamma radiation surveillance and environmental monitoring detection systems", in *2013 IEEE Nuclear Science Symposium and Medical Imaging Conference (2013 NSS/MIC)*, 2013, pp. 1–6. DOI: `10.1109/NSSMIC.2013.6829818` (cit. on p. 51).

[221] R. Luís, C. Fleta, J. Balbuena, *et al.*, "Response of the REWARD detection system to the presence of a Radiological Dispersal Device", *Radiation Measurements*, vol. 88, pp. 20–32, 2016. DOI: `10.1016/j.radmeas.2016.02.030` (cit. on p. 51).

[222] J. Balbuena, M. Baptista, S. Barros, *et al.*, "Study of gamma detection capabilities of the REWARD mobile spectroscopic system", *Nuclear Instruments and Methods in Physics Research Section A: Accelerators, Spectrometers, Detectors and Associated Equipment*, vol. 859, pp. 1–7, 2017. DOI: `10.1016/j.nima.2017.03.056` (cit. on p. 51).

[223] M. Kazemeini, Z. Cook, J. Lee, A. Barzilov, and W. Yim, "Plug-and-play radiation sensor components for unmanned aerial system platform", *Journal of Radioanalytical and Nuclear Chemistry*, vol. 318, pp. 1797–1803, 2018. DOI: `10.1007/s10967-018-6233-2` (cit. on pp. 50, 51).

[224] M. Kazemeini, A. Barzilov, J. Lee, and W. Yim, “Integration of CZT and CLYC radiation detectors into robotic platforms using ROS”, *AIP Conference Proceedings*, vol. 2160, no. 1, p. 050 019, 2019-10. DOI: 10.1063/1.5127711 (cit. on pp. 50, 51).

[225] J. Hartman, A. Barzilov, and I. Novikov, “Remote sensing of neutron and gamma radiation using aerial unmanned autonomous system”, in *2015 IEEE Nuclear Science Symposium and Medical Imaging Conference (NSS/MIC)*, 2015, pp. 1–4. DOI: 10.1109/NSSMIC.2015.7581763 (cit. on pp. 50, 51).

[226] A. Barzilov and M. Kazemeini, “Dual-Mode Radiation Sensor for UAS Platforms”, *Proceedings*, vol. 42, no. 37, 2020. DOI: 10.3390/ecsa-6-06541 (cit. on pp. 50, 51).

[227] C. J. Sullivan, “Radioactive source localization in urban environments with sensor networks and the internet of things”, in *2016 IEEE International Conference on Multisensor Fusion and Integration for Intelligent Systems (MFI)*, 2016, pp. 384–388. DOI: 10.1109/MFI.2016.7849518 (cit. on p. 51).

[228] Rapiscan, *Radiation detection products*, https://www.rapiscan-ase.com/radiation-detection-products/, Accessed: 2024-01-24 (cit. on p. 51).

[229] Kromek, *D3S ID*, https://www.kromek.com/product/d3s_id/, Accessed: 2024-01-24., 2024-01 (cit. on p. 51).

[230] Berkeley Nucleonics Corp, *Model PM1703GNA (PRD) - Gamma and Neutron Personal Radiation Detector*, https://www.berkeleynucleonics.com/model-pm1703gn-prd, 2024-01 (cit. on p. 51).

[231] Mirion technologies, *SPIR-Explorer Sensor: Light Wide Range Radiological Detection and Identification Sensor*, https://www.mirion.com/products/technologies/defense-security-systems/security-search-systems/mobile-systems/spir-explorer-sensor, Acessed: 2024-01-08, 2024-01 (cit. on p. 51).

[232] U.S. Department of Homeland Security, Science and Technology Directorate, “Mobile radiation detection systems market survey report”, National Urban Security Technology Laboratory, Market Survey Report SAVER-T-MSR-42, 2023-08, Approved for Public Release. [Online]. Available: https://www.dhs.gov/sites/default/files/2023-08/23_0816_st_mobile_radiation_detection_systems_msr.pdf (cit. on p. 51).

[233] J. K. Polack, A. Poitrasson-Rivière, M. C. Hamel, *et al.*, “Dual-particle imager for standoff detection of special nuclear material”, in *2011 IEEE Nuclear Science Symposium Conference Record*, 2011, pp. 1494–1500. DOI: 10.1109/NSSMIC.2011.6154355 (cit. on p. 51).

[234] H. Al Hamrashdi, D. Cheneler, and S. D. Monk, "A fast and portable imager for neutron and gamma emitting radionuclides", *Nuclear Instruments and Methods in Physics Research Section A: Accelerators, Spectrometers, Detectors and Associated Equipment*, vol. 953, p. 163 253, 2020. DOI: 10.1016/j.nima.2019.163253 (cit. on p. 52).

[235] H. Al Hamrashdi, D. Cheneler, and S. Monk, "Material optimization in dual particle detectors by comparing advanced scintillating materials using two Monte Carlo codes", *Nuclear Instruments and Methods in Physics Research Section A: Accelerators, Spectrometers, Detectors and Associated Equipment*, vol. 869, pp. 163–171, 2017. DOI: 10.1016/j.nima.2017.06.043 (cit. on p. 52).

[236] Al Hamrashdi, H., Monk, S. D., and Cheneler, D., "Design and optimisation of a three layers thermal neutron, fast neutron and gamma-ray imaging system", *EPJ Web Conf.*, vol. 225, p. 07 002, 2020. DOI: 10.1051/epjconf/202022507002 (cit. on p. 52).

[237] M. Cieślak, K. Gamagea, and R. Glover, "Pulse shape discrimination characteristics of stilbene crystal, pure and 6Li loaded plastic scintillators for a high resolution coded-aperture neutron imager", *Journal of Instrumentation*, vol. 12, 7 2017-07, ISSN: 17480221. DOI: 10.1088/1748-0221/12/07/P07023 (cit. on pp. 52, 53).

[238] M. Gerling, P. Marleau, and J. Goldsmith, *Comparison of Stilbene Neutron Detection Performance to EJ-309*, http://prod.sandia.gov/techlib/access-control.cgi/2014/1419914r.pdf, Accessed: 2024-01-05 (cit. on p. 52).

[239] E. Technology, *Elgen Technology: Pulse Shape Discrimination EJ-276 & EJ-276G*, https://eljentechnology.com/products/plastic-scintillators/ej-276, Accessed: 2024-01-05 (cit. on p. 52).

[240] B. Ayaz-Maierhafer, J. P. Hayward, K. P. Ziock, M. A. Blackston, and L. Fabris, "Angular resolution study of a combined gamma-neutron coded aperture imager for standoff detection", *Nuclear Instruments and Methods in Physics Research Section A: Accelerators, Spectrometers, Detectors and Associated Equipment*, vol. 712, pp. 120–125, 2013. DOI: 10.1016/j.nima.2013.02.005 (cit. on p. 52).

[241] L. Soundara-Pandian, J. Glodo, J. Christian, *et al.*, *Combined gamma-ray/neutron imaging system for detecting nuclear material*, https://www.aptechnologies.co.uk/images/Data/Vertilon/a513_1.pdf, Accessed: 2024-01-05 (cit. on p. 52).

[242] International Atomic Energy Agency, "Nuclear security systems and measures for the detection of nuclear and other radioactive material out of regulatory control", International Atomic Energy Agency, Vienna, Tech. Rep. 21, 2013 (cit. on p. 52).

[243] E. Commission, J. R. Centre, S. Ihantola, *et al.*, *Impact of novel technologies on nuclear security and emergency preparedness – ERNCIP Thematic Group Radiological & Nuclear Threats to Critical Infrastructure*, G. Karagiannis, Ed. Publications Office, 2018. DOI: 10.2760/52056 (cit. on pp. 52, 54).

[244] D. S. McGregor, "Materials for gamma-ray spectrometers: Inorganic scintillators", *Annual Review of Materials Research*, vol. 48, no. 1, pp. 245–277, 2018. DOI: 10.1146/annurev-matsci-070616-124247 (cit. on p. 53).

[245] M. Kazemeini, J. C. Vaz, and A. Barzilov, "Study of radiation effects in electronics of a hexapod robotic platform", *AIP Conference Proceedings*, vol. 2160, no. 1, p. 060 003, 2019-10. DOI: 10.1063/1.5127720 (cit. on p. 53).

[246] J. Lahtinen, "Emergency monitoring strategy and radiation measurements document of the NKS project emergency management and radiation monitoring in nuclear and radiological accidents (EMARAD)", Nordic nuclear safety research, Tech. Rep. NKS-142, 2006-04 (cit. on pp. 53, 54).

[247] G. Sannie, V. Kondrasov, G. Corre, *et al.*, "SCINTILLA European project, the successful research results", in *2015 4th International Conference on Advancements in Nuclear Instrumentation Measurement Methods and their Applications (ANIMMA)*, 2015, pp. 1–4. DOI: 10.1109/ANIMMA.2015.7465619 (cit. on p. 53).

[248] Hamamatsu, *How does temperature affect the gain of an SiPM?*, https://hub.hamamatsu.com/us/en/technical-notes/mppc-sipms/how-does-temperature-affect-the-gain-of-an-SiPM.html, Accessed: 2024-08-05 (cit. on p. 53).

[249] E. Technology, *General purpose EJ-200, EJ-204, EJ-208, EJ-212*, https://eljentechnology.com/products/plastic-scintillators/ej-200-ej-204-ej-208-ej-212, Accessed: 2024-08-04 (cit. on pp. 53, 59, 61).

[250] T. J. Hajagos, C. Liu, N. J. Cherepy, and Q. Pei, *High-Z Sensitized Plastic Scintillators: A Review*, 2018-07. DOI: 10.1002/adma.201706956 (cit. on p. 53).

[251] I. K. Ukaegbu and K. A. A. Gamage, "Ground Penetrating Radar as a Contextual Sensor for Multi-Sensor Radiological Characterisation", *Sensors*, vol. 17, no. 4, 2017. DOI: 10.3390/s17040790 (cit. on p. 54).

[252] Y. Liu, J. Gao, J. Zhao, and X. Shi, "A new disaster information sensing mode: Using multi-robot system with air dispersal mode", *Sensors*, vol. 18, no. 10, 2018. DOI: 10.3390/s18103589 (cit. on p. 54).

[253] V. O. Sivaneri and J. N. Gross, "UGV-to-UAV cooperative ranging for robust navigation in GNSS-challenged environments", *Aerospace Science and Technology*, vol. 71, pp. 245–255, 2017. DOI: 10.1016/j.ast.2017.09.024 (cit. on p. 54).

[254] H. Wei and J. Huang, *Halide lead perovskites for ionizing radiation detection*, 2019. DOI: 10.1038/s41467-019-08981-w (cit. on p. 54).

[255] UKRSPEC systems, *Unmanned aerial systems*, https://ukrspecsystems.com/drones, Accessed: 2024-01-28 (cit. on p. 54).

[256] Popular science, *The PLIMP is a plane-blimp mashup that promises safe air transport*, https://www.popsci.com/plimp-plane-blimp-drone/, Accessed: 2024-01-28 (cit. on p. 54).

[257] IEEE Spectrum, *Boston Dynamics' Spot Is Helping Chernobyl Move Towards Safe Decommissioning*, `https://spectrum.ieee.org/boston-dynamics-spot-chernobyl`, Accessed: 2024-01-28 (cit. on p. 54).

[258] C.-W. Huang, C.-H. Huang, Y.-H. Hung, and C.-Y. Chang, "Sensing pipes of a nuclear power mechanism using low-cost snake robot", *Advances in Mechanical Engineering*, vol. 10, no. 6, p. 1 687 814 018 781 286, 2018. DOI: `10.1177/1687814018781286` (cit. on p. 54).

[259] G. Darivianakis, K. Alexis, M. Burri, and R. Siegwart, "Hybrid predictive control for aerial robotic physical interaction towards inspection operations", in *2014 IEEE International Conference on Robotics and Automation (ICRA)*, 2014, pp. 53–58. DOI: `10.1109/ICRA.2014.6906589` (cit. on p. 54).

[260] R. A. Mattar and R. Kalai, "Development of a wall-sticking drone for non-destructive ultrasonic and corrosion testing", *Drones*, vol. 2, no. 1, 2018. DOI: `10.3390/drones2010008` (cit. on p. 54).

[261] VOLIRO, *Gravity-defying robots*, `https://voliro.com/`, Accessed: 2024-01-28 (cit. on p. 54).

[262] M. S. Alvissalim, B. Zaman, Z. A. Hafizh, *et al.*, "Swarm quadrotor robots for telecommunication network coverage area expansion in disaster area", in *2012 Proceedings of SICE Annual Conference (SICE)*, 2012, pp. 2256–2261 (cit. on p. 54).

[263] J. Iqbal, A. M. Tahir, R. ul Islam, and Riaz-un-Nabi, "Robotics for nuclear power plants — challenges and future perspectives", in *2012 2nd International Conference on Applied Robotics for the Power Industry (CARPI)*, 2012, pp. 151–156. DOI: `10.1109/CARPI.2012.6473373` (cit. on p. 54).

[264] Live Science, *This tiny radioactive battery can last 50 years without recharging*, `https://www.livescience.com/technology/engineering/betavolt-bv100-radioactive-battery-can-last-50-years-coming-in-2025`, Accessed: 2024-01-05 (cit. on p. 54).

[265] The Economic Times, *China develops groundbreaking nuclear battery that can last 50 years without charging*, `https://economictimes.indiatimes.com/news/international/business/china-introduces-revolutionary-nuclear-battery-that-lasts-50-years-without-charging/articleshow/106880627.cms?from=mdr`, Accessed: 2024-01-05 (cit. on p. 54).

[266] Israel Defense, *Hevendrones launches hydrogen-powered drone for commercial and defense use*, `https://www.israeldefense.co.il/en/node/57261`, Accessed: 2024-01-05 (cit. on p. 54).

[267] H. E. Baidoo-Williams, *Maximum likelihood localization of radiation sources with unknown source intensity*, 2016. arXiv: `1608.00427 [math.OC]` (cit. on pp. 57, 67).

[268] M. Popović, G. Hitz, J. Nieto, I. Sa, R. Siegwart, and E. Galceran, "Online informative path planning for active classification using UAVs", in *2017 IEEE International Conference on Robotics and Automation (ICRA)*, 2017, pp. 5753–5758. DOI: 10.1109/ICRA.2017.7989676 (cit. on p. 58).

[269] M. Popović, T. Vidal-Calleja, G. Hitz, *et al.*, "An informative path planning framework for UAV-based terrain monitoring", *Auton. Robot.*, vol. 44, pp. 889–911, 2020. DOI: 10.1007/s10514-020-09903-2 (cit. on p. 58).

[270] Hamamatsu, *What is an SiPM and how does it work?*, https://hub.hamamatsu.com/us/en/technical-notes/mppc-sipms/what-is-an-SiPM-and-how-does-it-work.html, Accessed: 2024-08-04 (cit. on p. 60).

[271] Eljen Technology, *Thermal neutron detection EJ-426*, https://eljentechnology.com/21-products/neutron-detectors, Accessed: 2022-02-28 (cit. on p. 60).

[272] L. Marques, A. Vale, and P. Vaz, "A mobile radiation detection system for security and defence", in *EDA research, technology, and innovation papers award 2023*. Brussels, Belgium: Publications Office of the European Union, 2023, pp. 40–47. DOI: 10.2836/568224 (cit. on p. 61).

[273] Scionix, *Scintillation-detectors*, https://scionix.nl/scintillation-detectors/, Accessed: 2022-02-28 (cit. on pp. 60, 217, 219, 221).

[274] BrightSpec, *Topaz-SiPM*, https://www.brightspec.be/brightspec/?q=node/45, Accessed: 2024-02-28 (cit. on pp. 61, 213).

[275] Septentrio, *GPS / GNSS + INS receivers*, https://www.septentrio.com/en/products/gnss-ins-receivers, Accessed: 2024-08-01 (cit. on p. 62).

[276] T. D. Institute, *Real-Time Kinematic and Differential GPS*, https://www.e-education.psu.edu/geog862/node/1828, Accessed: 2024-08-05 (cit. on p. 62).

[277] ESA, *Real time kinematics*, https://gssc.esa.int/navipedia/index.php/Real_Time_Kinematics, Accessed: 2024-08-05 (cit. on p. 62).

[278] Sparkfun, *Ultrasonic Distance Sensor - HC-SR04 (5V)*, https://www.sparkfun.com/products/15569, Accessed: 2023-02-28 (cit. on p. 63).

[279] Benewake, *TFmini-S 12m LiDAR Ranging Module*, https://en.benewake.com/TFminiS/, Accessed: 2023-02-28 (cit. on p. 63).

[280] DFRobot, *TFmini-S ToF Single-Point Ranging Solid State LiDAR Sensor*, https://www.dfrobot.com/product-1702.html, Accessed: 2024-08-16 (cit. on p. 63).

[281] I. P. Computing, *Distance sensors: The basics*, https://itp.nyu.edu/physcomp/distance-sensors-the-basics/, Accessed: 2024-08-05 (cit. on p. 63).

[282] Laboratoire National Henri Becquerel, *Table de radionucléides*, http://www.lnhb.fr/nuclides/Cs-137_tables.pdf, Accessed: 2023-06-05 (cit. on pp. 64, 114).

[283] D. Reilly, N. Ensslin, H. J. Smith, and S. Kreiner, "Passive nondestructive assay of nuclear materials", 1991-03. [Online]. Available: `https://www.osti.gov/biblio/5428834` (cit. on p. 65).

[284] National Institute of Standards and Technology, *Photon mass attenuation coefficient for dry air*, `https://physics.nist.gov/PhysRefData/XrayMassCoef/ComTab/air.html`, Accessed: 2023-07-01 (cit. on p. 65).

[285] National Institute of Standards and Technology, *Photon mass attenuation coefficient for iron*, `https://physics.nist.gov/PhysRefData/XrayMassCoef/ElemTab/z26.html`, Accessed: 2023-07-01 (cit. on p. 65).

[286] Mobile modular, *Shipping container wall*, `https://www.mobilemodularcontainers.com/blog/shipping-container-walls`, Accessed: 2023-07-01 (cit. on p. 65).

[287] K. D. McManus, "Radiological and nuclear threat detection using small unmanned aerial systems", Ph.D. dissertation, UC Berkeley, 2019. [Online]. Available: `https://escholarship.org/uc/item/7b241431` (cit. on p. 66).

[288] C. R. Rao, "Information and the accuracy attainable in the estimation of statistical parameters", in *Breakthroughs in Statistics: Foundations and Basic Theory*, S. Kotz and N. L. Johnson, Eds. New York, NY: Springer New York, 1992, pp. 235–247. DOI: `10.1007/978-1-4612-0919-5_16` (cit. on p. 68).

[289] D. B. Pelowitz, *MCNP6 USER'S MANUAL Version 1.0*. Los Alamos National Laboratory, 2013 (cit. on p. 71).

[290] L. Marques, A. Vale, and P. Vaz, "Development of a portable neutron detection system for security and defense applications", in *Developments and Advances in Defense and Security*, Á. Rocha, C. H. Fajardo-Toro, and J. M. Riola, Eds., ser. Smart Innovation, Systems and Technologies, vol. 328, Singapore: Springer, 2023, pp. 283–293, ISBN: 978-981-19-7689-6. DOI: `10.1007/978-981-19-7689-6_24` (cit. on pp. 71, 73–75, 78, 79, 81).

[291] Rochling, *Thermoplastics*, `https://www.roechling.com/industrial/materials/thermoplastics`, Accessed: 2022-03-05 (cit. on pp. 72, 73).

[292] 43D All for 3D printing, *How Much Filament Is Used in 3D Printing?*, `https://43dprint.org/how-much-filament-is-used-in-3d-printing/`, Accessed: 2022-03-10 (cit. on p. 72).

[293] 3D Realize, *PET-G properties*, `https://www.3drealize.com/petg-filament-material-properties-guide/`, Accessed: 2022-03-10 (cit. on p. 72).

[294] 3Dprint.pe, *Technical data sheet nylon*, `https://3dprint.pe/wp-content/uploads/2018/09/TDS_BCN3D_Filaments_Nylon.pdf`, Accessed: 2022-03-10 (cit. on p. 72).

[295] Troxler Electronic Laboratories, *Manual of operation and instruction model 3440 surface moisture-density gauge*, 2009 (cit. on pp. 76, 223).

[296] L. Marques, L. Félix, G. Cruz, *et al.*, "Neutron and gamma-ray detection system coupled to a multirotor for screening of shipping container cargo", *Sensors*, vol. 23, no. 1, 2023. DOI: `10.3390/s23010329` (cit. on pp. 82–86, 94–103, 105–109, 111, 112, 145).

[297] Laboratoire National Henri Becquerel, *Table de Radionuclides Am-241*, `http://www.lnhb.fr/nuclides/Am-241_tables.pdf`, Accessed: 2024-01-08 (cit. on p. 83).

[298] Laboratoire National Henri Becquerel, *Table de Radionuclides Cs-137*, `http://www.lnhb.fr/nuclides/Cs-137_tables.pdf`, Accessed: 2024-01-08 (cit. on p. 83).

[299] DJI, *Dji matrice 600 pro*, `https://www.dji.com/pt/matrice600-pro`, Accessed: 2022-02-28 (cit. on p. 89).

[300] E. Abelquist, J. Clements, A. Huffert, D. King, T. Vitkus, and B. Watson, "Minimum detectable concentrations with typical radiation survey instruments for various contaminants and field conditions", U.S. Nuclear Regulatory Commission, Tech. Rep. NUREG-1507, Revision 1, 2020, `https://www.nrc.gov/docs/ML2023/ML20233A507.pdf` (cit. on pp. 94, 118, 119).

[301] Secure Container Solutions, *Shipping container dimensions & sizes*, `https://www.securecontainer.ca/shipping-container-dimensions`, Accessed: 2024-01-05 (cit. on p. 114).

[302] L. Marques, R. Coito, S. Fernandes, T. Costa, A. Vale, and P. Vaz, "A mobile radiation detection system for security inspection and monitoring", *EPJ Web Conf.*, vol. 288, p. 06 001, 2023. DOI: `10.1051/epjconf/202328806001` (cit. on pp. 116, 118, 121–125).

[303] L. Marques, R. Coito, T. Costa, S. Fernandes, A. Vale, and P. Vaz, "Path optimization of a mobile radiation detection system in security inspection", in *Developments and Advances in Defense and Security*, Á. Rocha, C. H. Fajardo-Toro, and J. M. Riola, Eds., ser. Smart Innovation, Systems and Technologies, vol. 423, Singapore: Springer, 2025, pp. 293–305, ISBN: 978-981-96-0235-3. DOI: `10.1007/978-981-96-0235-3_24` (cit. on pp. 116, 117, 119, 120, 131).

[304] L. Marques, R. Coito, T. Costa, S. Fernandes, A. Vale, and P. Vaz, "Radioactive source localization using a mobile radiation detection system featuring informed path-based decisions", *IEEE Transactions on Nuclear Science*, vol. 71, no. 5, pp. 1064–1071, 2024. DOI: `10.1109/TNS.2024.3354461` (cit. on pp. 138–140, 143, 145–153).

[305] Raspberry Pi, *Raspberry Pi 3 Model B*, `https://www.raspberrypi.com/products/raspberry-pi-3-model-b/`, Accessed: 2023-02-28 (cit. on p. 214).

A

Uncertainties formulas

This Appendix presents the equations used to calculate the source activity uncertainty and intermediate uncertainties.

A.1 Intermediate uncertainties

A.1.1 Uncertainty of the estimated source-detector distance

$$\hat{d}_s = \sqrt{(x_d - x_s)^2 + (y_d - y_s)^2 + (z_d - z_s)^2} \tag{A.1}$$

$$\sigma_{\hat{d}_s} = \sqrt{\left(\frac{\partial \hat{d}_s}{\partial x_d}\right)^2 \sigma_{x_d}^2 + \left(\frac{\partial \hat{d}_s}{\partial y_d}\right)^2 \sigma_{y_d}^2 + \left(\frac{\partial \hat{d}_s}{\partial z_d}\right)^2 \sigma_{z_d}^2 + \left(\frac{\partial \hat{d}_s}{\partial \hat{x}_s}\right)^2 \sigma_{\hat{x}_s}^2 + \left(\frac{\partial \hat{d}_s}{\partial \hat{y}_s}\right)^2 \sigma_{\hat{y}_s}^2 + \left(\frac{\partial \hat{d}_s}{\partial \hat{z}_s}\right)^2 \sigma_{\hat{z}_s}^2} \tag{A.2}$$

$$\sigma_{\hat{d}_s} = \frac{1}{\hat{d}_s}\sqrt{(x_d - x_s)^2(\sigma_{x_d}^2 + \sigma_{x_s}^2) + (y_d - y_s)^2(\sigma_{y_d}^2 + \sigma_{y_s}^2) + (z_d - z_s)^2(\sigma_{z_d}^2 + \sigma_{z_s}^2)} \tag{A.3}$$

where x_d, y_d and z_d are the detector coordinates and σ_{x_d}, σ_{y_d} and σ_{z_d} the respective uncertainties. Similarly, $\hat{x_s}$, $\hat{y_s}$ and $\hat{z_s}$ are the estimated coordinates of the source and $\sigma_{\hat{x}_s}$, $\sigma_{\hat{y}_s}$ and $\sigma_{\hat{z}_s}$ their uncertainties.

A.1.2 Uncertainty of the estimated vertical distance

$$\hat{H}_s = |q_d - \hat{q}_s| \tag{A.4}$$

$$\sigma_{\hat{H}_s} = \sqrt{\left(\frac{\partial \hat{H}_s}{\partial q_d}\right)^2 \sigma_{q_d}^2 + \left(\frac{\partial \hat{H}_s}{\partial \hat{q}_s}\right)^2 \sigma_{\hat{q}_s}^2} \tag{A.5}$$

$$\sigma_{\hat{H}_s} = \sqrt{\sigma_{q_d}^2 + \sigma_{\hat{q}_s}^2} \tag{A.6}$$

where q_d and $\hat{q}_s$ are the coordinates of the source and detector, respectively, used to calculate the vertical distance and σ_{q_d} and $\sigma_{\hat{q}_s}$ are their uncertainties (depending on the face of the container, either the x or y coordinate can be used).

A.1.3 Uncertainty of the estimated lateral distance

$$\hat{D}_s = \sqrt{(q_d - \hat{q}_s)^2 + (z_d - \hat{z}_s)^2} \tag{A.7}$$

$$\sigma_{\hat{D}_s} = \sqrt{\left(\frac{\partial \hat{D}_s}{\partial q_d}\right)^2 \sigma_{q_d}^2 + \left(\frac{\partial \hat{D}_s}{\partial \hat{q}_s}\right)^2 \sigma_{\hat{q}_s}^2 + \left(\frac{\partial \hat{D}_s}{\partial z_d}\right)^2 \sigma_{z_d}^2 + \left(\frac{\partial \hat{D}_s}{\partial \hat{z}_s}\right)^2 \sigma_{\hat{z}_s}^2} \tag{A.8}$$

$$\sigma_{\hat{D}_s} = \frac{1}{\hat{D}_s}\sqrt{(q_d - \hat{q}_s)^2(\sigma_{q_d}^2 + \sigma_{\hat{q}_s}^2) + (z_d - \hat{z}_s)^2(\sigma_{z_d}^2 + \sigma_{\hat{z}_s}^2)} \tag{A.9}$$

where q_d and $\hat{q}_s$ are the coordinates of the source and detector which, together with the coordinates z_d and $\hat{z}_s$, are used to calculate the lateral distance and σ_{q_d} and $\sigma_{\hat{q}_s}$ their uncertainties (depending on the face of the container, either the x or y coordinate can be used).

A.1.4 Uncertainty of the estimated geometric efficiency

A.1.4.1 spherical detector approach

$$\sigma_{\hat{\varepsilon}_g} = \sqrt{\left(\frac{\partial \hat{\varepsilon}_g}{\partial r}\right)^2 \sigma_r^2 + \left(\frac{\partial \hat{\varepsilon}_g}{\partial \hat{d}_s}\right)^2 \sigma_{\hat{d}_s}^2} \tag{A.10}$$

$$\sigma_{\hat{\varepsilon}_g} = \frac{r}{2\hat{d}_s^{\,2}}\sqrt{\sigma_r^2 + \left(\frac{r\sigma_{\hat{d}_s}}{\hat{d}_s}\right)^2} \tag{A.11}$$

A.1.4.2 Cylindrical detector approach

$$\sigma_{\hat{\varepsilon}_g} = \sqrt{\left(\frac{\partial \hat{\varepsilon}_g}{\partial r}\right)^2 \sigma_r^2 + \left(\frac{\partial \hat{\varepsilon}_g}{\partial \hat{d}_s}\right)^2 \sigma_{\hat{d}_s}^2 + \left(\frac{\partial \hat{\varepsilon}_g}{\partial \hat{H}_s}\right)^2 \sigma_{\hat{H}_s}^2 + \left(\frac{\partial \hat{\varepsilon}_g}{\partial \hat{D}_s}\right)^2 \sigma_{\hat{D}_s}^2 + \left(\frac{\partial \hat{\varepsilon}_g}{\partial l}\right)^2 \sigma_l^2} \tag{A.12}$$

$$\sigma_{\hat{\varepsilon}_g} = \frac{1}{2\hat{d}_s^{\,3}}\sqrt{\frac{1}{\pi^2}\left[(\sigma_r(\hat{D}_s l + \pi\hat{H}_s r)^2 + \left(\frac{3\sigma_{\hat{d}_s} r(2\hat{D}_s l + \pi\hat{H}_s r)}{2\hat{d}_s}\right)^2 + (lr\sigma_{\hat{D}_s})^2 + (\hat{D}_s r\sigma_l)^2\right] + \left(\frac{r^2\sigma_{\hat{H}_s}}{2}\right)^2} \tag{A.13}$$

where r is the radius of the detector, l its length and σ_r, σ_l the respective uncertainties.

A.1.5 Uncertainty of the intrinsic efficiency and intermediate uncertainties

A.1.5.1 Uncertainty of the expected counts

$$\sigma_R = \sqrt{\left(\frac{\partial R}{\partial b_r}\right)^2 \sigma_{b_r}^2 + \left(\frac{\partial R}{\partial A}\right)^2 \sigma_A^2 + \left(\frac{\partial R}{\partial \varepsilon_g}\right)^2 \sigma_{\varepsilon_g}^2 + \left(\frac{\partial R}{\partial d_s}\right)^2 \sigma_{d_s}^2 + \left(\frac{\partial R}{\partial B}\right)^2 \sigma_B^2} \tag{A.14}$$

$$\sigma_R = \sqrt{e^{-2\mu_{ar} d_s}[(A\varepsilon_g \sigma_{b_r})^2 + (b_r \varepsilon_g \sigma_A)^2 + (b_r A \sigma_{\varepsilon_g})^2 + (b_r A \varepsilon_g \mu_{ar} \sigma_{d_s})^2] + B} \tag{A.15}$$

A.1.5.2 Uncertainty of the detector intrinsic efficiency

$$\sigma_{\varepsilon_i} = \sqrt{\left(\frac{\partial \varepsilon_i}{\partial C}\right)^2 \sigma_C^2 + \left(\frac{\partial \varepsilon_i}{\partial R}\right)^2 \sigma_R^2} \tag{A.16}$$

$$\sigma_{\varepsilon_i} = \frac{1}{R}\sqrt{C + \left(-\frac{C\sigma_R}{R}\right)^2} \tag{A.17}$$

where R are the expected counts with an intrinsic efficiency of 1, and C are the counts recorded by the detector.

A.2 Source activity uncertainty

$$\sigma_A = \frac{\sqrt{C + B + (C-B)^2 \left[\left(\frac{\sigma_{b_r}}{b_r}\right)^2 + \left(\frac{\sigma_{\hat{\varepsilon_g}}}{\hat{\varepsilon_g}}\right)^2 + \left(\frac{\sigma_{\varepsilon_i}}{\varepsilon_i}\right)^2 + \left(\frac{(\mu_{iron}-\mu_{air}) l_{cont}}{2}\right)^2 + \sigma_{\hat{d}_s}^2 \mu_{air}^2\right]}}{b_r \hat{\varepsilon_g} \varepsilon_i e^{-\mu_{air}(\hat{d}_s - l_{cont}) - \mu_{iron} l_{cont}}} \tag{A.18}$$

where C are the counts recorded by the detector, B the average value of the *background*, b_r the branching fraction of the 662 keV gamma rays, ε_i the intrinsic efficiency of the detector, μ_{iron} the attenuation coefficient of iron, μ_{air} the attenuation coefficient of air and l_{cont} the average thickness of the container.

B

Algorithms pseudo-codes

B.1 Source position estimation pseudo-code

Algorithm 1 Source position estimation and source activity calculation pseudo-code

for $i = 1$ to N **do**
  $r_d \leftarrow$ List of detector positions $[x_d, y_d, z_d]$
  $r_f \leftarrow$ Previous guess of the source position $[x_s, y_s, z_s]$
  $C \leftarrow$ List of counts measured by the detector
  $A \leftarrow$ Previous guess of the source activity
  $\lambda \leftarrow$ List of values of the variable given by (4.9)
  $L \leftarrow$ Log-likelihood function given by (4.13)
  $negative\_L \leftarrow -L$
  $\hat{r_f} \leftarrow$ Minimize($negative\_L$) using SciPy library of Python
  $A \leftarrow$ New value for the activity given by (4.16)
end for
return $\hat{r_f}, A$

B.2 Simulator pseudo-code

Algorithm 2 Simulator pseudo-code

r_f ←List of source positions, $[x, y, z]$;
A_0 ←Average value of source activity;
V ← Platform speed (of the radiation detection system);
r ←Detector radius;
l ←Detector length (if applicable);
ε_i ←Intrinsic efficiency of the detector;
t ←Time between measurements (equal to detector acquisition time);
$container\_dimensions$ ←List of container dimensions [length,width,height];
h_list ←List of trajectory heights $[h_1, h_2, ..., h_n]$; ▷ The dimension of this list is automatically the number of trajectories to be performed.
$safe\_distances$ ←List of safety distances for each path $[sd_1, sd_2, ..., sd_n]$;
λ ←Average value of the *background*;
$detector\_step \leftarrow V \times t$
for h **in** h_list **do**: ▷ Each *while* cycle corresponds to scanning each container side
    while x_d < length + safe_distance **do**: ▷ x_d is the x coordinate of the detector and "length" is the second x dimension of the container
        #First container side
        B ←**Poisson**(λ); ▷ Using the $random.poisson$ function from the $Numpy$ library
        C ←Counts in the detector according to the formulas and considerations in Section 4.5.4;
        MLE ▷ Runs MLE algorithm (Algorithm 1 of Appendix B);
        $x_d \leftarrow x_d + detector\_step$
    end while
    while y_d >-(width + safe_distance) **do**: ▷ y_d is the y coordinate of the detector and width is the second y dimension of the container
        #Second container side
        ... #Procedure analogous to the first container side
    end while
    while x_d >-safe_distance **do**:
        #Third container side
        ... #Procedure analogous to the first container side
    end while
    while y_d <-safe_distance **do**:
        #Fourth container side
        ... #Procedure analogous to the first container side
    end while
end for

B.3 Up and Down profit function pseudo-code

Algorithm 3 UD profit function pseudo-code

```
c ← List of counts
p_h ← Horizontal component of the detector's position vector
p_v ← Vertical component of the detector's position vector
v_h ← Horizontal component of the detector's velocity vector
v_v ← Vertical component of the detector's velocity vector
l ← 2.5 // Baseline threshold considered
b ← Average of the counts acquired at the start of the path (baseline)
j ← Moving average window
up_lim ← Path's upper limit
low_lim ← Path's lower limit
while This code runs once on each face of the container do
    c ← MovingAverage(c, window = j) [1]
    if v_h ≠ 0 then
        peak ← FindPeak(c)
        if Height(peak) > l × b then
            p_h ← horizontal component of peak's position
            v_v ← v_h / 2
            v_h ← 0
        end if
    else if v_v ≠ 0 then
        peak ← FindPeak(c)
        if Height(peak) > l × b then
            p_v ← vertical component of peak's position
            v_h ← v_v × 2
            v_v ← 0
        else if p_v ≥ up_lim then                                ▷ Starts to descent
            v_v ← −v_v
        else if p_v ≤ low_lim then
            p_v ← low_lim
            v_h ← v_v × 2
            v_v ← 0
        end if
    end if
end while
```

[1] The moving average calculation applied to the count list (*MovingAverage* function) acts as a low-pass filter, effectively smoothing out fluctuations in the data. This process is critical for peak identification (performed with *FindPeak* function), as it ensures that the detected peaks are more likely to originate from the radiation source rather than background noise. The window parameter, which defines the number of data points used in the moving average calculation, plays a key role in this process. A larger window results in greater attenuation of fluctuations but also introduces a delay in peak detection. In this thesis, a window size of 4 was chosen, as it offers an optimal balance between reducing fluctuations and preserving the integrity of the peak targeted for detection. Moreover, this choice minimizes the time delay in peak detection and consequently the path duration.

B.4 *STUD* profit function pseudo-code

Algorithm 4 STUD profit function pseudo-code

```
c ← List of counts
λ ← Wavelength
p ← Detector's position
v_h ← Horizontal component of the detector's velocity vector
l ← 4.0 // Baseline threshold considered
b ← Average of the counts acquired at the start of the path (baseline)
up_lim ← Path's upper limit
low_lim ← Path's lower limit
while This code runs once on each face of the container do
    if c > l × b then
        UpperAmplitudeLimit ← up_lim
        LowerAmplitudeLimit ← low_lim
        p ← SinusoidalMovement(UpperAmplitudeLimit, LowerAmplitudeLimit, λ, v_h) [2]
    else
        Continue with predefined path
    end if
end while
```

[2]The vertical component of the path's velocity during sinusoidal motion depends on the defined "wavelength" λ parameter defined for the sinusoidal movement, with maximum and minimum amplitude values constrained by the upper and lower limits of the path height. In this thesis, a wavelength of 2 m was considered, along with a horizontal component of the path's velocity v_h of 0.2 m/s and an upper and lower path height limits of 20 cm above the top of the container and a minimum height of 50 cm (safe distance from the ground), respectively, resulting in a vertical component of the path's velocity of 0.13 m/s ($\approx$ 0.1 m/s).

C

Topaz-SiPM Multichannel Analyzer device

C.1 Topaz-SiPM MCA characteristics

Figure C.1: Topaz-SiPM MCA device.

A summary of the Topaz-SiPM MCA device characteristics is shown in Table C.1.

Table C.1: TOPAZ-SiPM MCA characteristics. Adapted from [274].

TOPAZ-SiPM MCA characteristics
ADC with a spectral memory capacity of up to 4096 channels
Analog signal amplification capabilities (up to 16x).
Traditional trapezoidal shaper for digital pulse processing
Digital baseline restorer
Pile-up rejection mechanism
A 5V low-ripple (low-noise) power supply dedicated to the SiPMs preamplifiers

C.2 Topaz-SiPM MCA connections

With a power consumption of approximately 1.1 W, the TOPAZ-SiPM MCA is equipped with three connectors:

- A Lemo connector (type ERN.03.302.CLL) is utilized to capture the analog signals from the detectors and to supply power to the SiPMs integrated onto the scintillators (5V, 20 mA);
- A Lemo connector (type ERN.00.250.CTL) for programmable GPIO signals, which can be repurposed as an external counter input; and
- A USB Type Mini B connector to facilitate data output, device power supply, and control, leveraging platforms such as the Raspberry Pi model 3B. Therefore, the TOPAZ-SiPM MCA can be used for a single detector data acquisition (with analog or digital signals) or for the simultaneous reading of analog and digital electrical signals.

Given the availability of only one TOPAZ-SiPM MCA equipment, simultaneous reading of signals from both the EJ-200 plastic scintillator and neutron detection system require strategic connectivity (as shown in Figure 4.2). While the analog input of the TOPAZ-SiPM MCA was linked to the EJ-200 scintillator, the GPIO input was connected to the TTL output of the EJ-426HD neutron detector. Notably, the analog output of the EJ-426HD neutron detector (LEMO connection) was solely utilized for power-supply purposes, being connected to a +5 V plug available in the EJ-200 scintillator casing. Sensor data acquisition and processing was efficiently conducted using a Raspberry Pi 3B (connected to TOPAZ-SiPM MCA through a USB cable), a versatile single-board computer accessible remotely via Wi-Fi [305].

C.3 Topaz-SiPM MCA settings

The TOPAZ-SiPM MCA optimized settings used for each detector (analog input/output) are shown in Table C.2. For laboratory tests (static measurements) PHA mode was used, while Multi-Channel Scaling (MCS) mode was chosen for field tests (in motion measurements).

The neutron detector settings were only applied when it was connected to the analog input of TOPAZ equipment. Otherwise, the EJ-426HD neutron detector is connected to the GPIO input of TOPAZ equipment, and the analog signals are directly converted to digital pulses by the detector electronics.

Table C.2: Optimized parameters for the TOPAZ-SiPM MCA device considering different detectors

Parameters	**SiPM based ϕ110mm×30mm EJ-200 plastic scintillator**	**SiPM based ϕ51mm×51mm CsI(Tl) scintillator**	**SiPM based EJ-426HD (with ^{6}Li content) neutron detector**
MCA channels	1024	4096	1024
LLD	4	4	4
ULD	4095	4095	4095
Coarse gain	4 (2)	1 (0)	1 (0)
Fine gain	1 (0)	1.608 (2490)	1 (0)
Digital gain	x32 (5)	x128 (7)	x32 (5)
Input polarity	Negative (0)	Negative (0)	Positive (1)
Threshold	25	5	55-75
Rise time (μs)	2 (50)	3 (75)	2 (50)
Flat top (μs)	2.52 (63)	3 (75)	2.52 (63)
Poles/zeros (μs)	1 (25)	2.6 (65)	1 (25)
Digital BLR	On (1)	On (1)	On (1)
Pile-up reject	On (1)	On (1)	On (1)
High voltage status (V)	Off (0)	Off (0)	Off (0)

.

I

EJ-200 PLASTIC SCINTILLATOR

Scionix drawing: VS-1769-10, type: 110BA30/SIP-E3-P-X [273]. Dimensions are in mm.

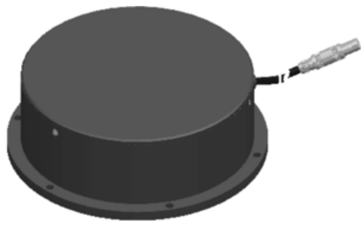

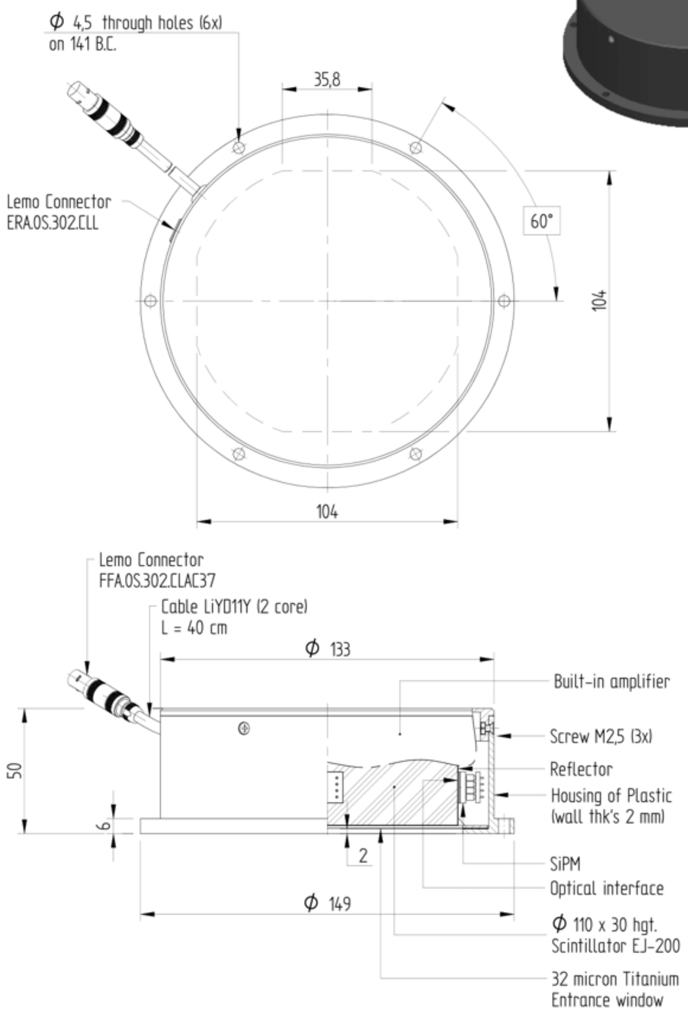

II

EJ-426HD PLASTIC SCINTILLATOR

Scionix drawing: VS-1579-20, type: R25*4B90/SIP(3)-EJ-426HD-X2 [273]. Dimensions are in mm.

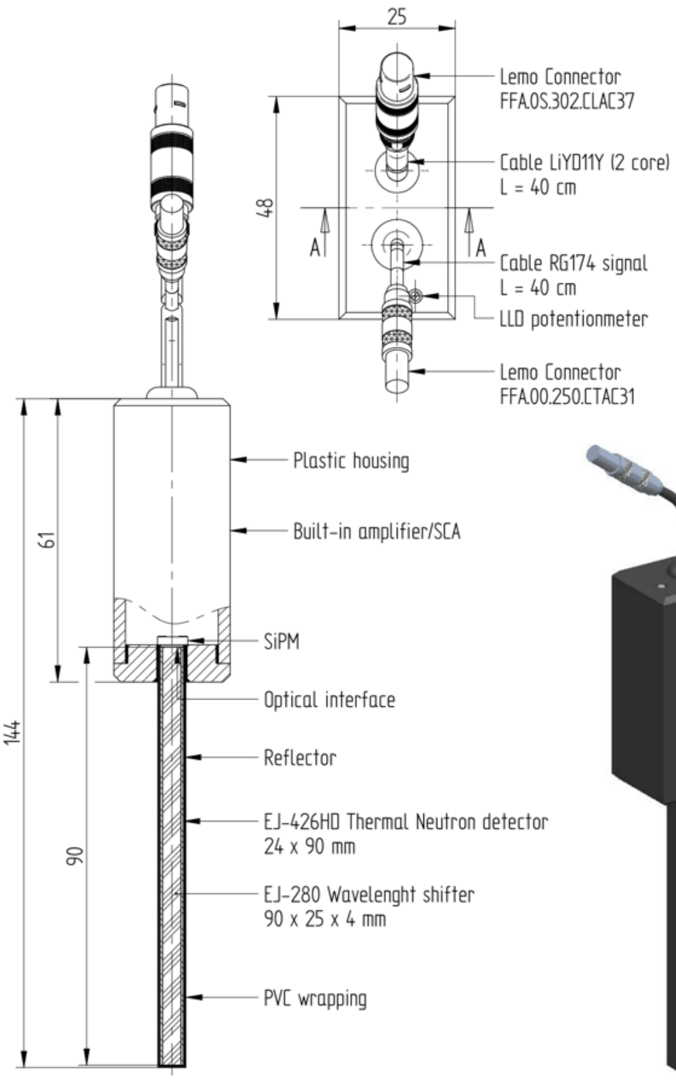

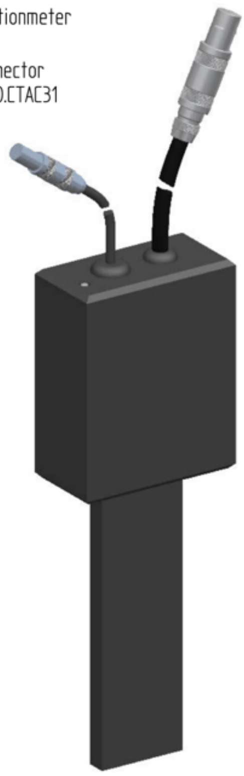

III

CsI(Tl) scintillator

Scionix drawing: VS-1593-20, type: 51B51/SiP-Cs-E3-X [273]. Dimensions are in mm.

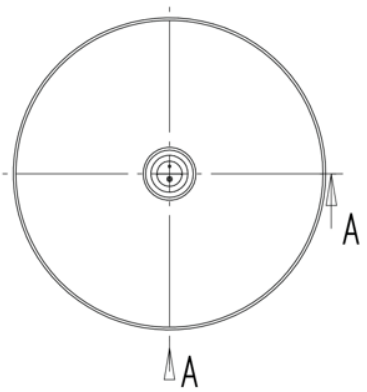

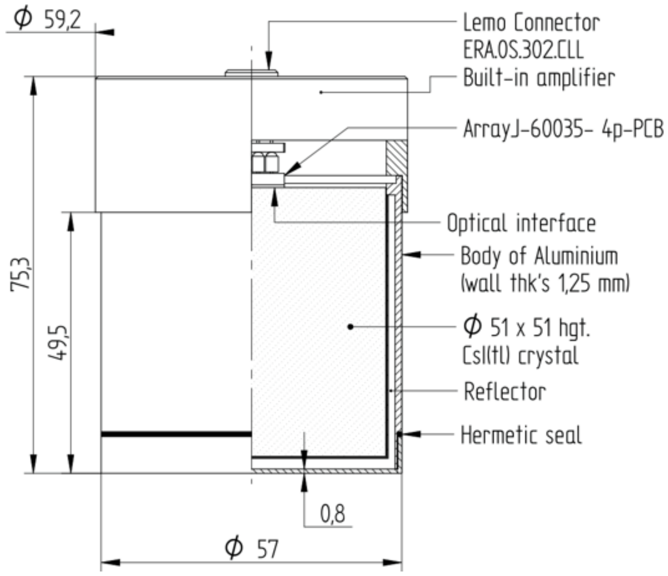

IV

Troxler equipment

Schematic and images of the Troxler equipment [295].

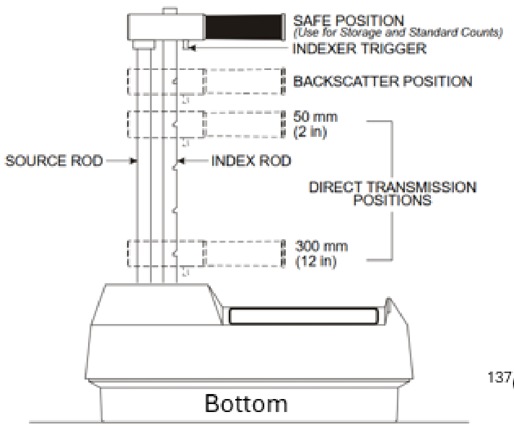

Source rod positions.

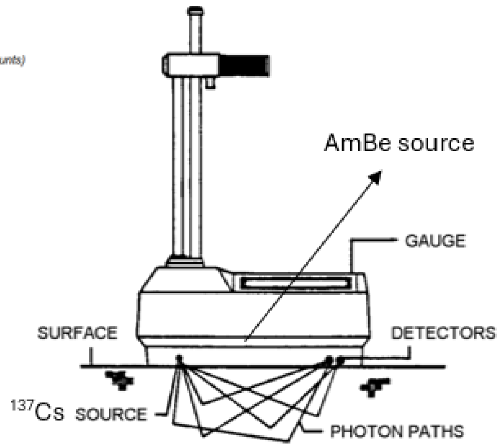

Backscatter geometry.

Troxler transporting case.

Troxler equipment inside the transporting case.